IMPROVING CORROSION AND WEAR RESISTANCE OF CARBON STEEL PIPING SYSTEM IN OIL AND GAS APPLICATION THROUGH THERMAL SPRAY COATING TECHNIQUES

MITRA AKHTARI ZAVAREH

FACULTY OF ENGINEERING

UNIVERSITY OF MALAYA

KUALA LUMPUR

2015

This thesis is dedicated to my parents.

For their endless love, support and encouragement

ACKNOWLEDGEMENT

First and foremost, I would like to thank God, the compassionate the merciful, for giving me the strength, self-confidence and inner peace to have made absolutely everything possible in this work.

Above all, I wish to express my immense gratitude and thanks to my dear supervisors, Associate Prof. Dr. Ahmed Aly Diaa Mohammed Sarhan and Dr. Bushroa Binti Abdul Razak for their valuable guidance, motivation, patience, and constant supports throughout the completion of this work.

I owe my deepest gratitude to my family, especially my beloved parents for their constant love, endless encouragement and support. Thanks to both for supporting me to study in Malaysia and follow my dreams. I wouldn't be who I am and where I am today without their overwhelming love, affection and blessing. My kind sisters, Maryam, Mehrnoosh and Parisa deserve my wholehearted thanks as well.

I would like to gratefully and sincerely acknowledge Meta-Tech and ULVAC companies for giving this chance to use their facilities for completing my project.

Thanks to all the people and friends who helped me in this work.

ABSTRAK

Dalam industri petroleum dan petrokimia, sistem luar pesisir dan darat perlu berfungsi dalam persekitaran yang agresif yang mendedahkan komponen peralatan pengeluaran untuk berbasikal terma, haus dan kakisan. Walaupun penyelenggaraan degradasi bahan dalam minyak dan gas adalah bahagian yang mahal, dalaman dan luaran peralatan dan saluran paip perlu juga diperiksa dan terus dikekalkan. Atas sebab ini kakisan yang sangat maju dan memakai-sistem pemantauan mesti dipasang di kawasan-kawasan kritikal kilang untuk mengesan paip dan peralatan daripada air laut dan minyak mentah. Oleh itu, penyelidik sedang mencari bahan dan kaedah canggih yang boleh diguna pakai dalam saluran paip minyak dan gas dan aksesori untuk meningkatkan masa kerja mereka.

Bersama kaedah pemprosesan pembuatan untuk meningkatkan permukaan paip dan aksesori kimpalan overlay atau pelapisan. Kaedah ini mempunyai beberapa batasan, seperti had untuk memilih bahan-bahan. Di samping itu, suhu yang tinggi menyebabkan kimpalan permukaan dikimpal mempunyai tegasan baki haba yang tinggi yang mungkin mewujudkan keretakan pada permukaan sampel. Suhu proses ini menyebabkan penyelewengan dalam substrat, mewujudkan halangan untuk ketebalan substrat. Kaedah ini juga memakan masa dan mahal. Walau bagaimanapun, kaedah salutan yang menyediakan gabungan ciri-ciri unik dengan kos yang rendah. Kaedah semburan haba adalah teknik semburan sejuk yang mempunyai tekanan agak kurang haba, tegasan baki dan kecacatan lain. Antara terma teknik salutan semburan yang berbeza, halaju tinggi bahan api oksigen (HVOF) dan plasma adalah proses penyemburan yang paling biasa haba lapisan untuk menghasilkan anti-haus dan kakisan salutan dengan pelbagai jenis bahan seperti logam, aloi, komposit seramik, dan lain-lain lagi, HVOF dan plasma terma disembur proses salutan mendorong mikrostruktur heterogeneities, yang meningkatkan kakisan dan rintangan haus. Dalam kajian ini, lima komposisi kimia yang

berbeza seperti aloi dan komposit seramik telah dipilih. Komposisi kimia adalah Inconel 625, NiCkolAY, Al8Si20BN, Cr_3C_2-25Cr dan Al_2O_3-13% TiO_2.

Untuk menyiasat sifat-sifat ini komposisi kimia, ujian polarisasi potentiodynamic, polarisasi litar terbuka dan spektroskopi impedans elektrokimia (EIS) telah digunakan dalam 3.5% penyelesaian NaCl (air laut) pada 30°C selama 30 hari. Kakisan juga diukur dengan menggantung sampel di dalam minyak mentah pada 60°C selama 30 hari. Mengukur potensi kakisan dan karat ketumpatan arus dari keluk polarisasi dan TEFAL cerun masing-masing ditubuhkan ranking kakisan umum bahan yang berbeza. Di samping itu, korelasi antara ciri mikrostruktur individu dan tindak balas elektrokimia mereka telah ditubuhkan oleh EIS termasuk pemodelan litar setara.

A harta haus setiap kumpulan bahan telah disiasat oleh mesin pin ke cakera dari suatu jarak gelongsor 9048,96 m di bawah beban yang berbeza. Kadar haus dan kehilangan berat Keputusan setiap bahan kumpulan mempunyai tingkah laku yang berbeza. Beberapa sampel lebih tahan lama semasa memohon beban yang berbeza dan kadar penurunan berat badan dalam sampel ini adalah sangat terhad.

Membandingkan semua kakisan dan memakai menggambarkan keputusan sampel komposit seramik mempunyai kakisan yang paling tinggi dan tingkah laku memakai rintangan. Yang kurang berkesan daripada sampel komposit seramik, sampel aloi bersalut menunjukkan besar anti-kakisan dan memakai tingkah laku.

ABSTRACT

In petroleum and petrochemical industries, offshore and onshore systems have to function in an aggressive environment that exposes the production equipment components to thermal cycling, wear and corrosion. Although maintenance of material degradation in oil and gas is costly, internal and external parts of the equipment and pipelines must be well inspected and continually maintained. For this reason highly advanced corrosion and wear-monitoring systems must be installed in the critical areas of the plant to protect pipes and equipment from seawater and crude oil. Therefore, researchers are in search of advanced material and methods that could be applied in oil and gas pipelines and accessories for increasing their working time.

The common manufacturing processing method for improving the surface of piping and accessories is overlay welding or cladding. This method has some limitations, such as its limitation for choosing materials. In addition, the high temperature of welding causes the final surface has some defects such as, thermal residual stress, cracking and distortion in the substrate. The method is also time-consuming and costly. However, the coating method provides a blend of unique properties with low cost. Thermal spray methods are cold spraying techniques that have a considerably less thermal stress, residual stress and other defects. Among different thermal spray coating techniques, high velocity oxygen fuel (HVOF) and plasma is the most commonly thermal spraying coating process to produce anti-wear and corrosion coatings with different types of materials such as metal, alloys, ceramic composite, etc. Furthermore, HVOF and plasma thermally sprayed coating process induces microstructure heterogeneities, which increase the corrosion and wear resistance. In this research, five different chemical compositions such as alloys and ceramic composite were chosen for increasing corrosion and wear resistivity of carbon steel piping. The chemical

compositions are Inconel 625, NiCrCoAlY, Al8Si20BN, Cr_3C_2-25NiCr and Al_2O_3-13%TiO_2.

For investigating properties of these chemical compositions, potentiodynamic polarization testing, open circuit polarization and electrochemical impedance spectroscopy (EIS) were used in 3.5% NaCl solution (seawater) at 30°C for 30 days. Corrosion was also measured by suspending the samples inside the crude oil at 60°C for 30 days. Measuring corrosion potential and corrosion current density from polarization curves and Tefal slope respectively established the general corrosion ranking of different materials. In addition, the correlation between individual microstructure features and their electrochemical response was established by EIS including equivalent circuit modeling.

A wear property of each group of materials was investigated by pin-on-disk machine over a 9048.96 m sliding distance under different loads. The wear rate and weight loss results of each group materials had a different behavior. Some samples were more durable during applying different loads and the rate of weight loss in these samples was very limited.

Comparing all the corrosion and wearing results illustrate that the ceramic composite samples have the highest to resistance corrosion and wear behavior. Significantly less effective than the ceramic composite samples, the alloy coated samples showed considerable anti-corrosion and wear behavior.

TABLE OF CONTENTS

LIST OF FIGURES

LIST OF TABLES

LIST OF SYMBOL AND ABBREVIATIONS

a	Crack length
AC	Alternating Current
AFM	Atomic Force Microscopy
AISI	American Iron and Steel Institute
Al_2O_3-13%TiO_2	Aluminum Oxide 13% Titanium Dioxide
ASTM	American Society for Testing and Materials
b	tafel slope
C	Monotonic effective shear strain
C	Capacitor
c	Experimental constants
C_{dl}	Capacitance of the double layer
CE	Counter Electrode
CO_2	Dioxide carbon
CPE	Constant Phase Element
CRAs	Corrosion Resistant Alloys
Cr_3C_2	Chromium Carbide
$CrNbO_4$	Chromium Niobate
Cr_2O_3	Chromium Oxide
Cr_3C_2-25NiCr	Chromium Carbide – 25 Nickel Chromium
D	Experimental constant in the low-cycle fatigue law
DC	Direct Current
E	Potential
E_{corr}	Corrosion Potential
E_{dl}	Electrical double layer

E_{oc}	Open circuit Potential
ECM	Electrochemical equivalent Circuit Modeling
EIS	Electrochemical Impedance Spectroscopy
Fe	Iron
Fe_3C	Cementite
$FeCO_3$	Siderite
FRA	Frequency Response Analyzer
GNP	Gross National Product
GPES	General Purpose Electrochemical Software
H_2	Hydrogen
H+	Hydrogen Ion
H_V	Hardness
HIT	Hilbert transforms Method
H_2O	Water
HRC	Rockwell Hardness
H_2S	Hydrogen Sulfide
H_2SO_4	Sulfuric Acid
HVOF	High Velocity Oxygen Fuel
Hz	Hertz
in	Inch
j	Current at any given potential
j_{corr}	Corrosion current
JCPDS	Joint Committee on Powder Diffraction Standards
K	Wear coefficient
KK	Kramers-Kronig Method
KPa	Kilopascal

kW	Kilo Watt
L	Sliding distance
LPR	Linear Polarization Resistance
m	Experimental constants
MPa	Megapascal
n	Experimental constants
N	Number of friction cycles
N_f	Critical number
NACE	National Association of Corrosion Engineers
NaCl	Sodium Chloride
Ni	Nickel
NiCr	Nickel Chromium
NiCoCrAlY	Nickel Cobalt Chromium Aluminum Yttrium
O_2	Oxygen
OCP	Open Circuit Potential
OH	Hydroxide
OH^-	Hydroxide Ion
Pa	Pascal
PD	Potential Difference
ppm	Parts per million
psi	Pound per square inch
Pt	Platinum
q	Charge stored at the capacitor (in coulombs)
R_a	Roughness
R_{ct}	Polarization resistivity

RE	Reference Electrode
R_p	Polarization Resistance
R_u	Solution Resistance
S	Sulphur
SAE 4140	Stainless steel Grade
SCC	Stress Corrosion Cracking
SCE	Saturated Calomel Electrode
SECM	Scanning ElectroChemical Microscopy
SEM	Scanning Electron Microscopy
SCFH	Standard Cubic Feet per Hour
Torr	torr
vol	Volume
WE	Working Electrode
XPS	X-ray Photoelectron Spectroscopy
XRD	X-ray Diffraction
W	Load
Z	Total Impedance
Z_C	Capacitor impedance
Z_L	Inductor impedance
Z_Q	Constant phase element impedance
Z_R	Resistor impedance
Z_W	Warburg resistor impedance
Z’	Real impedance
Z”	Imaginary impedance
α	Shape factor of an asperity
β	Degree of wear by abrasive asperity

^0C	Centigrade
e^-	Electron
°F	Fahrenheit
θ	Phase shift
ΔK	Change in the stress intensity factor
ω	Angular frequency
ω_s	Wear rate
f	Radial frequency
η	Overpotential
η_c	Cathodic over potential
η_a	Anodic over potential
μ	Friction Coefficient
μ_F	Microfarad
μ_C	Microcoulombs
μ_m	Micrometer
μ_{in}	Microinch
γ_t	Normalized shear strength

CHAPTER 1: INTRODUCTION

1. Overview

Offshore oil and gas production environments denote aggressive conditions in terms of erosion and corrosion. Up to 15% of failures amid oil and gas production are caused by erosion and corrosion, mainly in gravel packs, nozzles and Christmas trees, before hydrocarbons reach the first separator (Al-Odwani, Al-Tabtabaei, Al-Hashim, Carew, & Al-Atram, 2000; Stack & Abd El Badia, 2006). Such phenomena accelerate the metal deterioration rate through the combined action of mechanical erosion and electrochemical attack. This combined effect, often known as termed synergy, can lead to greater damage and higher metal loss rate beyond what occurs due to either erosion or corrosion alone, and consequently, it can considerably shorten the service life of components (D Toma, Brandl, & Marginean, 2001).

Accordingly, material selection must receive detailed attention in every stage of designing, constructing and operating the systems and equipment including piping systems and their accessories, such as bends, elbows, tees and valves (El Rayes, Abdo, & Khalil, 2013). Other significant devices are those that impart movement to fluid, such as pumps, impellers, propellers and blowers, which are exposed to, or transport particle-laden fluid like seawater (Y Wang, Li, Tian, & Yang, 2009). Thus, the specifications and use of materials that combine erosion and corrosion resistance with high mechanical strength are a fundamental requirement in the petroleum industry. For this reason, such materials have become of special interest in numerous research works.

In the petroleum industry, carbon steel is the most common material employed in piping both upstream and downstream. It is so popular mainly owing to the high performance and relatively low cost compared with highly alloyed materials (You Wang et al., 2000). Corrosion of carbon steels in CO_2-containing, oxygen-free aqueous

solutions are linked to the formation of layers of more or less corrosion protective products. In many cases, the surface layer contains siderite ($FeCO_3$) and cementite (Fe_3C). These deposits are neither compact nor dense (Antaki, 2008; Cooper, Slebodnick, & Thomas, 1996; Lucci, Demofonti, & Spinelli, 2011). Their protective effect depends on the aqueous solution's salt content, pH value, temperature, CO_2 partial pressure and flow velocity besides the chemical composition and microstructure of formation layer (Azarmi & Salimi, 2014). To protect oil piping from destructive phenomena, oil and gas companies have applied several different materials, including alloy steels, stainless steels, duplex stainless steel and nickel alloys. Alloy steel and nickel alloy seamless and welded pipes, tubes, fittings, plates, sheets and bars are produced into equipment to be used in the most demanding environments, from well bottoms through to refined product distribution (Craig & Smith, 2011).

Presently, the industry has access to the largest, most corrosion resistant casings, mechanical tubes, as well as coiled and straight length seamless and welded tubular products. Stainless steels and nickel alloys offer important environmental benefits. When properly selected, they facilitate the safe containment of oil and gas processing fluids. Their durability ensures long life, as replacement and resource demand are minimized with improving operating efficiencies. At the end of the structure's life, nickel alloys are completely recyclable. Overall, stainless steels and nickel alloys are exceptional lifecycle performers from both environmental and economic perspectives (Boussu et al., 2005; S. D. Cramer & Covino, 2006).

Generally, choosing suitable materials is an important factor in the resistance of instruments against environmental phenomena. Nonetheless, the method and fabrication of products are vital to prolonging product lifespan. Improving the quality of metallic and non-metallic coatings along with cladding or surface modifications are among the most common corrosion and wear prevention methods. Their effective implementation

depends on the careful selection and regular service monitoring of corrosion and wear. Corrosion prevention, monitoring and testing can save billions of dollars besides minimize hazards (Veazey, 2002(Craig, 1998).

For example, casings for high-pressure barrel pumps for seawater applications are typically forged in super duplex steel. The method used to fabricate this product has many disadvantages, such as difficulty forging thick casings in super duplex steel, problems achieving rapid and homogeneous cooling, insufficient corrosion resistance at high temperature, formation of brittle phases during welding, as well as high cost of raw material. Inhomogeneous cooling causes microstructural instability of ferritic austenitic phases and also the formation of brittle sigma phases, which lead to severe loss of impact strength, tensile ductility and corrosion resistance.

It is also difficult to ensure consistent mechanical properties across the entire thickness, particularly when greater casing wall thickness is required for high-pressure applications. Depending on the design requirements, dimensions may exceed the sizes with which related heat treatments and welding procedures can be applied. For certain casing designs, forged super duplex design is not an option at all. Welding nozzles and other big attachments to thick super duplex casing are also considerably difficult compared to carbon steel, due to challenges with post-weld heat treatment of large parts (Cooper et al., 1996; Davis, 2001; Eadie, Szklarz, & Sutherby, 2005).

Currently, the overlay method of applying alloys is used in vessels and pipes. In this process, coating is fused to a substrate surface via a welding process. Overlay welding is done by manual or automatic wire feed processing. However, with this method, the coating is diffused in the substrate but still has some disadvantages. First of all, the high temperature of wire welding causes substrate distortion; thus, depending on the thickness of welding, the substrate thickness must be increased. Also, in both manual and automatic methods, the final surface has a waved shape, and after one or

two welding passes, the sample surface needs to undergo turning and machining in preparation for the next welding passes. This is because the thickness tolerance with this method is not accurate and causes problems with adjusting and fixing vessels and piping, and thus depending on product application and tolerance, the number of turning processes differs. Also, the minimum coating thickness with this method is 2 mm after machining, so the amount of raw material used is very high (Cadenas, Vijande, Montes, & Sierra, 1997; Fernández et al., 2005; Sexton, Lavin, Byrne, & Kennedy, 2002).

Moreover, the rate of stress-corrosion cracking and pitting corrosion, especially with the manual method, is quite high. Manually, each worker performs differently; besides, there is human error during sample preparation with the automatic process. However, welding speed is controllable and adjustable, but one of the drawbacks of this method is that the tool used for welding is fixed during the process and the work piece should be moved and rotated. Therefore, a lathe machine or another machine should be utilized, which has this property of gripping and rotating the work piece (Galvan-Martinez, Salazar, Orozco-Cruz, Morales-Cabrera, & Contreras, 2013). Work piece and tool setup is also time consuming. But with the thermal spray method, the maximum coating thickness is 2 mm with a dense and homogenous surface. Turning is not necessary throughout and after completing the coating process.

In thermal spraying, the samples are fixed and the tool rotates and moves, even over long lengths. In small-diameter pipes, the tool enters the work piece and the nozzle is perpendicular to the handle and rotates 360^{o} to coat inside the samples (Cadenas et al., 1997; Sexton et al., 2002; Tucker Jr, 2013).

Generally, in the thermal spray process, deposited material is melted by a heat source generated at the spray torch nozzle. The heat source can be fuel gas or an electric arc. Thus, this process is very versatile to coat metals and non-metals on the substrate material for different purposes. After melting, the atomized material is accelerated by

pressured gas against the surface to be coated, reaching it in melted state (Review, 2000). When colliding with the substrate, the particles flatten and form fine flakes that adhere to the base material, resulting in a typical layer structure (coating). The coating adhesion is sufficiently high for use in several engineering applications. This layer is generally composed of oxides, inclusions, voids and porosities, while the final performance depends on metallographic aspects besides the nature of the environment and mechanical efforts (Kushner, 1992; Xie et al., 2004).

A major advantage of thermal spray coating is the ability to apply a coating to a substrate without significant heat. Thus, materials with very high melting points can be applied to final machined, fully heat-treated parts without altering the parts' properties or creating thermal distortion. A second advantage is the ability, in most cases, to strip and recoat worn or damaged coatings without changing the part properties or dimensions. The total coating thickness is often generated in multiple coating device passes, but the speed of this method is higher than welding (Sexton et al., 2002; Xie et al., 2004).

Flame spraying, electric arc spraying, plasma spraying, detonation gun spraying and high velocity oxygen fuel are the main thermal spray coating types (Davis, 2004). The deposition methods for corrosion and wear protective coatings are plasma spray and high velocity oxygen fuel (HVOF). Both of these methods have unique characteristics in terms of particle velocity and flame temperature, which result in coated layers with diverse microstructures and properties (Douglas, 2013; Xie et al., 2004).

High velocity oxygen fuel (HVOF) is one of the most common thermal spraying processes used to produce wear and corrosion resistant coatings. Alongside wear and corrosion resistant properties, the HVOF thermally sprayed coating process induces

microstructural heterogeneities that decrease corrosion and wear resistance properties (Lima, Moreau, & Marple, 2007; Tuominen et al., 2000).

The plasma spray process is additionally used for wear and corrosion protection, thermal insulation, repair and restoration. This is because it is the most flexible of all thermal spray process coatings, so it can be applied onto all suitable base materials with the widest variety of powders (Douglas, 2013; Xie et al., 2004).

In this research work, potentiodynamic polarization testing, electrochemical impedance spectroscopy and wear testing are used to determine if the combined results can provide a broader picture of the corrosion and wear processes occurring in HVOF and plasma coatings. Plasma and HVOF coatings are tested on five different microstructural compositions (i.e., Inconel 625, Nickel Cobalt Chromium Aluminum Yttrium (NiCoCrAlY), Aluminum silicon boron nitride (Al8Si20BN), Chromium Carbide – 25Nickel Chromium (Cr_3C_2-25NiCr) and Aluminum Oxide 13% Titanium Dioxide (Al_2O_3-13%TiO_2)).

Measurements of corrosion potential, corrosion current density and passive current density from polarization curves establish the general corrosion rankings of different materials. Polarization curve analysis reveals that without carefully considering the experimental details, significant errors can arise. Electrochemical Impedance Spectroscopy (EIS) including equivalent circuit modeling establishes the correlation between individual microstructural features and their electrochemical response.

The wear results of samples are also investigated by pin-on-disc machine under different loads. The wear rate and weight loss under normal loads in all cases are determined.

1.2 Aims and objectives

1) Improving corrosion and wear properties of oil piping by using different type of alloys and ceramic composite materials that coated by HVOF and Plasma coating techniques.

2) Investigating the corrosion properties of coated samples in seawater (3.5% NaCl) on 30°C and Crude oil on 60°C for 30 days.

3) Investigation the wear behavior of each coated materials under different loads (5,10, 15 and 20N)

4) Determine the optimum condition from the high coating performance.

1.3 Methodology

In this research electrochemical testing, wear testing; field emission scanning electron microscopy (FESEM) and X-ray diffraction (XRD) are the main testing components. Plasma and HVOF coatings of Inconel 625, NiCoCrAlY, Al 8Si20BN, Cr_3C_2-25%NiCr and Al_2O_3-13%TiO_2 are applied on carbon steel. Potentiodynamic polarization, EIS and wear testing are carried out on the coated samples. All potentiodynamic polarization tests are done with reference to open circuit potential (E_{oc}), where E_{oc} is the potential difference between the working electrode and reference electrode just before the potential scan starts.

1.4 Thesis structure

This thesis comprises five chapters, including an introduction as chapter one. A brief overview of the remaining chapters is provided next.

Chapter two presents a literature review with a summary of previous works carried out in the field. The basics of corrosion and types, electrochemical nature of corrosion, plasma and high velocity oxygen fuel coating processes, wear and types, as

well as wear testing and corrosion testing and monitoring, with more emphasis on electrochemical corrosion testing, are presented. This chapter also gives general information about potentiodynamic polarization testing and electrochemical impedance spectroscopy testing. Chapter three presents the experimental details, including the materials used, methods employed, equipment and procedures of conducting different experiments. The results and a discussion of the experiments with the plasma and HVOF methods are given in chapter 4. This chapter includes potentiodynamic polarization testing, electrochemical impedance spectroscopy and wear results under different loads. Conclusions of this research and recommendations for future work are presented in chapter five.

CHAPTER 2: LITERATURE REVIEW

2.1 Introduction

This literature review chapter covers background knowledge of the corrosion process, corrosion protection by HVOF and plasma coatings, the wear process, thermal spray techniques, selecting materials, electrochemical corrosion testing techniques and previous research in the field of electrochemical corrosion testing. The literature review is centered on choosing adequate materials to be exposed in aggressive conditions, such as the corrosive environment of seawater, as well as the wear conditions that can help control and protect oil piping from these phenomena.

2.2 Corrosion types

Corrosion is generally defined as the destructive disintegration process through which a metal is gradually destroyed by electrochemical reactions with the environment (Fantana, 1978). There is no hard and fast rule to classify corrosion, but it can normally be divided into two main groups, uniform and localized corrosion (Jones, 1996). In uniform corrosion, damage occurs on the entire surface at a uniform rate. In localized corrosion, damage occurs on localized spots due to heterogeneities in the material microstructure (galvanic, intergranular, dealloyed) and the environment (crevices, hydrogen damage). Localized stress (stress corrosion cracking, corrosion fatigue, fretting) and the geometry of closed chemical fluid flow system parts (erosion, cavitation) also cause localized corrosion damage (Perez, 2004; R.D. Angal, 2010).

Corrosion damage depends on the extent of particular factors, e.g. aggressive ions or stress amplitude. Figure 2.1 shows a comprehensive view of different types of corrosion taking place in various industrial environments (R.G, J.R, D.W, & R.G, 2002).

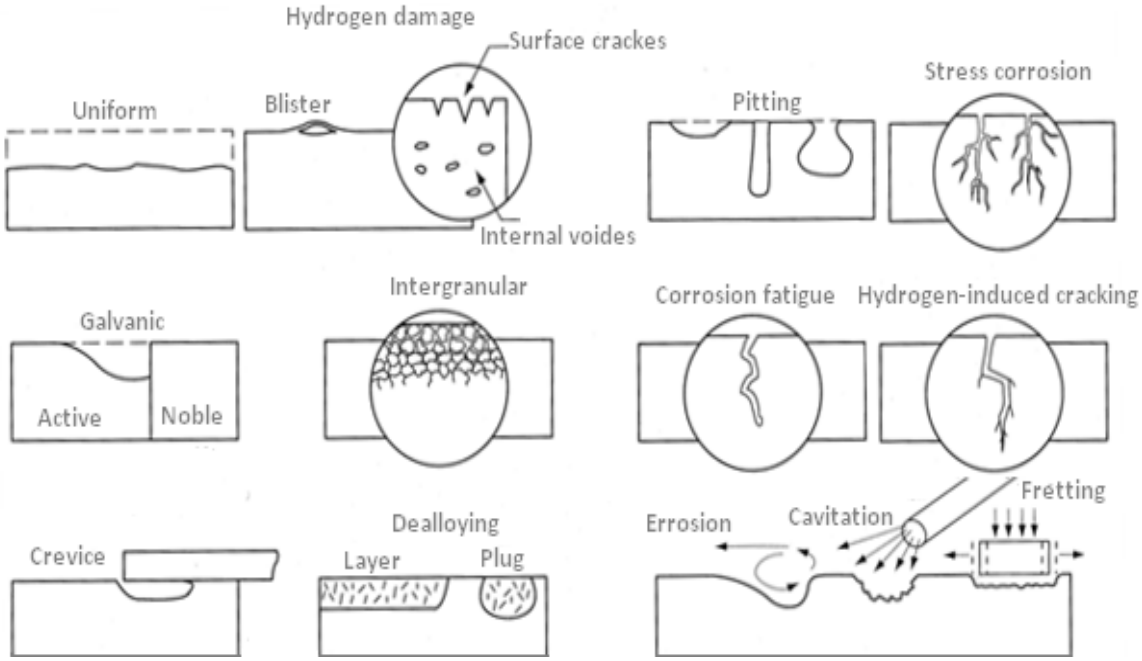

Figure 2.1 Types of corrosion in different industrial environments (Kelly et al., 2002)

2.3 Electrochemical nature of corrosion

Corrosion of engineering metals and alloys in aqueous environments is an electrochemical process. There are at least two reactions taking place in electrochemical corrosion, one being anodic and the other cathodic (Contreras, Albiter, Salazar, & Perez, 2005; S. D. Cramer & Covino, 2003). An anodic reaction entails metal dissolution to form ions and release electrons, as per equation 2.1.

$$M \xrightarrow{\textit{Metal oxidation}} M^{+} + ne^{-} \qquad 2.1$$

The main cathodic reaction is oxygen reduction (equation 2.2) is happened in neutral or alkaline environments (Contreras et al., 2005).

$$O_2 + 2H_2O + 4e^{-} \xrightarrow{\textit{Cathodic reaction (neutral and alkaline)}} 4OH^{-} \qquad 2.2$$

The overall corrosion reaction in neutral or alkaline environment is given in equation 2.3.

$$M(s) + O_2\,(g) + H_2O\,(l) \xrightarrow{\textit{Corrosion (neutral and alkaline sol.)}} M(OH)_n \qquad 2.3$$

In acidic environments, an anodic reaction entails the dissolution of metal to form ions as in neutral environments, but the dominant cathodic reaction is hydrogen evolution (equation 2.4).

$$2H+2e^{-} \xrightarrow{\textit{Cathodic reaction (Acidic)}} H_2 \qquad 2.4$$

The overall corrosion reaction in acidic environments comprises metal dissolution to form ions and evolve H_2 gas (equation 2.5). Metal ions can further react with anions to form metal salts or oxides (S. D. Cramer & Covino, 2006; Perez, 2004).

$$M(s) + (l) \xrightarrow{\textit{Corrosion (Acidic sol.)}} M^{+}(l) + H_2(g) \qquad 2.5$$

During electrochemical corrosion the anodic and cathodic reactions proceed simultaneously. The tendency of metal to corrode is defined by the standard electrode potential, the more negative the standard electrode potential the greater the tendency to corrode (Jones, 1996; Nicoletti, de Souza, & Barros, 2009). Figure 2.2 shows the electrochemical nature of corrosion by a drop of water on a metal surface. The dissolved oxygen is consumed and more rapidly replenished at the periphery of the drop via diffusion as compared to the center of the drop. Therefore the center of the drop acts as anode and periphery as cathode. The metal dissolution takes place at the center and oxygen reduction at the periphery of the drop. The metal ions further react with OH^{-} ions to form metal hydroxide, which if insoluble precipitates at the surface. The surface of the metal changes from center to periphery due to corrosion product. The metal hydroxide can further react with oxygen to form more stable corrosion product (e.g. oxides) (R.G et al., 2002; Review, 2000).

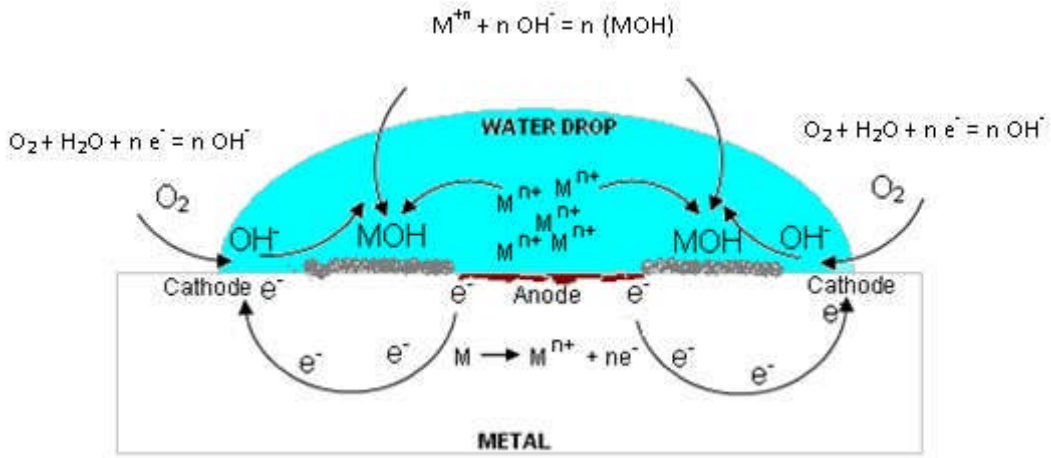

Figure 2.2 Corrosion by oxygenated water drop on metal surface (Ebbing et al., 1990)

2.4 Economic aspects of corrosion

Corrosion has huge economic and environmental impact on infrastructure worldwide like highways, bridges, oil and gas industries, chemical processing, as well as water and wastewater systems. Corrosion cannot be fully eliminated but its effects can be minimized by using different protection and prevention methods (S. D. Cramer & Covino, 2003). The direct cost attributed to corrosion damage has been estimated in the order of 3 to 4% of industrialized countries' gross national product (GNP) (S. Cramer et al., 1999; S. D. Cramer & Covino, 2006).

According to the National Association of Corrosion Engineers (NACE), the global corrosion cost, through direct and indirect losses, was $US 552 billion in 2001, which increased to $US 1.3 trillion in 2009 (Schmitt, 2009). Direct and indirect damage to the environment is massive if corrosion-related problems are overlooked in sensitive oil/gas industries and nuclear power plants. For instance, radiation and poisonous gas leakage due to severe pitting in nuclear plants can put workers' health at risk (Villalobos, 2005).

2.5 Corrosion protections and monitoring

Corrosion measurement and prevention covers a large field of technical activities, among which, measuring corrosion rate, controlling physical parameters like temperature, pH and pressure stress, protecting against corrosion like cathodic and anodic protection (Antaki, 2008; Parker & Peattie, 1984), chemical dosing, and prevention by material selection or organic/inorganic coatings. Measuring corrosion rate by weight loss is one of the corrosion testing methods commonly used since the past till now (Younis, Ensinger, El-Sabbah, & Holze, 2013). A material is exposed to an environment in which it needs to be in service for a prolonged time (90 days). The corrosion rate is measured from the net weight loss per unit time, i.e. difference in weight before and after the exposure divided by exposure time. In this way, corrosion damage can be assessed for the future by extrapolating the weight loss results. With advancements in electrochemical sensor technology, different sorts of resistance probes, linear polarization resistance probes and H_2 evolution probes are used for monitoring corrosion systems (Samples, 2002; Eckert, 2002).

Metallic and non-metallic coatings along with cladding or surface modifications are also common corrosion prevention methods. Their effective use depends on carefully selecting and regular service monitoring of corrosion. Corrosion prevention, monitoring and testing can save billions of dollars besides minimize hazards (S. D. Cramer & Covino, 2003; Ni, Ling, & Peng, 2005).

2.6 Wear and its types

Wear mechanisms are briefly classified as mechanical, chemical and thermal wear, while wear modes are classified into seven sub-classes. Some offer wear models and mathematical expressions for wear rate, but many still do not provide satisfactory

wear models and wear equations for reliable predictions. This section reviews current understanding on wear mechanisms and models (Koji Kato, 2000).

Wear is not a material property, but instead, a framework's reaction. The wear rate of a material can differ from 10^{-3} to 10^{-10} mm^3/Nm relying upon contact conditions, for example, partner material, contact weight, sliding speed, contact shape, suspension stiffness, environment and lubricant (K Kato, 2006).

The wear rate changes all through the rehashed contact process under consistent load and speed. It is for the most part high in an introductory unsteady state and generally brings down in the later steady state. Introductory wear and steady wear are the terms used to depict wear rate changes coming about because of rehashed contact. Lubrication lessens adhesive wear by decreasing attachment; on the other hand, it expands abrasive wear by diminishing the rubbing.

The exchange layer lessen adhesive wear when the grinding between the transfer layer and worn surface in air is low, for instance with poly tetrafluoro ethylene (Cai, Guo, Zhou, & Liu, 2013; X. Wang, Kwon, Schrock, & Kim, 2013). Early corrosive wear decreases ensuing corrosive wear when worn surfaces get to be smoother and adjust better (Koji Kato, 2000). Since wear is intricate, it must be considered as far as multi-parameter delicate phenomena.

Mechanical wear portrays wear represented primarily by the procedures of distortion and breaking. The misshapening procedure has a significant part in the general wear of pliable materials and the breaking procedure has a noteworthy part in the wear of fragile materials. Synthetic wear depicts wear represented basically by the development rate of a substance response film (Hoek, Bhattacharjee, & Elimelech, 2003; Y. Liu, Fischer, & Dent, 2003). Thus, synthetic wear is called 'tribochemical wear'. Thermal wear portrays wear administered primarily by neighborhood surface

dissolving because of frictional warming. Diffusive wear is additionally incorporated into the term 'warm wear', since it gets to be recognizable just at high temperatures. The wear of brittle materials brought on by cracks taking after thermal shocks might likewise be incorporated into thermal wear (C.-J. Li et al., 2007; G. Xu, He, Li, Wang, & Han, 2011).

Abrasive, adhesive, flow and fatigue wear are more graphic expressions for mechanical wear, and their wear procedures are outlined schematically in Figures 2.3(a), (b), (c) and (d), separately.

The abrasive wear of flexible materials is appeared in Figure 2.3(a). Three-dimensional wear models of surface scratching by a hard acrimony have been proposed and affirmed through quantitative assentions between exploratory results and hypothetical forecasts (K Kato, 2006; Koji Kato, 2000). The wear volume, V, is given by the accompanying expression (equation 2.6):

$$V = \alpha\beta\frac{WL}{H_V} \qquad 2.6$$

Where W is the heap, L the sliding separation, α the shape factor of an asperity and β the degree of wear by abrasive asperity. Tentatively, α takes an estimation of around 0.1 and β fluctuates somewhere around 0 and 1.0, contingent upon the level of entrance of a abrasive asperity, the shear strength at the contact interface, and the wearing material's mechanical properties. On the off chance that the wear rate is given by a specific wear rate, ω_s (= wear volume/load x sliding separation), or a wear coefficient, K (= $\omega_s H_V$), where H_V is the hardness), they are gotten from equation (2.6) as follows:

$$\omega_s = \frac{\alpha\beta}{H_V} \qquad 2.7$$

$$K = \alpha\beta \qquad 2.8$$

Equations (2.7 and 2.8), on the other hand, are only legitimate for single-abrasive scratching. A abrasive wear mode guide has been appeared to be helpful for abrasive wear rate expectation when different contacts are included, where the level of infiltration and the contact shear strength are conveyed among numerous asperity contacts keeping in mind the end goal to discover statistical values (Koji Kato, 2000). With respect to the adhesive wear of flexible materials, delineated schematically in Figure 2.3(b) (K Kato, 2006), no prescient hypotheses have been quantitatively affirmed by examinations. Suppositions have been made managing the unit volume of wear particles expelled from the unit contact locale (Knuuttila et al., 1998) yet they don't concur alright with exploratory information to give a premise for a quantitative hypothesis.

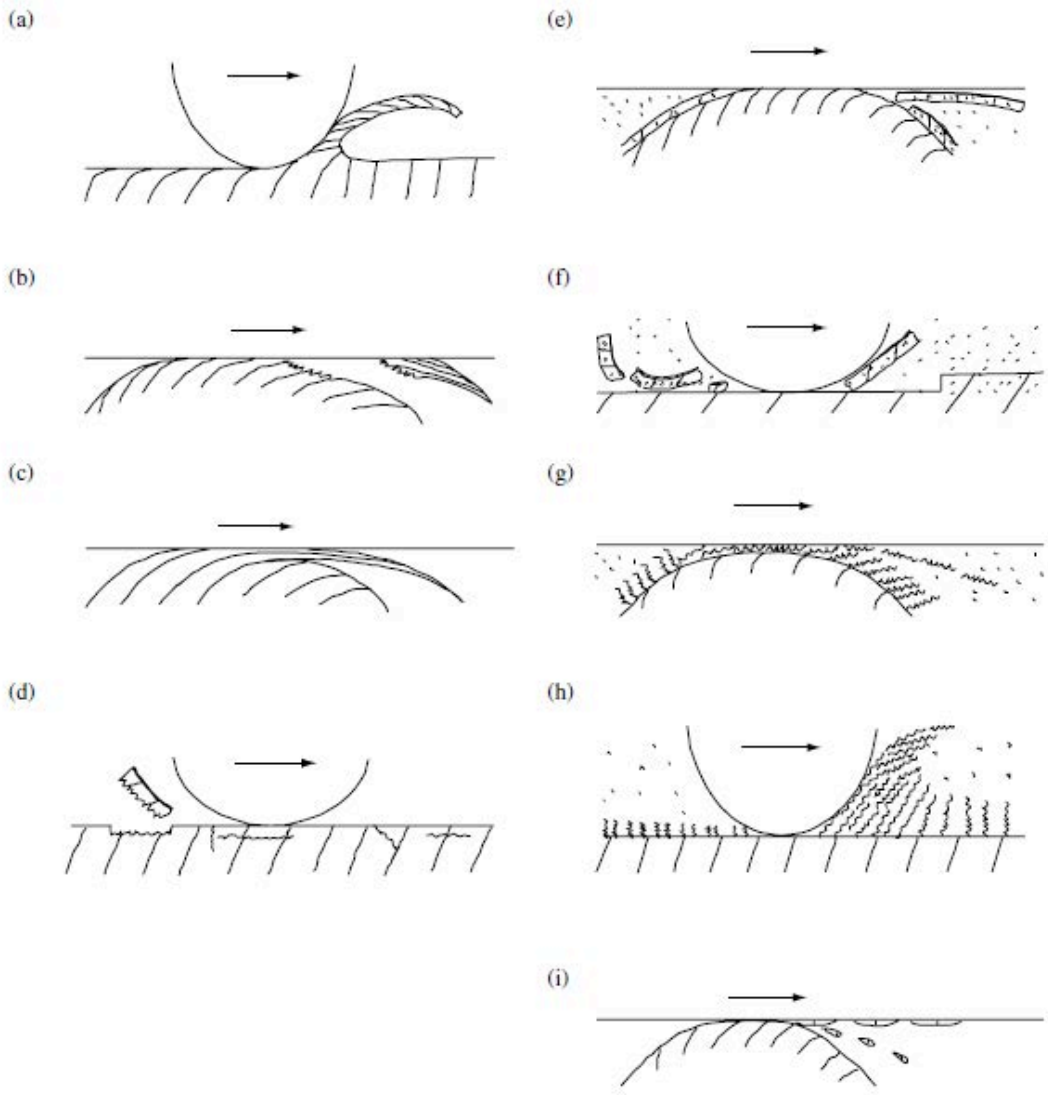

Figure 2.3 Schematic wear modes: (a) abrasive wear by miniaturized scale cutting a ductile bulk surface; (b) adhesive wear by adhesive shear and exchange; (c) flow wear by amassed plastic shear stream; (d) fatigue wear by split start and proliferation; (e) corrosive wear by shear fracture of a pliable tribofilm; (f) corrosive wear by delamination of a weak tribofilm; (g) corrosive wear by aggregated plastic shear stream of a delicate tribofilm; (h) corrosive wear by shaving of a delicate tribofilm; and (i) melt wear by neighborhood softening and exchange or diffusing (Hori & Kato, 2008)

Wear equations for adhesive wear are given by the accompanying expressions, which are like equation 2.6:

$$V = \omega_s WL \qquad 2.9$$

$$V = K\frac{WL}{Hv} \qquad 2.10$$

As per adhesive wear trial comes about, the wear volume increments directly with load and sliding separation. In any case, helpful physical models don't appear to

clarify the watched variety in ω_s and K values, where, for instance ωs fluctuated from 10^{-2} to 10^{-10} mm^3/Nm. Different factual variables, for example, material microstructure, surface roughness, flash temperatures, local contamination, adhesive exchange, free wear particles and small scale tribochemical responses on the contact surfaces, are all identified with the constants the neighborhood erosion coefficient values and contact material quality. It is important that the neighborhood-grinding coefficient is a component of the nearby shear strength at the contact interface and the nearby contact geometry.

Concerning flow wear, appeared in Figure 2.3(c) experimental perceptions of steel are clarified well by a hypothetical model called 'ratchetting', and the wear coefficient, K, is given as an element of the plasticity index, surface roughness and friction coefficient (You Wang et al., 2000). The subject of whether the wear of a spread like tribofilm covering a hard substrate could be dealt with as another type of stream wear stays unanswered.

If there should be occurrences of fatigue wear, high-cycle fatigue wear is anticipated first. In this wear mode, crack start and spread, as appeared in Figure 2.3(d), rule in a rehashed contact fatigue cycle. Fatigue conditions are thought to be either flexible or elasto-plastic. The wear molecule shape or unit wear volume is chosen from the crack propagation path. The basic number N_f of rolling cycles for surface spalling by high-cycle fatigue in a steel ball bearing is tentatively given by the accompanying mathematical statement:

$$N_f = bW^{-n} \qquad 2.11$$

Where W is the heap and b and n are experimental constants. The estimation of n is 3 for metal rollers. Its fundamental reason is that spalling can be dealt with as a statistical fracture phenomenon taking after the hypothesis of Weibull (Davis, 2001; Fervel et al., 1999).

In the event that the contact stress is at a level adequately high for plastic distortion to happen and rehashed contact cycles are required to create wear particles through crack initiation and proliferation, a Coffin–Manson-sort connection of the exhaustion crack can be utilized to demonstrate the low-cycle fatigue wear. The wear rate for this mode is hypothetically presented by making a two-dimensional abrasive wear model of the plastic wave arrangement (K Kato, 2006; Mann & Arya, 2001). The wear coefficient, K, is given as takes after:

$$K = \frac{9\times\sqrt{3}r\mu}{C^{D}\gamma_t^{-D}} \qquad 2.12$$

where r, μ and γt are all decided from the wave model as elements of attack angle and normalized shear strength of the contact interface, C is the monotonic effective shear strain and D a trial constant utilized as the force as a part of the low-cycle fatigue law. Wear should happen when strain gathers to a critical value, bringing about crack. Mathematical statement 2.12 gives the anticipated K worth running from 10^{-10} to 100 in connection to the adjustments in friction coefficient and asperity attack angle. This forecast appears to sensibly clarify some test results (Koji Kato, 2000; Shankar, Bhanu Sankara Rao, & Mannan, 2001).

The outcomes acquired from mathematical statements (2.11) and (2.12) depend on the test power law of fatigue fracture. The instrument of fatigue can be broke down through linear fracture mechanics to a sure degree. Additionally, the fatigue wear component can be comprehended by investigating the procedure of crack initiation and propagation in shaping wear particles.

The crack propagation rate is hypothetically figured from a model of a subsurface crack that is parallel to the surface and structures through linear fracture mechanics for elasto-plastic solids. The accompanying equation is proposed:

$$\frac{da}{dN} = C(\Delta K)^{m} \qquad 2.13$$

where *a* is the crack length, N the quantity of friction cycles, c and m are test constants and ΔK is the adjustment in stress intensity factor. The conceivable crack profundity and effective crack length are additionally computed with linear elastic fracture mechanics. On the other hand, in instances of steel sliding in air with a high friction coefficient (μ = 0.5) the quantity of critical friction cycles expected to create a void around a hard inclusion in the substrate was hypothetically computed as around 3 (K Kato, 2006; You Wang et al., 2000). This implies further hypothetical displaying of low-cycle fatigue wear could be progressed through the improvement of the split-spread hypothesis (equation 2.13). Then again, it is settled that the split start process and void nucleation procedure are the rate controlling procedures in high-cycle fatigue wear (Knuuttila et al., 1998).

2.7 Thermal spray coatings

It is a generic term for a group of processes in which metallic, ceramic, cermet and some polymeric materials in the form of powder, wire or rods are fed to a torch or gun that heats them to near or somewhat above their melting point. The resulting molten or nearly molten droplets of material are accelerated in a gas stream and projected against the surface to be coated (i.e., the substrate). On impact, the droplets flow into thin lamellar particles adhering to the surface, overlapping and interlocking as they solidify (Berndt & Berndt, 2003). The total coating thickness is usually generated in multiple passes of the coating device. The invention of the first thermal spray process is generally was attributed to in 1911 and was changes to being now known as flame spraying. Wire arc splashing, detonation gun deposition (concocted by R.M. Poorman, H.B. Sargent and H. Lamprey and licensed in 1955), plasma spray (concocted by Gage et al. in 1962) and high speed oxy-fuel (concocted by Smith et al., protected in 1958) etc. are other notable thermal spray procedures (Berndt & Berndt, 2003; Kushner, 1992).

A variation of plasma spraying is an exchanged arc to warm the surface being covered. It is considered by some welding procedure likened to hard facing instead of a genuine thermal spray process, on the grounds that the substrate surface turns out to be quickly liquid promptly underneath the torch (Davis, 2004; Douglas, 2013).

A noteworthy point of preference of thermal spray procedures is the to a great degree wide assortment of materials that can be utilized to make coatings. For all intents and purposes any material that melts without breaking down can be utilized. Another real point of interest is the capacity in most warm splash procedures to apply a covering to a substrate without significantly warming it. In this manner, materials with high melting points can be connected to at long last machined, completely heat-treated parts without changing the characteristics or thermal distortions of the parts. A third advantage is the ability, in most cases, to strip and recoat worn or damaged coatings without changing the part’s properties or dimensions. Also, applying thin coatings on low-cost substrates results in increased efficiency and cost savings. A noteworthy weakness of these deposition processes is that those only involves coating what the torch or gun can "see." Obviously there are additionally estimate impediments disallowing the covering of little, profound pits into which a torch or gun won't fit (Herman & Sampath, 1996; Kushner, 1992).

The system of particles clinging to the surface is not surely known but rather is accepted to be to a great extent. This is due to fact that mechanical interlinking of the solidifying and contracting particles, with asperities on the surface being covered unless supplemental combination or dissemination heat treatment is utilized. Surely, most thermal spray coatings require a scratched substrate surface for satisfactory holding. Some bury dissemination or limited combination of as-stored coatings with the substrate has been seen in a couple occurrences with special mixes of coatings and substrates (Douglas, 2013).

There is confirmation of synthetic holding in` few covering/substrate frameworks, which is not absurd when the high-speed effect of particles may be relied upon to rupture any film on either the powder molecules or the substrate. What's more, van der Waals forces may assume a part if the substrate is to a great degree clean and no noteworthy oxidation happens amid testimony. Thermal spray are normally shaped by various torch or gun passed over the surface (Dejang et al., 2011; Pasandideh-Fard et al., 2002).

A coating can be made of essentially any material that can be liquefied without breaking down. Besides, the testimony forms itself can generously modify the material piece and additionally structure. Thus, the coating's microstructure and properties can vary extremely (Trompetter et al., 2006; Vardelle et al., 1995).

Coating specifications must therefore regularly include more than essentially expressing the beginning powder or wire composition and general procedure type to be utilized. Restrictions of the thermal spray coating process include maximum coating thickness restriction to few millimeters, thin machine parts that cause problems holding them, and surface positions in narrow/awkward places where the coating torch cannot reach (Davis, 2004; Xie et al., 2004).

The utilizations of thermal spray coatings are to a great degree changed, yet the vital use classes include upgrading surface wear and/or erosion resistance. Different applications incorporate their utilization for dimensional reclamation, as thermal obstructions, thermal conduits, and electrical channels or resistance, for electromagnetic protecting, and improving or retarding radiation. Thermal spray coatings are utilized in for all intents and purposes each industry, including aviation, farming, car, essential metals, mining, paper, oil and gas creation, chemicals and plastics, and biomedicine. Figure 2.4 outlines the primary strides in the thermal spray covering procedure (Oksa et al., 2011).

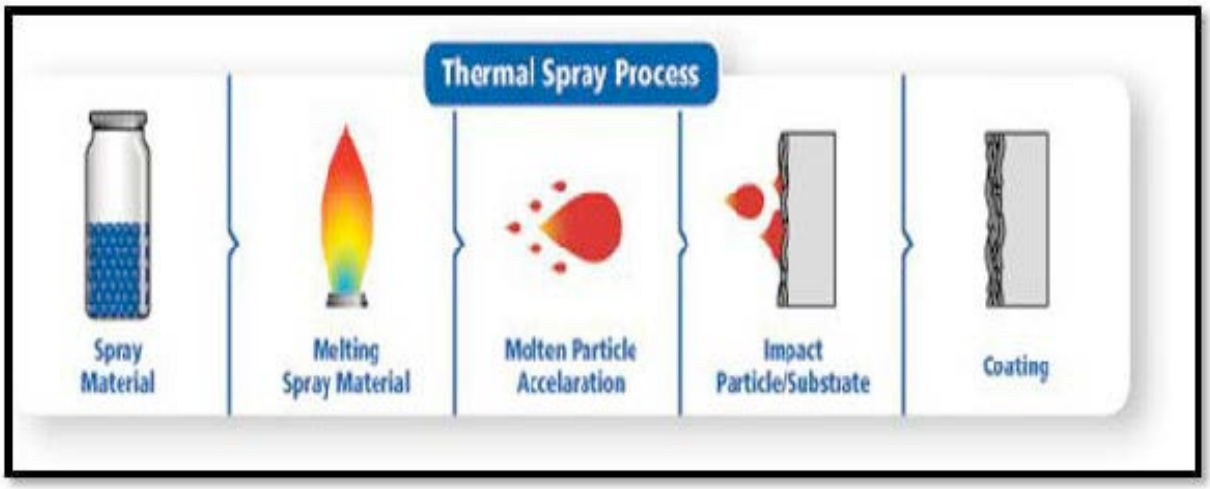

Figure 2.4 Schematic diagram of thermal spray coating process (Oksa et al., 2011)

2.7.1 Plasma Spray

A plasma spray torch schematic is shown in Figure 2.5. A gas, for the most part argon, also including nitrogen, hydrogen, or helium in some cases, is permitted to stream between a water-cooled copper anode and a tungsten cathode. An electric arc is started between the two anodes through a high recurrence release and is then managed utilizing a powder (Berndt, 2001; Liu et al., 2003).

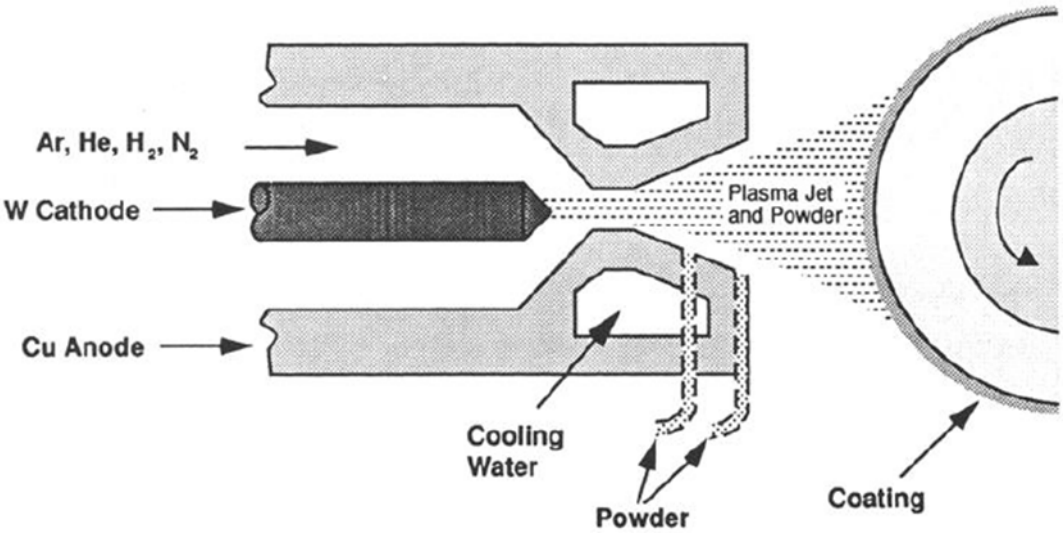

Figure 2.5 Plasma sprays process (Courtesy of Praxair Surface Technologies, Inc)

The arc ionizes the gas, making high-pressure plasma. The subsequent increment in gas temperature, which may surpass 30,000^{o}C, thus expands the gas volume and consequently its pressure and speed as it leaves the nozzle. Gas speed, which may be supersonic, ought not be mistaken for molecule speed (Dejang et al., 2011; Herman & Sampath, 1996). Power levels in plasma splash torches for most part range from 30 to 80 kW, reaching as big as 120 kW. Argon is generally picked as the foundation gas in light of the fact that it is chemically inactive and has great ionization qualities. Including the diatomic gasses, hydrogen or nitrogen can build the gas enthalpy.

Powder is generally brought into the gas flow either simply outside the light or in the separating way out locale of the nozzle (anode) (Davis, 2004; Dejang et al., 2011; Pasandideh-Fard et al., 2002). The powder is warmed and quickened by the high-temperature, high-speed gas plasma flow. Torch working parameters and design are vital in deciding the speed and temperature achieved by the powder molecules. The working items incorporate not just gas stream, power level, powder feed rate, and bearer gas flow, additionally the separation from the substrate (standoff) to the torch and the deposition angle. Standoff is of significant importance in light of the fact that satisfactory separation must be accommodated warming and quickening the powder, yet excessive separation will permit the powder to cool and lose speed as the gas stream is quickly extending, chilling & moderating off (Pawlowski, 2008; Vardelle et al., 1995; Xie et al., 2004).

The size and morphology of powder particles emphatically impact their rate of warming and speeding up and thus, the effectiveness of testimony and covering quality. As often as possible, a to some degree higher cost for powder with more tightly size appropriation is more than adjusted for by the enhanced deposition effectiveness. Powder speeds as a rule accomplished in plasma splash deposition range from around

300 to 550 m/s. Temperatures are frequently at the melting point or marginally above. By and large, higher temperatures and molecule speeds over the melting point however without extreme super-heating, yield coverings with the most astounding densities and bond qualities. Plasma spray coating densities are regularly in the scope of 80 to 95% of hypothetical density ((Geaman et al., 2014; Laul et al., 2001; Pasandideh-Fard et al., 2002; D Toma et al., 2001).

Notwithstanding powder speed and temperature, a third, essential variable is the extent of the reactivity between the process gasses and powder particles or encompassing environmental gasses amid deposition. With ordinary plasma splashing in air, the degree of oxidation of the powder particles is a component of the particular torch design, standoff and working parameters. Broad oxidation of metallic and carbide powders can bring about exceptional lessening in covering density, cohesive quality and bond power with associative changes in execution. Either viable gas covering of the effluent or spraying in a diminished pressure, inert gas chamber, can essentially wipe out such oxidation.

Straightforward inert climate chamber spraying can likewise be utilized to bind hazardous materials, which are gathered into two classifications: toxic and pyrophoric. Poisonous materials incorporate beryllium and its compounds. Pyrophoric materials incorporate magnesium, titanium, lithium, sodium and zirconium, which tend to burn promptly when in finely isolated structure or when sanitized by the plasma process. A basic inert air chamber spray framework may incorporate a jacketed water cooled chamber, a sealed area, a plasma framework, work piece handling gear, glove ports, a vacuum pumping framework and an inert gas backfill manifold. Ordinarily, the chamber is pumped down to a pressure of 0.001 to 0.01 Pa, then backfilled with high purity dry argon. In any great latent gas chamber, oxygen levels can be effectively kept up underneath 30 ppm. Through the same system, some oxide powders tend to in part

lessen when splashed in an inert gas chamber ((Berndt, 2001; Berndt & Berndt, 2003; Davis, 2004; Pasandideh-Fard et al., 2002).

Inert climate spraying in a low-pressure chamber offers a few one of a kind focal points over customary plasma spraying in inert air at atmospheric pressure. Attributable to the lower pressure, the plasma gas stream temperature and speed profiles stretch out to more noteworthy separations, so the covering properties are less delicate to standoff (Dejang et al., 2011; Laul et al., 2001). Moreover, the substrate can be preheated without oxidation, permitting better control of residual stress and superior bond strength. Deposition efficiency can be expanded with broadened molecule stay time in a more drawn out plasma-heating zone and higher substrate temperature. The closed framework additionally minimizes ecological issues, for example, dust and noise. Figure 2.6 demonstrates normal inert environment and/or low pressure plasma chamber (Pasandideh-Fard et al., 2002; Pawlowski, 2008).

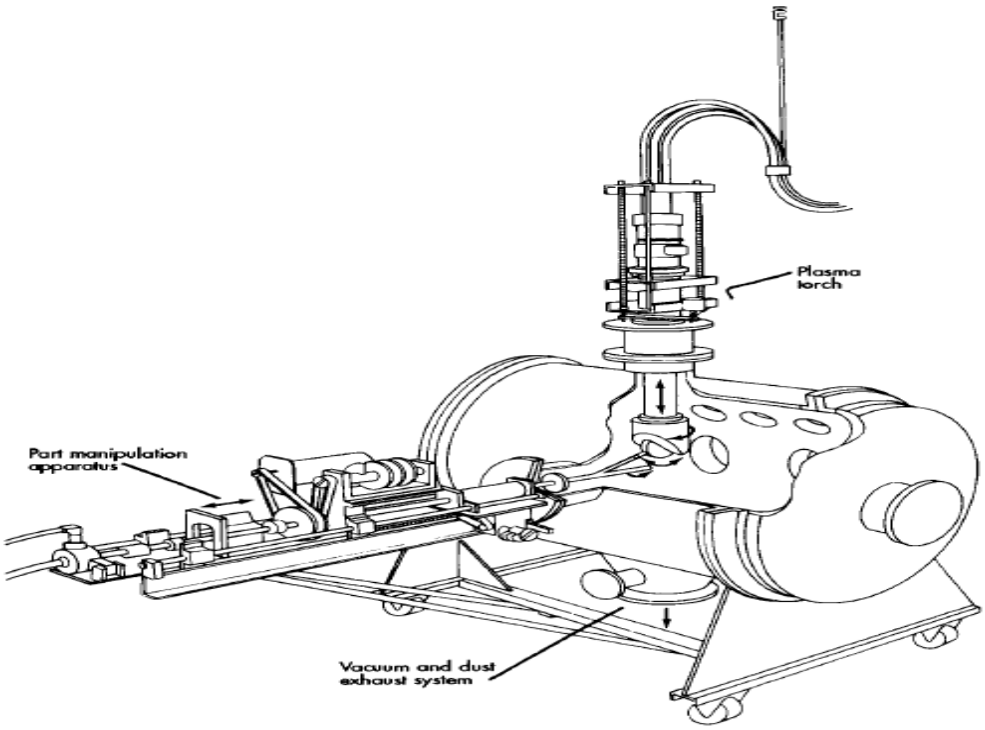

Figure 2.6 Typical inert-atmosphere and/or low-pressure plasma chamber (Courtesy of Metco, Inc)

Typical working methodology needs the spray chamber pumped down to generally low pressures as noted above, or be over and over cycled in the wake of pumping to roughly 55 Pa (0.4 Torr) and after that refilled with inert gas to around 40 kPa (300 Torr). Once the system has been adequately cleansed to accomplish a satisfactory inert environment, the plasma spray operation is actuated and the chamber pressure is changed in accordance with the desired level for spraying (Toma et al., 2001; Vardelle et al., 1995).

The optimum spray condition exists when the plasma temperature at the substrate approximates the melting point of the powder particles; be that as it may, ideal spraying conditions shift with the chemistry and molecule size of every spray material. These variables are like those of conventional plasma spraying. On account of the multifaceted nature of low pressure splashing, PC is used to guarantee complete reproducibility and consistency all through the covering best controls the whole process. Utilizing load/lock pre-pumping and venting chambers and mechanical technology can build productivity (Laul et al., 2001; Xie et al., 2004).

Plasma spray utilizing a latent gas cover around the plasma gas effluent can be pretty much as compelling in averting oxidation amid depostion while spraying in an inactive gas, low pressure chamber. Plasma shower has been utilized widely to splash NiCoCrAlY composites as undercoat on turbine blades, vanes, external air seals and thermal obstructions. Contrasted with chamber spraying, it has much lower capital cost however more prominent affectability to standoff. It is hard to preheat the substrate to high temperatures without oxidizing the substrate a method utilized with low pressure chamber spray to control the residual stress in some high-temperature, oxidation-resistant coatings.

Then again, residual stress in these coatings can in any case be controlled when controlling so as to utilize inert gas covering the deposition rates, assistant cooling etc. (Douglas, 2013; Toma et al., 2001; Xie et al., 2004).

2.7.2 High Velocity Oxygen Fuel Coating (HVOF)

Union Carbide conceived the high velocity oxygen fuel process in 1958. HVOF has brought significant development to the field of thermal spray coating over the last 3 decades (Davis, 2001). Updates include equipment design modifications, process automation and modeling to estimate particle velocity and melting (Kato, 2006; Kushner, 1992).

A schematic perspective of a HVOF gadget is appeared in Figure 2.7. Fuel, usually propane, propylene, methyl acetylene propadiene propane (MAPP), or hydrogen, is blended with oxygen and blazed in chamber (Herman & Sampath, 1996).

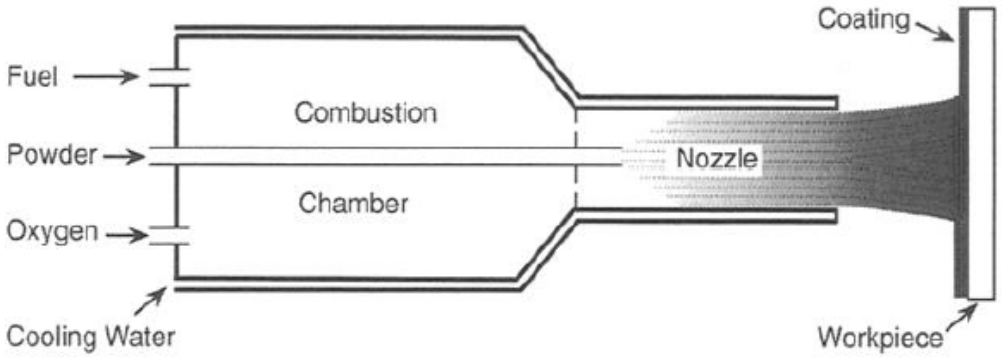

Figure 2.7 High-velocity oxygen fuel process (Courtesy of Praxair Surface Technologies, Inc.)

In different cases, liquid kerosene may be utilized as fuel and air as oxidizer. The combustion resultants are permitted to grow through a nozzle where the gas speeds may get to be supersonic. Powder is presented in the nozzle, usually pivotally, and it is warmed and accelerated. The powder is normally completely or somewhat dissolved and accomplishes speeds of up to around 550 m/s. Since the powder is presented to the

combustion products, it may dissolve in either an oxidizing or reducing environment, and critical oxidation of metallic parts and carbides is conceivable (Eadie et al., 2005) With fitting hardware, working parameters and decision of powder, coatings with high density and bond strengths as often as possible surpassing 69 MPa (10,000 psi) are achievable. Covering thickness as a rule ranges from 0.05 to 0.50 mm (0.002 to 0.020 in.), yet generously thicker coatings can occassionally be utilized with a few materials when necessary. Coatings delivered by HVOF procedure show low porosity and oxidation (<2%) because of the quick travel and high effect of the powder particles with the substrate surface (Al-Fadhli et al., 2006; Wang et al., 2000).

HVOF procedures can deliver coverings of practically any metallic or cermet material, and in some cases, most earthenware production. Those few HVOF frameworks that utilization acetylene as fuel requires applying the highest melting point earthenware production, for example, zirconia or some carbides. To date, HVOF coatings have essentially been utilized for wear resistance, however their field of use is extending (Davis, 2004; Douglas, 2013).

2.7.3 Microstructure of HVOF and Plasma coating

Coating produced by HVOF and plasma processes is characterized by lamellar structure embedded with solid particles, oxide and inclusions (surface residue from shot blasting or surface cleaning) (Eadie et al., 2005). The schematic in Figure 2.8 shows the main components of such coatings. Molten or semi-molten particles deform upon hitting the substrate. Deformed particles in the coating are called splats and are approximately 1-20 μm thick. The high striking speed of particles produces compact coating, but some voids/pores still form at the surface and inter-lamellar particle boundaries (Al-Fadhli et al., 2006; Tang et al., 2014). The impaction of solid particles at high speed also adds strength due to the peening effect (relieving tensile stress or adding compression by low level mechanical stresses). The high temperature and

presence of oxygen in the environment also causes the formation of oxides. The adhesion between substrate and coating is predominantly by mechanical interlocking (Marple et al., 2007).

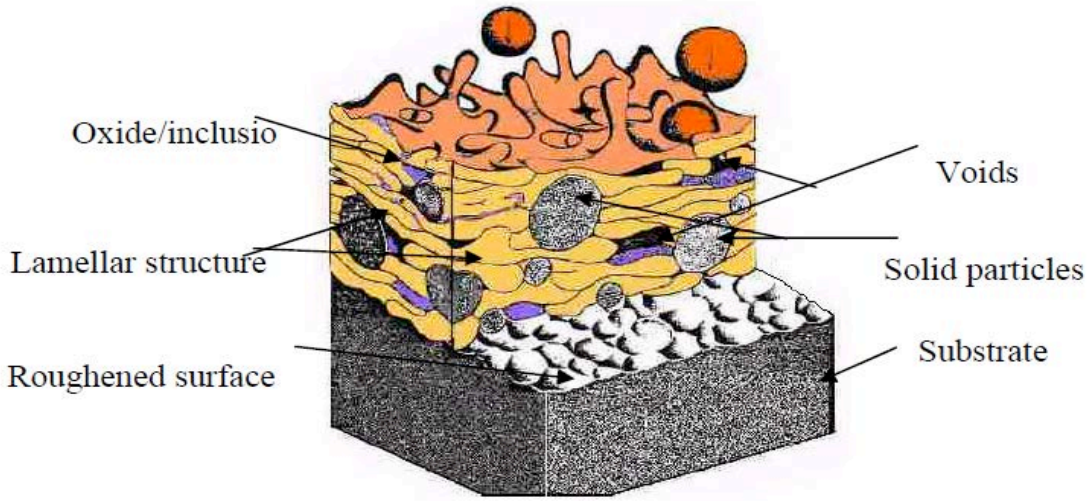

Figure 2.8 Schematic showing typical microstructure of Plasma and HVOF coating (Davis, 2004)

2.7.4 Surface Preparation

One of the main steps in thermal spray coating is surface preparation, because for adequate thermal spray coating bonding, a surface with proper conditions is critical. Surfaces required being perfect, and for the most part substrates must be roughened subsequent to cleaning by coarseness impacting or different means. Clearly, the surface must stay uncontaminated by oil from taking care of gear or body oil from hands and arms after it is readied. It is prescribed to coat the readied surface instantly after arrangement to keep the likelihood of pollution or surface oxidation (Dejang et al., 2011; Kushner, 1992).

2.7.4.1 Cleaning and Degreasing

Rust or other corrosion items, oil, oil or different greases, and paint or other surface contaminants must be got rid of before covering deposition starts. Scratching,

wire brushing, machining, grit blasting, or compound activity can remove these. Consideration ought to be taken not to install scales and so forth in the surface when attempting to get rid of them, especially when utilizing grit blasting. Dissolvable degreasing has been the most well-known strategy for uprooting greases and body oils, most helpfully with vapor degreasers (Fauchais et al., 2010; Fervel et al., 1999). Huge parts and parts with connected equipment that may be harmed by vapor degreasing, ought to be degreased physically utilizing the minimum risky material accessible. Properly secured personnel who are prepared to utilize the solvents and follow neighborhood regulations for solvent utilization, care and handling, should utilize those in very much ventilated territories. Lately, there has been an expanding pattern towards utilizing fluid cleansers and soluble cleaners, some of the time with ultrasonic unsettling, to stay away from dangers and ecological worries with organic solvents (Pawlowski, 2008).

2.7.4.2 Surface Roughening

Three strategies for surface roughening for thermal splashing are generally utilized: rough threading, grit blasting, and a mix of rough threading took after by grit blasting. Rough threading is by and large utilized on tube shaped surfaces and with thick flame showered coatings. The part to be arranged is mounted in a machine and a solitary thread cut is made (Boussu et al., 2005).

Grit blasting hardware utilized for thermal spray ought not be utilized for different purposes, on the grounds that soil, paint and oil debasing the grit can redeposit on the grit-blasted surfaces (Hoek et al., 2003; Mumtaz & Hopkinson, 2009). The grit ought to be persistently renamed to uproot fine particles. The air supply to the grit blasting gear must be perfect and dry (counting oil and particle straining). Aluminum oxide and chilled iron are the most broadly utilized abrasive grits for thermal spray

surface readiness. In any case, sand, smashed steel and silicon carbide are likewise utilized as a part of a few circumstances. Sand is ordinarily utilized on huge outside structures, for example, extensions, towers and funneling, where coarseness recuperation is unreasonable (Davis, 2004; Mumtaz & Hopkinson, 2009; Bowen & Doneva, 2000).

Additionally, the substrate ought to be cleaned taking after grit blasting to evacuate residual dust. Neat, dry air may be utilized. Once more, it is critical for the surface to be free of oil from taking care of hardware or body oil from hands and arms. It is prescribed that the readied surface covered as quickly as time permits after readiness to forestall surface oxidation or pollution (Boussu et al., 2005; Douglas, 2013).

2.7.5 Coating Finishing

However thermal spray coatings are used for some application without any surface finishing. But for some service conditions, their surfaces are too rough. For this reason grinding, lapping, polishing, machining, abrasive brushing, or vibratory finishing are a most common techniques that usually finishes their surface. However must be careful during these process otherwise can be pulled out of coating particles or make a cracks (Pasandideh-Fard et al., 2002; Pawlowski, 2008).

The last surface complete that can be accomplished with a thermal spray covering is depend on two main factors, one of them is amount and size of porosity in the deposited layers and another one is cohesive strength or particle to particle bonding within the coating. On the off chance that a covering is to be fixed, the fixing ought to be done before any completing operation. Because removing finishing debris is quite difficult from unsealed samples. Also these debris is be embedded in the surface and

make a abrasive wear during service. Generally lower feed rate are normally used for wrought materials (Laul et al., 2001; Lima et al., 2007).

For soft materials such as zinc, tin mostly used burnishing, while cermet and ceramic coatings require grinding. Likewise cubic boron nitride or diamond wheels could be required for the hardest coatings (Lima et al., 2007; Marple et al., 2007; Takahashi et al., 2002). If the final surface is not enough smooth by grinding machine, it may be necessary to lap the coating after grinding (Takahashi et al., 2002).

2.8 Thermal spray process modification and corrosion behavior

An important application of HVOF and plasma coatings is dynamic components in various off-shore oil and gas industrial equipment (Parker & Peattie, 1984). In service.9, these components are subjected to severe cyclic loading in aggressive environments. Consequently, investigating the fatigue properties of HVOF and plasma coatings is of utmost importance. This has led to considerable studies that have being carried out to investigate various parameters affecting the fatigue properties of HVOF and plasma-coated surfaces (El Rayes et al., 2013).

Some parameters such as speed of powder particles, oxygen/fuel ratio, transvers speed and thickness of coatings directly affect to properties of deposited layers. For example when the coating materials is longer exposed to the high temperature, the deposited layers has homogeneous microstructures, that causes the corrosion resistivity of deposited layer considerably increased (El Rayes et al., 2013).

Suegama et al. (2004) investigated the corrosion behavior of Cr_3C_2 -25%NiCr that coated by HVOF on mild steel substrate at two different transvers speeds. The results show that the sample that coated by 1000 mm s^{-1} gun transverse speed was higher corrosion resistivity (100mV) than the sample that coated by 500 mm s^{-1} gun transverse speed (Suegama, 2004).

Guilemany et al. (2002) investigated the effect of thickness of coating in corrosion resistivity of product. The impedance spectroscopy, voltammetry and potential polarization results was shown, when the thickness of deposited layer was very thin, the electrolyte passed through interconnected porosity that exist in the deposited layer. While residual thermal stress in the thick coating causes to make cracks on the deposited layer, which alloyed the electrolyte penetrate to the coated layer and reduce the corrosion resistivity of coated layer (Guilemany et al., 2002).

2.9 Corrosion Resistant Alloys

In oil and gas, many components such as valve, wellhead, Xmass tree, exchanger and so on exposed to the harsh environments and causes the long life of equipment significantly decreased. For this reason choosing a suitable alloys that have a specific properties depend on environment is essential for increasing corrosion resistivity of equipment (Craig & Smith, 2011).

2.9.1 Selection of corrosion resistant alloys (CRAs)

The selection of Corrosion Resistant Alloys is an important step that is directly affected on the long life system. Therefore any mistakes for choosing the materials it make some issues for system (S. D. Cramer & Covino, 2003). Companies with high research facilities, first simulate a certain part of the field environment under study. Then a group of alloys selected some different alloys based on the available information. Then test all the candidate alloys at the same time and finally choose the best alloys for a certain condition. This method can easily take 1-3 years to accomplished at significant cost (S. D. Cramer & Covino, 2006; Eadie et al., 2005).

Another selection method is review literature on corrosion data that generally applied to the expected fiels. It is quickest and cheapest technique because neglected some group of alloys that is not suitable for specific condition. Then the selected alloys

tested under specific condition (Craig & Smith, 2011; Ni et al., 2005). However the chance of error in this method greater than previous method, for example introducing potential for CRAs failure or using a more expensive alloy than required (Antaki, 2008; Reza Javaherdashti, 2013).

Other resources for material selection are using available standards, such as the 2003 ISO 15156 publications derived from the previous NACE 0175 publication for "sour service". ANSI/NACE MR0175/ISO 15156 gives general information for service in oil and gas productions and in natural gas sweetening plants in Hydrogen sulfide (H_2S)-containing environments. Also recommended some materials in the appropriate design codes, standards and regulations. Generally it can be applied to help avoid costly corrosion damage to the equipment itself (Juchniewicz, Jankowski, & Darowicki, 2000; Reza Javaherdashti, 2013; Rigney & Schilke, 1975; Younis et al., 2013).

Finally, before accepted the final CRAs for specific condition, it is necessary to simulate the field of environment or analysis the effective cost of several control alternatives (S. D. Cramer & Covino, 2006; Eadie et al., 2005).

2.9.2 Environmental parameters for selecting CRAs

Temperature, Chloride ion concentration, CO_2 and H_2S, environment pH, and the presence or absence of Sulphur (S) is some parameters that directly affect to the corrosion properties of alloys (S. D. Cramer & Covino, 2003; Lucci et al., 2011).

These parameters cause the risk of stress corrosion cracking (SCC), rate of metal solution from pits and other things is considerably increased (Lucci et al., 2011; Ni et al., 2005).

Generally three items directly affect to the corrosion rate of sample, temperature, pressure and the chloride content in sodium chloride. In order to make the

scale for these parameters is universal, centigrade (°C), pounds per square inch, psi and gram/liter or percent for each item use respectively (Ni et al., 2005; R.D. Angal, 2010).

Also the absence of oxygen is critical to the application of these alloys under the conditions shown. While if the environment has a oxygen (typically greater than 10 parts per billion), the other alloys should be consider (Lucio-Garcia et al., 2009; Selman, 2011).

According to the information presented above, nickel alloys have a long life for oil and gas process fluids. Also it has a high performance and relatively low cost and at the end of the structure's lifecycle, nickel alloys are completely recyclable. For this reasons, this alloy is offer for both of environment (Parker & Peattie, 1984; R.D. Angal, 2010).

2.9.3 Nickel alloy

Depend on the condition of environment; the behavior of each material is different. For this reason choosing the correct material is very important step for increasing the longevity of product. For example Nickel alloy 625 has a higher corrosion resistivity in CO_2/NaCl environment and decreased the cracking problem. Also this alloy is not very perceptive to chloride concentration, unless the amounts of chloride are considerably high (Al-Fadhli et al., 2006; Arafin, Medraj, Turner, & Bocher, 2007).

Duplex stainless steel is more sensitive to presence of chloride ion and has a resistivity in H_2S environment; while Nickel alloy 625 has a limitation by H_2S content and temperature. Figure 2.9 is based on data derived from environments containing relatively high chloride levels (i.e. approximately 25,000 to 100,000 ppm) (Ganesh et al., 2010; K. Mumtaz & Hopkinson, 2009).

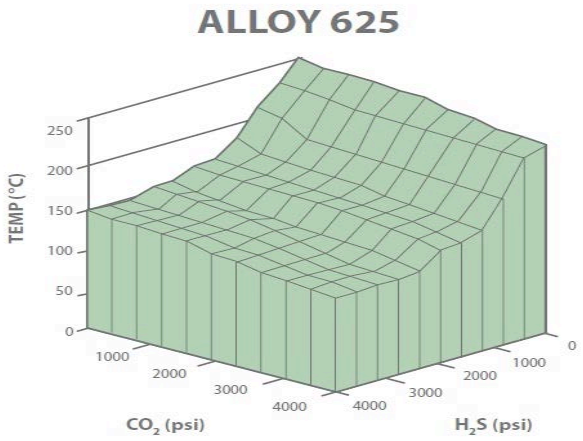

Figure 2.9 Corrosion resistance of Alloy 625 Stainless steel in H_2S/CO_2 environments in the absence of elemental Sulphur. Corrosion rate of ≤ 0.05mm/yr (2mpy) and no SCC (Nesic et al., 2010)

Sulphur is one of the component of some gas stream that significantly effect on this alloy and causes the sever pitting and catastrophic cracking happened for this, in comparison a free Sulphur condition. (Z. Liu, Cabrero, Niang, & Al-Taha, 2007; Paul et al., 2007).

2.10 Selecting the material and composition powder for thermal spray coating

The material selected should cover and protect the inside of oil piping from wear and corrosion in different situations (Craig, 1998). The basis of HVOF and plasma coating is powder. In this research, Nickel-chromium based alloy, Nickel Cobalt Chromium Aluminum Yttrium, Aluminum Silicon Boron Nitride, Chromium Carbide – 25% Nickel Chromium, and Aluminum Oxide- 13% Titanium Dioxide powders were selected for their specific wear and corrosion resistance properties in different situations.

2.10.1 Nickel-chromium (NiCr) base alloy powder

Nickel-chromium based super alloy powders produce dense, self-bonding, single-step coatings that are oxidation and corrosion resistant at elevated temperatures.

This composition is similar to Inconel 625, thus the coatings have excellent high temperature oxidation up to 982°C (1800°F) and corrosion resistance for super alloy component restoration and repair (Rai et al., 2004; Tuominen et al., 2000).

The coatings exhibit high tensile bond strength and thickness limits exceeding 1.5 – 2.5 mm (0.06 – 0.1 in.) when sprayed with liquid-fuel or gas-fuel HVOF guns, depending on part geometry. The coated samples can be machined, milled, drilled and tapped with no chipping and excellent edge retention (K. Mumtaz & Hopkinson, 2009; Shankar et al., 2001).

Therefore, these materials are suitable for the restoration of worn or mismatched Inconel 625 components or similar substrates. Figure 2.10 shows a SEM photomicrograph of Nickel-chromium base alloy powders. The figure displays a gas atomized morphology typical of these materials (Z. Liu et al., 2007; Marple et al., 2007).

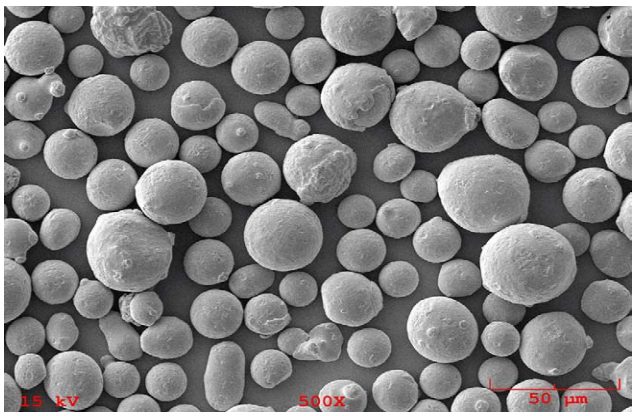

Figure 2.10 SEM photomicrograph of Nickel-chromium base alloy powder morphology (Metaltech Industry, Malaysia)

2.10.2 Nickel Cobalt Chromium Aluminum Yttrium (NiCoCrAlY) powder

The Nickel Cobalt Chromium Aluminum Yttrium family of gas-atomized powders is designed to produce thermal sprayed coatings with excellent high-temperature oxidation and high temperature corrosion resistance. The presence of

cobalt improves coating ductility and high temperature corrosion resistance. The presence of chromium and yttrium improves oxidation resistance by increasing the activity of aluminum and improving the spallation resistance of the oxide scale. The function of chromium and aluminum is to provide a reservoir that continually replenishes the oxide scale. Maintaining the chromium and aluminum ratio is critical to avoiding coating embrittlement (Islak et al., 2013; Marple et al., 2007).

Adding tantalum to the chemical composition exhibits superior oxidation resistance at high temperatures. This chemical composition can serve as overlay coating on moving and rotating instruments to improve their performance and service life, even under harsh environmental conditions. Gas atomization ensures excellent chemical homogeneity and high purity, which results in consistent coating results. Figure 2.11 represents a SEM photomicrograph of Nickel Cobalt Chromium Aluminum Yttrium powder. The SEM photomicrograph shows gas atomized morphology that is typical of these materials (Ni et al., 2005; Tuominen et al., 2000).

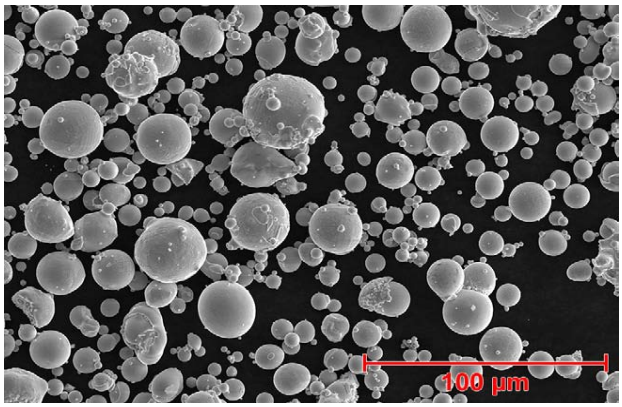

Figure 2.11 SEM Photomicrograph of Nickel Cobalt Chromium Aluminum Yttrium powder morphology (Metaltech Industry, Malaysia)

This chemical composition is a premium grade NiCoCrAlY gas atomized powder that produces thermal spray coatings with excellent surface resistance against oxidation and corrosion at high temperatures (K. Mumtaz & Hopkinson, 2009).

High temperature corrosion resistant bond coats act as thermal barrier and oxide-based abradable coatings for hot section components. They also produce superior low oxide coatings that machine well and closely resemble wrought alloys in terms of characteristics (Tucker Jr, 2013).

2.10.3 Aluminum Silicon Boron Nitride (Al8Si20BN) powder

Al–Si powder is a well-known alloy with high wear resistance, low thermal expansion coefficient, good corrosion resistance, and mechanical properties over a wide range of temperatures. These properties have led to the vast application in different industries (Lei et al., 2014; Toptan et al., 2013). The wear properties of this alloy have been studied mainly under dry sliding conditions against a steel counter face. Previous studies include the effect of silicon content in the alloy on mild wear (Bobzin et al., 2012), the mechanics of mild wear in hypoeutectic alloys and hypereutectic alloys (Vu et al., 2013), and the construction of wear maps of Al–Si alloys (Choi et al., 1999; Saheb et al., 2001).

It has been reported that adding silicon to pure aluminum improves wear and seizure resistance (Johnston, 2011). Torabian et al. (2008) showed that the hardness of Al–Si alloy increases with increasing Si content, and under specific conditions of constant applied load and sliding velocity, the corrosion and wear rate decrease as well (Biermann et al., 2008; Pardo et al., 2009). Silicon additionally reduces the melting temperature to 577°C (1071°F) while increasing fluidity, specific gravity and the coefficient of thermal expansion. It also decreases the contraction associated with solidification. Coatings of AlSi have a lower melting temperature (577°C/1071°F) than coatings of pure aluminum (660°C/1220°F); therefore, AlSi is more suitable for co-spraying with temperature sensitive materials. In addition, aluminum silicon materials produce coatings that are harder and slightly denser than coatings of pure aluminum,

and worn or mismachined components can be dimensionally restored by these components (Cao et al., 2011).

Adding hexagonal boron nitride powder reduces the temperature to 450°C (842°F) and improves corrosion resistance, particularly in marine environments. The reason is that hexagonal boron nitride (hBN) is a very inert lubricant that improves abradability by reducing frictional heating on contact, especially at high translational speeds. It also helps weaken interparticle bond strength within the aluminum silicon matrix for better friability (Miyai et al., 2002; Pardoa et al., 2009). Figure 2.12 shows a SEM photomicrograph of Aluminum Silicon Boron Nitride powder morphology.

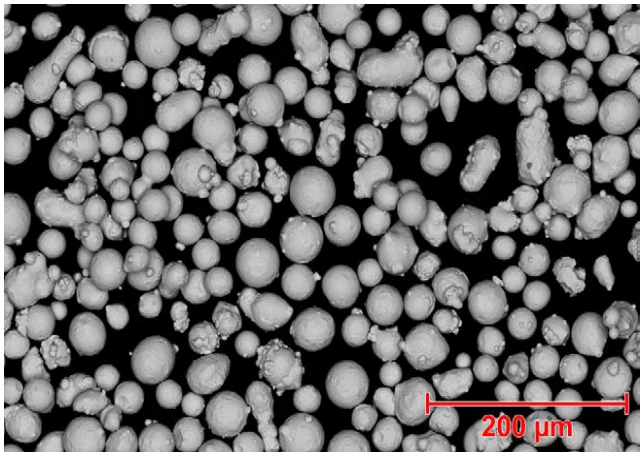

Figure 2.12 SEM photomicrographs of Aluminum silicon boron nitridepowder morphology (Metaltech Industry, Malaysia)

2.10.4 Chromium Carbide – 25% Nickel Chromium (Cr_3C_2-25NiCr) powder

Chromium carbide powder is a blend of chromium carbide and nickel-chromium powders used in HVOF and plasma coating. The nickel-chromium alloy serves as a matrix that improves overall coating integrity and corrosion resistance, while the chromium carbide constituent acts as a hard phase that assures wear resistance. Such coatings effectively combat solid particle erosion (SPE), high temperature wear (abrasion, erosion, fretting and cavitation) up to 870°C (1600°F) and hot corrosion (K Kato, 2006; Laul et al., 2001; D Toma et al., 2001).

A coating applied using the HVOF process is dense and very well bonded, with a more homogeneous structure. Also, coatings applied by plasma gun consume high energy, so the result is similar to HVOF coatings in terms of density and homogeneous structure; however, HVOF coatings have higher bond strength and more favorable residual coating stresses. The high temperature of coating up to 725°C (1340°F) for approximately 1 hour causes carbide dissolution into the matrix and increases coating microhardness (Davis, 2001; Gaona, Lima, & Marple, 2008; Goward, Grey, & Krutenat, 1981). Experts generally agree that micro structures, such as carbide content, carbide particle size and carbide distribution within splats, as well as porosity and so on, predominately influence the wear resistance of cermet coating (Murthy, & Venkataraman, 2006; Yuping et al., 2012; Magnani et al., 2009). Figure 2.13 shows a SEM photomicrograph of Chromium Carbide–Nickel Chromium powder morphology.

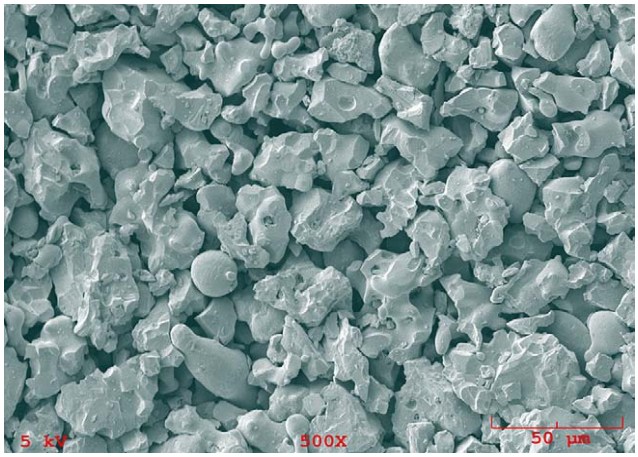

Figure 2.13 SEM Photomicrographs of Chromium Carbide – Nickel Chromium Powder morphology (Metaltech Industry, Malaysia)

Coating applied by HVOF spraying is hard, dense and well-bonded owing to the high thickness limit of over 0.63 mm (0.025 in), which is substantially greater than observed for standard chromium carbide coatings. This chemical composition can be used for many applications with no subsequent finishing as a result of its fine as-sprayed surface roughness. In addition, it produces thin, dense, hard and smooth coatings that are extremely resistant to wear and oxidation. Plasma spray coatings with

this powder are very smooth and can often be used without post finishing (Trompetter et al., 2006).

2.10.5 Aluminum Oxide-13% Titanium Dioxide (Al_2O_3-13TiO_2) powders

Oxide ceramics, such as alumina, zirconia, titania, chromia, silica and yttria are used extensively as surface coating materials to improve wear, erosion, cavitation, fretting and corrosion resistance (Knuuttila et al., 1998; Wang et al., 2009). They are especially useful in applications where wear and corrosion resistance are required simultaneously (Knuuttila et al., 1999). Ceramics made from Al_2O_3–TiO_2 composite powder are prospectively attractive. Aluminum titanate ceramic composite has excellent abrasion, heat and corrosion resistance properties. It also reportedly that it has high fracture toughness and a low frictional coefficient (Berndt, 2001; Satapathy et al., 2004).

Alumina and 13% titania (nominal) powder is used to produce coatings for applications that require moderate hardness and grind ability, but higher fracture toughness compared to coatings produced from pure alumina, alumina 3% titania. Coatings with this material are suitable for applications that necessitate hard bearing surfaces, resistance to abrasive grains, fretting and particle erosion at operating temperatures up to 540°C (1000°F) (Cheng, Ding, Rong, & Zhao, 2013; Jordan et al., 2001; Normand, Fervel, Coddet, & Nikitine, 2000). When polished, the coatings have low wettability, which makes them suitable for applications in the chemical processing industry to resist weak acidic environments. Figure 2.14 shows a photomicrograph of aluminum oxide 13% titanium dioxide morphology. The SEM photomicrograph indicates that this powder has the same particle morphology and size distribution same. The spheroidal morphology generally improves the powder’s flow ability.

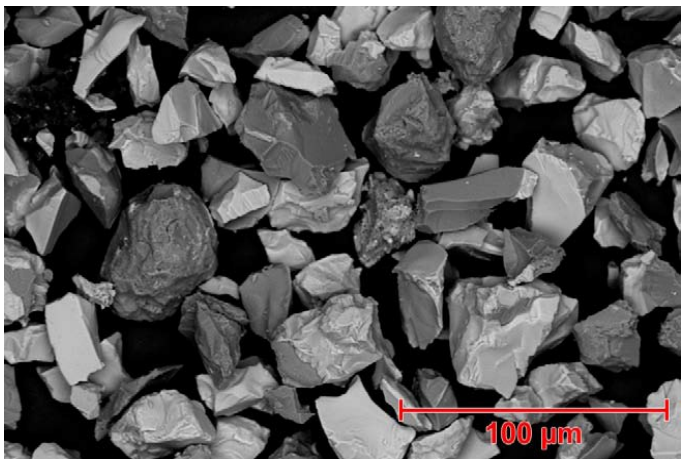

Figure 2.14 SEM photomicrograph of ceramic oxide, a fused and crushed product showing the angular and blocky morphology (Metaltech Industry, Malaysia)

This material was developed for application using combustion powder thermo spray to produce thin, wear-resistant coatings capable of being finished easily to any of a number of surface textures and smoothness (Singh, Sil, & Jayaganthan, 2011; Yugeswaran, Selvarajan, Vijay, Ananthapadmanabhan, & Sreekumar, 2010).

2.11 Electrochemical testing

In this section, the details of three-electrochemical corrosion testing methods, open circuit potential and potentiodynamic polarization are explained. The theory of these electrochemical testing methods, test protocols, data analysis and interpretation are included in the following sections.

2.11.1 Open circuit potential versus time

Open circuit potential (OCP) is defined as the PD between the WE and RE in a solution. One or more anodic or cathodic reactions take place. However, the current flow due to anodic reactions is equal to the current flow due to cathodic reactions. Hence, the term E_{OC} is interchangeable with corrosion potential, rest potential and freely corroding potential (Cramer & Covino, 2003). E_{OC} measurement is the easiest in electrochemical testing which requires a stable RE and a potentiostat, or an RE and high impedance potentiometer (ASTM, 1999). The E_{oc} measurements are made over a period

of time to determine how long it takes to reach a stable value.

The basic purpose of the E_{oc} vs. time experiment is to achieve a stage where E_{oc} becomes approximately constant with time (Reviona, 2000). E_{OC} often increases with time for passive materials and then decreases when localized corrosion begins. Based on the information obtained from E_{oc} alone, it is not possible to make a conclusive remark about the mechanism of corrosion; hence the E_{OC} test is normally combined with polarization resistance or other electrochemical techniques (Roberge, 1999).

2.11. 2 Potentiodynamic polarization curves

Potentiodynamic polarization is frequently used to study the mechanism and rate of corrosion reactions (Angal, 2010). It provides information about corrosion rate, pitting susceptibility and passivity can be determined. The results obtained are averages representative of the area exposed. Potentiodynamic polarization entails sweeping the half-cell potential away from the E_{oc} to more positive and more negative potentials (Enos, 1997).

In cathodic polarization, electrons are supplied, while in anodic polarization electrons are drained out by the potentiostat. The reaction occurs at the working electrode, and the counter electrode depends on the potential applied between the working electrode and reference electrode. Applied potential is more positive than the open circuit potential, which will drive dominant anodic reactions to the working electrode and dominant cathodic reactions to the counter electrode (Angal, 2010).

2.11.3 Electrochemical Impedance Spectroscopy (EIS)

Electrochemical impedance spectroscopy (EIS) is one type of techniques that used for measuring the corrosion rate of surface. This method has some advantages such as the system remains at equilibrium, non-destructive method. Also it can be

applied in many fields such as semiconductor, biosensor, corrosion, batteries and etc. In this technique a series of small voltage with different frequencies applied on the system (Bard & Faulkner, 2001). In the EIS system, mostly Nyquest and Bode plots in used for determining the corrosion behavior of surface. An equivalent electrical circuit can be simulated from EIS results in a corrosion system. The equivalent electrical circuit is called Randless circuit, which includes solution resistance (R_s), polarization resistance (R_p), capacitor for the interface (double layer) and capacitance (C_{dl}).

In the EIS measurement, the kinetic reaction connected with charge transfer controlled and mass transport control process is in frequency domain. Figure 2.15 shows the Nyquist plot.

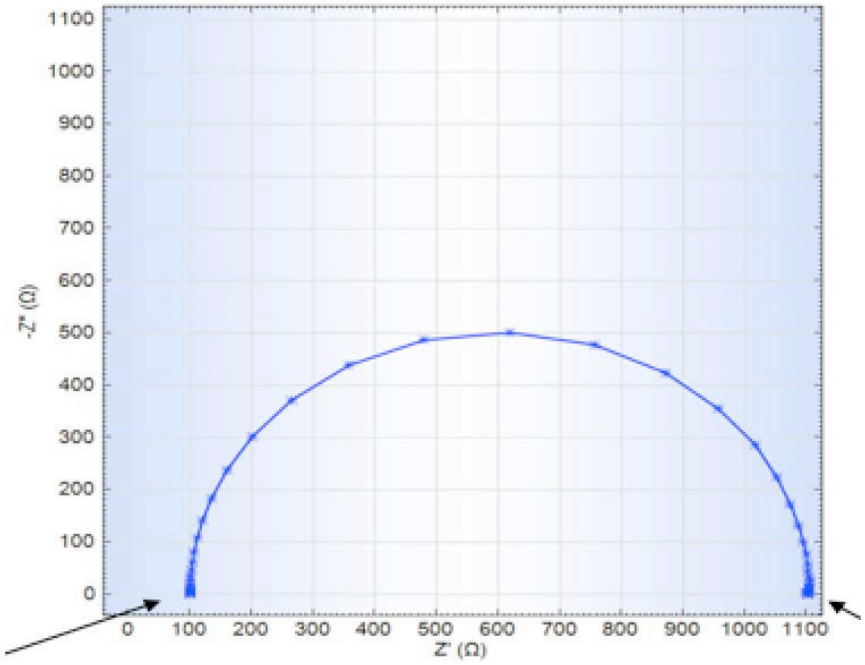

Figure 2.15. The Nyquist plot from low frequency to high frequency

The impedance modulus Z (jω) for the equivalent circuit (EC) can be calculates through the Nyquist plot.

Under the charge transfer controlled, this is defined as:

$$Z(j\omega) = R_s + \frac{R_p}{(1 + j\omega C_{dl} R_p} \qquad 2.14$$

Where the R_S (electrolyte resistance) and R_p (polarization resistance of electrode) can be calculated at the high and low frequency limiting:

At high frequency

$$R_s = \lim_{f \to \infty} |Z| \qquad 2.15$$

At low frequency

$$R_s + R_p = \lim_{f \to \infty} |Z| \qquad 2.16$$

According to the Nyquist plot, there is no information for frequency. For this reason, Bode plot is used to find an explanation of corrosion elements. The Bode plots are plotted through the log $|Z|$ and phase angle (θ). The value of R_p and R_S can be determined from the peak frequencies by Bode plot (*log z vs log f*). The low Z values are visible. Usually, the phase angle θ *vs. log f* is combined by Bode plot (Figure 2.16). As for the Nyquist plot, the Bode plot depends on the circuit diagram, whether the capacitor and resistor element is in parallel and in series, and the shape of the plot will depend on the frequency. In the ideal aspect of the Bode plots, the phase angle of a pure capacitor is always 90° and the phase angle of a pure resistor is always 0°. By definition, the phase angle is the angle between the voltage and the current of the capacitor (Popa et al., 2002).

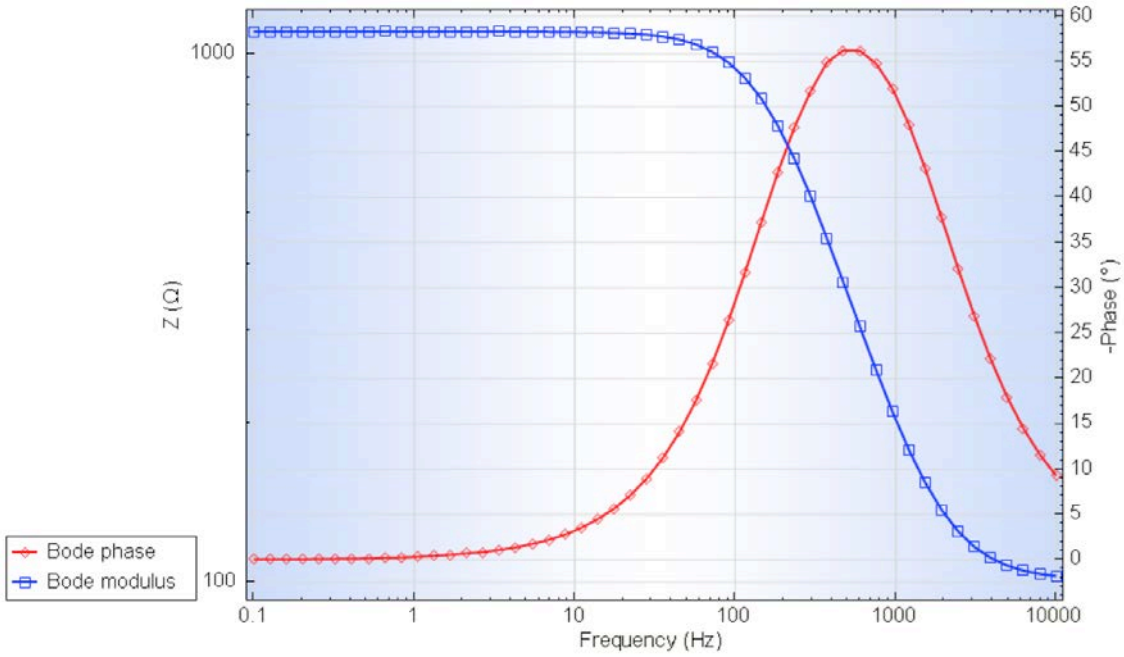

Figure 2.16 Bode plot for a simple circuit (Metrohm, Autolab)

At very low frequencies, the impedance of the capacitor Z_I is very large; so the current will not pass through the capacitor rather take pass through the resistor R. The overall circuit is like joining the resistor R in series with the solution resistance R_S, so the total resistance is $R + R_S$, or $Z = Z_S + Z_R$. At these frequencies, only the resistance component will dominant, so the phase angle, θ will be zero. The capacitance (C_{dl}) value could be calculated from the slope of the curve (Park et al., 2006; Sathiyanarayanan et al., 2008).

The phase angle is correlated with the roughness of electrode surface. Numerous researchers (Srivastava, et al., 2006) have attempted to evaluate the corrosion behavior of surface by EIS technique. They found that the charge transfer resistance (R_{ct}) is reduced with the increase of applied potential. The R_{ct} value can be determined by the Nyquist plot. At high-frequency charge transfer reaction occurs and at low frequency the mass transfer takes place. Darowicki (1995) has reported that the corrosion rate could be calculated by EIS when the electrode surface was tested in various applied

electrical potential. Additionally, he found a small difference between the experimental and simulated curve at various potentials. Fletcher (1994) has simulated many types of equivalent circuits for the complex system in Electrochemical Impedance Spectroscopy (EIS). EIS is very successfully used in evaluating the properties of ceramic and alloys-coated and their gradual changes when comes in contact with corrosive environments. Moreover, EIS has replaced traditional DC techniques in testing various polymer coatings on metals and alloys. As an advanced and very powerful method, EIS allows the investigation of the electronic resistance and the ionic conductivity, pore resistance and enables the measurement of film porosity in the polymer. However, experimental results from EIS can be compared to a circuit diagram representing the physical model understudy making the interpretation of the EIS results possible (Albery & Mount, 1994).

2.12 Summary

Corrosion and wear of engineering metals and alloys generally occur in the majority of industrial environments, costing billions of dollars. Therefore, spending resources on corrosion and wear prevention and protection is a rational approach. The purpose of coating is to obtain a blend of unique surface properties at low cost. This can be done by coating expensive materials on economical substrates rather than using bulk alloys. Superior corrosion/wear resistant properties while maintaining tougher substrate properties can also be achieved by HVOF and plasma thermally sprayed coating processes. Despite enhanced properties with employing HVOF and plasma coatings compared to substrate, the corrosion and wear performance of coatings is generally lower than an equivalent bulk material. Researchers have endeavored to improve the corrosion performance of coating by modifying different process parameters, relieving stress and through surface modifications. A few of these techniques improve corrosion and wear performance, but coating modifications further add to processing costs.

Considerable research has also been reported on the use of electrochemical testing techniques for corrosion testing and pin-on-disc wear testing.

CHAPTER 3: METHODOLOGY

3.1 Introduction

In this chapter, the details about the materials and equipment used for producing and characterizing HVOF and plasma coatings are given. The experimental procedures for wear; potentiodynamic polarization, electrochemical impedance spectroscopy and scanning electrochemical microscopy testing techniques are also discussed. The sequence of experimental testing is presented in Figure 3.1.

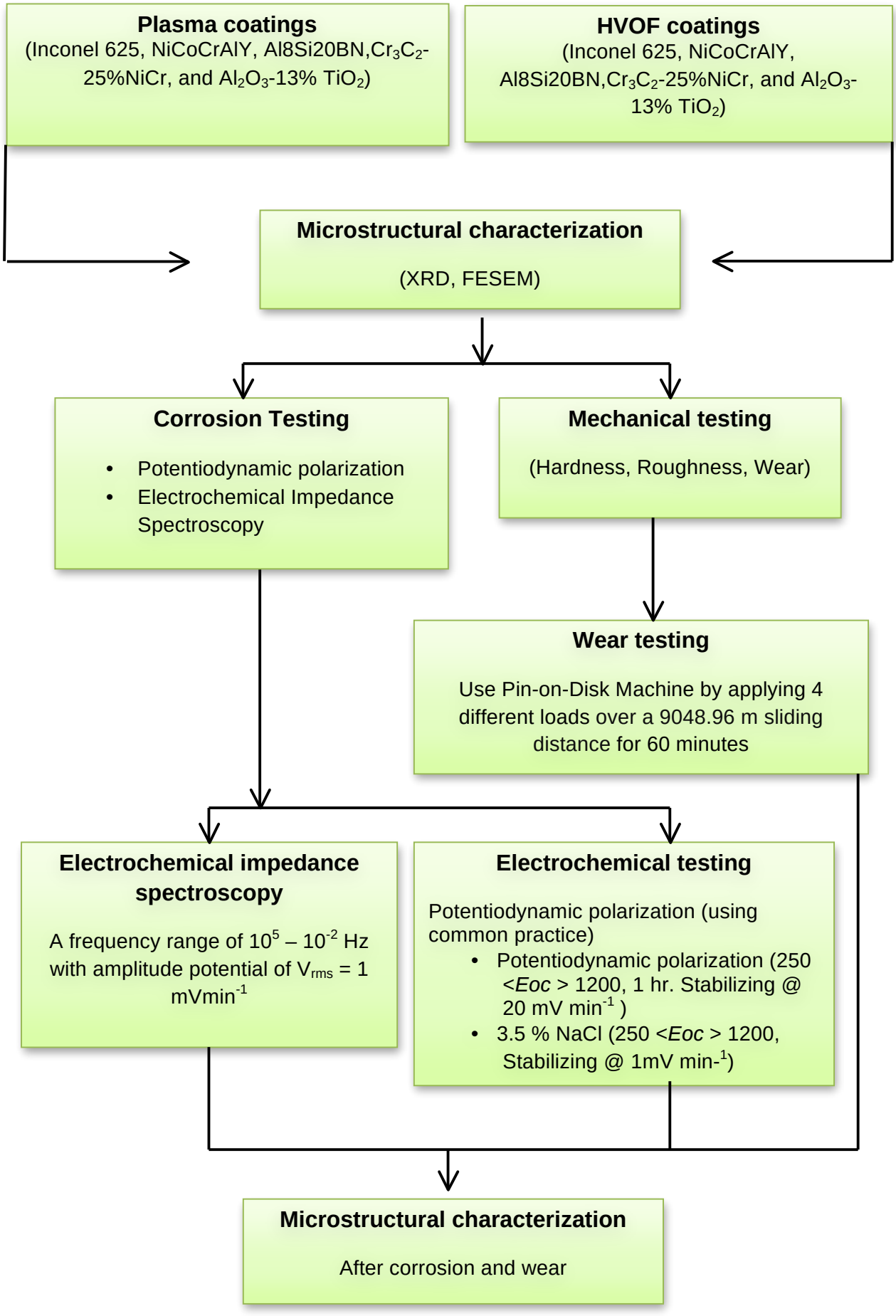

Figure 3.1 Experiments performed on coated materials

3.2 Materials and method

3.2.1 Materials

The substrate material used is carbon steel (S45) because it is one of the most popular materials used in oil piping production in both upstream and downstream domains. The substrate material was supplied by Kelvin Steel, Glasgow, with the chemical composition in percentage as follows: C 0.42-0.50, Mn 0.5-0.80, Si 0.17-0.37, Cr (max%) 0.25, Cu (max%) 0.25, Ni (max%) 0.25, S (max%) 0.035, P (max%) 0.035 and Fe balance. The mechanical properties of S45 Carbon Steel are tabulated in Table 3.1.

Table 3.1 Mechanical properties of S45 Carbon Steel

Tensile Strength σb(MPa)	Yield Strength σS(MPa)	Reduction of area Psi (%)	Impact merit AKV(J)	Resilient value AKV (J/cm^2)	Degree of hardness	Annealed steel hardness	Test Specimen Size (mm)
≥600	≥355	≥40	≥39	≥49	≤229HB	≤197HB	25

For the layer deposited onto the carbon steel surface, gas-atomized and spheroidal Inconel 625 and NiCoCrAlTaY powders (Diamalloy 1005, AMDRY 997 powders) with nominal size ranges of 45+11 μm and 37+15μm were used for both methods. Gas-atomized and spheroidal Al8Si20BN (AMDRY 355) with nominal size of 45+11μm and water atomized Al8Si20BN (Metco 320NS) with nominal size range of 45+10 μm was used for the HVOF and plasma methods respectively. Cr_3C_2-25 (Ni20Cr) (Diamalloy 3004) with nominal size range of 45+5 μm and blended Cr_3C_2-25 (Ni20Cr) (Metco 81VF_NS) with nominal range size of 45+5μm was used for the HVOF and plasma methods respectively. The last group comprised spherical ceramic oxide Al_2O_3-13%TiO_2 (Metco 131VF) with nominal range of 45+11μm used for both methods. The chemical composition of each powder sprayed on the substrate isshown

in Table 3.2. Table 3.3 briefly displays the particle size, morphology and application of each group of powders' chemical composition that was presented in Section 2.14.

Table 3.2 Chemical composition of the powders used for producing HVOF and Plasma coatings

Inconel 625 powder						
Element	Ni	Cr	Fe	Mo	Nb+Ta	-
Weight %	Bal*	21.5	2.5	9.0	3.7	-
Nickel Cobalt Chromium Aluminum Yttrium (NiCoCrAlY)						
Element	Ni	Co	Cr	Al	Y	-
Weight %	Bal*	20-26	18-23	6 -11	2.0-6.0	-
Aluminum Silicon Boron Nitride (Al8Si20BN)						
Element	Al	Si	BN	-	-	-
Weight	Bal*	8	20	-	-	-
Chromium Carbide Cr_3C_2-25 (80Ni 20Cr)						
Element	Cr	Ni	C_{TOTAL}	Fe	O	-
Weight	Bal*	17.5-22.5	9.0-10.2	<0.5	-	
Alumina-titania Al_2O_3-13TiO_2						
Element	Al_2O_3	TiO_2	Organic Solids (Max)	Others (Max)	-	
Weight	Bal*	13.0-16.0	2.0	1.0	-	

Bal*: Balance

Table 3.3 Properties and applications of different chemical composition powder used for HVOF and Plasma coating

Chemistry	Particle Size (µm)	Manufacture	Applications
Inconel 625	**45+11**	**Gas Atomized**	▪ Dense, self-bonding ▪ Excellent high temperature oxidation and corrosion resistance ▪ For repair of super alloy component and protection for less noble substrates ▪ Machinable and drillable, excellent edge retention ▪ Service up to 982°C (1800°F)
NiCoCrAlY	**37+15**	**Spheroidal & Gas Atomized**	▪ Excellent high temperature oxidation and hot corrosion resistance ▪ Excellent corrosion resistance bond coat ▪ It is a premium grade material with superior high temperature oxidation resistance ▪ Service up to1050°C(1920 °F)
Al8Si20BN	**45+10**	**Spheroidal & Gas Atomized**	▪ Good erosion resistance ▪ Superior corrosion resistance ▪ Service up to 450°C(840°F)
Cr_3C_2-25NiCr	**45+5**	**Agglomerated & Densified**	▪ Resists solid particle erosion, abrasion, tribocorrosion, high temperature corrosion ▪ Excellent hard chromium plating alternative with better chloride, acidic and alkaline resistance ▪ Minimal decarburization during spraying ▪ Densification improves corrosion resistance ▪ Service up to 870°C (1600°F)
Al_2O_3-13TiO_2	**45+11**	**Agglomerated & Sintered**	▪ Resists abrasion, sliding wear, oxidation, acids, alkalis ▪ Titania adds toughness but reduce hardness ▪ It has a homogeneous coating structure ▪ Service up to 540°C (1000°F)

3.2.2 Sample surface preparation

Surface preparation is a very important step in thermal spraying. This is because coating adhesion is directly related to surface roughness and is controlled by the type of grit blasting machine, blasting pressure, angle, distance, time and grit blasting nozzle (Mann & Arya, 2001).

Grit blasting was carried out with a high efficiency sand blaster with Alumina grit (size 10-20 mesh), 8/10mm nozzle and operating at a blasting pressure of >0.5 MPa. The distance between substrate and nozzle was 150mm with a 30° angle. The grit blasting time was dependent on obtaining the required surface roughness. Upon grit blasting completion, powders with different chemical compositions were sprayed using HVOF and/or plasma gun systems.

The coating thickness selected for all samples in this research after trial and error was approximately 400 µm. Generally, increasing some initial parameters such as arc current, power feed rate, etc., helps increase the thermal spray coating thickness. However, increasing the coating thickness leads to a decrease in bonding strength and an increase in residual stresses. Two residual stress sources can be considered (Sarikaya et al., 2007), one of which is macroscopic thermal stress that arises due to the mismatch in thermal expansion coefficients between the coating (matrix + reinforced particles) and the substrate. The other microscopic stress is due to the deposition of sprayed particles at high temperature onto a cold surface ((Yugeswaran et al., 2010) studied the effect of coating thickness on the corrosion behavior of thermally sprayed coatings.

Thicker coatings permit electrolytes to pass due to the stresses generated during coating deposition and the corresponding crack formation between different layers. Thinner coatings cause electrolytes to pass through the coating ((Yugeswaran et al., 2010). Hence, it was concluded that optimizing the spraying parameters and stress relaxation process is as important as optimizing thickness when base carbon steel

protection is needed with coatings of varying chemical composition materials (Sarikaya et al., 2007).

3.2.3 Thermal spray coating

Following surface preparation, the process of coating begins. In this research, different types of materials with various properties and melting points were used, so each group requires a specific setup. For example for ceramic composite materials need to use a high temperature and the distance between gun and substrate should be less than alloys. Also the nozzle that use for ceramic composites should be narrowed, because the small size of nozzle give this chance the percentage of fully melted particle is increased. The setup of each powder for HVOF and plasma is presented in sections 3.2.3.1 and 3.2.3.2 respectively. Also these parameters are selected based on the pretested investigation to identify the best working condition for each case. All of the coating process was done in Metatech Industry in Malaysia.

3.2.3.1 HVOF Coating

For the deposition of different powder types by HVOF machine, a Model 9MP machine was employed in this research. However, depending on the powder type, the nozzle and setup was changed because the parameter used for metal base alloy cannot be used for ceramic powders. The setup for ceramic composite should be created with adequate temperature for melting ceramic powder; otherwise, non-melted or semi-melted regions cover the coating surface. Figure 3.2(a) shows the HVOF thermal spray setup and Figure 3.2 (b) shows the HVOF-9MP thermal spray gun. The specifications of each powder coated by HVOF machine are tabulated in Tables 3.3 to 3.7.

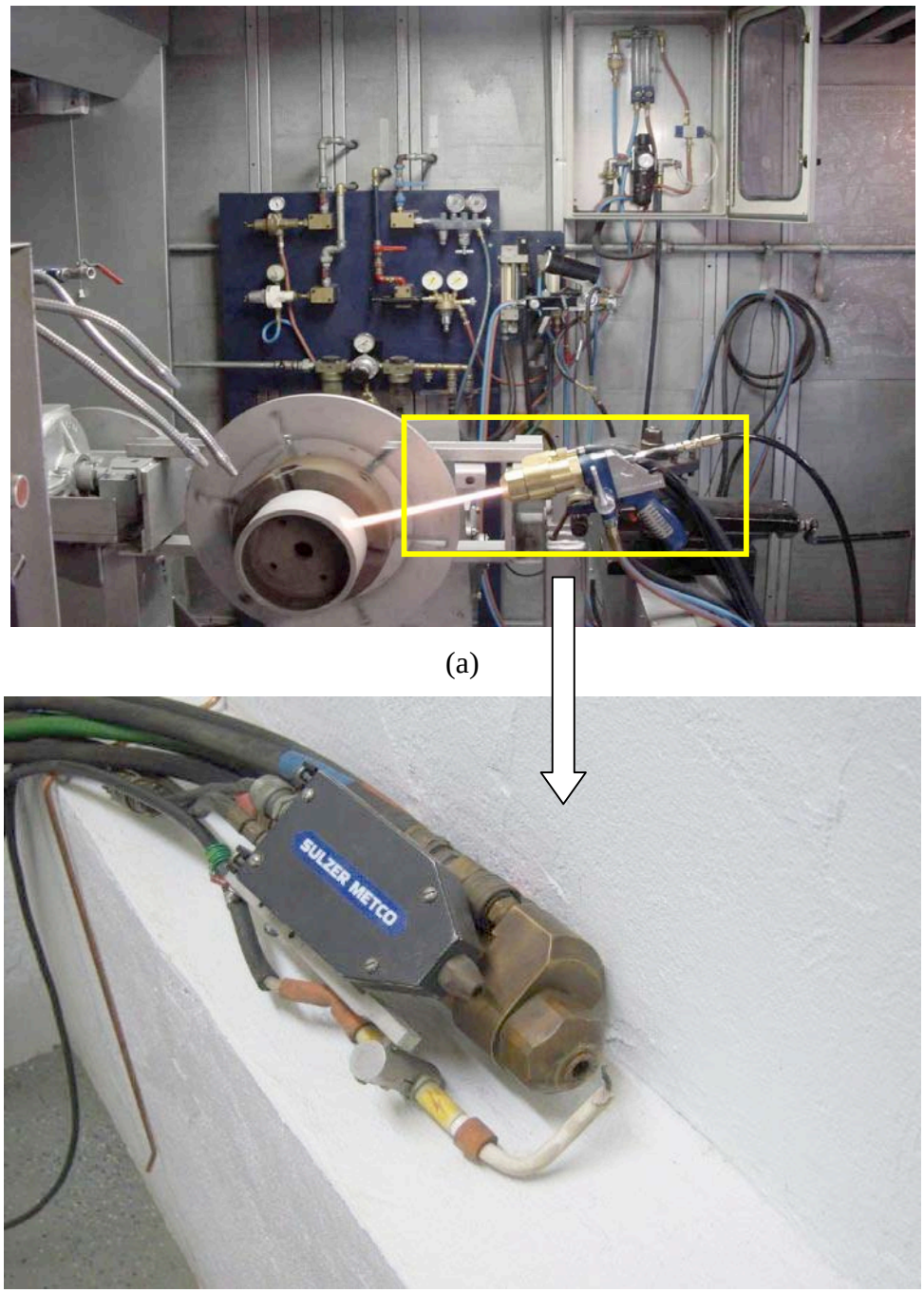

(a)

(b)

Figure 3.2 HVOF thermal sprays (a) HVOF-Set up, (b) HVOF- Gun (Metatech Industry, Malaysia)

Table 3.3. The parameters of Inconel 625 powder for HVOF coating

Model: 9MP		**DJ2700 Hybrid**		
Nozzle		Standard		
Powder Port				
	Type	DJ2702		
	Injector	#8		
Gases		Pressure (psi)	Flow (FMR)*	SCFH**
	Oxygen	150	49	707
	Propylene	100	39	171
	Carrier gas (N_2)(1)	175	50	789
Amps		20		
Voltage		66		
Spray Distance		150-300mm (6-12”)		
Spray Rate		60.5 g/min (8 lb./hr)		
(1) Nitrogen tank pressure should be set at 175 psi. *: Flow Meter Group **: Standard cubic feet per hour				

Table 3.4 Parameters of NiCrCoAlY powder for HVOF coating

Model: 9MP		**DJ2700 Hybrid**		
Nozzle		Standard		
Powder Port				
	Type	DJ2702		
	Injector	#9		
	Angle	90^O		
Suction and spreader		L/L		
Gases		Pressure (psi)	Flow (FMR)	SCFH
	Oxygen	155	282.2	645
	Natural Gas (CH_4)	110	140.2	320
	Carrier Gas (N_2)(1)	105	350	799
Spray Distance		254 mm (10”)		
Spray Rate		38 g/min (5 lb./hr)		
(1) Using Nitrogen as a shroud gas will reduce coating oxide content.				

Table 3.5 Parameters of Al8Si20BN powder for HVOF coating

Model: 9MP		**DJ2700**		
Nozzle		Standard		
Powder Port				
	Type	DJ2702		
	Injector	#3		
Gases		Pressure (psi)	Flow (FMR)	SCFH
	Oxygen	150	24	347
	Propylene	100	45	198
	Air	100	48	858
Spray Distance		230 mm (9”)		
Spray Rate		38 g/min (5lb./hr)		

Table 3.6 Parameters of Cr_3C_2-25NiCr powder for HVOF coating

Model: 9MP		**DJ**		
Nozzle		Standard		
Powder Port				
	Type	DJ2702		
	Injector	#3		
Gases		Pressure (psi)	Flow (FMR)	SCFH
	Oxygen	150	42	606
	Propylene	100	38	168
	Air	75	47	742
Spray Distance		150-200mm (6-8”)		
Spray Rate		38 g/min (5lb./hr)		

Table 3.7 Parameters of Al_2O_3-13%TiO_2 powder for HVOF coating

Model: 9MP		**DJS**		
Nozzle		#6		
Powder Port				
	Type	DJ2702		
	Injector	#3		
Gases		Pressure (psi)	Flow (FMR)	SCFH
	Oxygen	130	38	546
	Propylene	90	29	147
	Air	68	39	687
Spray Distance		130-160mm (6-8”)		
Spray Rate		36 g/min (5lb./hr)		

3.2.3.2 Plasma Coating

For plasma coating, the same specific setup was used as for HVOF coating in each material powder group. However, for metal base alloy deposition, Plasma-F4 was used while for ceramic composite powder Plasma-9Miller was used, because this gun model can melt ceramic powders to create a fully melted surface. Figure 3.2(a) shows the plasma thermal spray setup and Figure 3.2(b) shows the F4 and 9 Miller guns for plasma thermal spray. Also, the setup of each powder coated by plasma machine is tabulated in Tables 3.8 to 3.12.

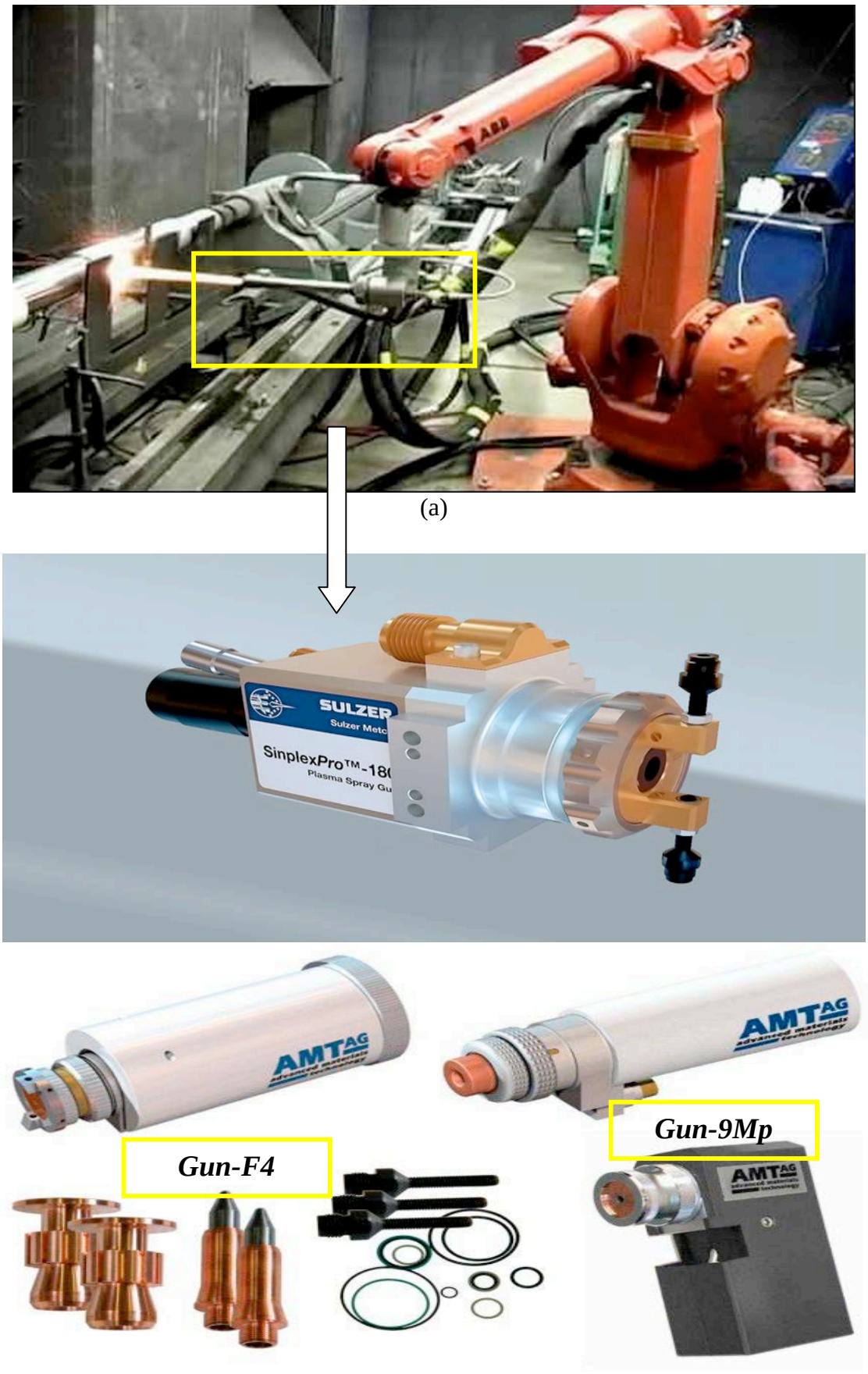

(a)

(b)

Figure 3.3 Plasma thermal sprays (a) Plasma-Set up, (b) Plasma- Guns (Metatech Industry,Malaysia)

Table 3.8 Parameters of Inconel 625 powder for Plasma coating

Gun		**F4**		
Nozzle		8mm		
Powder Port				
	Type	#2 (1.8mm/0.071")		
	Gauge	#6		
	Angle	90^{O}		
	Disc Rpm	23		
Suction and spreader		L/L		
Gases		Pressure (psi)	NLPM*	SCFH
	Primary (Ar)	75	50	114.1
	Secondary (H_2)	50	6	13.7
	Carrier (Ar)	100	4	9.1
Amps	400			
Voltage	67 ±3			
Spray Distance		100 ±3mm (4.25 ±0.12")		
Spray Rate		30 g/min (4 lb./hr)		
*: Units of Flow Rate, practiced in Europe, define what shall be a Flow Rate of a given gas stream at T_{gas}, P_{gas} temperature & pressure, if it changed to pressure of 1atm (101.325 kPa) and temperature of 0°C (273.15K).				

Table 3.9 Parameters of NiCrCoAlY powder for Plasma coating

Gun		**F4**		
Nozzle		Standard		
Powder Port				
	Type	#2 (1.8mm/0.071")		
	Gauge	#6		
	Angle	90^{O}		
	Disc Rpm (1)	23		
Suction and spreader		L/L		
Gases		Pressure (psi)	NLPM	SCFH
	Primary (Air)	75	65	1218
	Secondary (H_2)	50	14	32
	Carrier (Air)	100	2.3	5.2
Amps	600			
Voltage	66			
Spray Distance		114-140mm(4.5-5.5")		
Spray Rate		40-57 g/min (5.3-7.5lb./hr)		
(1) As a starting point, adjust to indicate spray rate.				

Table 3.10 Parameters of Al8Si20BN powder for Plasma coating

Gun		**F4MB/F4MB-*XL***		
Nozzle		9mm		
Powder Port				
	Gauge	#6		
	Angle	90^{O}		
	Disc Rpm (1)	23		
Suction and spreader		L/L		
Gases		Pressure (psi)	NLPM	SCFH
	Primary Gas (Ar)	75	76	123.5
	Secondary (H_2)	50	14	32
	Carrier Gas (Ar)	100	5	11.4
Amperage	250A			
Voltage	91±3 V			
Spray Distance		120 ±3mm(4.75± 0.125")		
Spray Rate		33 g/min (4.3lb. /hr)		

Table 3.11 Parameters of Cr_3C_2-25NiCr powder for Plasma coating

Gun		**9Miller**		
Nozzle		9mm		
Powder Port				
	Type	2 used #1000450		
	Gauge	#6		
	Angle	90^{O}		
	Disc Rpm	23		
Suction and spreader		L/L		
Gases		Pressure (psi)	NLPM	SCFH
	Primary Gas (Ar)	75	100	228.3
	Air Jets (2used-Item #1000540)	58	47	18
	Carrier Gas (Ar)	49	2.4	5.5
Amperage	480A			
Voltage	111±3 V			
Spray Distance		99 ±3mm		
Spray Rate		18 g/min (2.4 lb./hr)		

Table 3.12 Parameters of Al_2O_3-13%TiO_2 powder for Plasma coating

Gun		**9Miller**		
Nozzle		6mm		
Powder Port				
	Type	#2 (1.8mm/0.071")		
	Gauge	#6		
	Angle	90^O		
	Disc Rpm (1)	23		
Suction and spreader		L/L		
Gases		Pressure (psi)	NLPM	SCFH
	Primary (Ar)	75	39	89.0
	Secondary (H_2)	50	12	27.4
	Carrier (Ar)	72.5	3.2	7.3
Amps	625			
Voltage	68 ±3			
Spray Distance		85 ±3 mm		
Spray Rate		50 g/min (6.6 lb./hr)		

3.3 Microstructural analysis

The more popular surface characterization techniques for membranes include field emission scanning electron microscopy (FESEM) and energy dispersive X-ray. These are capable of providing atomic-level quantitative analysis of the morphological characteristics of membrane surfaces. It is possible to characterize membrane properties like surface roughness (Koyuncu, Brant, Lüttge, & Wiesner, 2006), porosity and pore size distribution, and deposit layer thickness (Boussu et al., 2005).

3.3.1 Field Emission Scanning Electron Microscopy (FESEM)

Field emission scanning electron microscopy is an analytical technique for surface topography and specimen composition analysis. FESEMreports the electrons and x-rays generated by the interaction between an electron beam and specimen either by elastic or inelastic process.. In the elastic process, beam electrons are deflected by atoms interaction without losing a significant amount of initial kinetic energy. The angle over which deflection occurs is large, ranging from average values of 2-5º up to 180º. Through this process, incident beam electrons can interact with the specimen and

escape back out of the surface, being detected as “back-scattered” electrons. Whereas, in inelastic scattering, an incident beams electron interacts with a substrate atom, giving up some of its initial kinetic energy. The beam electron is deflected, typically over angles of <0.1º and continues to penetrate into the sample.

The various mechanisms of beam electron-substrate atom interactions generated through inelastic scattering, those most relevant to this work involve energy transfer to the outer band of electrons and the ejection of an inner shell electron from the atom to the beam electron. The atom reaches an “excited” state after interaction with incident beam electron, then in a relaxed state, resulting in the formation of “secondary” electrons and “characteristic x-rays”, respectively. The intensity of these secondary electrons bears a signature of the sample’s surface topography. An image of the sample surface is therefore constructed by measuring secondary electron intensity as a function of the scanning primary electron beam’s position. Apart from the secondary electron imaging, backscattered electron imaging and Energy Dispersive X-Ray (EDX) analysis are are widely used for chemical analysis. In chemical analysis, the electron bombardment generated backscattered electrons are correlated to the atomic number of the element within the sampling volume. Hence, qualitative elemental information can be determined. FESEM with X-ray analysis is an efficient, inexpensive and non-destructive method of carrying out surface analysis.

The dispersive nature of the specimen’s primary beam electrons, combined with the multiple interactions of each electron, means that the signals generated from the point of the incident beam are generated over a larger “interaction volume”(Potts, 1987). The energy of the electrons or, x-rays formed determines the depth from which they can escape the surface and be detected, leading to significant variation in the volume of material analyzed in each technique (Figure 3.4).

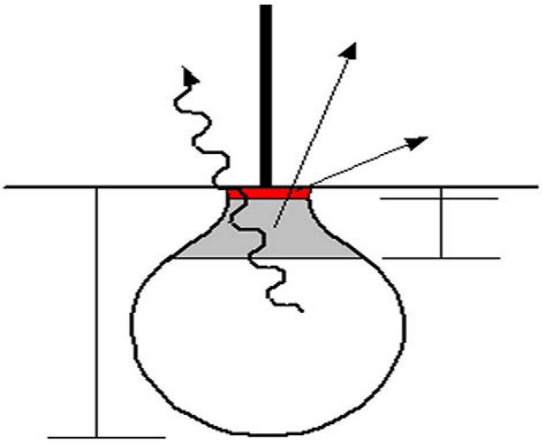

Figure 3.4 Schematic illustrations of the relative depths from which secondary electrons, backscattered electrons and characteristic x-rays may escape the surface to be detected. The numerical values are specified for a Cu-10Co alloy with incident beam energy of 20keV(Potts, 1987)

In our microscopy lab, a state-of-the-art, high-resolution FEI Quanta 200F field emission scanning electron microscope (FESEM) with an EDX system (INCA Energy 400) from OXFORD is used (Figure 3.5). This is a high-performance instrument designed for analytical applications and is controlled by a 32bit computer system using Microsoft Windows 2000 as the operating system. Figure. 3.4 shows a photograph of this microscope in our lab.

Figure 3.5 Photograph of the FEI Quanta 200F FESEM with EDX set-up

3.3.2 X-ray Diffraction (XRD)

X-ray diffraction exploits the similarity in magnitude between the wavelength of X-rays and the inter-atomic spacing of the planes of atoms in crystals that enables X-rays to be diffracted. X-rays of a fixed wavelength are projected onto a sample. They penetrate the surface and are scattered by the regular array of planes of atoms, only those travelling out of the specimen in the same direction as the incident beam being detected. Within a crystal, diffraction occurs if the different distances travelled in the direction of the detector by the scattered x-rays are equal to a whole number of wavelengths. If so, the wavelengths reinforce each other through constructive interference, generating a very large intensity signal. If the variation in distance travelled does not fit this criterion, diffraction does not occur and the detector registers only a low “background” signal of X-rays randomly scattered in this direction.

The peaks in intensity based on the inter-atomic spacing are characteristic for a specific set of atom planes for each compound. As a compound typically has several families of crystallographic planes that may diffract X-rays, several peaks occur at different incident angles. Scanning a range of incident angles and measuring the X-ray intensity generate a spectrum. The peak positions within this spectrum are related to the inter-atomic spacing, d, the wavelength of the X-rays, λ, and the angle of the incident beam to the surface. The relationship between these variables is described by Bragg’s Law, equation 3.1 (Wagner, 1978).

$$\lambda = 2d \sin\theta \qquad 3.1$$

Results are typically presented as spectra of intensity versus 2θ. Compounds within a spectrum are identified by comparing the relative intensities of the various peaks and their positions with standard spectra within the JCPDS (Joint Committee on Powder Diffraction Standards) database. Where mixtures of phases are present, the amount of each component is proportional to the intensity and area underneath the

peaks for that compound. Intensities for a given composition are dependent on the atomic number of that compound and are also affected by the material's mass absorption of x-rays.

Spectral intensities should be calibratedusing standard mixtures for quantitative compositional analysis. Two factors commonly complicate spectral interpretation. Standard spectra from the JCPDS database are generated from pure, homogeneous samples where crystals with diffracting planes are randomly oriented with respect to the incident beam. Where one family of diffracting planes occurs preferential to the others (preferential orientation), the position of the peaks will remain fixed but their intensity will be a lot higher than in standard spectra. Secondly, the compounds considered so far have been crystalline. Diffraction can also occur in materials where the periodicity of the atoms is not as regulated, such as amorphous materials. In this case, a broad peak is generated, centered on spacing where the amorphous material atoms show a preference for a particular inter-atomic distance.

The basic features of a typical XRD experiment, as well as our XRD setup, are shown in Figure 3.6. We used a Siemens D5000 XRD unit with an X-ray source having wavelengths of K_{α} = 1.5406 A°. Diffraction experiments are usually done with a fixed wavelength; therefore, diffraction angle measurement enables the calculation of associated d_{hkl} and the lattice constants.

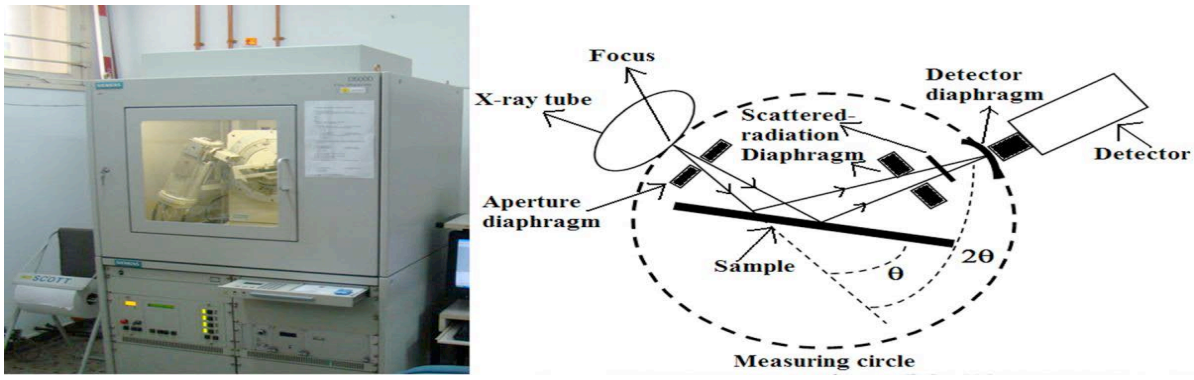

Figure 3.6 Basic features of a typical XRD experiment as well as the Siemens D5000 set- up

3.4 Vickers Microhardness and roughness Testing

The hardness of the coatings was tested on polished cross sections using a Vickers hardness tester (LECO M-400 Hardness Tester). In this test, a diamond indenter in the form of a square pyramid was forced into the surface. The two diagonal lengths of the square were measured and correlated via conversion tables to Vickers hardness numbers. Trials were conducted using a 300g load for 15 seconds, unless otherwise stated. Due to the inhomogeneous nature of thermal spray coatings, operator judgment was required to pass or fail each indent as being representative, especially in terms of cracking. Ten representative indents were averaged for each sample.

The roughness (Ra) of the coated samples was measured by optical surface texture analyzer (Alicona 3D Infinity Focus). The average of 100 points on the coated samples' surface was shown the roughness parameter (Ra).

3.5 Wear testing

In a thermal spray process, the quality of the end product matters. As reported in previous studies, the homogeneity in coating structure, adhesion to the substrate and operational durability are the main factors affecting the coating quality (Shukla, Tewari, & Jayaganthan, 2011). Consequently, investigating the mechanical properties of coating becomes important for improving the coating durability. Moreover, in order to better understand the influence of composition and microstructure on these properties, it is necessary to quantitatively evaluate the mechanical properties of coatings (Shukla et al., 2011).

The wear tests were performed in a pin-on-disc tester model TR-20LE as shown in Figure 3.7. This machine is designed to study friction and wear characteristics in sliding contacts. Sliding occurs between a stationary pin and a rotating disc. Normal load, rotational speed and wear track diameter can be varied. Tangential frictional force

and wear are monitored with electronic sensors. These parameters are available as functions of load, speed, lubrication or environmental condition for continuous monitoring. The TR-20LE has an additional lubricant recirculating system and consists of a lubricant pump, nozzle, splashguard and recollection. The nozzle position is adjustable to pour lubricant on the rotating disc just ahead of the pin-on-disc contact. Recollected lubricant is returned to the oil pump. The lubricant flow rate is adjustable. In this research, the wear tests for coated as well as uncoated specimens were conducted under four normal loads of 5, 10, 15 and 20 N, pushed against 120 grit SiC sand paper for metal base powders and WC-6%Co paper for ceramic composite powders in dry condition.

A track diameter of D=40 mm and sliding speed of v=1 m/s were kept constant and wear tests for each load were carried out for a total sliding distance of 9048.96 m (60 min). The weight loss for each sample was measured after applying each load to determine the wear loss. After the test, the samples were ultrasonically cleaned in ethanol and then dried, and their weight was measured with a microbalance with 0.0001 gm accuracy. The wear loss and rate were determined with the normal loads in all cases.

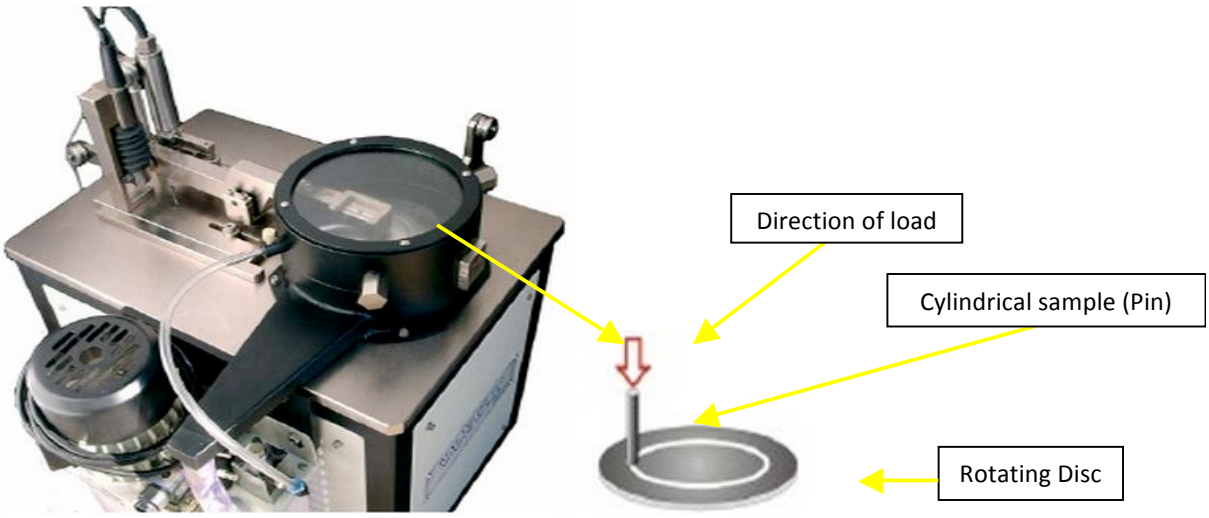

Figure 3.7 Schematic of Pin on Disc Model No: TR-20LE

3.6 Electrochemical Testing

Autolab PGSTAT-302N Potentiostat/Galvanostat were used to investigate the coatings and determine the polarization and passivation of the electrodeposited layers. GPES software is included in Autolab PGSTAT-302N. This software can run some useful DC techniques, such as cyclic voltammetery, chrono-amperometry, chrono-potentiometry and so on. The cyclic voltammetry technique is used for the electropolymerization of different types of polymers and copolymers. The experiments can be done at various scan rates and a wide range of potential windows through Autolab PGSTAT-302N. The polarization resistance of coated steel with different types of coatings was examined by linear sweep voltammetery (LSV) through a Tafel plot. Tafel slope lines were extrapolated to identify the corrosion factors, the results of which are explained in the next chapter.

In addition, the passivation of surfaces was studied by electrochemical impedance spectroscopy (EIS) through the FRA software. Generally, depending on the application, the connections of the instrument to the electrochemical cell can be (or must be) set up in different ways. Below, the three most commonly used

electrochemical cell setups are discussed, together with the role of electrodes used in electrochemical measurements.

3.6.1 Electrodes used in Electrochemistry

The counter-electrode (also known as auxiliary electrode) is an electrode used to close the current circuit in the electrochemical cell. It is usually made of an inert material (e.g. Pt, Au, graphite, glassy carbon) and does not normally participate in the electrochemical reaction. Because current is flowing between the WE and CE, the total surface area of the CE (source/sink of electrons) must be higher than the area of the WE, so that it will not be a limiting factor in the kinetics of the electrochemical process under investigation. The reference electrode has a stable and well-known electrode potential, and it serves as a point of reference in the electrochemical cell for potential control and measurement. The high stability of the reference electrode potential is usually reached by employing a redox system with constant (buffered or saturated) concentrations of each participant in the redox reaction. Moreover, the current flow through the reference electrode is kept close to zero (ideally zero), which is achieved by using the CE to close the current circuit in the cell together with very high input impedance on the electrometer (> 100 GOhm). Figure 3.9 provides an overview of some commonly employed reference electrodes.

Figure 3.8 shows a schematic of the working electrode, reference electrode and counter electrode in the electrochemical cell employed in this research. Figure 3.9 illustrates a schematic of Autolab PGSTAT-302N connected to the working electrode, reference electrode and counter electrode in the electrochemical cell. To fabricate each coated samples cell, the samples were cut into 2 x 2 cm squares and sockets sized 24/9 with 100mm height was stuck to the surface of coated samples. The samples were then placed in an oven at 80°C for 24 hours. Subsequently, 3.5% NaCl solution was poured

into the sockets, which were kept at 30°C.Measurements were made from day 3 until day 30 at 3-day intervals. For the crude oil solution, all samples were cut into 2x2 cm and suspended in crude oil solution at 60°C for 30 days. After that, FESEM photos helped investigate the corrosion on the coated samples' surfaces.

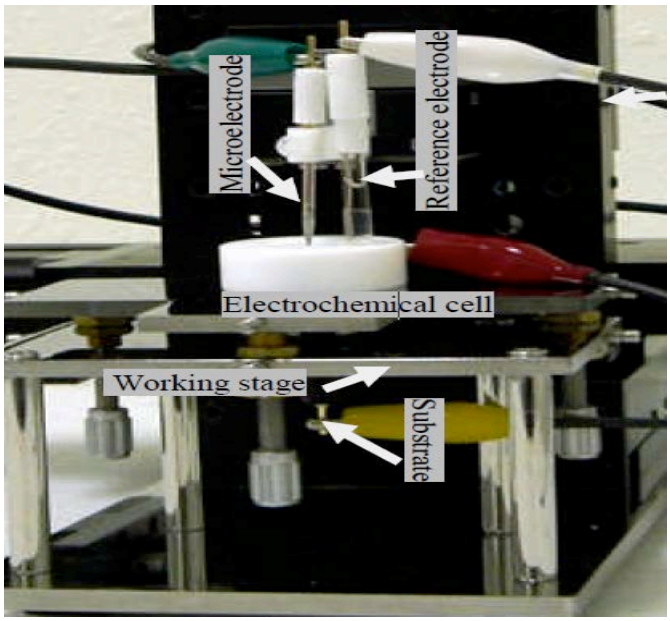

Figure 3.8 Electrochemical cell with mounted work piece

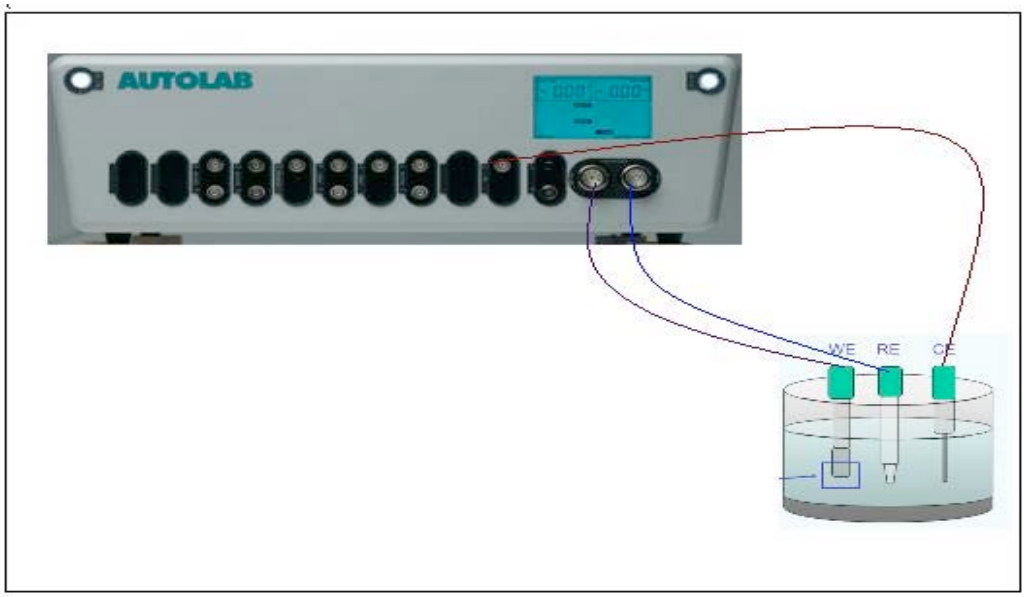

Figure 3.9 Schematic of Autolab PGSTAT-302N

3.7 Summary

This chapter describes the powders with different chemical compositions and properties that were sprayed by HVOF and plasma thermal spray techniques. Then the morphology of each group of materials was investigated by XRD and FESEM. To study the wear behavior of each group, a pin-on-disk machine was selected. The wear weight loss was examined by applying different loads over a 9048.96 m sliding distance. Finally, the potentiodynamic polarization and electrochemical impedance spectroscopy of each group of materials in 3.5% NaCl (seawater) solution were evaluated by Autolab Machine.

CHAPTER 4: RESULTS AND DISCUSSION

4.1 Introduction

In this chapter, the wear and corrosion behavior of materials with five different chemical compositions, which were coated with two techniques (HVOF and plasma) separately, are investigated for 6 times. Then, the best technique with the highest wear and corrosion resistivity behavior is chosen for each material group. Subsequently, the behaviors of all materials selected in the previous step are compared. Finally, the best material and method that achieve the highest wear and corrosion resistivity against an aggressive environment can be determined.

4.2 Analysis on carbon steel substrate

4.2.1 Microstructural analysis

Figure 4.1(a) shows an FESEM image of a carbon steel plate. The carbon steel surface is smooth. Figure 4.1(b) provides an XRD illustration of carbon steel with two elements, Iron-Cobalt (FeCo) and Iron-Nickel (FeNi), with the maximum peak belonging to FeCo.

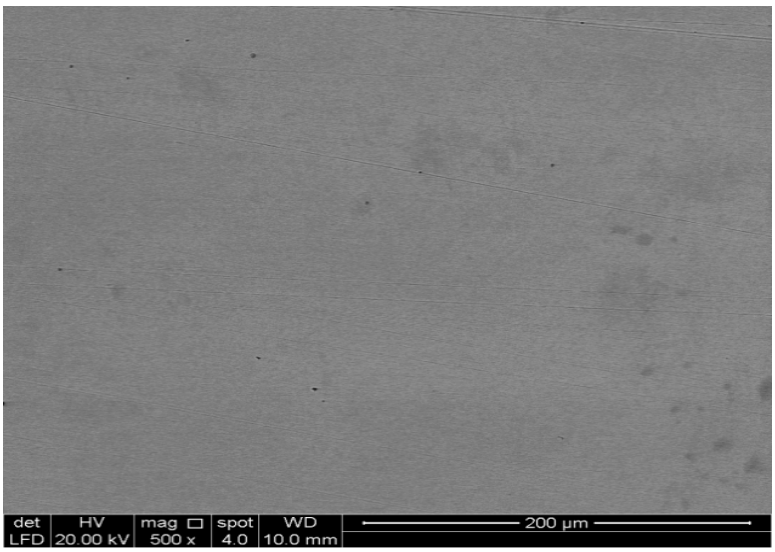

(a) FESEM

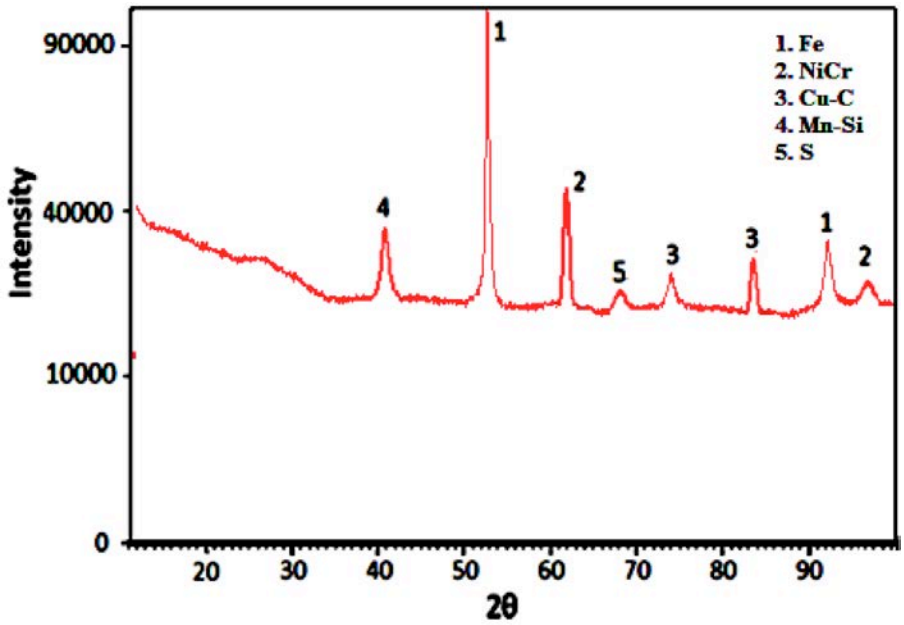

(b) XRD

Figure 4.1 FESEM micrograph and XRD of carbon steel

4.2.2 Wear analysis

For thermal spray coating method, substrate roughness has a strong effect on coating wear under given frictional conditions. The roughness of carbon steel (substrate) is around R_a=1.9102 µm for 100 points, as detected by optical surface texture analyzer software.

In this study, the region of wear and coarse, worn debris from the carbon steel sample at maximum load (20 N) of wear testing is investigated by FESEM. As shown

in Figure 4.2, the carbon steel sample is evidently worn. Wide and deep grooves appeared on the surface after wear testing. Figure 4.2(a) indicates that after applying maximum load, a significant crack was produced, which led to sample edge deformation. Obviously, wear tracks appeared on the entire carbon steel surface. These tracks are the effect of maximum load applied by the pin-on-disc machine during wear testing. After wear testing, wide grooves also appeared beside cracks on the surface. As Figures 4.2 (b) and (c) illustrate, although the worn carbon steel sample surface is smooth and flattened, its wear debris is coarse. This observation shows that the load was extremely high for this substrate, and as a result, the carbon steel surface lost a considerable amount of material. This surface became so rough due to not only for wear debris but also for surface deformation, material removal, cracks, voids nucleation, etc.

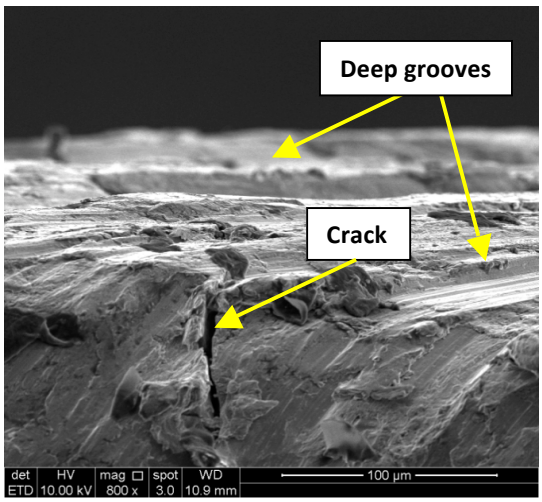

(a)

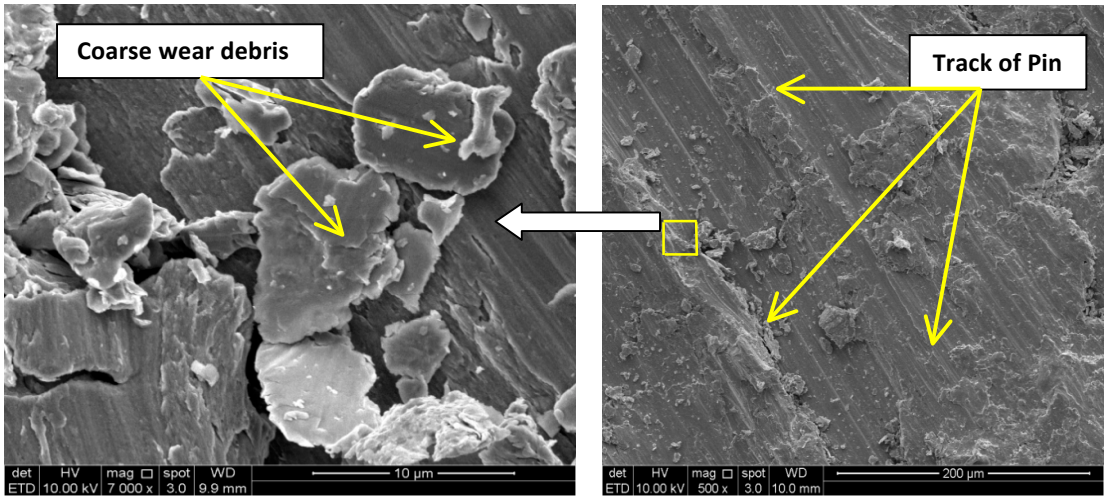

(c) (b)

Figure 4.2 FESEM images for carbon steel samples at maximum load (20 N)

Table 4.1 presents the mean scores of weight loss as well as the wear rate of carbon steel samples under varying loads. Based on the results, the wear rate in carbon steel changed significantly under different loads. Under 5N load, the carbon steel sample indicated minimum weight loss of 1.8949 mg and maximum weight loss of 8.2035 mg under 20N load. It was found that changing load from 15 N to 20 N increased the weight loss for carbon steel two-fold, from 4.0926 to 8.2035 mg.

Moreover, the wear rates for carbon steel signify that when load increased, the wear rate significantly increased. The carbon steel wears values at 5, 10, 15 and 20 N were 125, 200, 250 and 657 µm respectively.

Table 4.1 Weight losses and wear rate of carbon steel sample for different loads

Loads (N)	**Rate of weight loss (%)**	**Average of wear (µm)**
5	1.8949	125±3
10	2.3121	200±2
15	4.0926	250±1
20	8.2035	657±2

4.2.3 Electrochemical corrosion analysis

Polarization curves were drawn for carbon steel samples from day 3 to day 30, and the results are tabulated in Table 4.2. It can be seen that the corrosion current I_{corr} for the carbon steel sample is very high, and there is a big different between the first and last days. The open circuit potential (OCP) of the carbon steel sample moved toward very negative potential by the end of day 30. These results suggest that carbon steel has very low protection against a corrosive environment.

Table 4.2 OCP, I_{corr} and R_{CT}/kOhm of carbon steel sample in 3.5% NaCl solution for 30 Days

Day	Carbon steel Sample			
	OCP		I_{Corr} / A (x 10^{-5})	R_{CT} / kOhm
	Mean	SD		
3	-0.712	0.00052	9.792	2.827
6	-0.711	0.0005	9.549	2.974
9	-0.719	0.00058	9.891	2.608
12	-0.728	0.00061	11.081	0.763
15	-0.736	0.0005	10.749	1.402
18	-0.735	0.00091	10.292	1.798
21	-0.730	0.00082	10.899	0.730
24	-0.739	0.00072	11.363	0.445
27	-0.736	0.00054	11.509	0.314
30	-0.734	0.00075	11.976	0.173

Electrochemical Impedance Spectroscopy (EIS) was also performed on the carbon steel substrates. Figure 4.3 shows the EIS results for the carbon steel sample for day 3 and 30 measurements. For all measurements, a circuit diagram of $R_s(QR_{ct})$ accurately fits the experimental results, and this can be seen in the Bode phase plots with single maxima in Figures 4.3(b) and (d). The circuit diagram can be explained as follows. R_s are the solution resistance between the carbon steel surface and reference electrode, and it is in series with the parallel arrangement of the constant phase element (CPE) and charge transfer resistance R_{ct}. The CPE is often approximated to capacitance, where the parallel arrangement of capacitance and charge transfer resistance gives rise

to a time constant (CR), which appears as a peak in the Bode phase plot (Akhtari Zavareh et al., 2015). Therefore, the charge transfer resistance R_{ct} is the parameter that gives information about the resistance against electron transfer across the carbon steel sample/solution interface (Akhtari Zavareh et al., 2014).

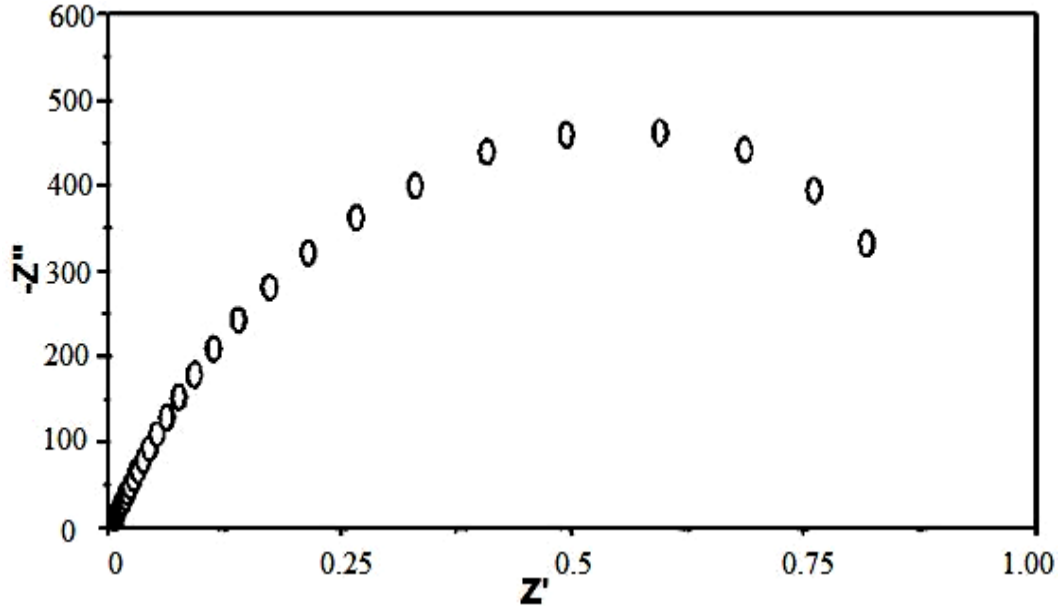

(a) Nyquist plot day 3

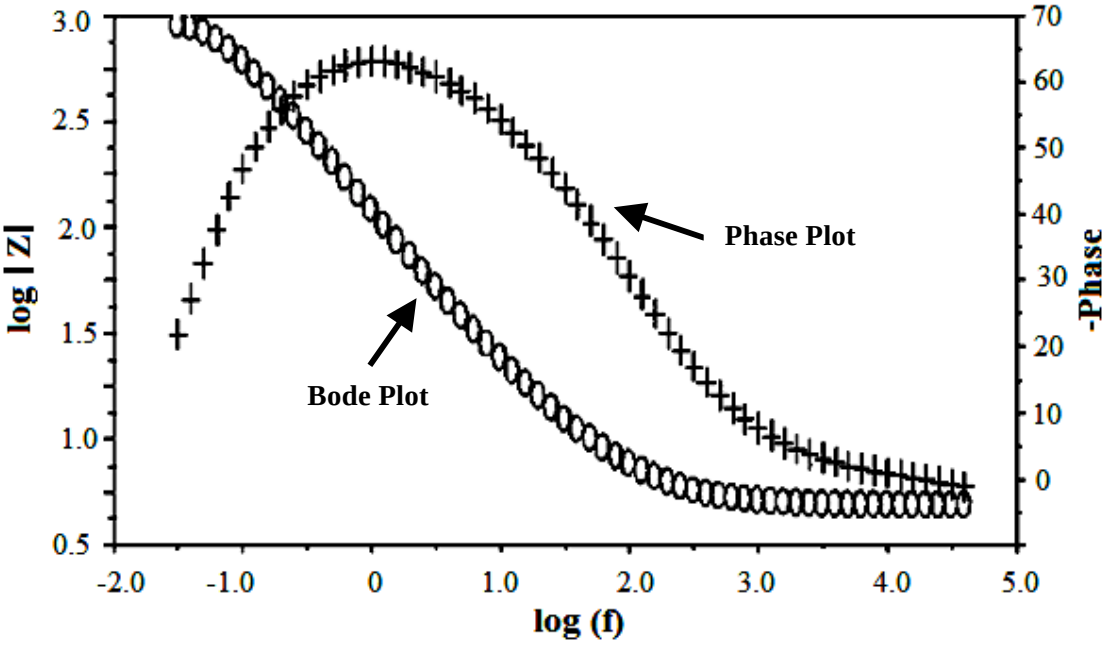

(b) Bode plot day 3

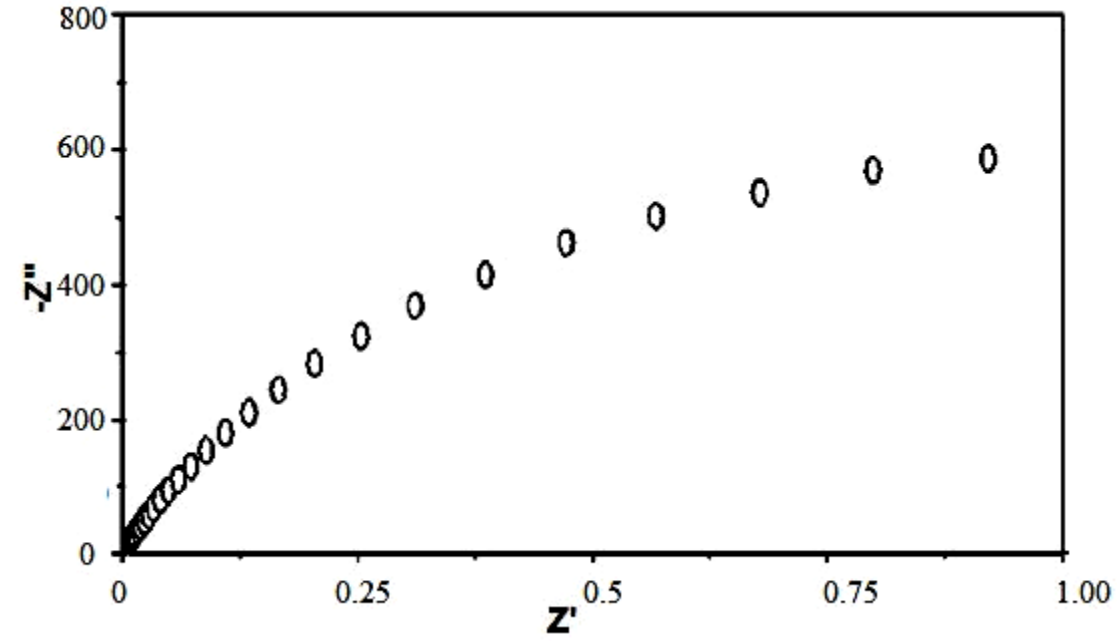

(c) Nyquist plot day 30

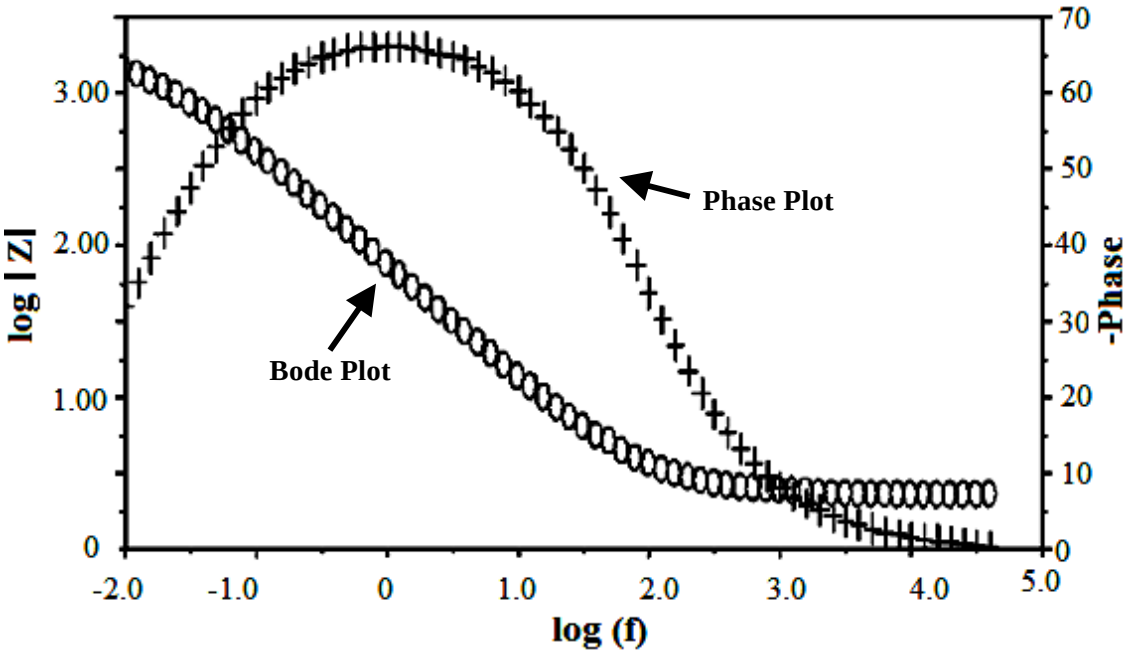

(d) Bode plot day 30

Figure 4.3 EIS for carbon steel sample

4.2.4 Microstructural analysis of corrosion

The X-ray diffraction (XRD) analysis result in Figure 4.4(a) indicates that the carbon steel surface corroded and oxidized to Fe_2O_3 because the reaction with NaCl solution and dissolved oxygen caused surface oxidation. FESEM micrographs of the

carbon steel sample surface after 30 days of immersion in crude oil at 60°C and in seawater (3.5% NaCl solution) at 30°C are shown in Figures 4.4(b) and (c) respectively.

There is a significant difference between the corroded and un-corroded surfaces. Figure 4.4(b) shows that violent corrosion, particularly pitting corrosion, occurred on carbon steel in crude oil after 30 days and destroyed the substrate surface. Figure 4.4(c) shows the region of corrosion in the seawater electrolyte. It can be seen that vigorous corrosion occurred after 30 days, which destroyed the surface and made deep holes on the sample surface. Also the crevice and pitting corrosion happened in the seawater, however the amount of crevice corrosion in seawater in more than crude oil. Generally, the amount of damage in seawater is significantly more than in crude oil. The formation of iron oxide on different areas of the samples is confirmed by the XRD results (Fig 4.4 (a)).

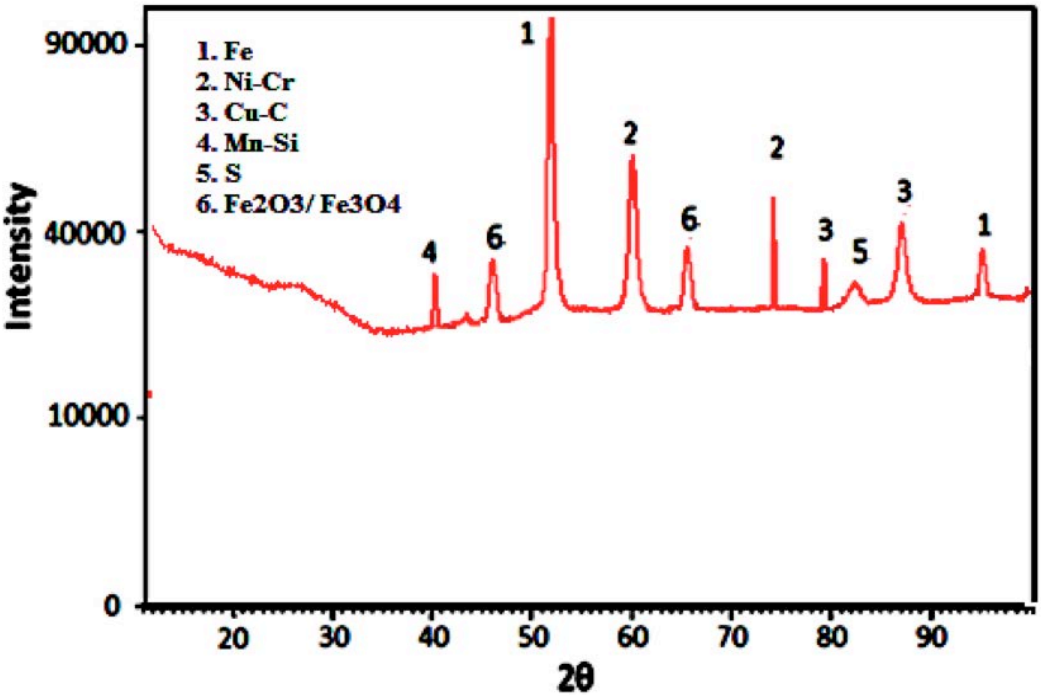

(a) XRD analysis after corrosion in seawater

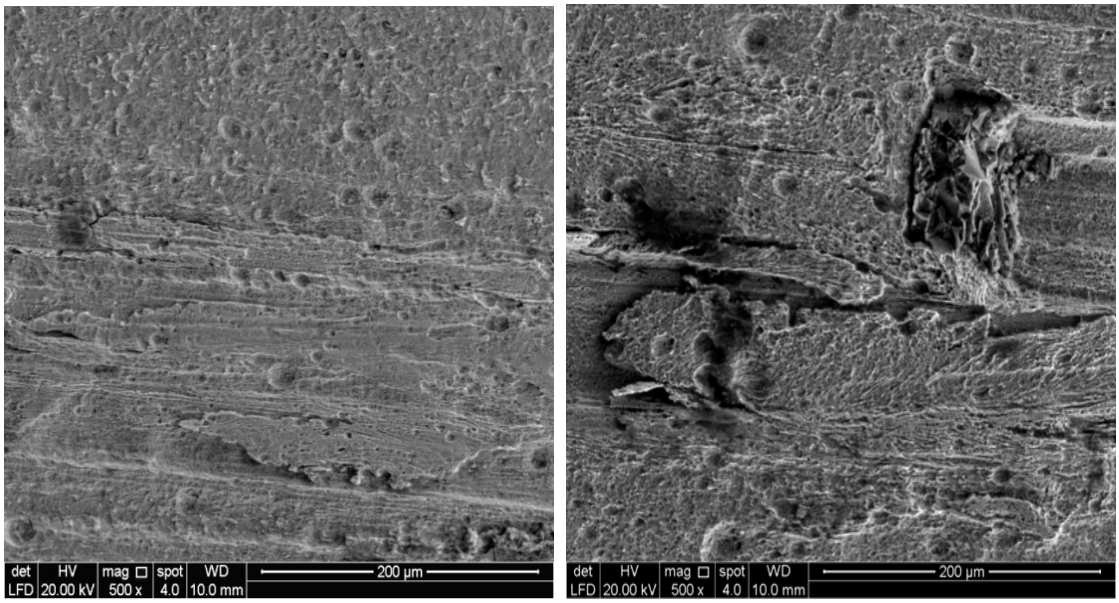

(b) Corrosion inside crude oil (c) Corrosion inside seawater

Figure 4.4 XRD and FESEM micrograph of carbon steel sample

4.3 Analysis of substrate coated with Inconel 625 powder

4.3.1 Microstructural analysis

As seen in Figure 4.5, the cross sections of coated samples demonstrate that the deposited layer covered the substrate uniformly and adhered well to the substrate.

Figures 4.5(a) and (b) display the polished and un-etched cross section of the coating with the plasma method that contains plate-like lamellae oriented parallel to the substrate. These lamellae signify that the molten droplets hit the substrate at high velocity to create splat morphology. Unlike with the HVOF spray coating in Figures 4.5(c) and (d), the splat boundaries are not clearly seen. As in the microstructure of typical sprayed coatings, the splat boundaries are smoothly curved. Some pores are observed as black spots in the micrograph and the amount of porosity with this method is less than with the plasma method. The HVOF-coated samples showed a denser surface compared to the plasma-coated samples (Yusoff et al., 2012). However, both methods protect the substrate from inward oxygen permeation and the corrosive environment.

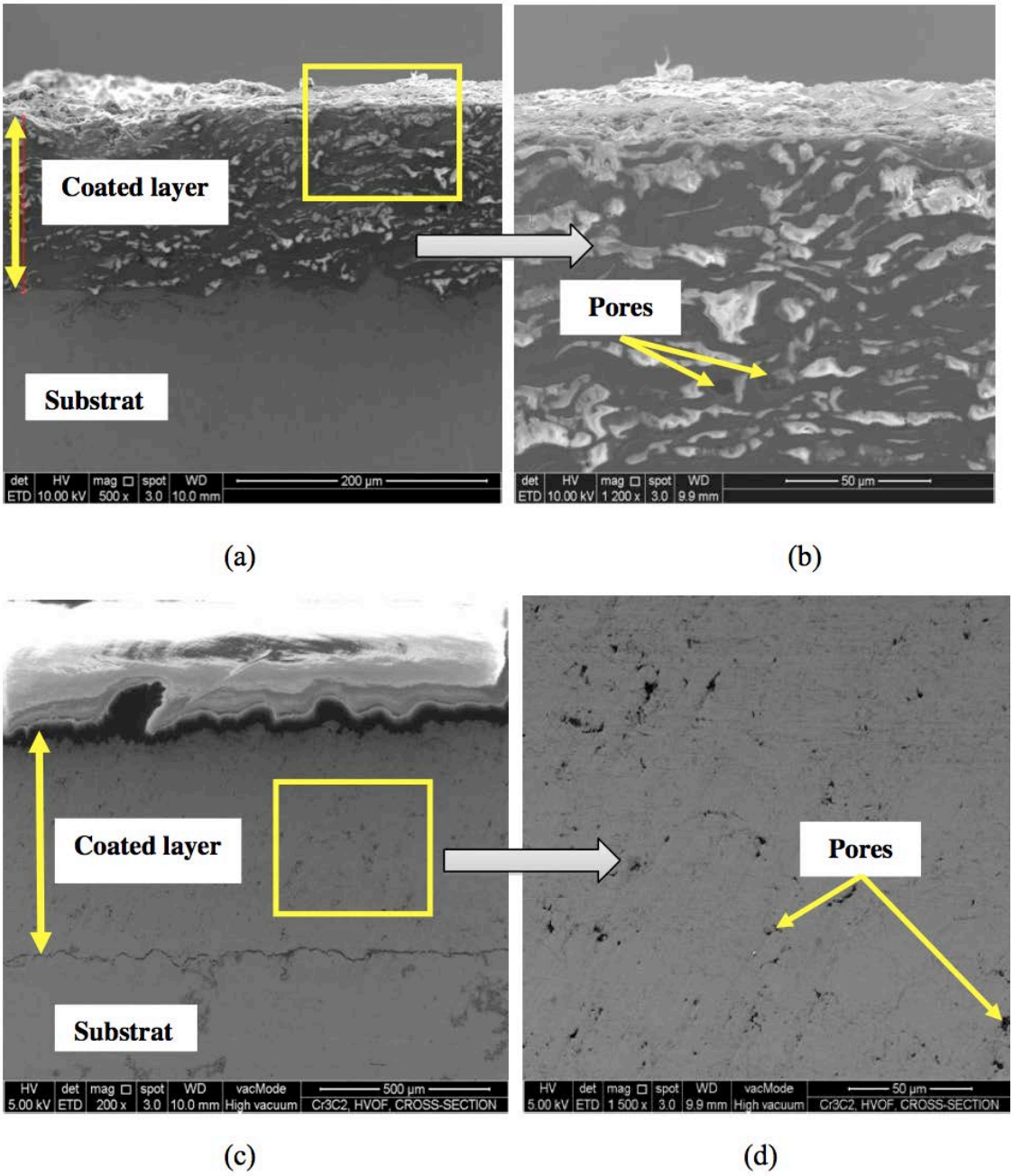

Figure 4.5 Cross section of (a), (b)plasma and (c), (d) HVOF sprayed coatings

Figure 4.6 shows the FESEM micrographs of Inconel 625 coated by plasma and HVOF methods before corrosion and wears testing. The top view image indicates a relatively dense, uniform and crack-free coating deposited on the substrate. However, the HVOF-coated samples have a denser surface compared to the plasma-coated samples. The FESEM indicates three different regions: fully melted, semi melted and un-melted. A small amount of semi-molten or un-molten particles that dispersed homogenously are visible on the top surface of the metal matrix. Figures 4.6 (a) and (b)

show that the un-melted region in plasma-coated samples is significantly less than the HVOF method (Figures 4.6 (c), (d)).

With the plasma method, the high temperature gradient prevents marked segregation to provide a supersaturated Ni-based matrix (Nauman et al., 2013), but still some amount of oxide exits; however, the amount of oxide is significantly less than in the HVOF method. According to Figures 4.6(c) and (d), with the HVOF method the temperature was not high enough to melt the oxide strings in this region because the melting point of $Cr_2O_3$is around 2435°C. As reported by Nauman et al. (2013), in this region any forces in the melt pool arising from fluid flow are not strong enough to disrupt the stringer structure. It causes the oxide stringer framework to remain in place while the metallic material melts and re-solidifies.

The fully melted region in Figures 4.6(b) and (d) is considered the γ-Ni phase, because it is richer in Ni, Cr and Fe compared to the semi-melted or partially melted regions. Conversely, semi- and non-melted regions are richer in Mo and Nb than the matrix. According to Zhang et al. (2003), rapid cooling causes the Mo- and Nb-rich inter-dendritic liquid, which is present in a semi-solid region of a particle. Also, Rombouts et al. (2012) identified Mo- and Nb-rich precipitates in the microstructure of Inconel coating (Abioye et al., 2015).

A few pores appear in black in the micrographs of both types of coating (Figure 4.6). The pore size and average porosity of the coating with the plasma method is greater than the HVOF method. The HVOF method produced coatings with low porosity and high adhesion, which can be applied to severe high temperature corrosion applications (Verdi et al., 2014).

Generally, some porosity is mainly located at the particle-particle interface (Verdi et al., 2014). As it was also previously reported, some small pores merge,

forming large and isolated pores located mainly around the un-melted and partially melted particles (Azarmi & Salimijazi, 2014).

In practice, there will be a range of particle conditions present in the powder stream just before impact with the substrate. This is because feedstock powders contain various particle sizes and also because the particles follow different trajectories through the gas jet. Therefore, some particles may arrive in fully molten state, others in fully solid state and still others in a semi-molten condition. The impact of semi-molten particles with the substrate will cause it to deform and solidify. Extensive deformation occurs if the particles comprise predominantly liquid and semi-solid regions, while fully solid material is more difficult to plastically deform. The high rate of heat extraction on impact will cause a fully liquid region (L) within a particle to solidify rapidly. Dendrite formation and solute micro segregation will be suppressed by the rapid solidification (Kashani et al., 2007).

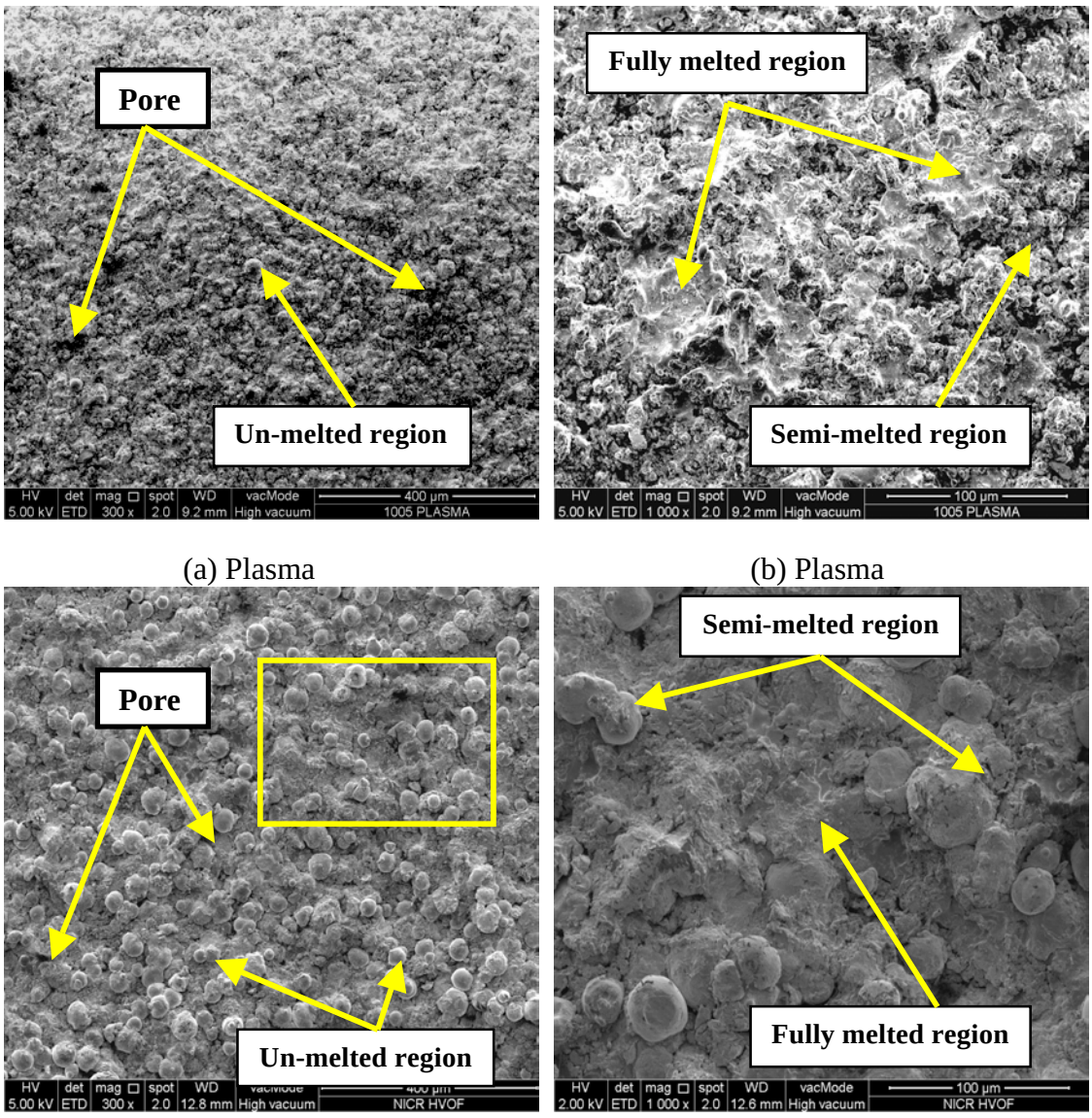

(a) Plasma (b) Plasma

(c) HVOF (d) HVOF

Figure 4.6 FESEM of Inconel 625 coated samples at different magnifications: (a), (c) 300X; (b), (d) 1000X

X-ray diffraction patterns and EDX for Inconel 625 plasma and HVOF-coated samples are shown in Figure 4.7. According Figures 4.7(a) and (b), in the coated samples, some of the phases detected were face-centered cubic (f.c.c.) γ (Ni), Cr_2O_3, Mo and (Fe,Nb+Ta) oxide. However, there were more oxide peaks in the plasma method than HVOF. The pure f.c.cγ-Ni phase peaks occurred at slightly higher 2θ values than other compositions, so they appear as major peaks in XRD. No phases other than an f.c.c γ-Ni with lattice parameter close to pure Ni could be detected. The second largest peaks belonged to chromium (Cr), because it is a primary alloying element in

Inconel 625 that is added to promote resistance to environmental degradation. Its role is to passivate the external alloy surface by forming Cr_2O_3, which is the main reason for resistance to corrosion. Previous research showed that the high temperature of the splats and presence of air molecules captured in voids between the non-melted or semi-molten particles produced Cr_2O_3 (Zhang et al., 2003). The loss of Cr from the solution would result in diminished corrosion resistance (Cooper et al., 1996). Chromium also improves pitting corrosion resistance as well as promotes a 2-3-time increase in surface hardness (Almeida et al., 1994).

As previous reports confirmed, it a metallic matrixes, containing Cr, Mo and Nb, which is increasing a resistant to localized corrosion at the micro crevice and galvanic (Oksa et al., 2004; Zhang & Zhang, 2005; Abioye et al., 2015).

Knorovsky et al. (1989) found that Nb and Mo segregate strongly into inter-dendritic regions, whereas Cr and Fe segregate weakly into dendrite cores. It would seem highly probable that similar segregation effects occur with Inconel 625, giving rise to the observed inter-dendritic regions of higher mean atomic number (Azarmi & Salimijazi, 2014).

Furthermore, the EDX of the Inconel 625 composite for plasma and HVOF methods in Figures 4.7(c) and Figures 4.7 (d) shows the existence of nickel, chromium, molibdynium, niobium, iron and oxygen. The EDX results confirm that the highest peak belongs to the nickel. Also the weight percentage of Oxygen in plasma-coated sample is higher than HVOF-coated sample. The weight percentage of each element is provided in Figure 4.7 (c) and Figure. 4.7 (d) (inset).

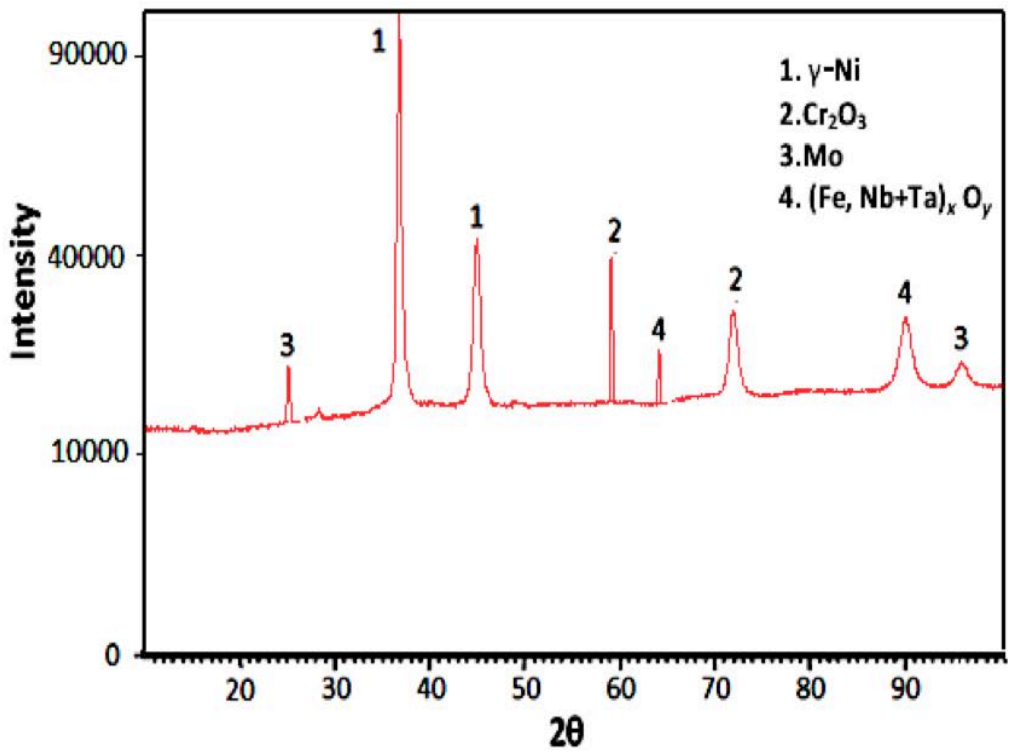
90000
40000
10000
0
Intensity
20
30
40
50
60
70
80
90
2θ
1
1
2
2
4
3
4
3
1. γ-Ni
2.Cr2O3
3.Mo
4. (Fe, Nb+Ta)x Oy

(a)

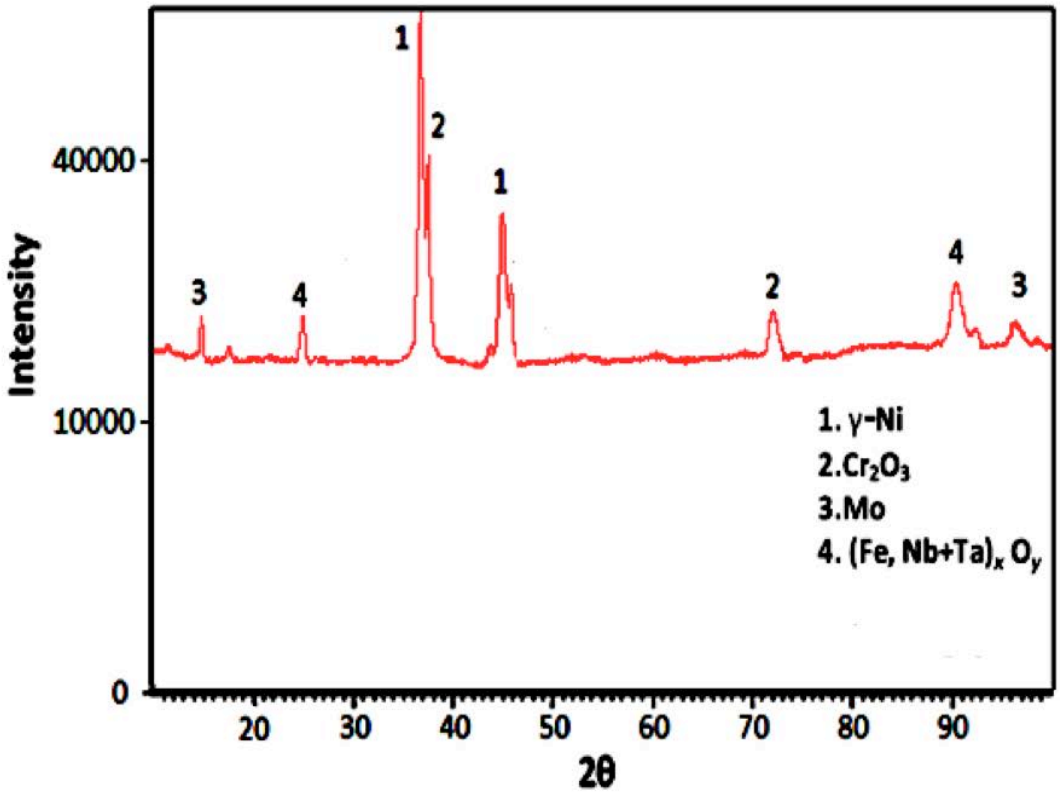
40000
10000
0
Intensity
20
30
40
50
60
70
80
90
2θ
1
2
1
3
4
2
4
3
1. γ-Ni
2.Cr2O3
3.Mo
4. (Fe, Nb+Ta)x Oy

(b)

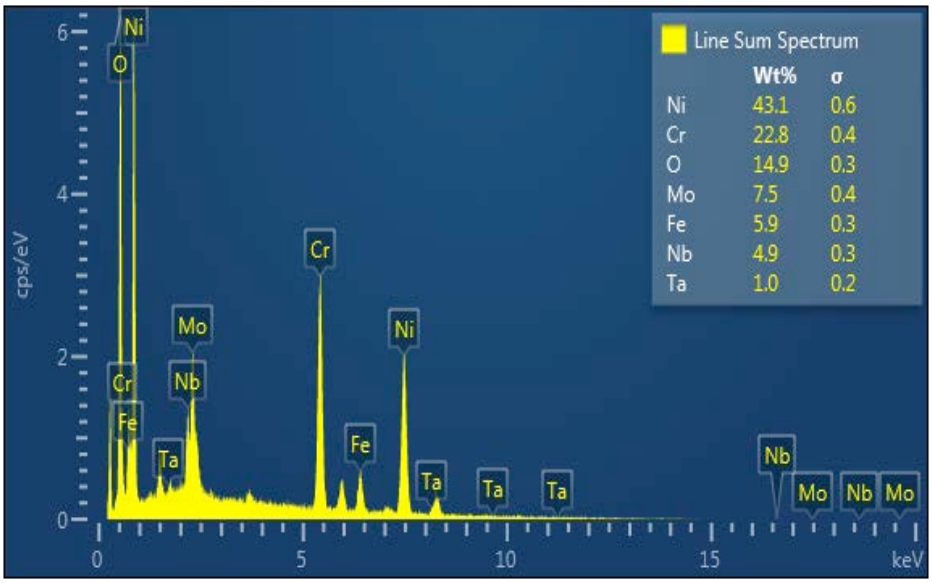

(c)

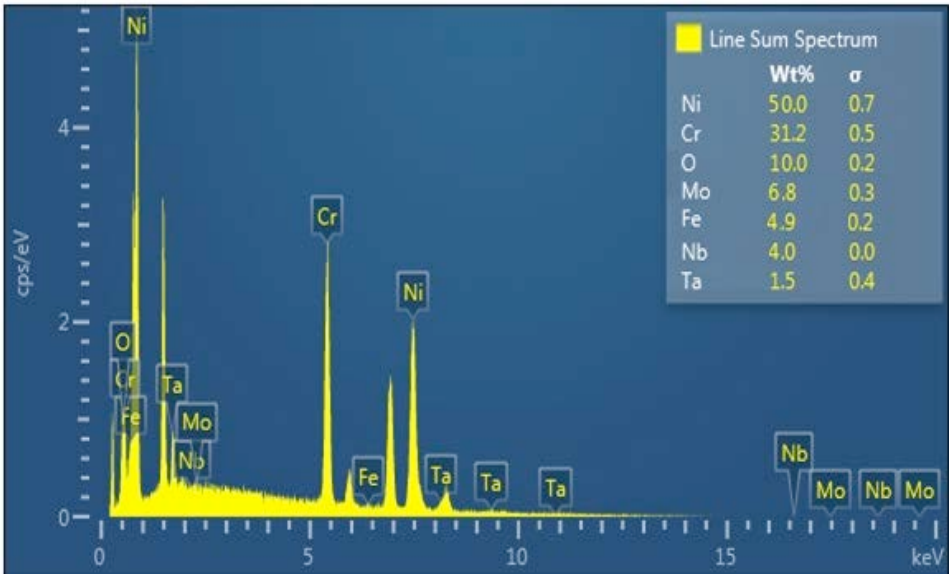

(d)

Figure 4.7 X-ray diffraction patterns of Inconel 625 samples coated by (a) plasma, (b) HVOF; and EDX of (c) plasma and (d) HVOF coated samples

4.3.2 Wear analysis

For any coating type achieved by thermal spray method, substrate roughness strongly affects coating wear under given frictional conditions (K Kato, 2006).

The roughness of plasma and HVOF-coated samples was 9 and 7.6 μm respectively. These values are in agreement with previous studies (Al-Fadhli et al., 2006). The very thick interface between the surface segregates and thick Cr_2O_3layer is most likely due to a significant increase in surface roughness on account of the plasma coating (Zhang et al., 2003).

A perusal of literature related to wear resistance (erosion, abrasion and sliding wear) of a variety of materials, including coatings, clearly indicates that in the majority of cases, hardness has been utilized as the primary parameter for correlating wear resistance (Sánchez Vilches et al., 2011). This has led to further investigations into deposited layer hardness.

The average microhardness of samples coated by plasma and HVOF methods are 310 and 400 Hv respectively. These hardness values are in agreement with previous studies (Al-Fadhli et al., 2002; Verdi et al., 2015). The microhardness values for each HVOF-sprayed coating were non-uniformly distributed along the depth due to the existence of discrete splats and pores (Liu et al., 2007). In addition, the partially-melted/treated layers exhibited higher microhardness values than the fully melted layers.

Song et al. (2002) compared the wear mechanism of fully melted with partially melted regions. They concluded that for coatings composed mainly of fully melted regions, the wear mechanism involves crack initiation and propagation, which lead to eventual delamination, spallation and coarse worn debris. Delamination is not serious

for partially melted regions, and the wear debris is smaller (Sánchez Vilches et al., 2011).In plasma-coated samples, high microstructure homogenization reduces the microhardness (Liu et al., 2007).

FESEMs of plasma and HVOF-coated samples after applying 20 N load are shown in Figure 4.8. Obviously, wear tracks appeared on the sample surfaces. But according to Figures 4.8(a) and (b), the pin track on the plasma-coated sample is significantly more clear than with the HVOF method in Figures 4.8(c) and (d). Also, the material removal rate from the surface of the plasma-coated samples is considerably higher than HVOF-coated samples. This observation indicates that this load was high for the plasma-coated samples. The presence of voids in the plasma coating additionally increased coating loss (Al-Fadhli et al., 2006).

In contrast, when maximum load was applied to the HVOF-coated samples illustrated in Figures 4.8(c) and (d), some non-melted and semi-melted particles randomly worn in different areas. Generally, this amount of load caused slight abrasion of the HVOF-coated sample with some worn regions.

For both methods, after applying 20 N load, no cracks or deformation occurred at the sample edges. Consequently, the plasma-sprayed coating had the lowest wear resistance, because when maximum load was applied, the surface of the coated samples became more worn than the HVOF samples, and the pin track was clear on the coated surface.

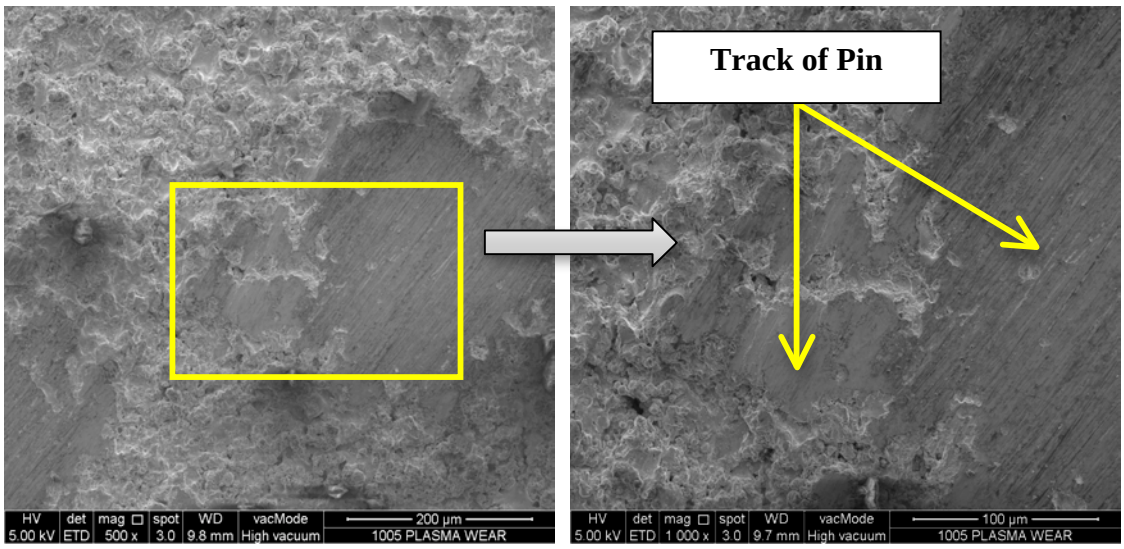

(a) Plasma (b) Plasma

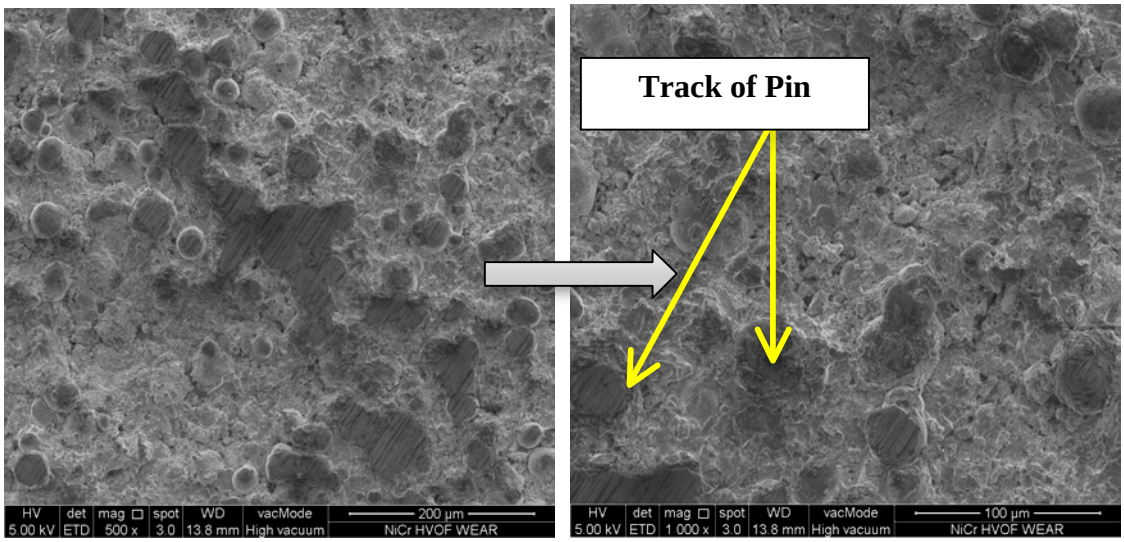

(c) HVOF (d) HVOF

Figure 4.8 FESEM of wear debris of Inconel 625 coated samples under maximum load (20 N) for: (a), (b) plasma coating and (c), (d) HVOF coating

Table 4.3 and Figure 4.9 present the average scores of wear and wear rate with both coating methods under varying loads. Based on the results, the abrasive wear resistance of the plasma coating changed significantly under different loads.

In previous studies, severe scratching/grooving of the wear surfaces was investigated in wear tests at room temperature. The results of dry sliding wear tests indicated that the wear volume loss of the coatings increased with increasing load (Kashani et al., 2007). The rates of wear and weight loss in this research confirm these

trends. According to Table 4.3 and Figure 4.9(a), when different loads were applied on both coated samples, the average amount of wear for the HVOF-coated sample changed between 36 and 58 μm, while for the plasma-coated sample the wear rapidly increased as a result of friction. The maximum wear values for the plasma-coated samples were 46, 52, 60 and 75 μm under 5, 10, 15 and 20 N loads, respectively. As seen in Figure 4.9(b), the rate of weight loss for plasma and HVOF-coated samples changed from 0.0118 to 0.0294, and 0.009 to 0.0227 g, respectively, and the maximum weight loss of both samples occurred under 20 N loads.

Table 4.3 Weight loss and wear rates of Inconel 625 coated samples under different loads

Loads (N)	**Rate of weight loss**		**Average of wear (μm)**	
	Plasma-coated Sample	HVOF-Coated Sample	Plasma - coated Sample	HVOF-Coated Sample
5	0.0118	0.0090	46±2	36±2
10	0.0152	0.0118	52±3	40±2
15	0.0230	0.0180	60±2	47±1
20	0.0294	0.0227	75±4	58±3

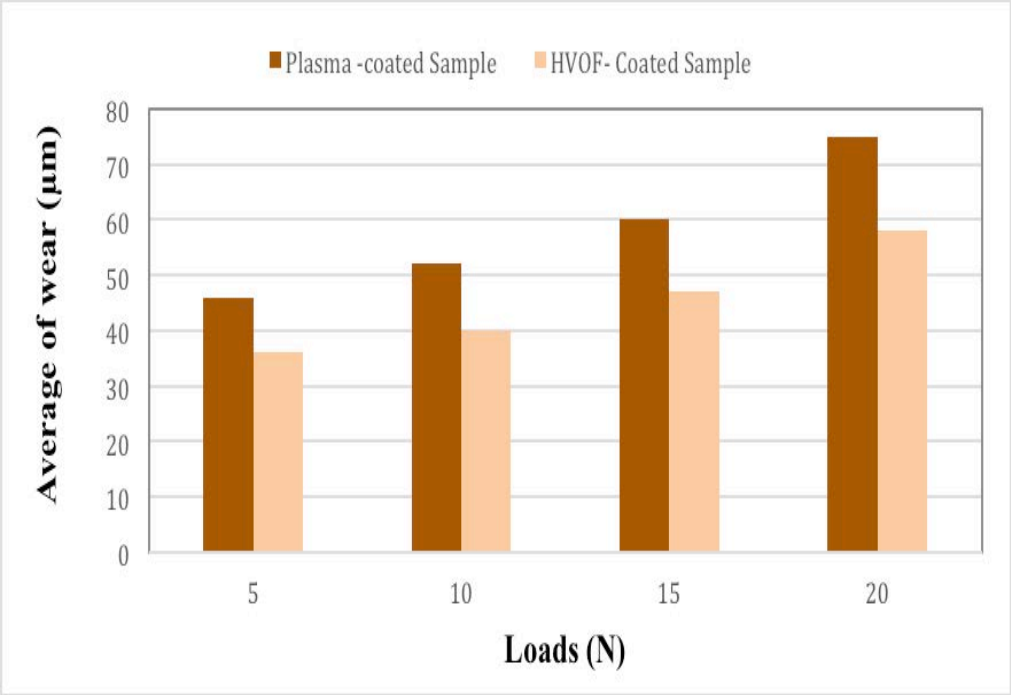

(a)

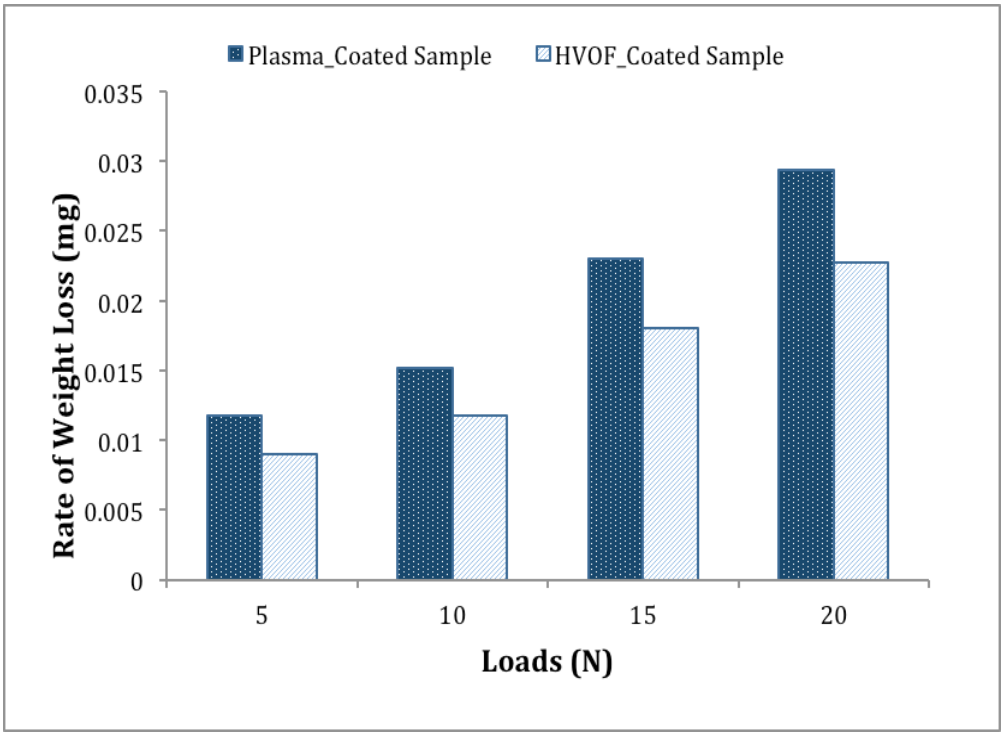

(b)

Figure 4.9 Behavior of Inconel 625plasma and HVOF-coated samples under different loads: (a) average wear, and (b) weight loss rate

4.3.3 Electrochemical Corrosion Analysis

Polarization curves were made for plasma and HVOF-coated samples from day 3 to day 30, and the results are tabulated in Table 4.4. The polarization curves for day 3 and day 30 are shown in Figure 4.10. For steady-state potential of all investigated samples, the electrode was immersed for 20 minutes in NaCl solution.

According to Table 4.4, the rate of corrosion for both methods slightly increased, while the potential of Inconel 625 coated by HVOF method in the whole testing period was more positive than plasma-coated samples. Figure 4.10(a) shows that the plasma-coated samples (blue) had a higher corrosion rate than HVOF-coated samples (red) at the start of measurement. Also, at the end of day 30, the OCP values for the HVOF-coated samples (in red) are nobler compared with plasma-coated samples (in blue). From the 3^{rd} to the 30^{th}day, the potential for plasma and HVOF-coated samples changed from -0.355 to -0.414 and -0.300 to -0.335 respectively. The higher difference in potential for the plasma method sample can be related to porosity. Porosity caused the electrolyte to penetrate and increase the corrosion rate. While on HVOF-coated samples, the coated layer is denser and protects the surface from corrosion. Thus the corrosion rate of these samples is slightly lower than of plasma-coated samples. It can be seen that the corrosion current I_{corr} for HVOF-coated samples is lower than for plasma-coated samples for nearly all measurements (Table 4.4).

Electrochemical Impedance Spectroscopy (EIS) was also performed on the plasma and HVOF-coated samples. Figures 4.11and 4.12 show the EIS results of plasma- and HVOF-coated samples for day 3 and 30 measurements, respectively. For all measurements, a circuit diagram of $R_s(QR_{ct})$ accurately fits the experimental results, and this is evident in the Bode phase plots with single maxima in Figures 4.11(b) and (d), as well as Figures 4.12(b) and (d). The circuit diagram is explained as follows. R_s is

the solution resistance between the samples' surface and reference electrode, and it is in series with the parallel arrangement of the constant phase element (CPE) and charge transfer resistance R_{ct}. The CPE is often approximated to capacitance (Fervel et al., 1999; Singh et al., 2011), where the parallel arrangement of the capacitance and charge transfer resistance gives rise to a time constant (CR) that appears as a peak in the Bo

de phase plot (Normand et al., 2000). Therefore, the charge transfer resistance R_{ct} is the parameter that provides information about the resistance against electron transfer across the coated sample/solution interface (Wang et al, 2000; Akhtari Zavareh et al., 2014).

Table 4.4 shows that the R_{ct} value for HVOF-coated samples is greater than for plasma-coated samples for nearly all measurements. These results also confirm the enhanced performance of HVOF coating compared with plasma coating in terms of corrosion protection of sample surface. The corrosion resistivity of plasma and HVOF-coated samples decreased from 10.891 to 8.001 kΩ on day 3, and 12.235 to 10.995 kΩ on day 30. From day 6 to day 9, the corrosion resistivity of the HVOF samples suddenly decreased from 12.009 kΩ to 11.779 KΩ. While after day 9 until the end of the period, the corrosion rate decreased slightly.

Table 4.4 shows that for HVOF-coated samples the corrosion current density from day 3 to 30 rose from 4.347×10^{-5} to 6.197×10^{-5} A, while the current density suddenly increased from 5.043×10^{-5} to 5.783×10^{-5} A and from day 18 to 21, after which it slightly increased up to 6.103×10^{-5}on day 30.

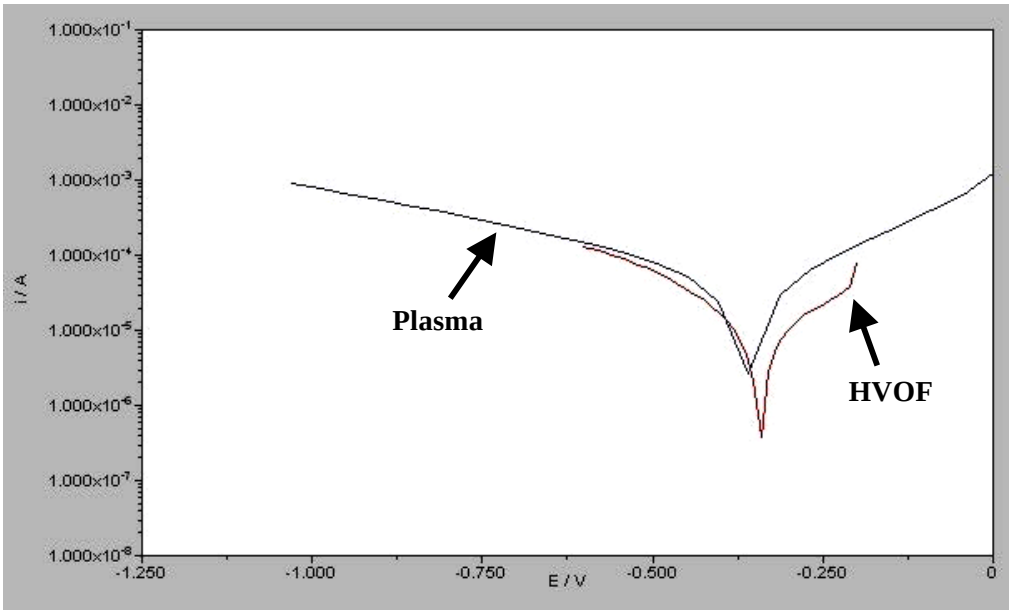

(a) 3rd day experiment

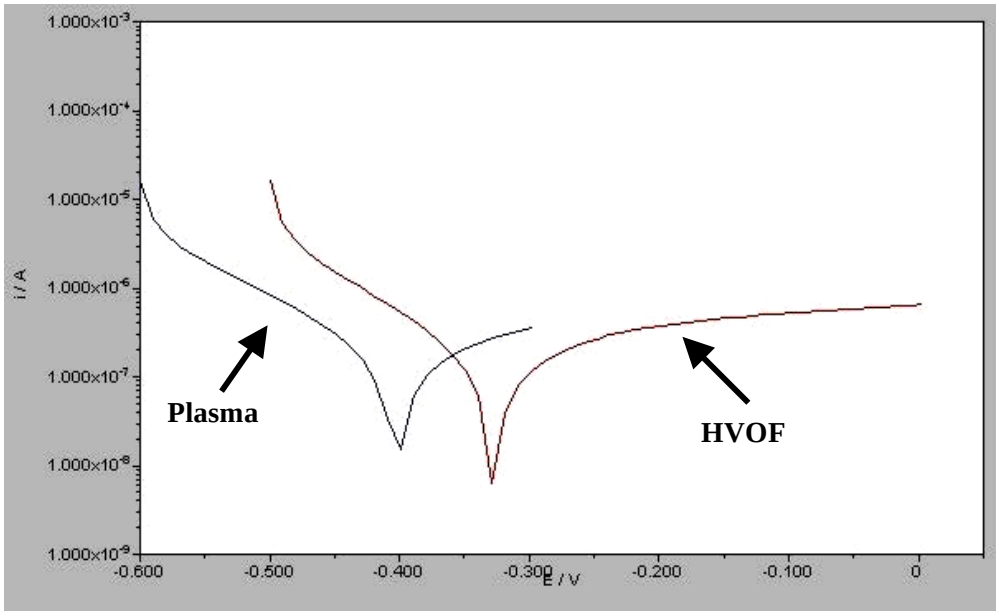

(b) 30th day experiment

Figure 4.10 Polarization curves (log I vs E) of Inconel 625 for: (a) 3rd day, and (b) 30th day experiments for plasma and HVOF methods

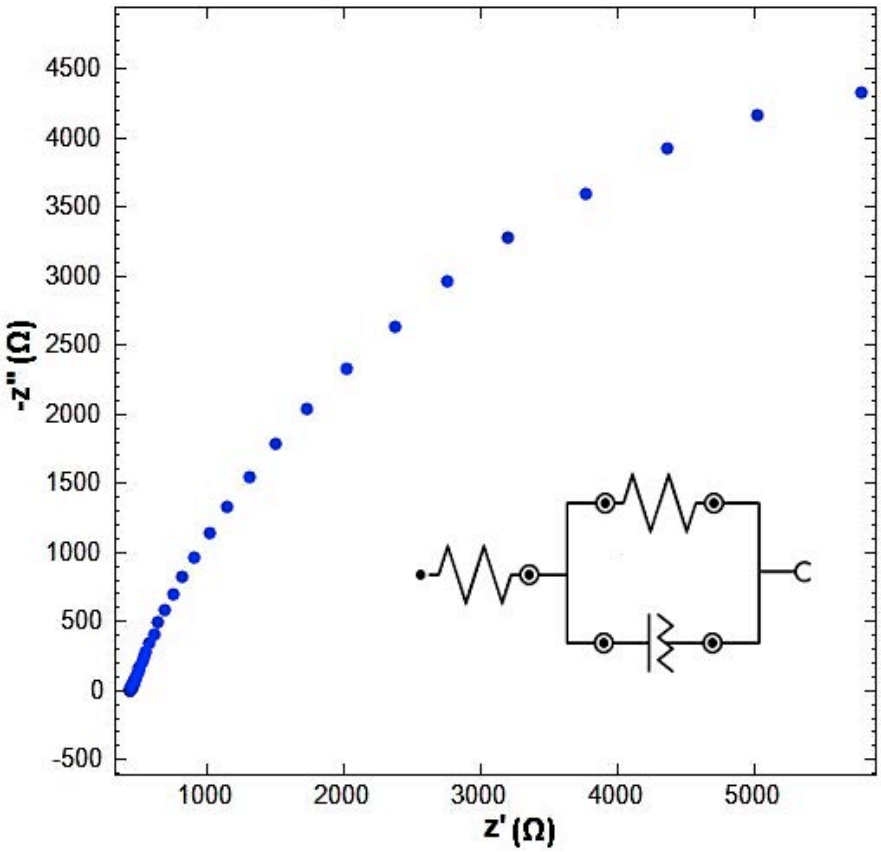

(a) Nyquist plot day 3

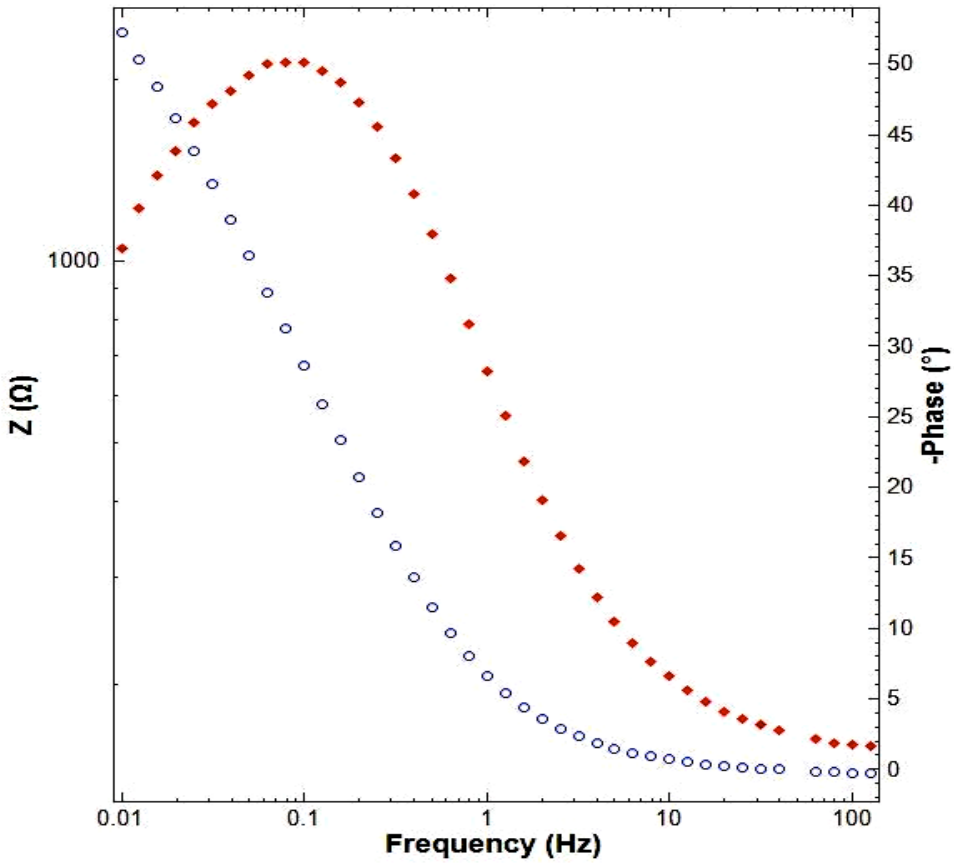

(b) Bode plot day 3

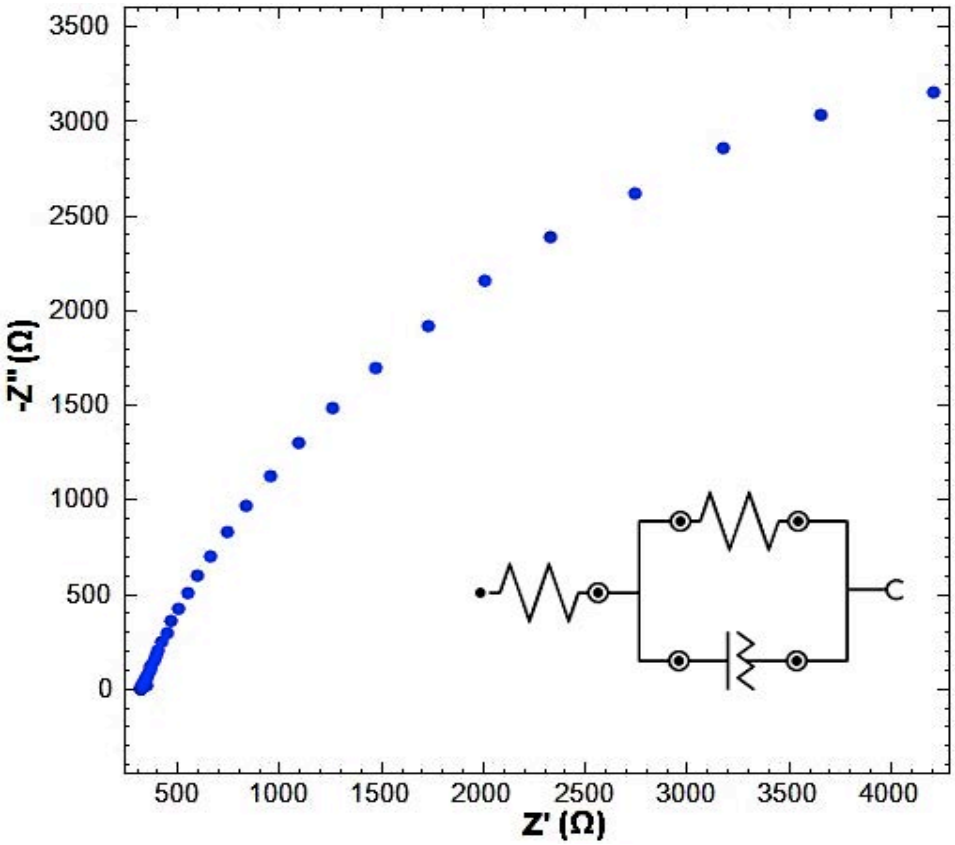

(c) Nyquist plot day 30

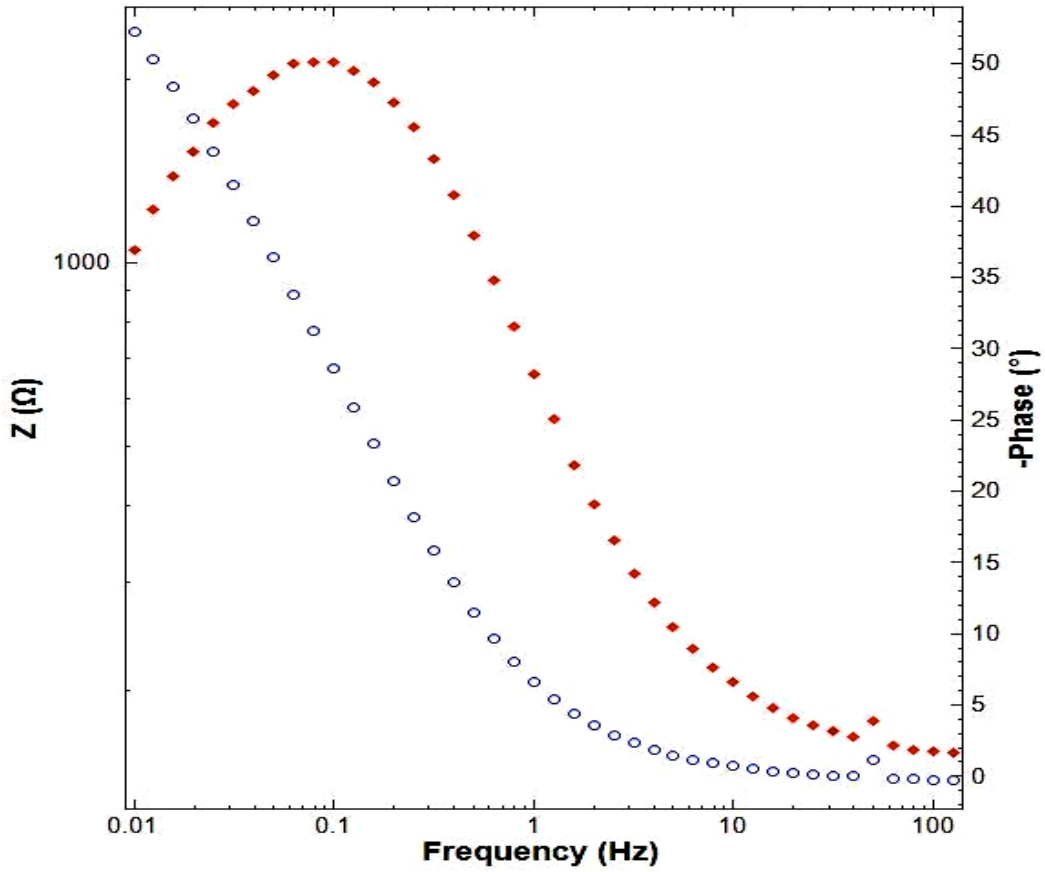

(d) Bode plot day 30

Figure 4.11 EIS of Inconel 625 plasma-coated sample

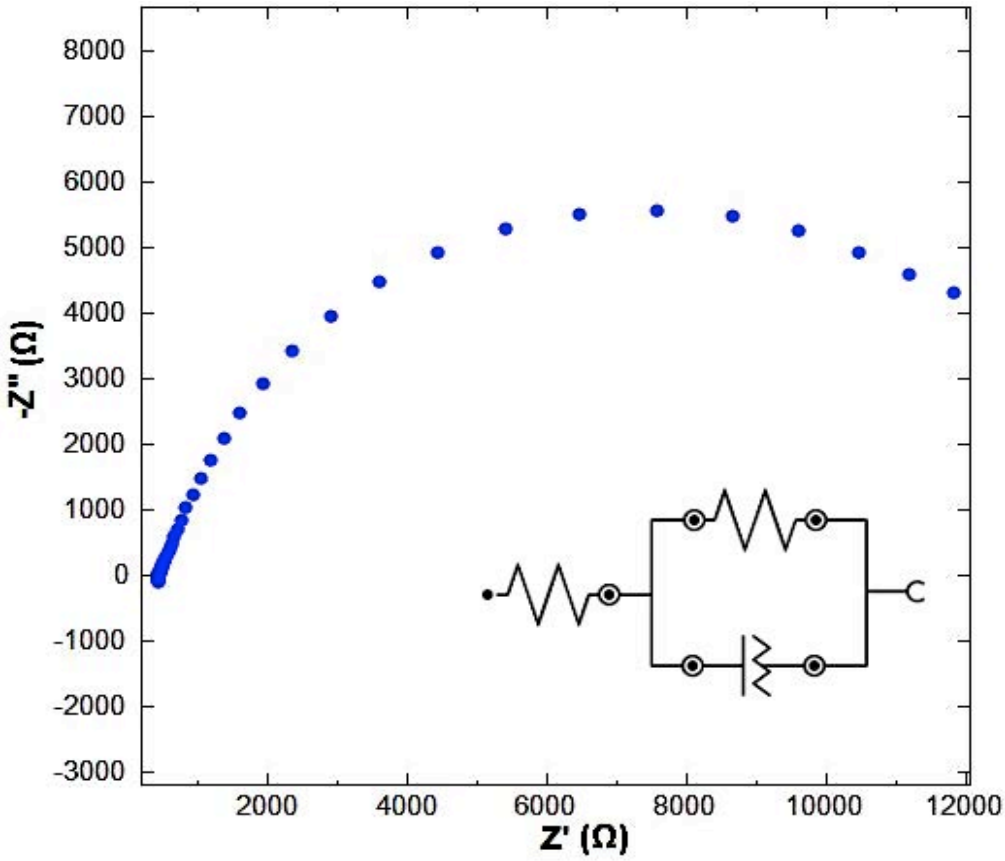

(c) Nyquist plot day 3

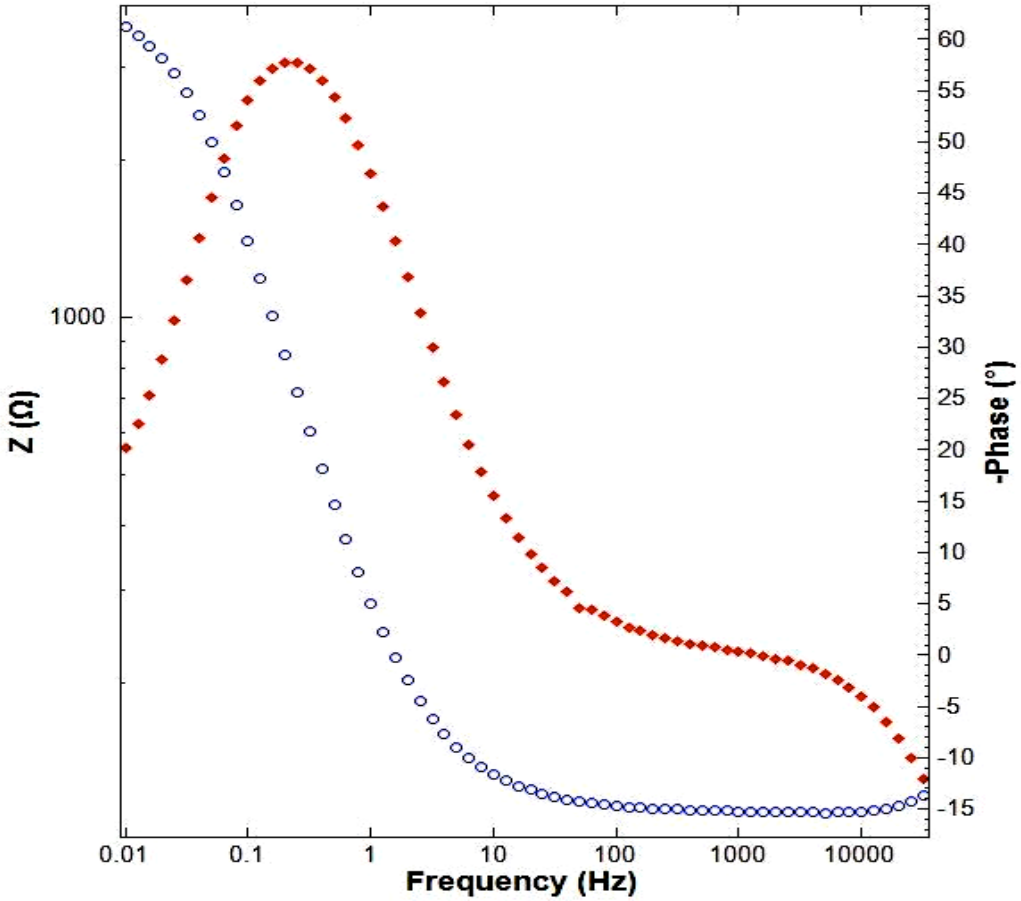

(d) Bode plot day 3

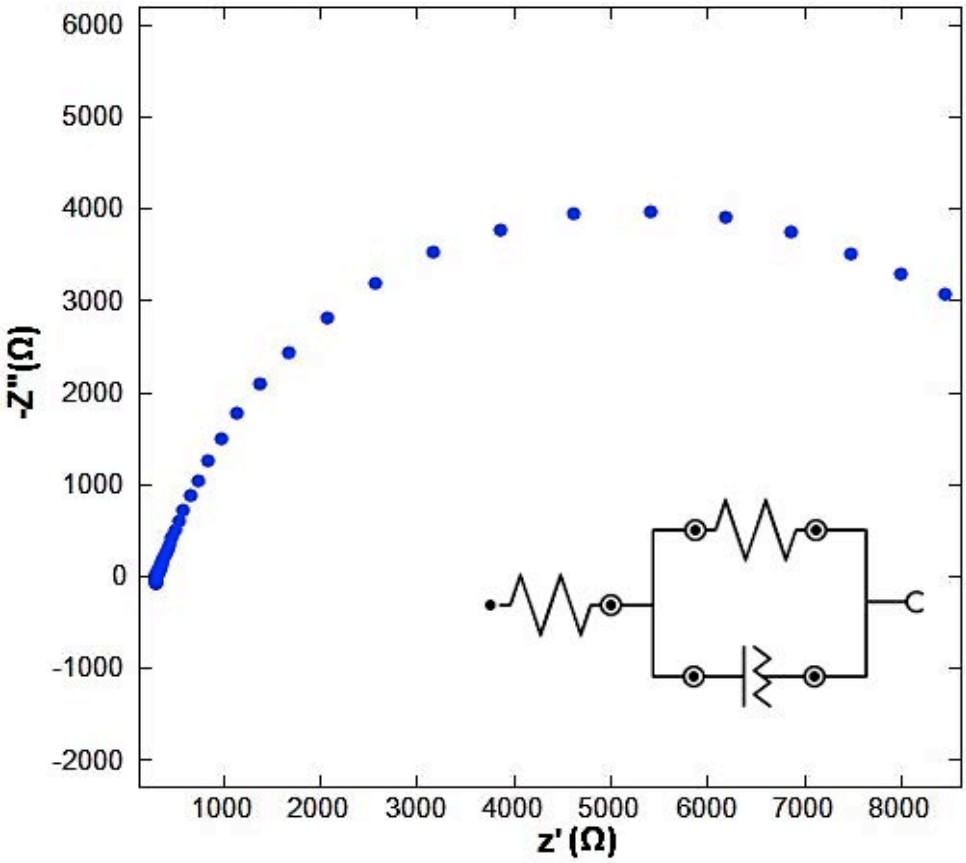

(c) Nyquist plot day 30

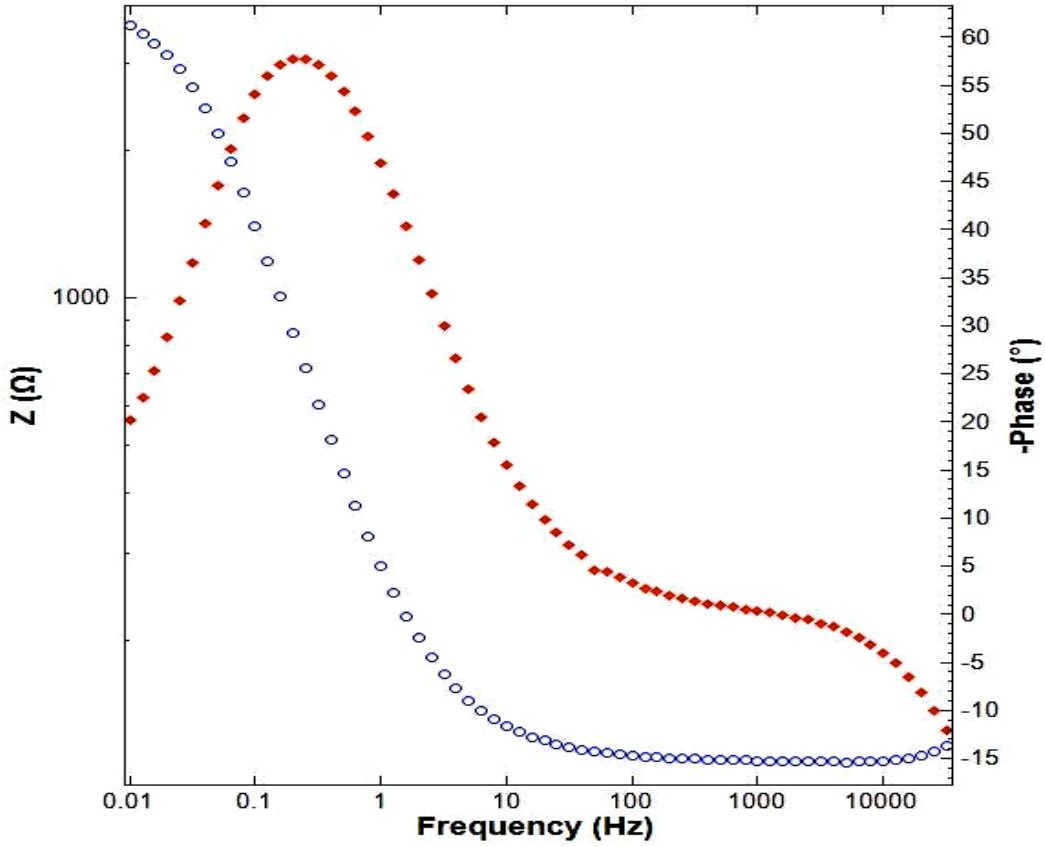

(d) Bode plot day 30

Figure 4.12 EIS of Inconel 625 HVOF-coated sample

Table 4.4 OCP, I_{corr} and R_{CT}/kOhm of Inconel 625 samples for plasma and HVOF coating methods in 3.5% NaCl solution for 30 days

Day	Plasma-coated Sample				HVOF-coated Sample			
	OCP		I_{Corr} / A (x 10^{-5})	R_{CT} / kOhm	OCP		I_{Corr} / A (x 10^{-5})	R_{CT} / kOhm
	Mean	SD			Mean	SD		
3	-0.355	0.00061	4.347	10.891	-0.300	0.0005	3.117	12.235
6	-0.366	0.00053	4.796	10.623	-0.303	0.00075	3.236	12.009
9	-0.370	0.00074	4.995	10.226	-0.309	0.00051	4.238	11.899
12	-0.379	0.00058	5.094	9.813	-0.310	0.0005	4.523	11.787
15	-0.384	0.0011	5.289	9.198	-0.314	0.00068	4.989	11.648
18	-0.390	0.00075	5.598	8.820	-0.319	0.0006	5.043	11.520
21	-0.398	0.00089	5.727	8.632	-0.321	0.0014	5.783	11.332
24	-0.407	0.0013	5.994	8.420	-0.324	0.0013	5.984	11.179
27	-0.412	0.0016	6.119	8.202	-0.329	0.00054	6.041	11.043
30	-0.419	0.0010	6.197	8.001	-0.335	0.00077	6.103	10.995

4.3.4 Microstructural analysis of corrosion

FESEM micrographs of both coated samples after 30 days immersion in crude oil and seawater are shown in Figures 4.13 and 4.14. According to Figures 4.13(a), (b) and 4.14(a), (b), when samples were exposed to the oil environment, the corrosion rate on the coated samples' surface was less than in NaCl electrolyte (seawater) solution, while in this research the temperature of crude oil was 30°C higher than seawater. As seen in Figure 4.13, the amount of pitting corrosion on the plasma sample is greater

than the HVOF-coated sample. The plasma coating in Figure 4.13 displays pitting corrosion in the microstructure, containing inter-splat porosity.

However, for the HVOF coating (Figure 4.14), there is no significant difference before and after corrosion testing. Regarding these figures, there is a difference between the corroded and un-corroded samples with the plasma coating method in both environments; while for HVOF-coated samples the difference between corroded and un-corroded (Figure 4.6) samples is considerably less than the plasma coating method. However, both methods protected the substrate from corrosion.

Previous studies showed that corrosion attack on HVOF-sprayed Inconel 625 coatings was in the form of pitting and localized corrosion on discrete splats (Neville et al., 1998), but the presence of Mo provided resistance to pitting (Cooper et al., 1996).In addition, galvanic corrosion is the main reason for corrosion (Liu et al., 2007). The performance gap between bulk and HVOF-sprayed Inconel 625 is largely due to galvanic corrosion between Cr-depleted re-solidified regions and non-melted material in the coatings. In previous studies it was found that non-interconnected porosity in the deposited layer may affect the corrosion behavior via crevice corrosion and decrease the deposited layer's corrosion resistance (Mumtaz et al., 2008; Ahmed et al., 2010).

Neville et al. (2000) studied thermal sprayed Inconel 625 coating and investigated the mechanism of attack in seawater. The contribution of porosity in the HVOF method is not a major issue, because porosity levels are typically less than 1–2% in this type of coatings under optimized condition. An initial attack occurs at the particle boundaries and within particles, while solution penetration through the interconnected porosity is not significant.

According to the FESEMs of coated samples, the corrosion rate in 3.5% NaCl solution is significantly higher than in crude oil. Thus, it is important to know whether

in these samples, the electrolyte solution (3.5% NaCl) can reach the substrate or not. For this reason, X-ray diffraction (XRD) analysis for plasma and HVOF-coated samples in 3.5% NaCl electrolyte after 30 days is illustrated in Figures 4.15(a) and (b) respectively. It was shown that the deposited layer oxidized and two oxide phase of $NiCr_2O_3$and $(Fe, Cr)_2O_3$ created on the coated surface that has a white color. According to Neville and Hodgkiess (2000), the passive film that forms on Inconel 625 is a mixed Fe-Cr oxide, which protects the material from further corrosion. Also, an Inconel alloy on a mild steel substrate has interconnected porosity and inter-splat oxide whose principal microstructural features affect corrosion resistance (Krepski, 1994; Zhang et al., 2003). Inconel 625 deposited by HVOF technique tends to produce higher quality coatings with less oxidation and porosity than other thermal spray methods. For this reason the amount of oxide layer (white area) in HVOF-coated sample (Figure 4.14) in both of corrosion environment less than plasma-coated samples (Figure 4.13).

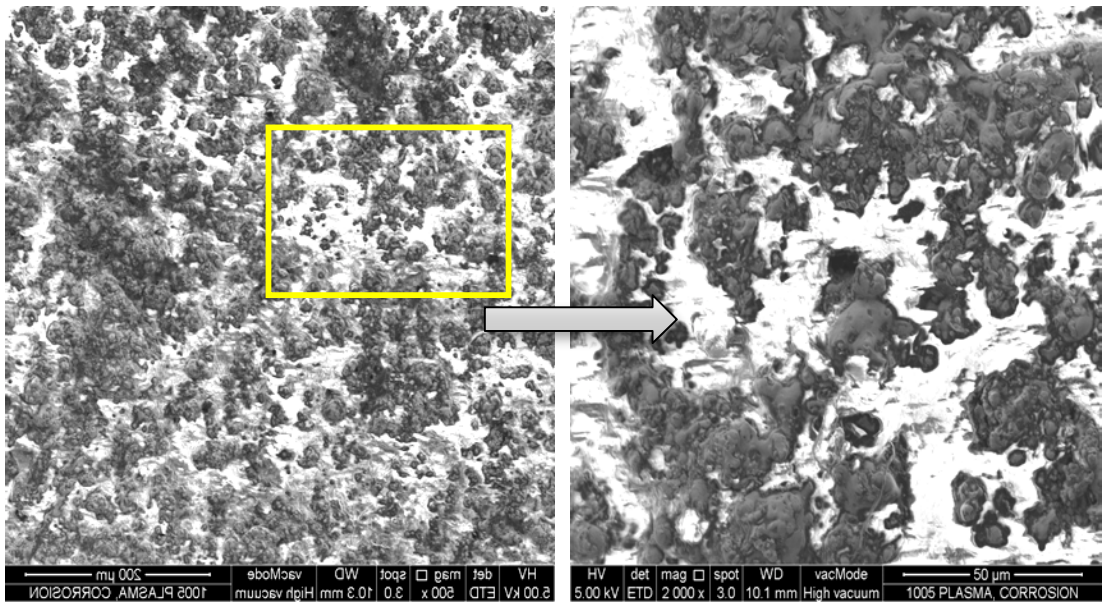

(a) (b)

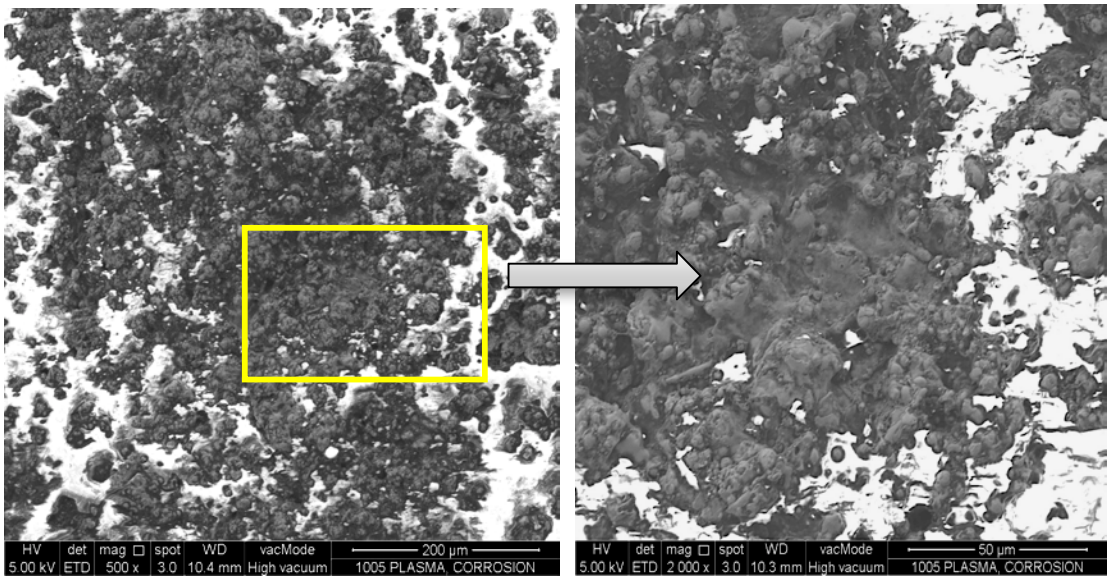

(c) (d)

Figure 4.13 FESEM micrographs of Inconel 625 plasma-coated sample surfaces after 30 days: (a), (b) in crude oil;(c), (d) in seawater

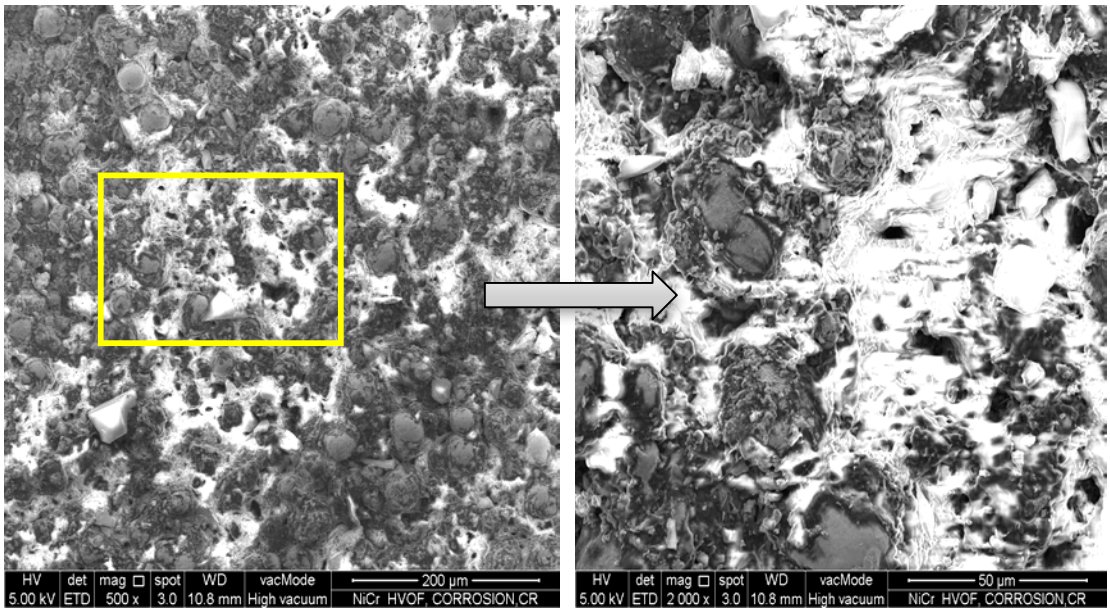

(a) (b)

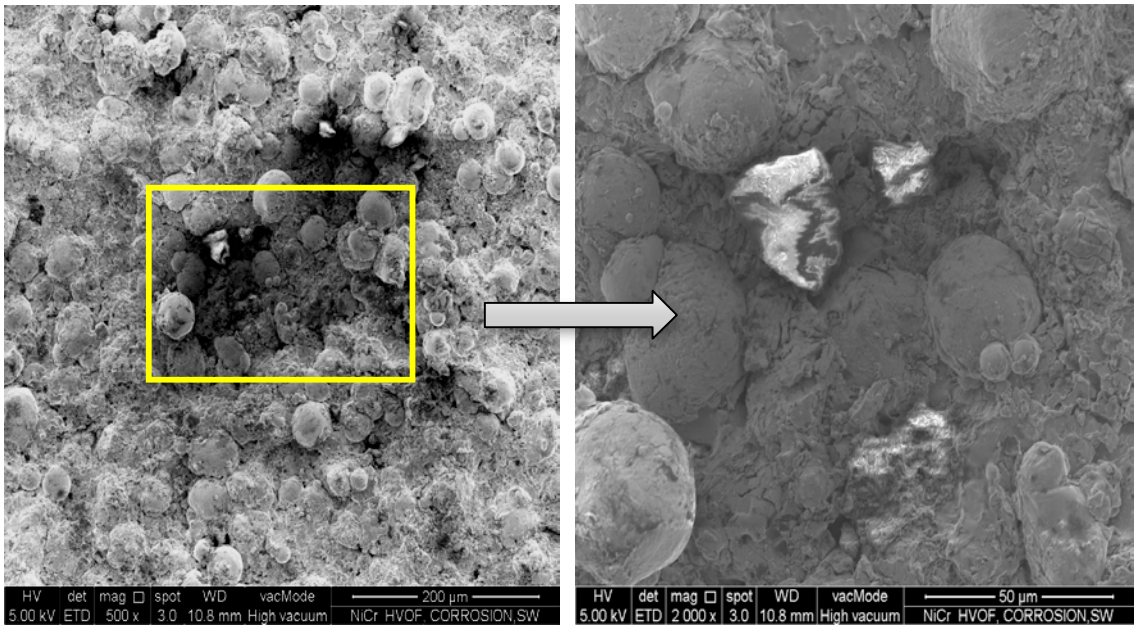

(c) (d)

Figure 4.14 FESEM micrographs of Inconel 625 HVOF-coated sample surface after 30 days: (a), (b) in crude oil;(c), (d) in seawater

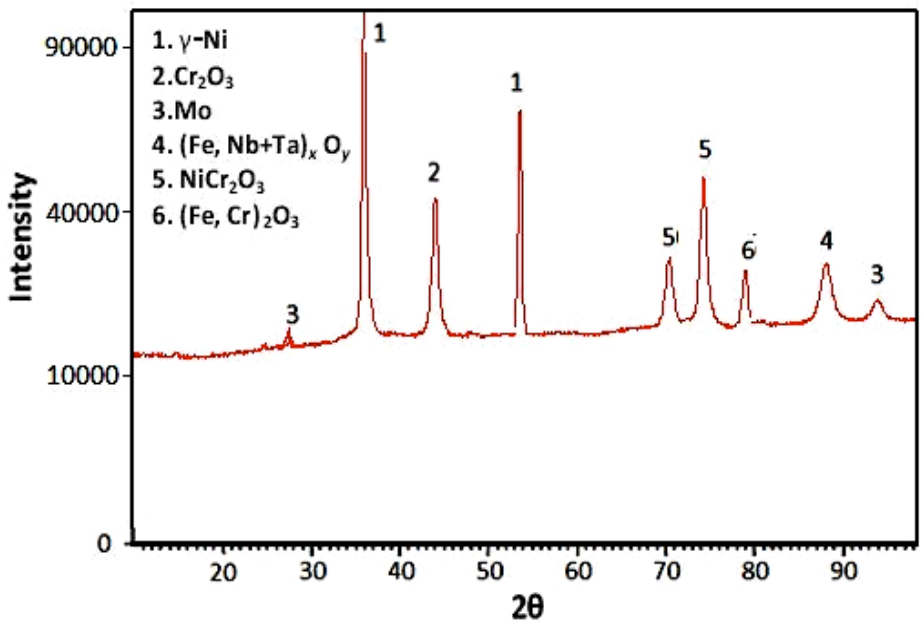

(a)

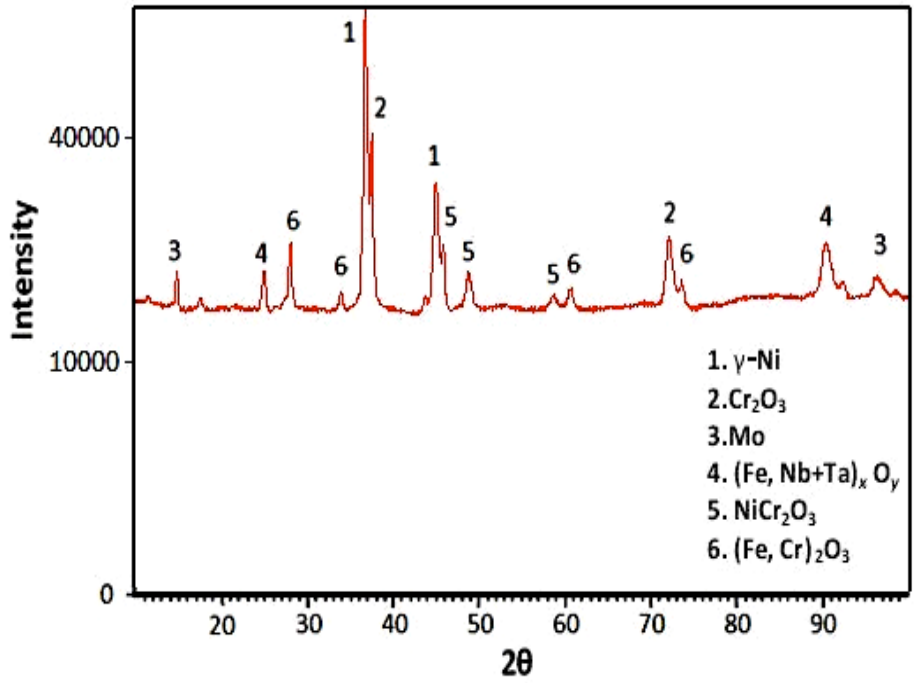

(b)

Figure 4.15 XRD results of Inconel 625 coated samples in 3.5%NaCl solution after 30 days with: (a) plasma, and (b) HVOF

According to the wear and corrosion results, Inconel 625 facilitated by plasma coating has less mechanical and chemical properties than the HVOF method. Also, the wear rate for plasma-coated samples under different loads is higher than HVOF-coated samples. Finally, HVOF-coated samples have higher charge transfer resistance, R_{ct},

compared to the plasma samples, due to the higher resistance of the Inconel 625 HVOF coated against corrosion compared to the plasma coated.

4.4 Analysis of substrates coated with Nickel Cobalt Chromium Aluminum Yttrium (NiCoCrAlY)

4.4.1 Microstructural analysis

Figure 4.16 displays FESEM micrographs of plasma and HVOF-coated samples before corrosion and wear testing. The top view image indicates a relatively dense, uniform and crack-free coating deposited on the substrate. However, the HVOF-coated samples show has a semi-uniform surface compared to the plasma-coated samples.

A small amount of semi- and non-molten particles is visible in the fully melted region (Ni) area. The presence of semi- and non-molten particles provides the coating with high bonding strength and good wear resistance (Wu et al., 2011; Somasundaram et al., 2014). A few pores appear in black in the micrographs of both types of coating. The porosity size and average porosity with the HVOF method are greater than with plasma.

The coatings deposited by plasma spray (Figures 4.16(a), (b)) exhibit the most visible defects. Shrinkage of the molten droplets as they splat onto the substrate and rapidly solidify is one of the main causes of porosity and visible defects in plasma spray coatings. Richer et al. (2010) reported single particle splats visible within the coating microstructure, due to the presence of numerous elongated inter-splat cracks. Evidence of porosity caused by insufficient deformation is also visible in the plasma coating in the form of equi-axed pores. These two types of porosity are not typically encountered with the HVOF technique given the lower process temperatures that cause limited to no melting of particles, thus resulting in minimal shrinkage upon cooling. Furthermore, the

inherent high particle impact velocities with HVOF promote particle compaction, thus resulting in high-density coatings (Zhang et al., 2008; Richer et al., 2010).

Coatings deposited by HVOF (Figures 4.16(c), (d)) feature the most desirable structure with minimal porosity, absence of cracks and a clean interface with the substrate. The finer pores within HVOF coating demonstrate the superior compaction and deposition of particles during spraying. Also, HVOF coating has a rough surface due to the overlap of different splats and the roughness of each single splat.

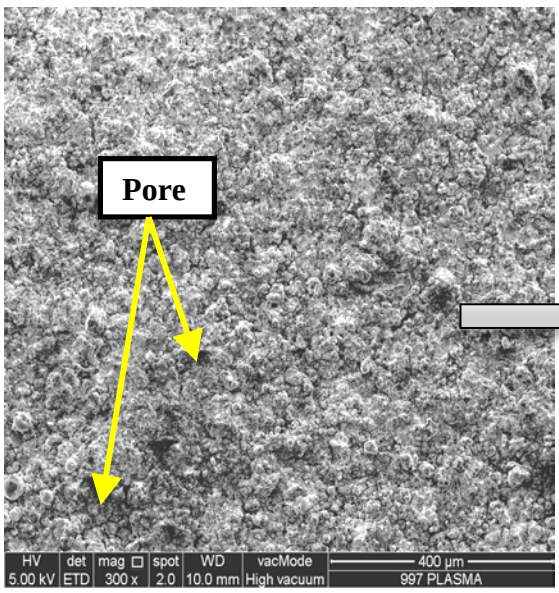

(a) Plasma

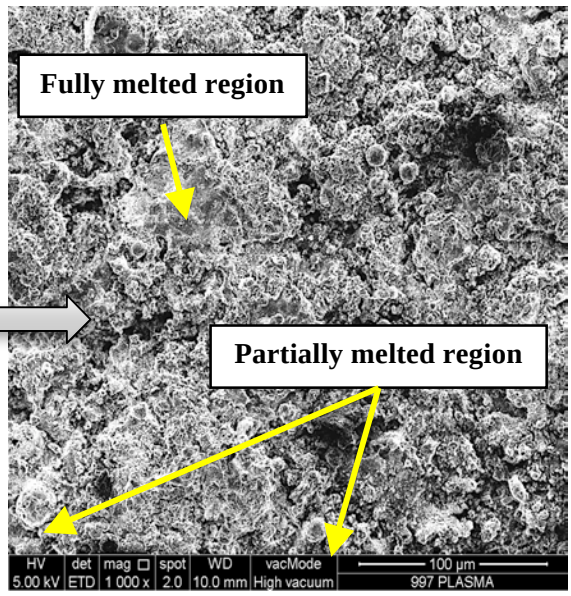

(b) Plasma

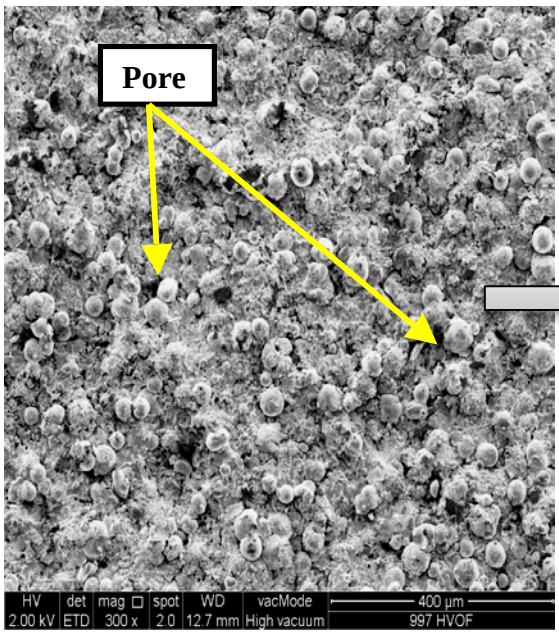

(c) HVOF

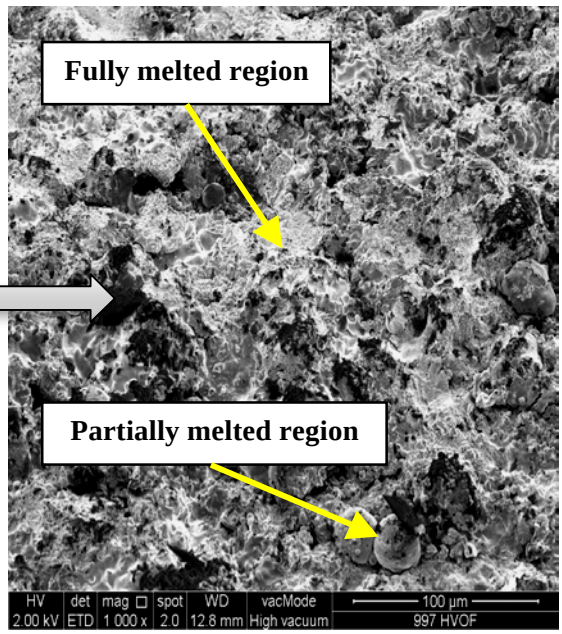

(d) HVOF

Figure 4.16 FESEM of NiCoCrAlY coated samples at different magnifications: (a), (c) 300X; (b), (d) 1000X

X-ray diffraction patterns and EDX for NiCoCrAlY plasma and HVOF-coated samples are shown in Figure 4.17. According Figures 4.17(a) and (b) in the coated samples, the only three phases detected were γ (Co, Ni,Cr), β(Co, Ni, Y)Al and Al_2O_3. The morphology of the coatings consists of single-phase splats separated by Al_2O_3veins as a result of the oxidation occurring in the deposition process. Yuan et al. (2008)

reported that the plasma spraying process facilitates greater oxidation compared to HVOF spraying, which causes aluminum reservoir depletion before the corrosion test.

In addition, alumina formed in the coating due to the fact that oxygen exists in the entrained air and combustion results during thermal spraying; accordingly, the sprayed particles in flight are subjected to oxidation (Jiang et al., 2012; Nijdam et al., 2005).

Previous studies showed that samples coated with NiCoCrAlY produced with vacuum plasma coating (VPS) have high performance. VPS coatings provide good adhesion to the metallic substrate and low porosity, but VPS is more expensive compared to other thermal spray processes. Thus, high-velocity oxygen fuel (HVOF) thermal spraying was attempted as an alternative to VPS to deposit NiCoCrAlY coatings. However, powder particle oxidation during HVOF spraying is inevitable due to the free-oxygen content in the combustion gas and the high temperatures required to melt the powder to ensure certain coating homogeneity. The aluminum and yttrium elements in the metallic powder have high affinity with oxygen, and are thus easily oxidized during thermal spraying; consequently, the coatings have high oxide content (Pindera et al., 2000; Yuan et al., 2008; Zhang et al., 2008).

A previous studied demonstrated that the presence of alumina in some coatings compared to coarse-grained HVOF CoNiCrAlYSi coatings is due to the fact that the CoNiCrAlYSi powder experienced cryomilling prior to spraying, where oxygen was incorporated from the air and liquid nitrogen environment during cryomilling (Jiang et al., 2012).

As reported by Somasundaram et al. (2014), yttrium (Y) provides thermal insulation to the metallic substrate and increases its oxidation and corrosion protection.

Furthermore, the EDX of the NiCoCrAlY composite for plasma and HVOF methods in Figures 4.17 (c) and Figures 4.17 (d) shows the existence of nickel, cobalt, chromium, aluminum and yttrium. The EDX results confirm that the highest peak belongs to the nickel, and the amount of cobalt is higher than chromium. Also the weight percentage of Oxygen in plasma-coated sample is higher than HVOF-coated sample, because plasma-spraying process facilitates greater oxidation compared to HVOF apraying. The weight percentage of each element is provided in Figure 4.17 (c) and Figure 4.17 (d) (inset).

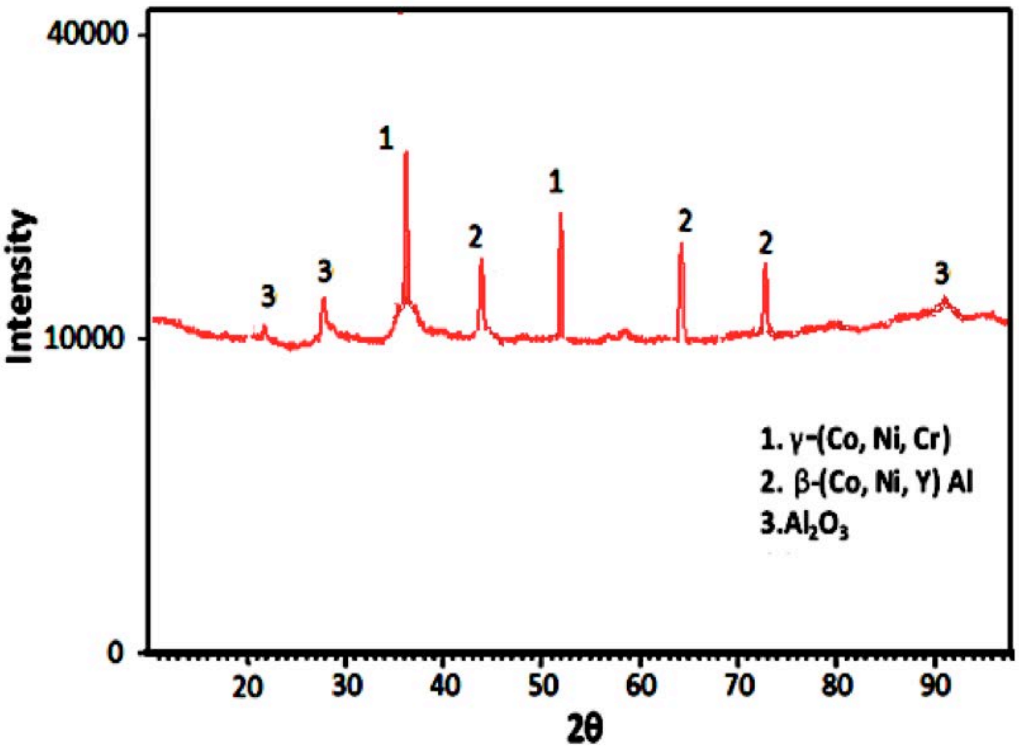
40000
10000
0
Intensity
20
30
40
50
60
70
80
90
2θ
1
2
3
1. γ-(Co, Ni, Cr)
2. β-(Co, Ni, Y) Al
3.Al2O3

(a)

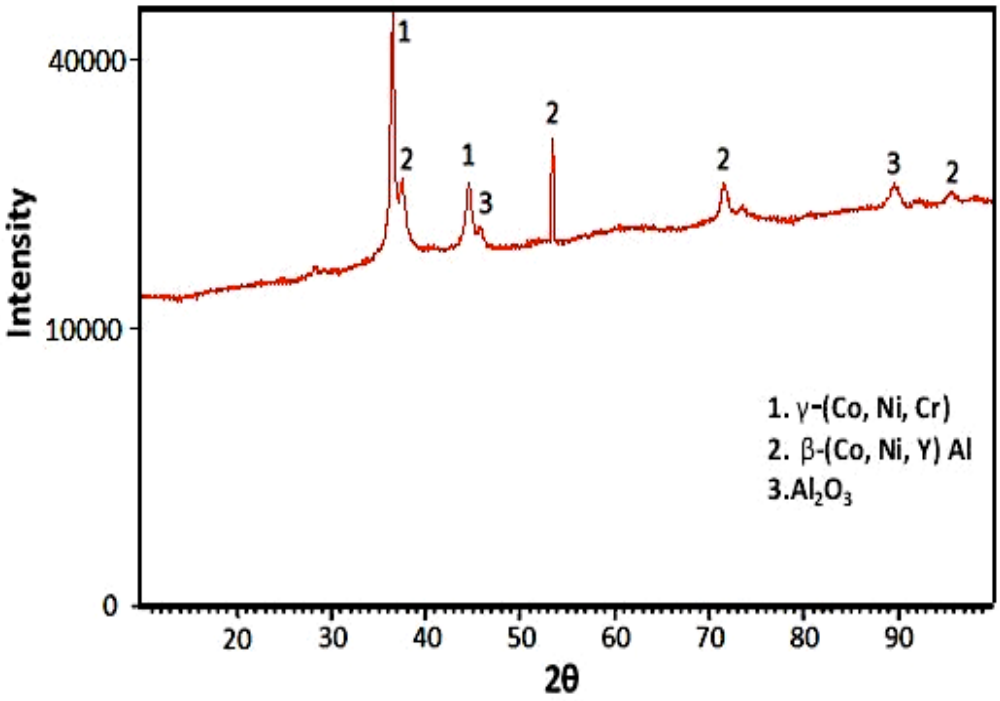
40000
10000
0
Intensity
20
30
40
50
60
70
80
90
2θ
1
2
3
1. γ-(Co, Ni, Cr)
2. β-(Co, Ni, Y) Al
3.Al2O3

(b)

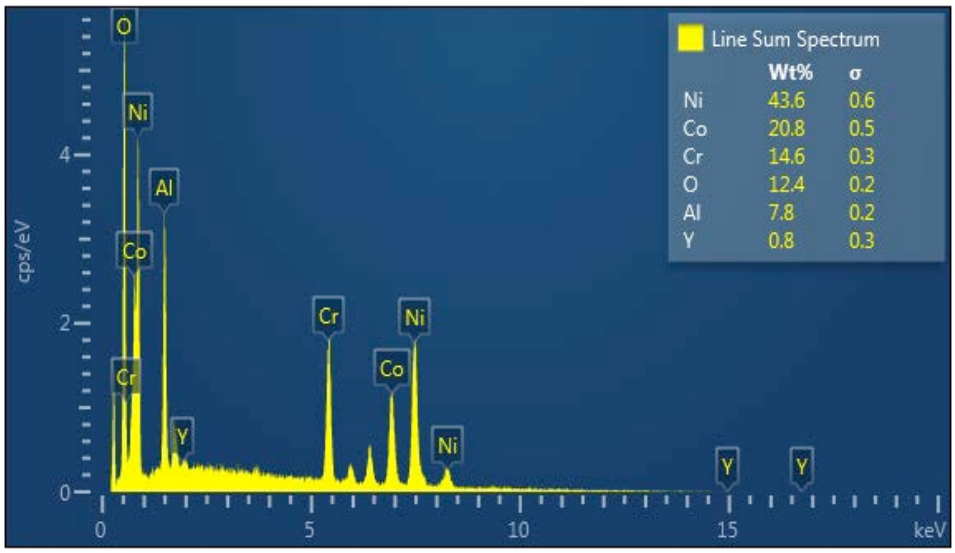

(c)

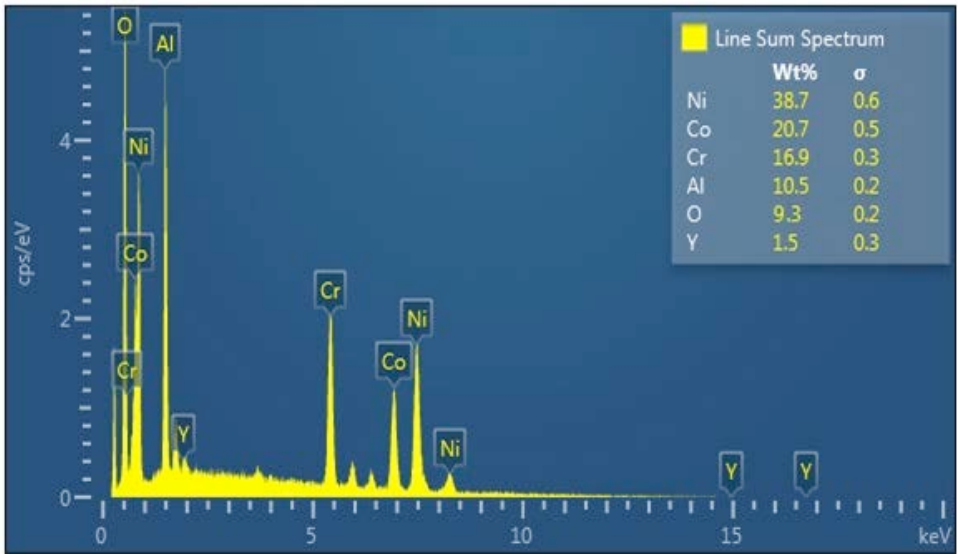

(d)

4.17 X-ray diffraction patterns for NiCoCrAlY coated samples with:(a) plasma, and (b) HVOF; and EDX of (c) plasma and (d) HVOF coated samples

4.4.2 Wear analysis

The roughness of plasma and HVOF-coated samples was found to be 5.8 and 5.1 µm respectively. Miguel et al. (2003) reported that plasma spraying produces higher roughness than HVOF spraying. The highest velocity of the powder particles during HVOF spraying enhances its better lamellae deposition, decreasing the coating roughness. Coatings melted by the post-fuse process strongly decrease the roughness

parameters, achieving a final soft surface (Miguel et al., 2003).

The average microhardness of samples coated by plasma and HVOF methods are 400 and 550 HV respectively. The hardness may increase at higher temperature (≥ 650°C or 1200°F) service conditions, particularly in an oxygen-containing atmosphere.

Also the hardness increase is a direct result of the formation of complex intermetallic in the coating as well as a protective oxide film on the coating surface (Mochizuki et al., 2007;Woo et al., 2014). As reported by Somasundaram et al. (2014), the average microhardness value measured across the coating is 490 HV. HVOF-sprayed NiCrBSi has the highest microhardness, because it combines coating cohesion with a high quantity of small precipitates perfectly distributed in the coating. For this reason, the hardness value is enhanced more than in the plasma coating, which contains a worse distribution of larger precipitates (Miguel et al., 2003).

Liu (2013) showed that optimized CoNiCrAlY nanostructure coating has a lamellar and compact structure that is metallurgically bonded to the substrate. When applying 100 g load, the average microhardness measured was about 854.4±157 HV. Afrasiabi et al. (2008) reported that CoNiCrAlY is well known for its good corrosion resistance, but the metallic binding and voids result in relatively low hardness.

FESEMs of plasma and HVOF-coated samples after applying 20 N load are shown in Figure 4.18. Obviously, wear tracks appeared on the surface of the plasma and HVOF-coated samples. According to Figures 4.18(a) and (b), the track of the pin on the plasma-coated sample is significantly clearer and larger than on the HVOF-coated samples. After applying the load, the amount of material removed from the plasma coating is more than the HVOF coating. This observation shows that the 20 N loads are rarely high for the plasma coating samples. In contrast, when maximum load was applied to the HVOF-coated samples illustrated in Figures 4.18(c) and (d), no obvious

difference is observed before the wear test. Moreover, no cracks or deformation were created at the edge of the samples after applying this load. This amount of load causes the HVOF-coated samples to become slightly abraded with some worn regions.

As a result, the plasma-sprayed coating exhibited the lowest wear resistance, because when maximum load was applied, the coated sample surface was more worn than the HVOF samples, and the pin track is clear on the coated surface.

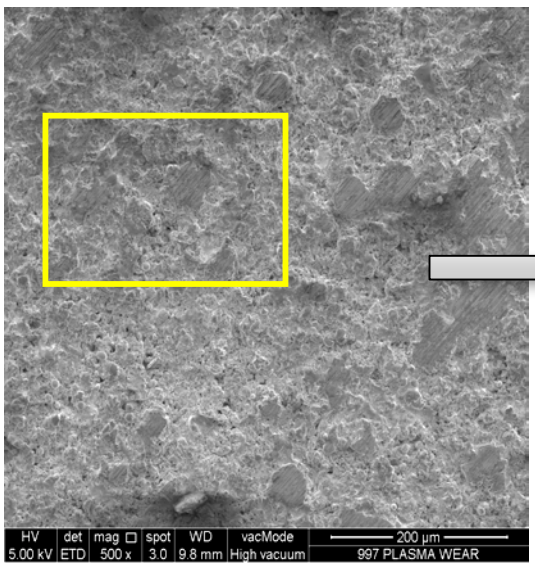

(a) Plasma

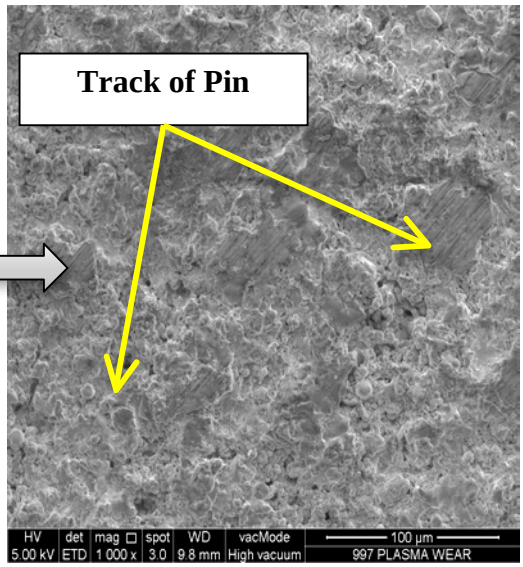

(b) Plasma

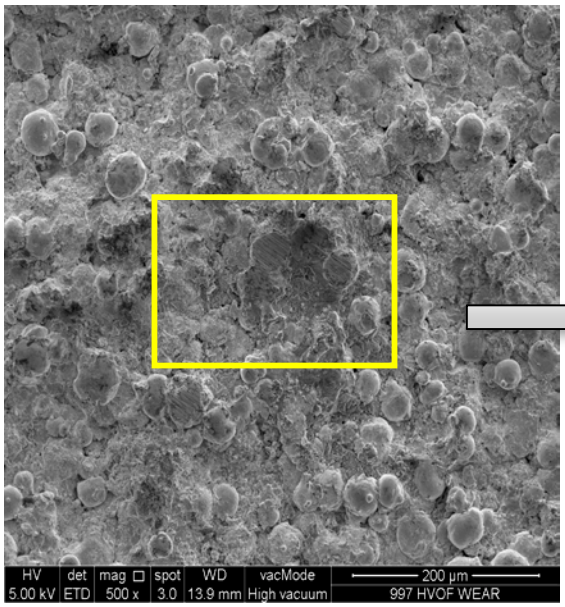

(c) HVOF

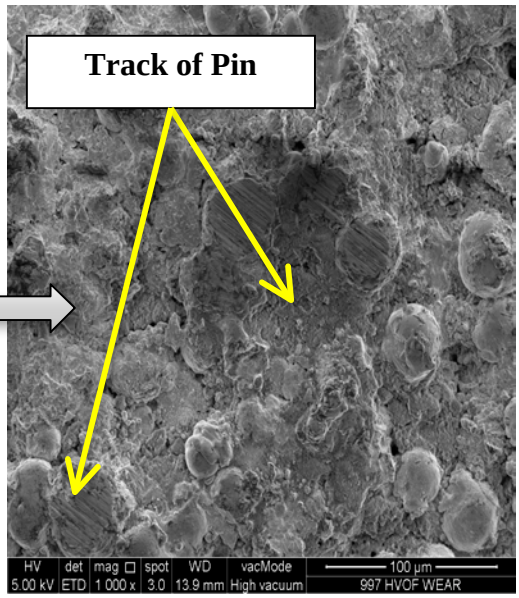

(d) HVOF

Figure 4.18 FESEM of wear debris on NiCoCrAlY coated samples at maximum load (20 N) for: (a), (b) plasma; and (c), (d) HVOF coating

Table 4.5 and Figure 4.19present the average wear and weight loss rate under varying loads. Based on the results, the abrasive wear resistance of plasma coating under different loads is considerably lower. The amount of weight loss for plasma-coated samples is higher than for HVOF-coated samples. According to Figure 4.19(a), by increasing the load, the average wear for plasma-coated samples changed by 38-63 μm while for HVOF-coated samples it varied from 32 to 48 μm. So the maximum wear value for plasma-coated samples was at 20 N, where it suddenly increased from 51 μm to 63 μm.

Also, in Figure 4.19(b) the weight loss trend for plasma and HVOF methods confirms the average wear results. The rate of weight loss for plasma-coated samples changed by 0.010 to 0.0247 g while for the HVOF method it changed by 0.0080 to 0.0189 g. Thus, the HVOF-coated samples have higher wear resistivity.

Table 4.5 Weight loss and wear rate of NiCoCrAlY coated samples under different loads

Loads (N)	**Rate of weight loss**		**Average of wear (μm)**	
	Plasma-coated Sample	HVOF-Coated Sample	Plasma - coated Sample	HVOF-Coated Sample
5	0.010	0.0080	38±1	32±2
10	0.0125	0.0106	43±3	35±2
15	0.0196	0.0154	51±3	40±3
20	0.0247	0.0189	63±2	48±2

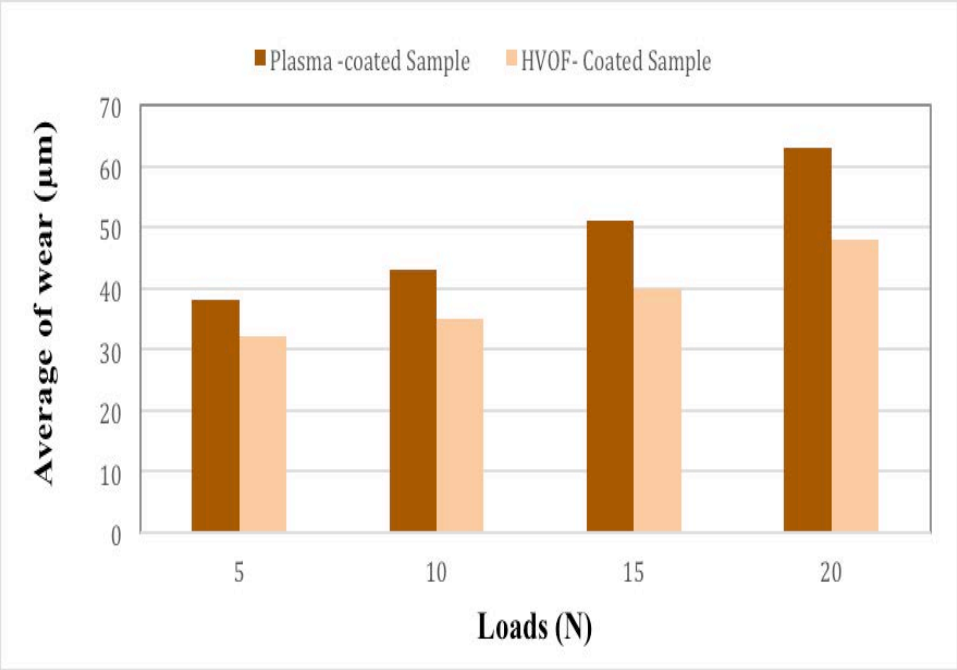

(a)

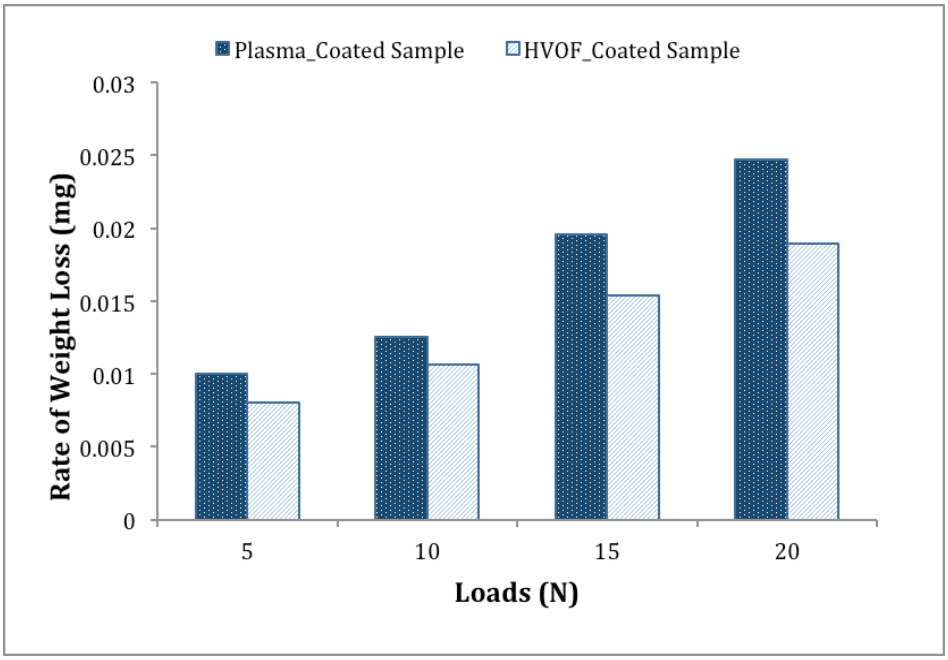

(b)

Figure 4.19 Behavior of NiCoCrAlY samples coated by plasma and HVOF under different loads: (a) average wear, and (b) weight loss rate

4.4.3 Electrochemical corrosion analysis

The open circuit potential (OCP) of coated samples is shown for day 3 and day 30 is shown in Figure 4.20. The plasma-coated sample (blue) shows the potential moved from -0.421 on day 3 towards noble regions with -0.341 at the end of that period, and the OCP of the HVOF-coated sample (red) was more negative compared to the plasma-coated sample, with a change from -0.305 on day 3 to -0.413 on day 30.

The charge transfer resistances R_{ct} were consistent with the OCP values from polarization measurements and I_{corr} illustrated in Table 4.6. It can be seen that the R_{ct} for plasma-coated samples changed from 11.735 to 10.098 kΩ from day 3 to day 30, and for the HVOF-coated samples it changed from 12.193 to 8.242 kΩ. The higher R_{ct} (EIS data) is due to the greater resistance to charge transfer across the electrode-electrolyte interface, which is consistent with the positive OCP result values belonging to the plasma-coated sample. From the computer simulations for the plasma-coated sample, the R_s (QR) circuit diagram accurately matches the experimental data. Only one semicircle is observed in the Nyquist plot (Figures 4.21(a) and (c)).

The Bode phase diagrams of the plasma-coated samples (Figures 4.21 (b) and (d)) show one-phase maxima, consistent with the presence of one semicircle in the Nyquist plots from Figures 4.21(a) and (c) with R_s (Q_1R_1) circuit. The R_s (QR) circuit diagram accurately matches the start day of the plasma-coated samples. Only one semicircle and one maximum phase were observed in the Nyquist and Bode plots (Figures 4.21(a), (b)). Figures 4.22(a) and (b) show that the R_s (QR) circuit diagram accurately matches the experimental data at the beginning of measurement. While for the HVOF-coated samples, at the end of the period the equivalent circuit R_s (Q_1 [R_1(Q_2R_2)] accurately fits the experimental data for HVOF coating, because two semicircles and maxima phases were observed in the Nyquist and Bode plots (Figures

4.22(c) and (d)). The resistance between RE and WE is the solution resistance R_s, which is in series with two time constants (parallel arrangement of R and Q) that are also in series.

It can be seen that the Nyquist plot (Figure 4.21(c)) is a "depressed semi-circle" with the center of the circle below the X-axis (Mansfeld, 1999). $Q_1$is parallel to R_1. $R_1$is the polarization resistance of the area at the substrate/coating interface where corrosion occurs. Also, Q_2 is in parallel with a charge transfer resistor R_2, corresponding to the pores on the coated layer surface. The main reason for the higher R_{ct} of the plasma-coated sample than the HVOF-coated sample at the end of the period is the presence of a bigger oxide layer on top of the plasma-coated samples that protects the deposited layers from electrolyte penetration to the interface.

In these simulations, the plasma coating had higher charge transfer resistances, R_{ct}, than the HVOF coating owing to the higher resistance against corrosion. The charge transfer resistance, $R_{ct,}$ values for plasma and HVOF-coated samples are tabulated in Table 5.6 and confirm the data represented by the Nyquist and Bode plots in Figures 4.21 and 4.22.

According to Table 4.6, the corrosion current density of plasma-coated samples increased from 5.683 x 10^{-5} to 6.030 x 10^{-5} from day 3 to day 18, then suddenly dropped to5.436 x 10^{-5}A on day 21. After that, it rose again up to 6.231x 10^{-5}A on day 30. The corrosion current density for HVOF-coated samples went from 5.267x $10^{-5}$to 5.635x10^{-5} on day 3 to day 9, but suddenly dropped to 4.897x 10^{-5}A on day 12. From the middle of the period until the end the current density increased from 5.593x 10^{-5} to 6.289x 10^{-5}A. The decreasing amount of corrosion current density related to the oxide layer created on top of the deposited layer protected the samples from the corrosive environment. Therefore, the amount of R_{ct} over this period increased.

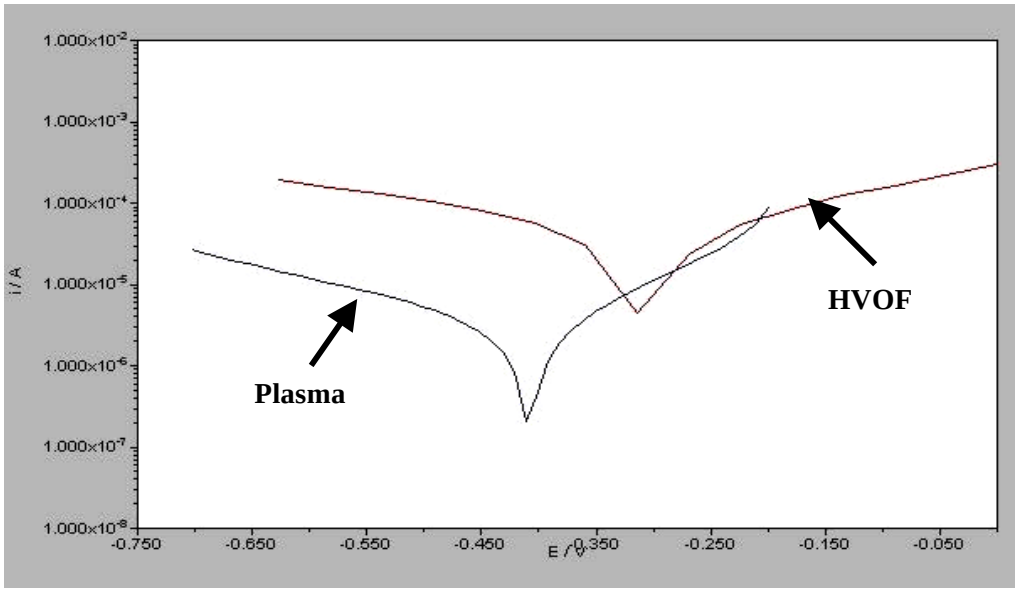

(a) 3rd day experiments

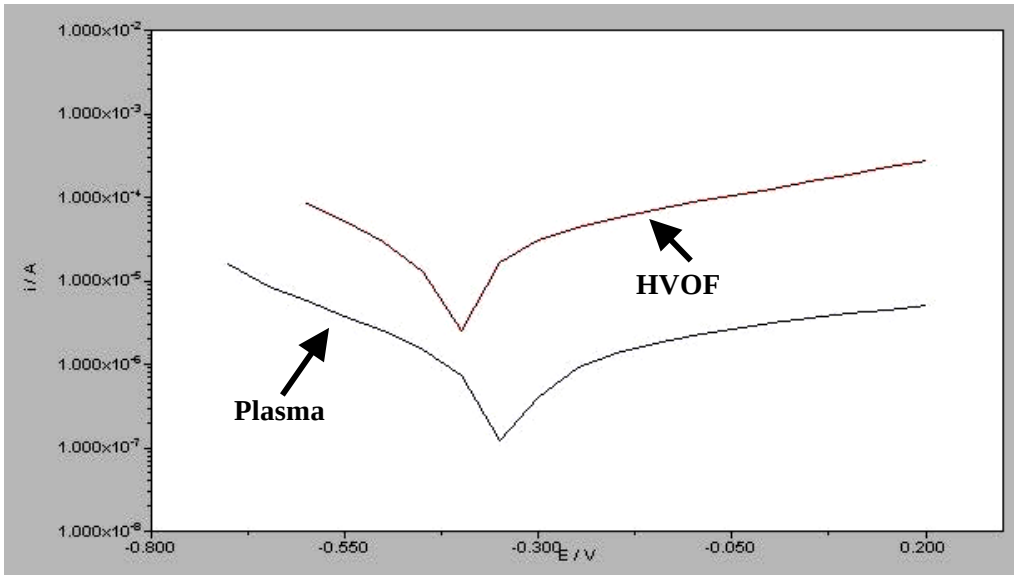

(b) 30th day experiments

Figure 4.20 Polarization curves (log I vs E) of NiCoCrAlY with plasma and HVOF methods for (a) 3rd day, and (b) 30th day experiments

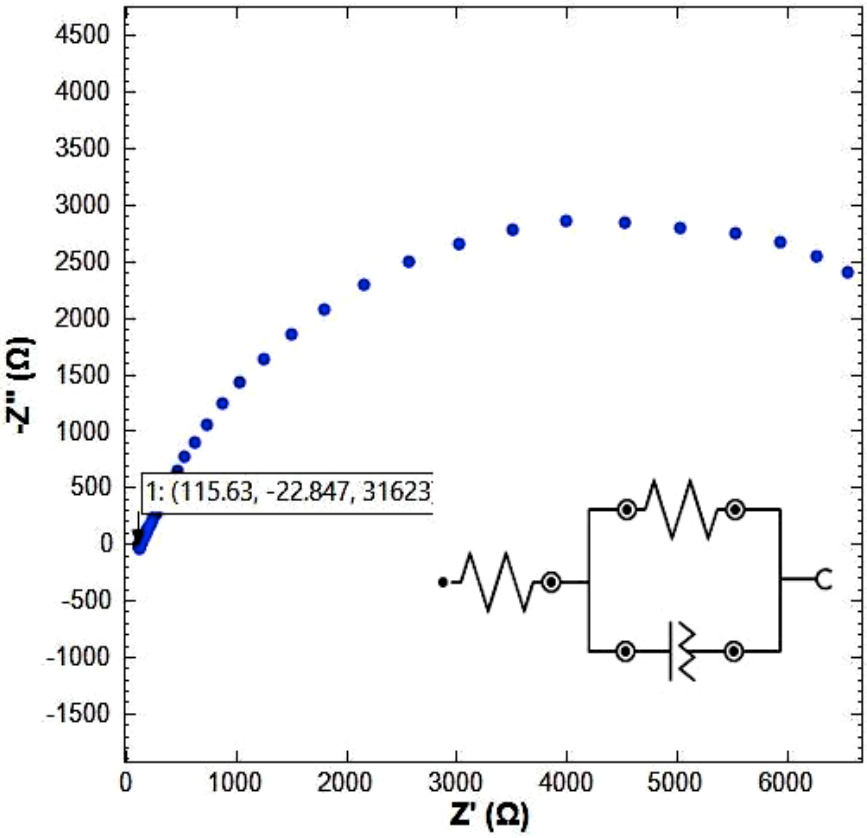

(a) Nyquist plot day 3

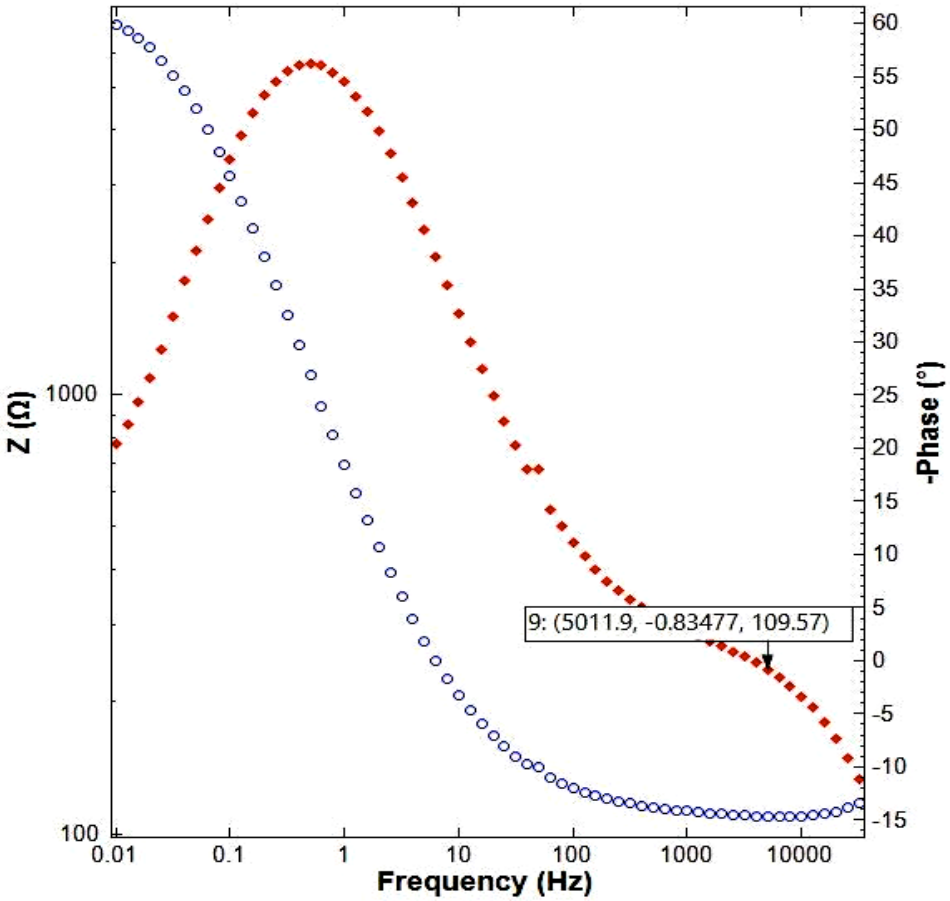

(b) Bode plot day 3

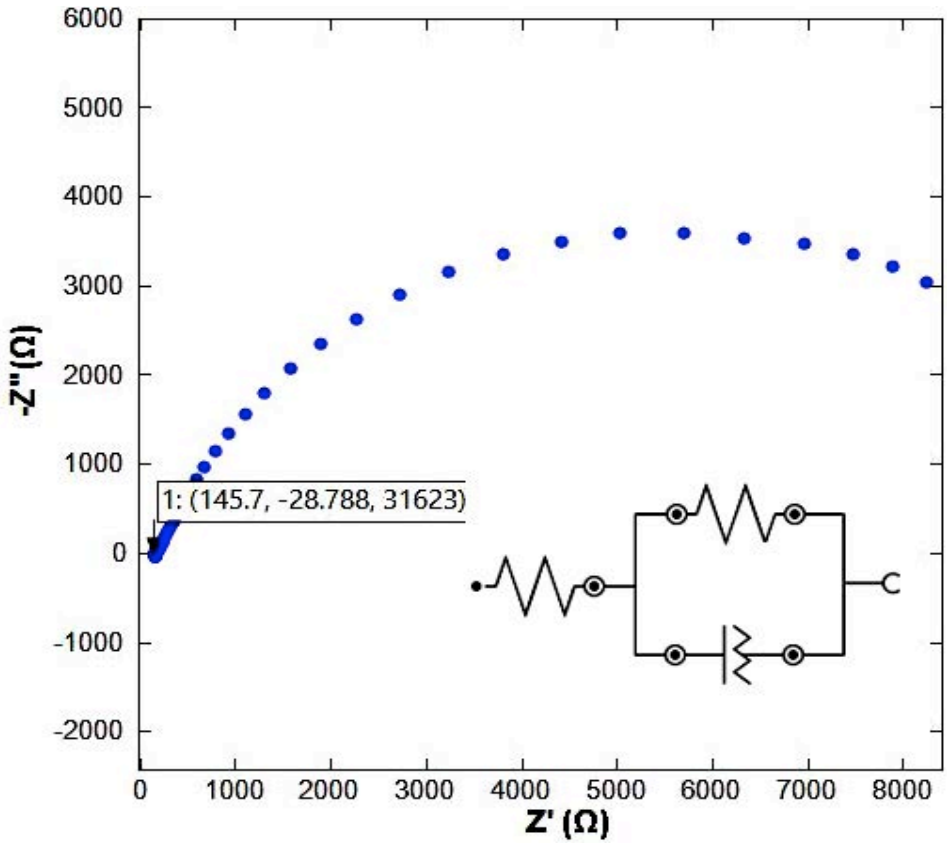

(c) Nyquist plot day 30

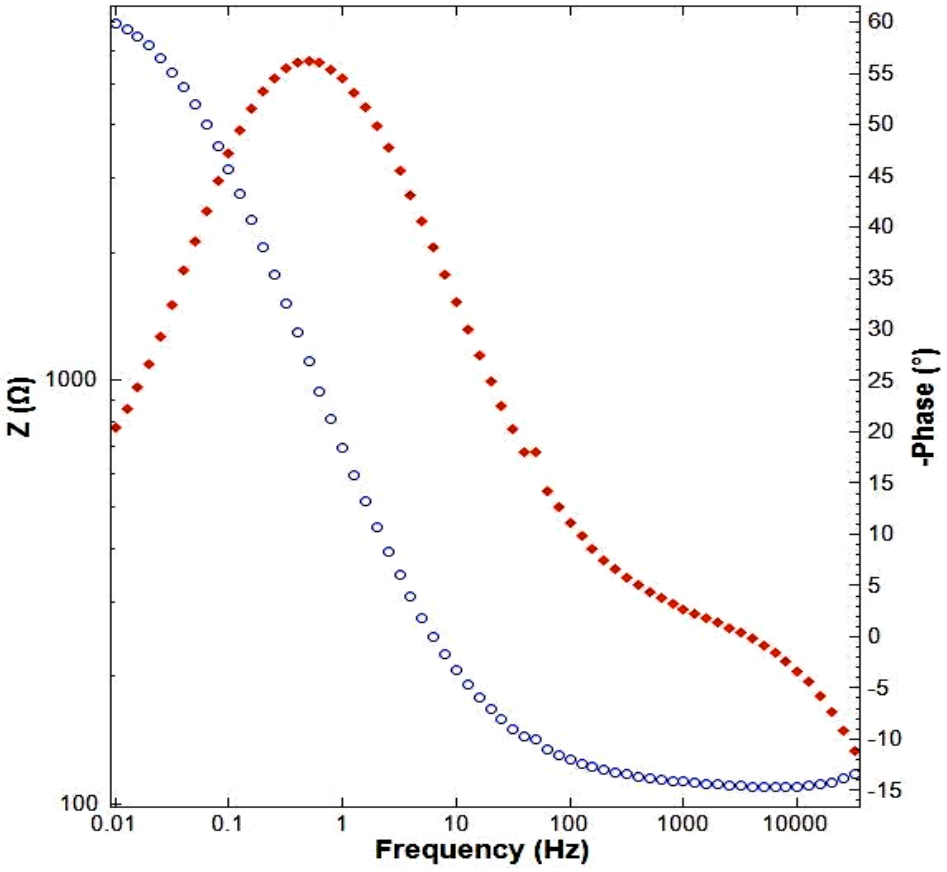

(d) Bode plot day 30

Figure 4.21 EIS of NiCoCrAlY plasma-coated samples

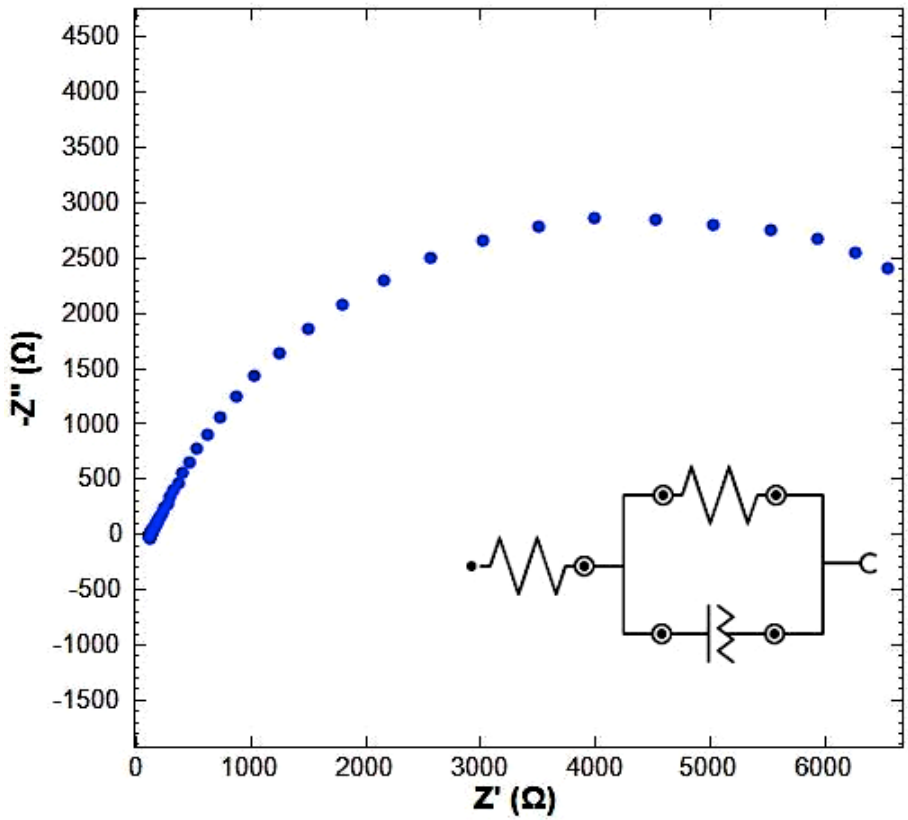

(a) Nyquist plot day 3

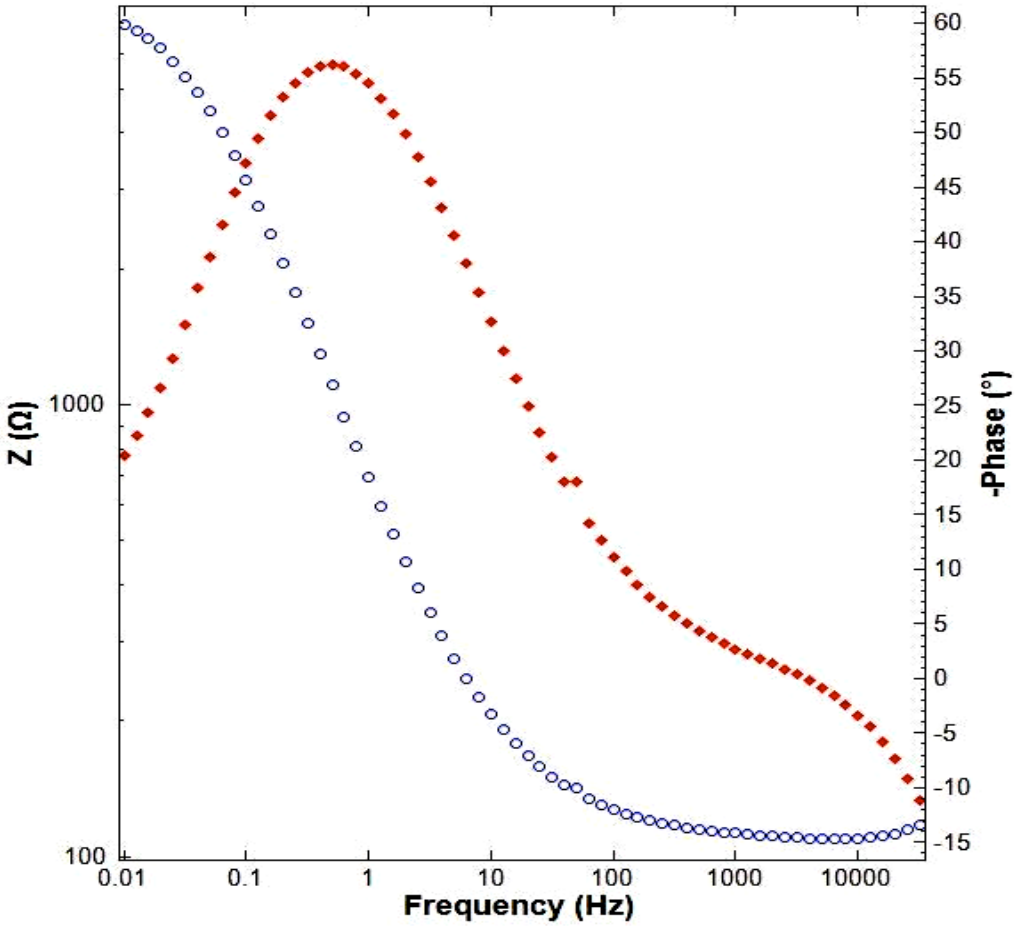

(b) Bode plot day 3

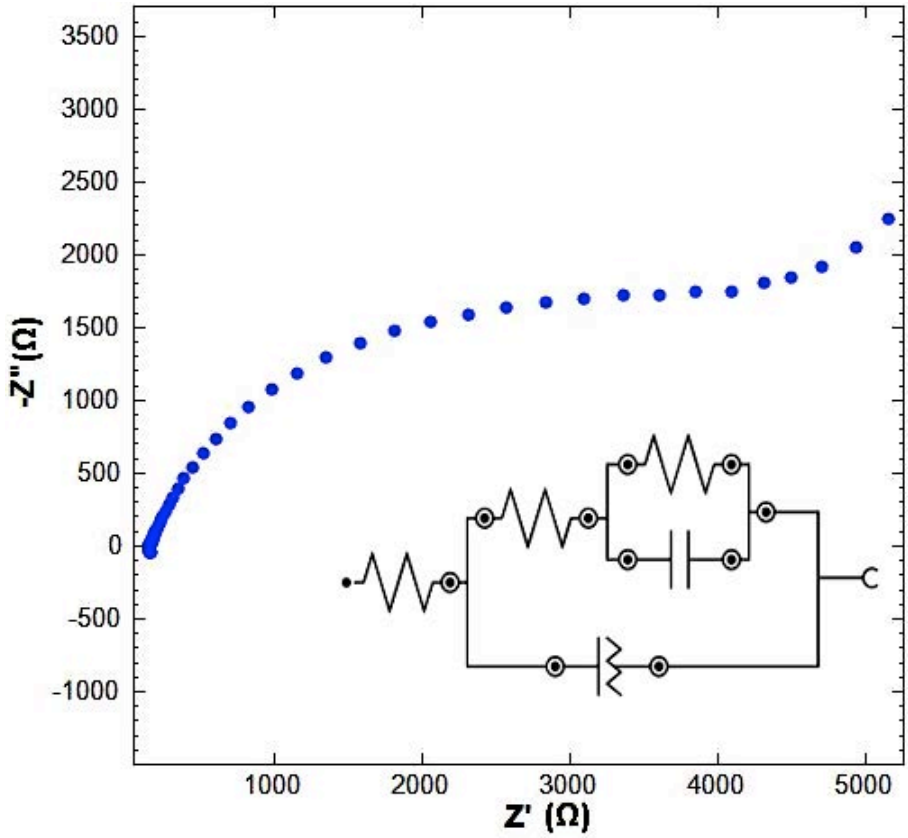

(c) Nyquist plot day 30

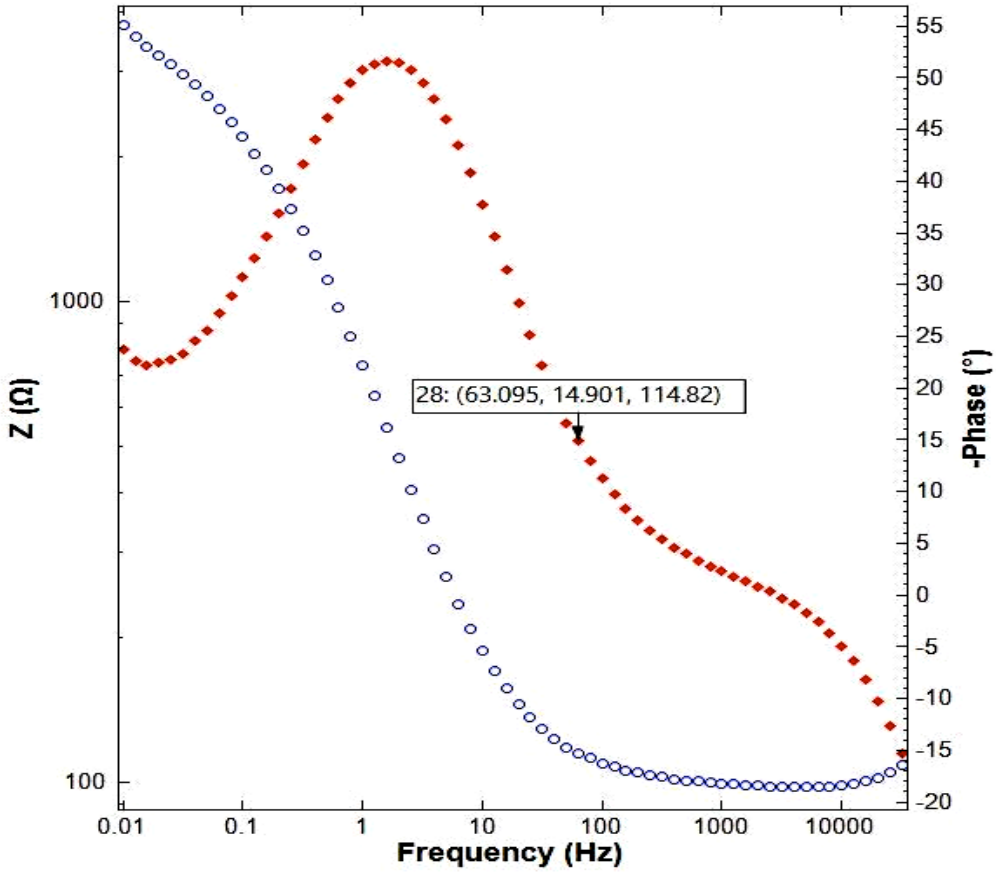

(d) Bode plot day 30

Figure 4.22 EIS of NiCoCrAlY HVOF-coated samples

Table 4.6 OCP, I_{corr} and R_{CT}/kOhm of NiCoCrAlY samples with plasma and HVOF coating methods in 3.5% NaCl solution for 30 days

Day	Plasma-coated Sample				HVOF-coated Sample			
	OCP		I_{Corr} / A (x 10^{-5})	R_{CT} / kOhm	OCP		I_{Corr} / A (x 10^{-5})	R_{CT} / kOhm
	Mean	SD			Mean	SD		
3	-0.421	0.00061	5.683	11.735	-0.305	0.00054	5.267	12.193
6	-0.413	0.00052	5.701	11.380	-0.319	0.00050	5.326	11.871
9	-0.404	0.00072	5.784	11.034	-0.328	0.00071	5.635	10.714
12	-0.389	0.00088	5.832	10.784	-0.289	0.00074	4.897	11.341
15	-0.379	0.00069	5.975	10.514	-0.340	0.00069	5.593	10.891
18	-0.367	0.0010	6.030	10.321	-0.367	0.00081	5.772	10.462
21	-0.360	0.00092	5.436	10.989	-0.378	0.00073	5.829	9.843
24	-0.354	0.00085	5.591	10.679	-0.382	0.0005	6.084	9.245
27	-0.348	0.00074	6.096	10.364	-0.395	0.0011	6.203	8.884
30	-0.341	0.00092	6.231	10.098	-0.413	0.00089	6.289	8.242

4.4.4 Microstructural analysis of corrosion

FESEM micrographs of both coated sample types after 30 days of immersion in crude oil and seawater are shown in Figures 4.23 and 4.24. According to Figures 4.23(a), (b) and 4.24(a), (b) when samples were exposed to the oil environment, the corrosion rate on the coated samples' surface was lower than in NaCl electrolyte (seawater) solution. According to Figure 4.23, the amount of pitting corrosion on the plasma samples was less than the HVOF samples, because there were fewer fine holes produced than on the HVOF samples.

In Figure 4.24, the HVOF-coated samples corroded significantly after 30 days and large holes appeared on their surface. This coating displayed evident crevices and pitting corrosion in the microstructure containing inter-splat porosity. A prior study confirmed these types of corrosion on the top surface of HVOF-coated samples (Deng et al., 2006). Also, the size and amount of corroded area inside NaCl solution (seawater) is obviously greater than in the crude oil.

Regarding Figures 4.23 and 4.24, there is a big difference between the corroded and un-corroded samples with the HVOF coating method in both environments, while in plasma-coated samples the difference between corroded and un-corroded samples is considerably less than the HVOF method. However, both methods protected the substrate from corrosion.

Generally, there are several factors affecting corrosion resistance, including adhesion force between coating layer and substrate, cooling rate, generation of oxides and compounds, and porosity (Weijie et al., 2011). The NiCoCrAlY coating material is an excellent corrosion resistant and oxides generated affect chemical stability, bond strength and durability. Because it has high adhesion to the base metal and creates a dense oxide layer, it yields high durability (Woo et al., 2014).

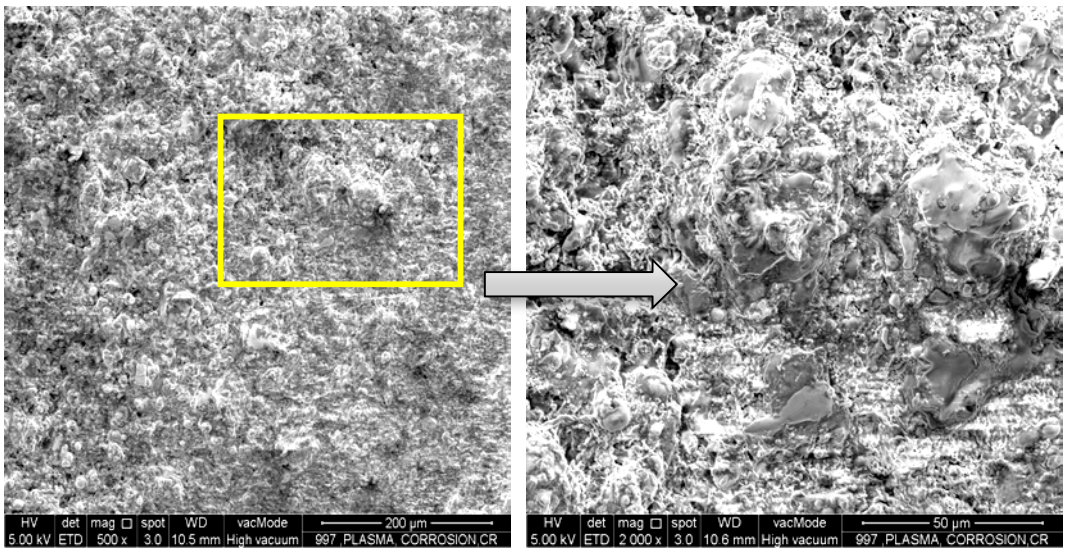

(a) FESEM-500X (b) FESEM-2000X

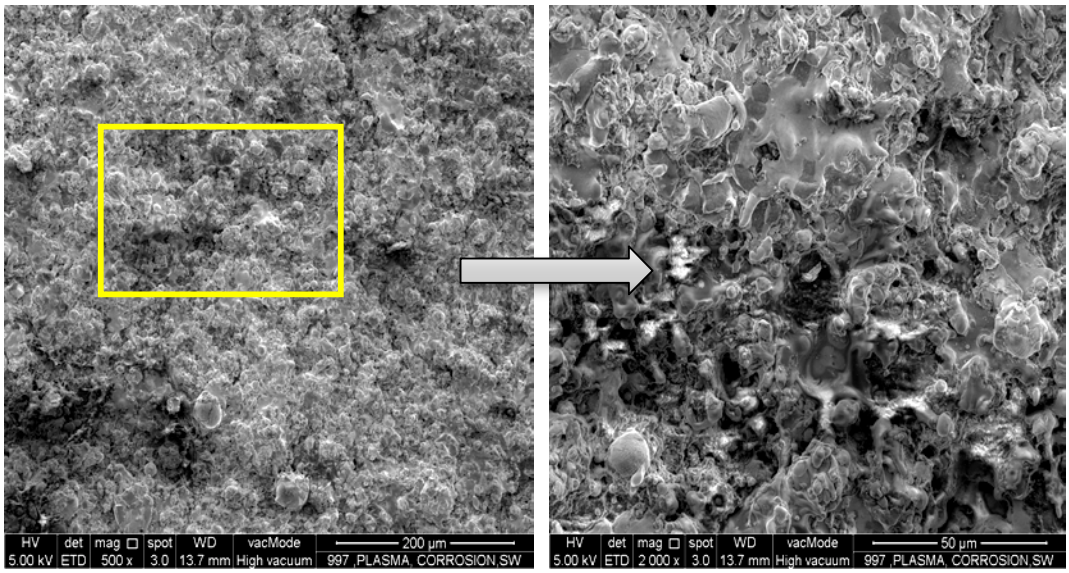

(c) FESEM-500X (d) FESEM-2000X

Figure 4.23 FESEM micrographs of NiCoCrAlY plasma-coated sample surfaces after 30 days: (a), (b) in crude oil; (c), (d) in seawater

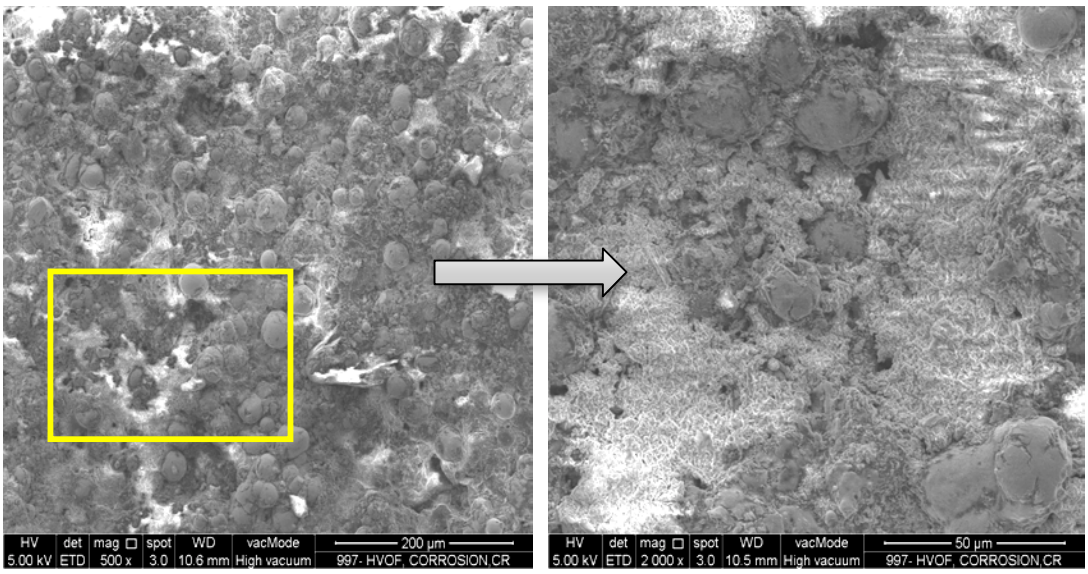

(a) FESEM-500X (b) FESEM-2000X

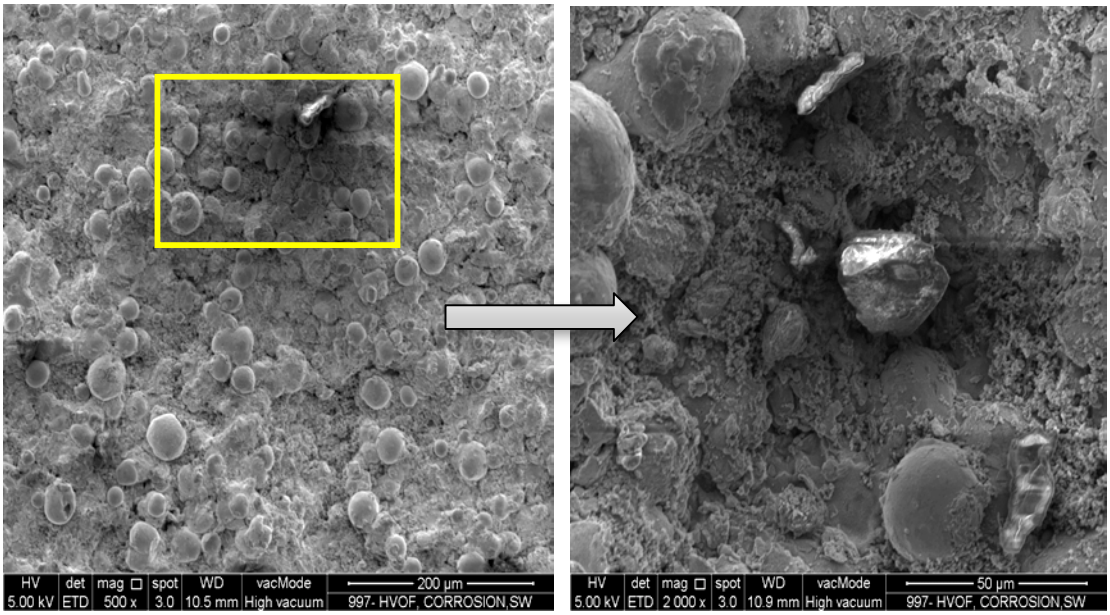

(c) FESEM-500X (d) FESEM-2000X

Figure 4.24 FESEM micrographs of NiCoCrAlY HVOF-coated sample surfaces after 30 days: (a), (b) in crude oil; (c), (d) in seawater

According to the FESEMs of the coated samples, the corrosion rate in 3.5% NaCl solution is significantly higher than in crude oil. The X-ray diffraction (XRD) analysis for the plasma and HVOF-coated samples in 3.5% NaCl electrolyte after 30 days is illustrated in Figures 4.25(a) and (b) respectively. The deposited layer has oxidized to $NiCr_2O_4$ and Al_2O_3 on the surface of the coating, and the amount of γ-(Co,

Ni, Cr) was reduced. The oxide layer protected the substrate from the inward permeation of oxygen. There is no formation of iron oxide according to the XRD results of the coated samples. Thus, it can be concluded that the coating prevented the corrosive electrolyte from penetrating the substrate, consequently protecting the substrate from the corrosive environment.

Chromium is the most important alloying element, which slowly forms a solid layer of Cr_2O_3at high temperature and protects the bulk material from the penetration of foreign elements, such as carbon. $Al_2O_3$is observed in the form of internal oxide precipitated underneath the Cr_2O_3layer in undiluted gas environments (Khan et al., 2014).

As reported by Peters et al. (1976) and Lee et al. (2005), the spinel $NiCr_2O_4$has much smaller diffusion coefficients of cations and anions than the parent oxides, hence helping to develop oxidation resistance.

Schutze et al. (2006) reported that overlay MCrAlY coating can act as a reservoir phase for the formation of a protective and slowly growing Al-based oxide layer by reacting with the oxidizing or corrosive environment, thus preventing the ingress of more aggressive species into the metal, thereby reducing metal consumption rates. Toma et al. (1999) conducted oxidation experiments on vacuum plasma-sprayed (VPS) and HVOF-sprayed MCrAlY coatings and reported that in the case of vacuum plasma spray coating, the rapid oxidation rate in the transient stage is due to the formation of metastable alumina, which also has effect during the steady-state stage.

Whereas in the case of the HVOF spray coating, the formation of α-$Al_2O_3$is the only phase in the oxide scale that determines the slow oxide growth. They opined that the fine oxide dispersion formed in HVOF spray MCrAlY coatings has a beneficial effect on the high-temperature oxidation behavior of coatings.

After corrosion testing, the β-(Co, Ni, Y) Al phase was still detected, suggesting that the plasma coating remained protective. This behavior contrasts that of the HVOF spray samples (Ferdinando et al., 2010).

The higher corrosion resistance of plasma samples compared to the HVOF samples could be ascribed to their microstructure.

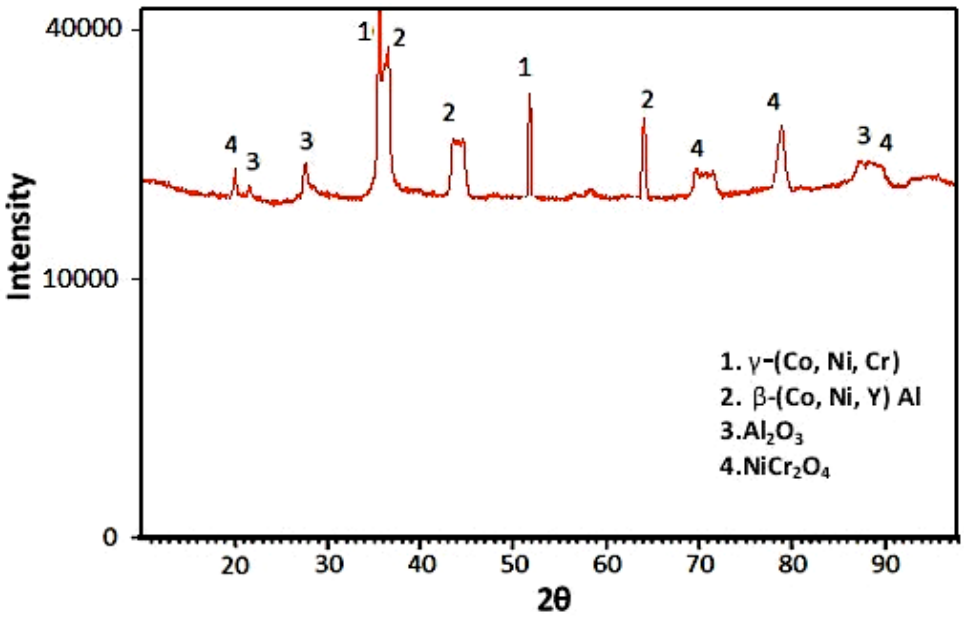

(a)

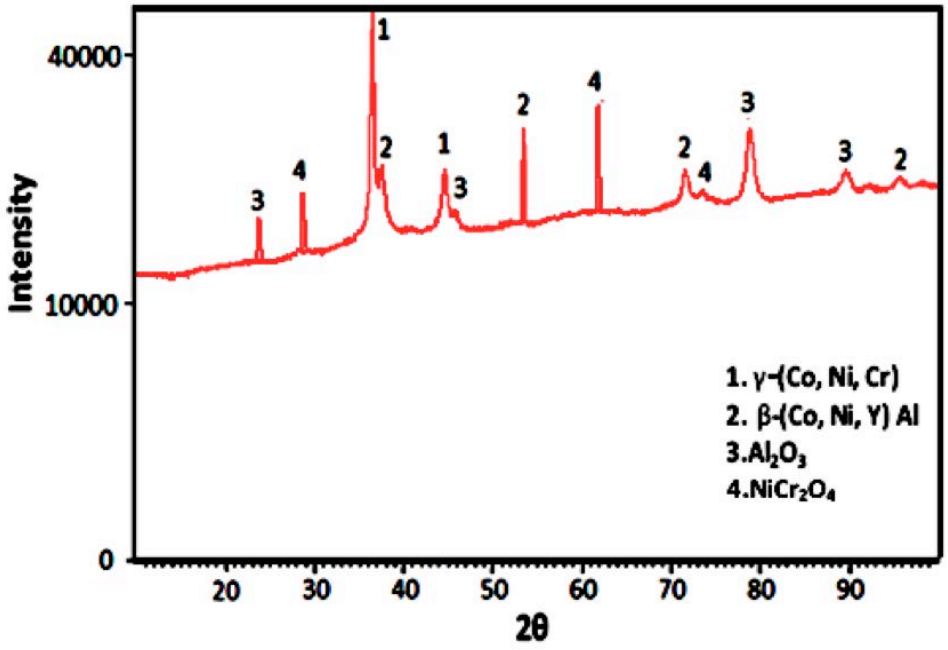

(b)

Figure 4.25 XRD results of NiCoCrAlY samples in 3.5% NaCl solution after 30 days coated with (a) plasma, (b) HVOF

Morphological, microstructural and compositional analyses were performed for both coating methods in order to characterize the samples before and after the wear and corrosion tests. The characterization for seawater (3.5%NaCl) and crude oil after 30 days showed both methods can protect the substrate from corrosion, but the corrosion

rate with HVOF is higher than with the plasma coating method. This result suggests that the potential impact of the plasma thermal spraying process against a corrosive environment is better than that of HVOF spraying systems. However, the wear resistance of the HVOF method is superior to plasma-coated samples, and the wear rate with the HVOF method is less than the plasma method. Therefore, from this chemical composition group, the plasma and HVOF samples were chosen for corrosion and wear resistivity, respectively.

4.5 Analysis of substrate coated with Aluminum silicon boron nitride (Al8Si20BN)

4.5.1 Microstructural analysis

The plasma and HVOF spray coatings in Figure 4.26 shows that the top coating surface exhibits dense microstructure with high cohesion. A fully melted region is seen in the Al matrix, where in Si and BN dispersed; however, during spraying, the temperature of the powder was not sufficiently high, so a partially melted region formed at the top of the Al matrix (Yan et al., 2008; Blanc et al., 1997). Also, there are a few nearly interconnected pores visible in black in the micrographs of both coating types.

The porosity amount with HVOF is significantly less than plasma-coated samples. In addition, the pores in the plasma method are bigger than the HVOF method HVOF-sprayed coatings are denser than plasma-sprayed coatings, due to a different coating formation mechanism of plastic deformation (Lacroix et al., 2012). Wang et al. reported platelet-like shaped BN distributed in the Al matrix and pores in the Al–BN layer that are almost interconnected (Wang et al., 2014).

As reported by Bobzin et al. (2013), dark spots, normally considered pores, were actually removed silicon particles leaving pores in many cases. This is considered a low porosity value due to the high impact velocity of the coating particles, which causes

high density and high cohesive strength of individual splats (Akhtari Zavareh et al., 2014). Pores and cracks vertically formed into splats due to the stress produced during rapid solidification. Figure 4.26 shows a micrograph of this coating, which is uniform, homogeneous and free from surface cracks. Generally, a relatively homogenous coating without segregation is critical for improving the wear and corrosion resistance of coatings (Akhtari Zavareh et al., 2014; Lacroix et al., 2012).

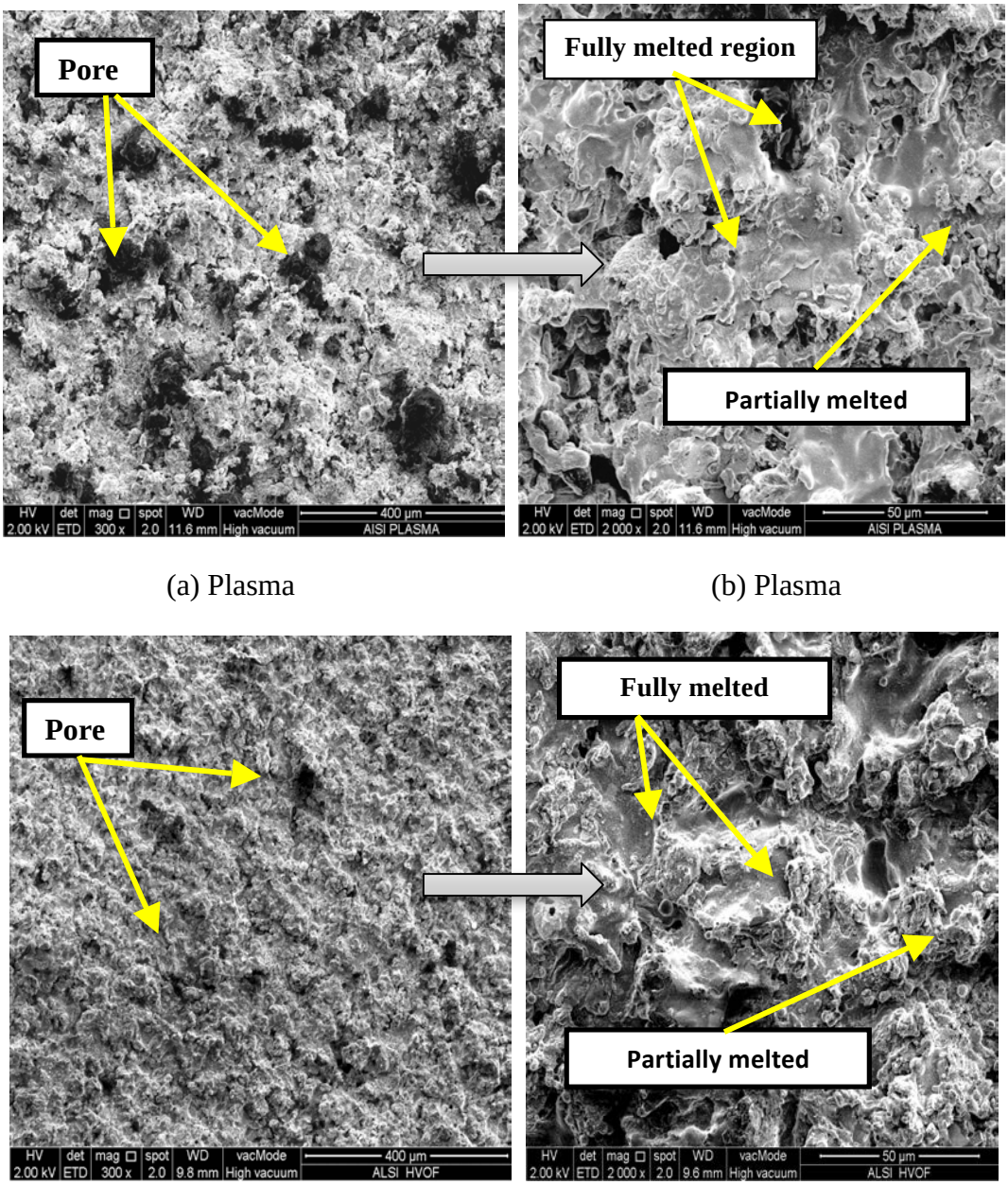

(a) Plasma (b) Plasma

(c) HVOF (d) HVOF

Figure 4.26 FESEM of Al8Si20BN coated samples at different magnifications: (a), (c) 300X; (b), (d) 2000X

X-ray diffraction and EDX patterns for Al8Si20BN plasma and HVOF-coated samples are shown in Figure 4.27. According Figures 4.27(a) and (b), in the plasma-coated samples only four phases were detected, AlSi, BN, $Al_2O_3$and Al_2SiO_5 while in the HVOF-coated samples three phases were detected, AlSi, BN, and Al_2O_3. AlSi is the main phase in the coatings. Diffraction peaks of Al and Si are very high and intensively observed in the samples. It was found that the diffraction lines of the BN phase have low intensities, because BN is a reinforcement material in coating. Lei and colleagues confirmed this result (Lei et al., 2014). It is worth noting that no interfacial reactions between molten Al alloy and BN particles occurred in the composite coatings. This is a good point because reaction products, which are very brittle, are severely detrimental to the mechanical properties of composite coatings (Sarikaya et al., 2007).

$Al_2O_3$and Al_2SiO_5 phases formed from Al and Si powders due to the spray system, but the amount of $Al_2O_3$with HVOF is higher than with plasma. As reported by Sarikaya et al. (2007), Al tends to form in the Al_2O_3 phase in coatings with longer spray distance and greater arc currents owing to the atmospheric plasma spray.

Furthermore, the EDX of the Al8Si20BN composite for plasma and HVOF methods in Figure 4.27 (c) and Figure 4.27 (d) shows the existence of Aluminum, Silicon, Boron, Nitride and Oxygen. The EDX results confirm that the highest peak belongs to the aluminum, and the summation of Boron and Nitride is higher than the Silicon. Also the weight percentage of Oxygen in plasma-coated sample is higher than HVOF-coated sample. The weight percentage of each element is provided in Figure 4.27(c) and Figure 4.27 (d) (inset).

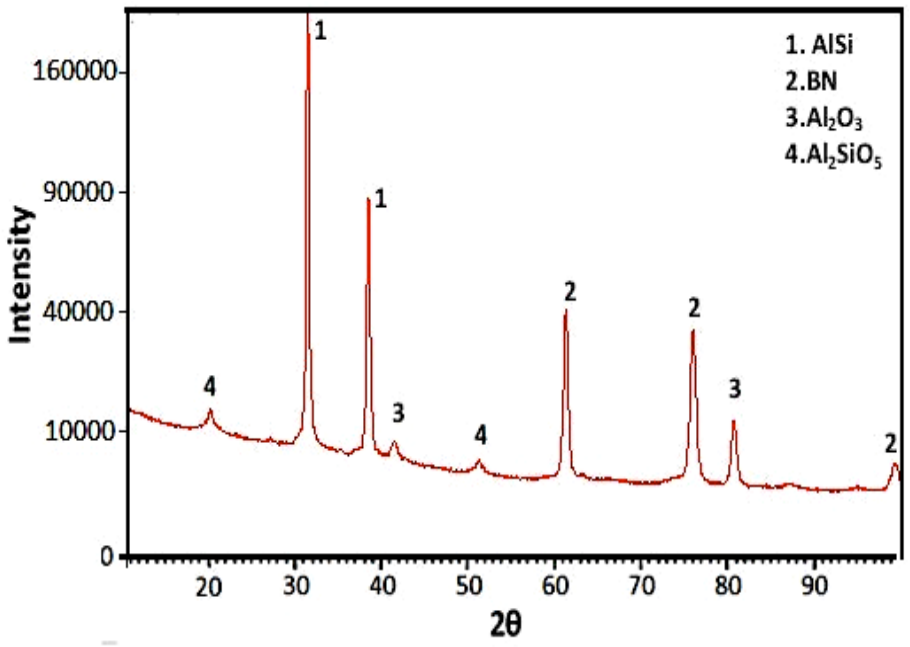
1. AlSi
2.BN
3.Al2O3
4.Al2SiO5
Intensity
2θ
160000
90000
40000
10000
0
20
30
40
50
60
70
80
90

(a)

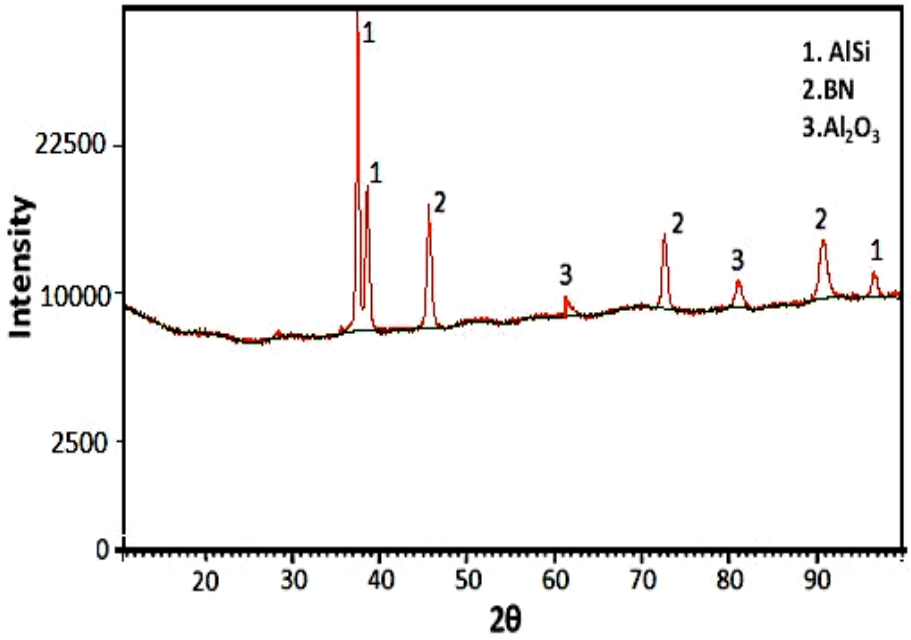
1. AlSi
2.BN
3.Al2O3
Intensity
2θ
22500
10000
2500
0
20
30
40
50
60
70
80
90

(b)

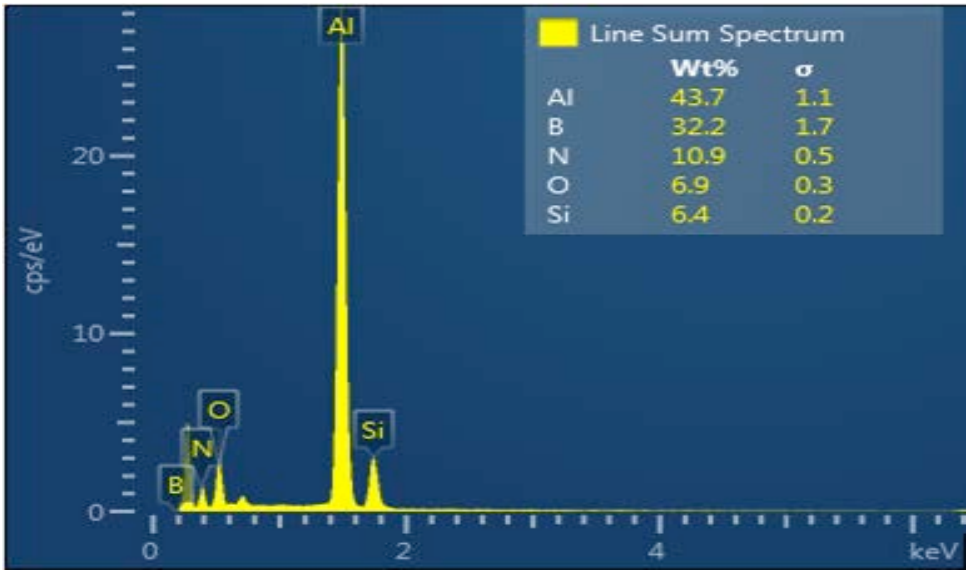

(c)

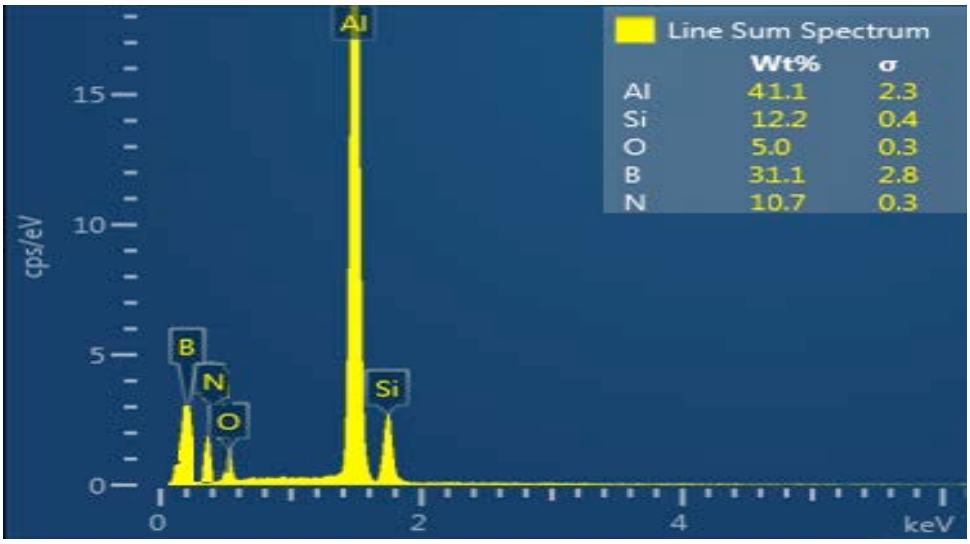

(d)

4.27 X-ray diffraction patterns for Al8Si20BN :(a) plasma, (b) HVOF-coated samples; and EDX of (c) plasma and (d) HVOF coated samples

4.5.2 Wear analysis

The roughness of plasma and HVOF-coated samples is 2.0 and 2.8 µm respectively. According to the roughness of the coated samples, the wear resistance of these coatings is not expected to be sufficiently high. Vaidya et al. (2001) reported decreasing wear resistance of a sample with smooth surface.

The average microhardness of samples coated with plasma and HVOF methods is175 and 220HV, respectively. According to Bobzin et al., (2013) the average microhardness in plasma coating of a sample with this chemical composition is around 165 HV. Also, Rolink et al. (2014) showed that the microhardness of Al20Si is around 157 HV.

FESEMs of plasma and HVOF-coated samples after applying 20 N load are shown in Figure 4.28. As seen in Figures 4.28(a) and (b), huge amounts of material were removed from plasma-coated samples when applying a 20 N load and the samples were evidently worn. Wear tracks appeared on the surface of these samples that caused the coating under this load to fail. This observation signifies that the load was extremely high for this coating, and as a result, the sample lost a considerable amount of material. In contrast, when maximum load was applied to HVOF-coated samples (Figures 4.28(c), (d)) no obvious difference was observed before the wear test. Moreover, no cracks or deformation appeared at the edge of the samples after applying this load. This amount of load caused slight abrasion of the HVOF-coated samples and some wear regions, while the worn was smooth (Figures 4.28 (c), (d)). No cracks were detected on the surface of HVOF-coated samples, which had been exposed to wear testing.

As a result, plasma-sprayed coating had the least wear because when maximum load was applied, the coated sample surface was more worn than HVOF samples, and the pin track was clear on the coated surface. It is assumed that the higher abrasion rate of the plasma spray coating is due to the inhomogeneous microstructure and abundant porosity on the surface of the coated samples (Yan et al., 2008; Bobzin et al, 2013).

Also, Lei et al. (2014) reported rapid wear of the soft aluminum-rich matrix and the hard SiBN particles accelerating the wear process. This is associated with the elevated bonding strength between splats and components, as well as the significant

role of bond strength in splat propagation and resistance to crack initiation (Bobzin et al., 2013). The surface of these coatings also consists of different regions. The hardness in the aluminum region is lower while in the SiBN region it is higher. In addition, the coating density directly affects the samples' hardness. According to the FESEMs in Figures 4.28(c) and (d), the HVOF-sprayed coatings are denser than the plasma-sprayed coatings due to the different coating formation mechanism of plastic deformation.

Moreover, the possibility of pullout of SiBN from the aluminum matrix is minimal because the SiBN particles are held strongly in this matrix (Bobzin et al., 2012). Meanwhile, plasma-sprayed coatings (Figures 4.28(a) and (b)) are formed by molten or partially molten droplets and thus possess certain porosity. Therefore, plasma coatings are not as dense as HVOF-sprayed coatings, as reflected in the pullout after metallographic preparation. In HVOF coating, the higher density prevents complete pulling out from occurring (Vaydia et al., 2001; Sampath et al., 2004).

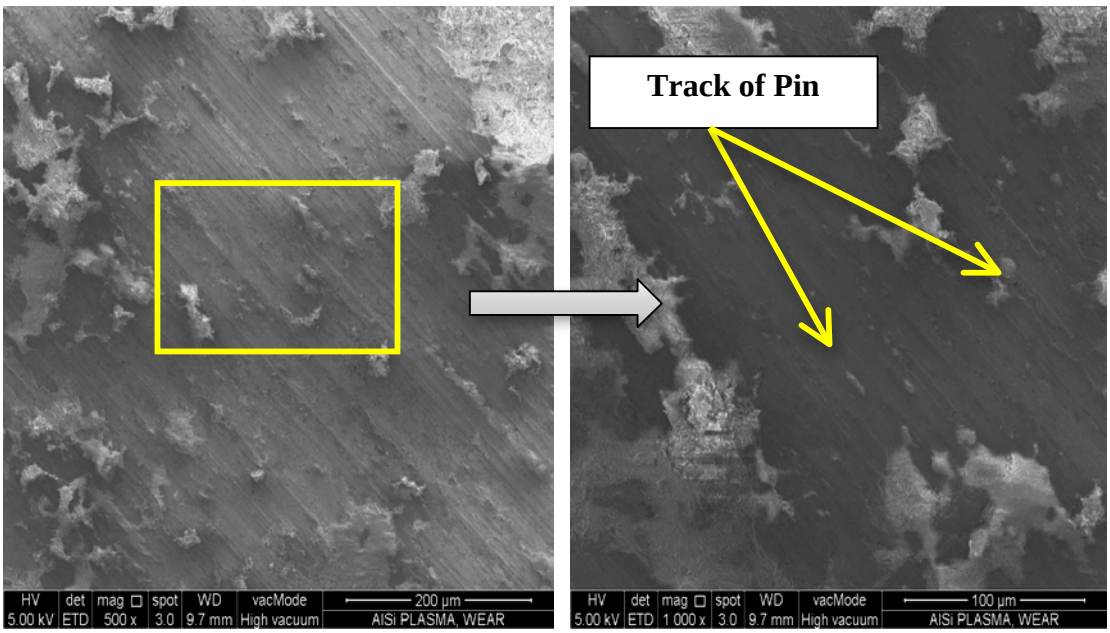

(a) FESEM-500X (Plasma) (b) FESEM-1000X (Plasma)

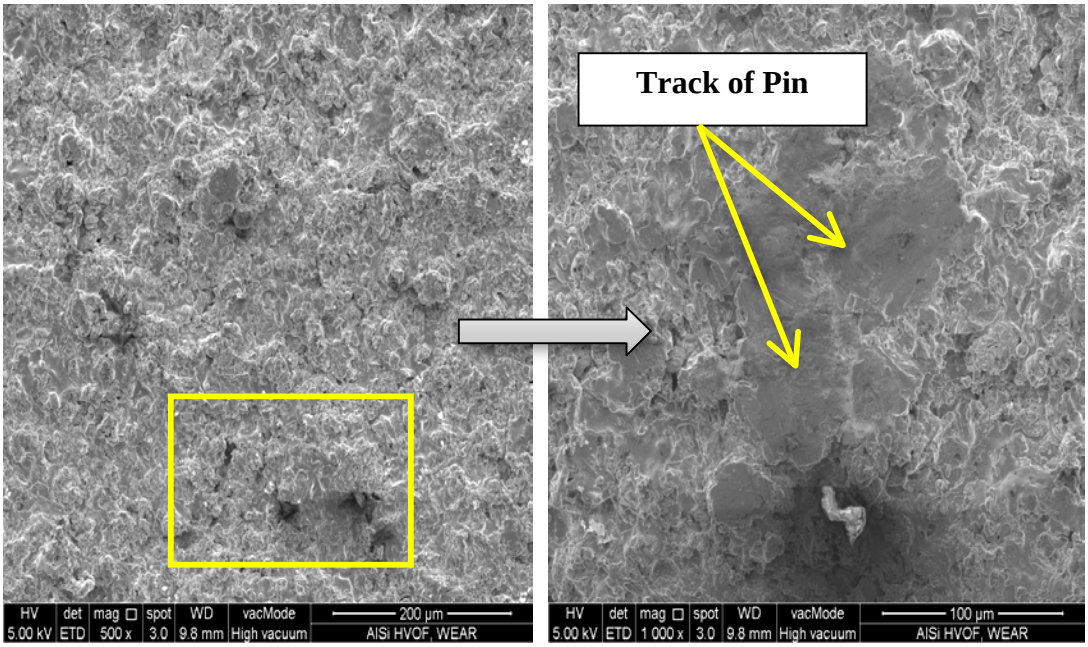

(c) FESEM-500X (HVOF) (d) FESEM-1000X (HVOF)

Figure 4.28 FESEM of wear debris of Al8Si20BN coated samples at maximum load (20 N) for (a), (b) plasma; and (c), (d) HVOF coating

Table 4.7 and Figure 4.29 illustrate the amount of wear and weight loss rate for plasma and HVOF-coated samples under 5,10, 15 and 20N loads. In general, there was an increase in the wear rate and weight loss with both methods under these loads. Figure 4.29(a) shows that with the HVOF method, the wear changed from 68 to 110µm while with the plasma method the average wear was around twice more. The maximum

values of wear for the plasma-coated sample were 108, 122, 140 and 163 μm for loads of 5, 10, 15 and 20 N respectively. In Figure 4.29 (b), the weight loss rate for the plasma and HVOF methods confirms the results of average wear. The weight loss for plasma-coated samples changed from 0.0276 to 0.0639 g while for HVOF it changed from 0.0173 to 0.0431 g.

Table 4.7 Weight losses and wear rate of Al8Si20BN-coated samples under different loads

Loads (N)	**Rate of weight loss**		**Average of wear (μm)**	
	Plasma-coated Sample	HVOF-Coated Sample	Plasma - coated Sample	HVOF-Coated Sample
5	0.0276	0.0173	108±4	68±2
10	0.0356	0.0224	122±3	76±4
15	0.0538	0.0342	140±3	89±2
20	0.0639	0.0431	163±2	110±5

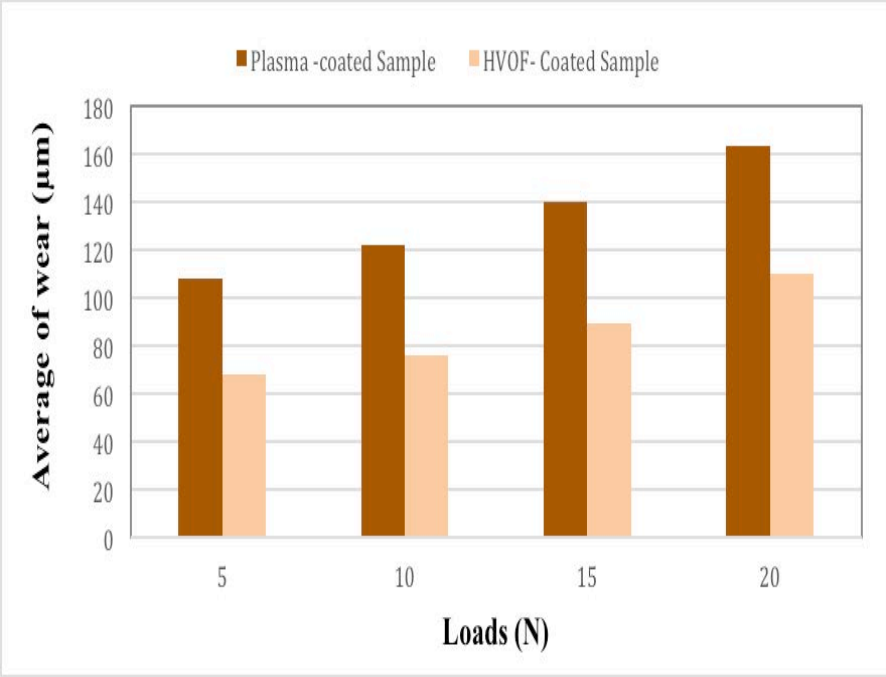

(a)

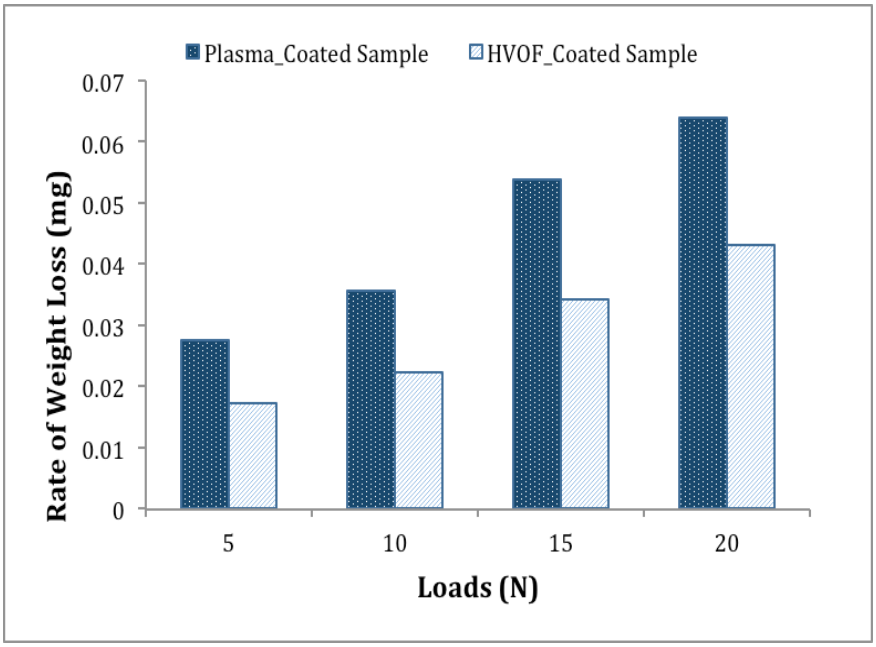

(b)

Figure 4.29 Behavior of Al8Si20BN plasma and HVOF-coated samples under different loads: (a) average, wear and (b) weight loss rate

4.5.3 Electrochemical corrosion analysis

The corrosion potential and corrosion current density were obtained by the intersection of the extrapolation of anodic and cathodic Tafel curves. The polarization resistivity (R_{ct}) determined based on a suitable fitting circuit procedure by Autolab Software is summarized in Table 4.8**.**

According to Table 4.8 and Figure 4.30, the R_{ct} for the plasma-coated samples (blue) from day 3 to day 30 changed from 4.121 to 2.491 kΩ, and for the HVOF-coated sample (red) the R_{ct} changed from 6.272 to 4.847 kΩ. The higher R_{ct} (EIS data) belonged to the HVOF-coated samples.

According to the computer simulations for plasma- and HVOF-coated samples on day 3, the R_s (QR) circuit diagram accurately matches the experimental data. Only one semicircle was observed in the Nyquist plots (Figures 4.31(a), 4.32(a)). The Bode phase diagrams of plasma- and HVOF-coated samples (Figures 4.31(b), 4.32(b)) show one-phase maxima. However, the $R_{ct}$for HVOF-coated sample is bigger than for plasma-coated samples. The R_{ct} of plasma and HVOF-coated samples from day 3 to day 30 are shown in Table 4.8.

Plasma- and HVOF-coated sample simulation results signify that the equivalent circuit R_s (Q_1 [R_1 (Q_2R_2)]) accurately fits the experimental data, because two semicircles and a maxima phase were observed in the Nyquist and Bode plots (Figures 4.31(c), (d), 4.32(c), (d)). However, the semicircle in the HVOF-coated sample is bigger than the plasma-coated sample. The resistance between RE and WE is the solution resistance R_s, which is in series with two time constants (parallel arrangement of R and Q) that are also in series. It can be seen that the Nyquist plots (Figures 4.31(c), 4.32(c)) show a "depressed semi-circle" with the center of the circle below the X-axis. $Q_1$is parallel with R_1. The $R_1$is the polarization resistance of the area at the

substrate/coating interface where corrosion occurs. $Q_2$is in parallel with a charge transfer resistor R_2, corresponding to the pores in the coated layer surface.

Generally, the HVOF coating displays higher charge transfer resistance R_{ct} compared to the plasma-coated sample, owing to the greater resistance against corrosion.

According to Table 4.8, the corrosion current density of plasma-coated samples with advancing days slightly increased from 9.107 x 10^{-5} to 13.977 x 10^{-5} A, while for HVOF-coated samples the corrosion current from day 3 to day 15 fluctuated. The corrosion current plunged from 6.432 x 10^{-5} to 8.321x 10^{-5} A from day 3 to day 6, then it dropped to 7.653 x 10^{-5} A on day 12. After that, the corrosion current rose slightly from 8.889 x 10^{-5} to 11.247 x 10^{-5} A from the middle of the period until the end. Thus, HVOF-coated samples have higher corrosion resistivity than plasma-coated samples.

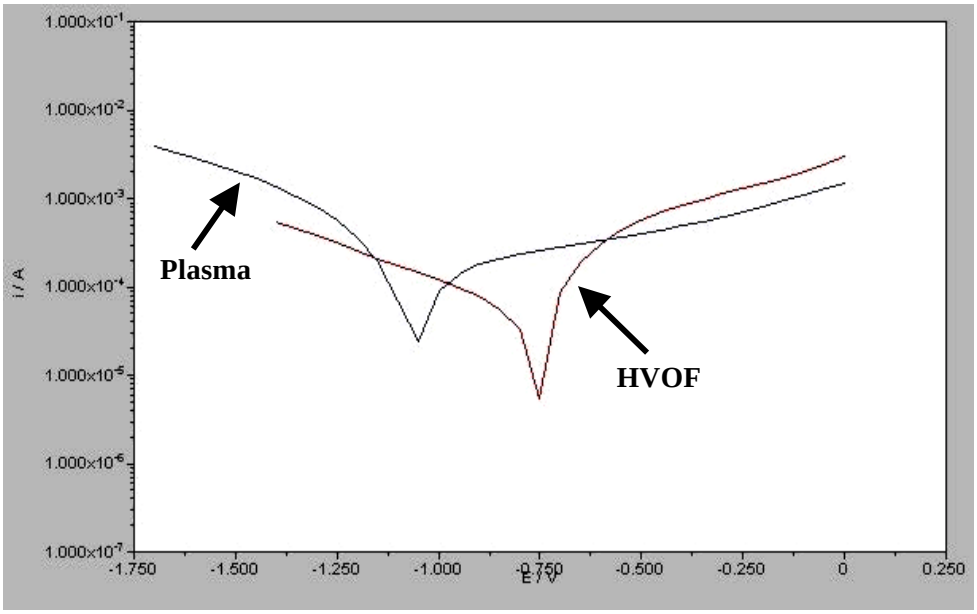

(a) 3rd day experiments

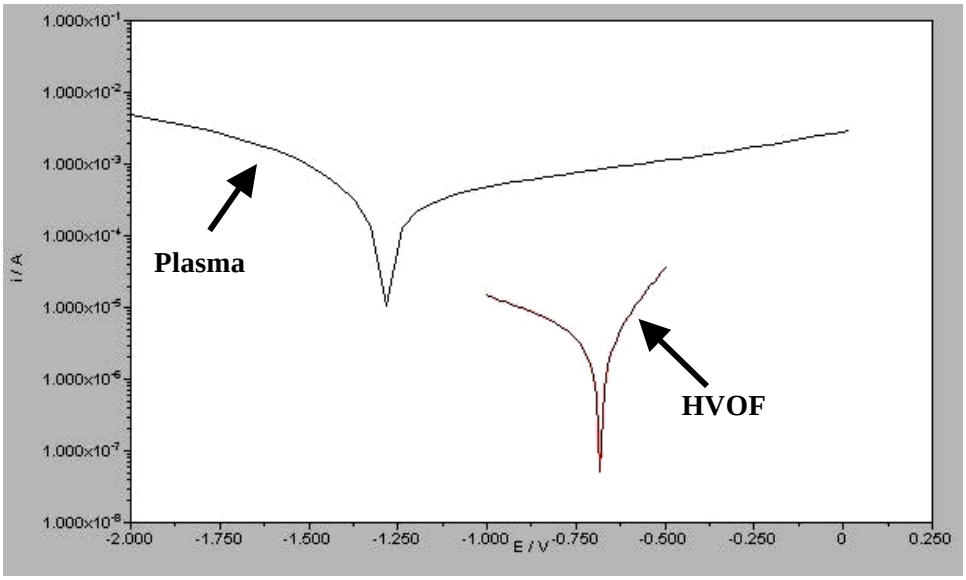

(b) 30th day experiments

Figure 4.30 Polarization curves (log I vs E) of Al8Si20BN coated by HVOF: (a) 3rd day and (b) 30th day

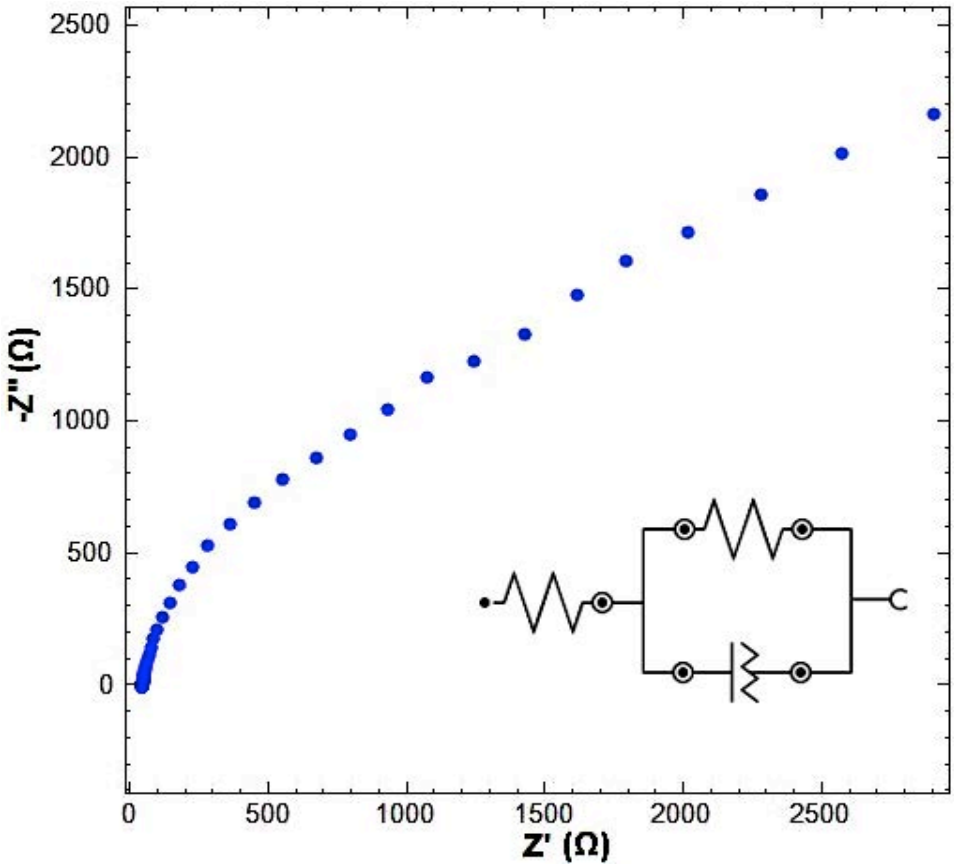

(a) Nyquist plot day 3

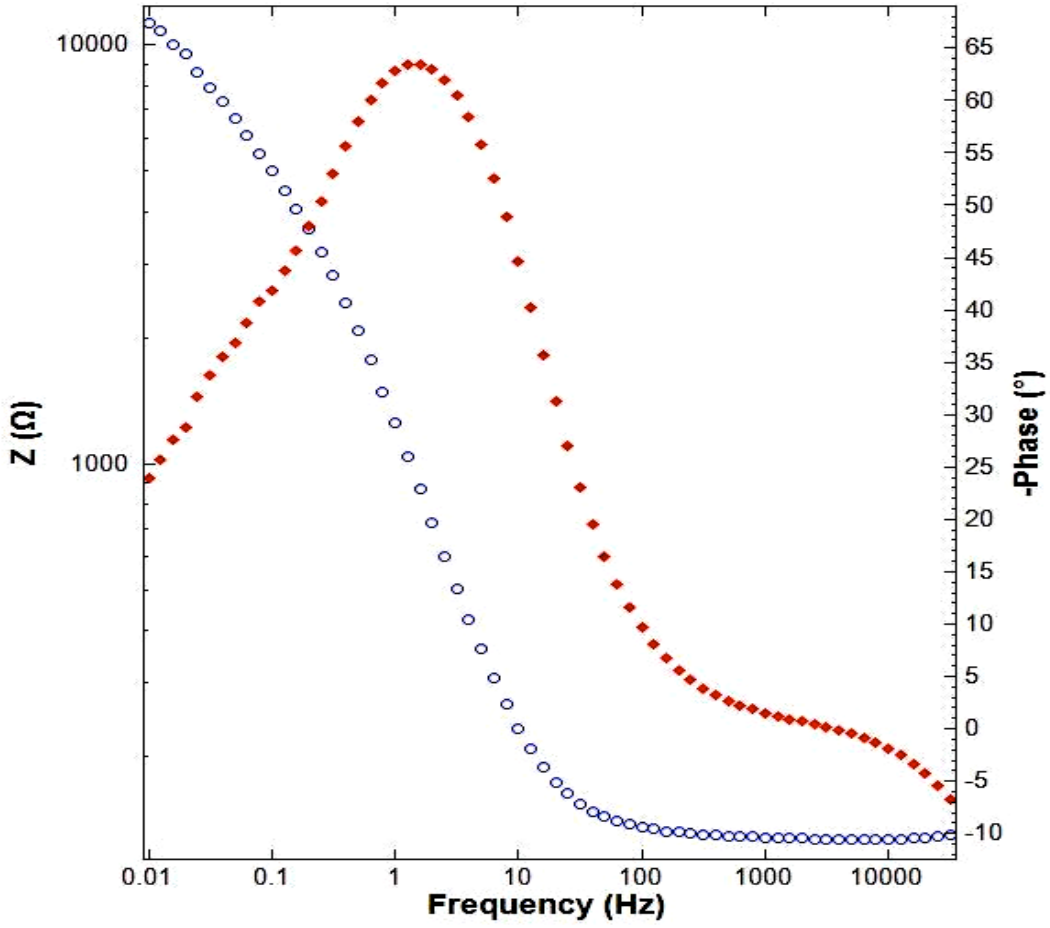

(b) Bode plot day 3

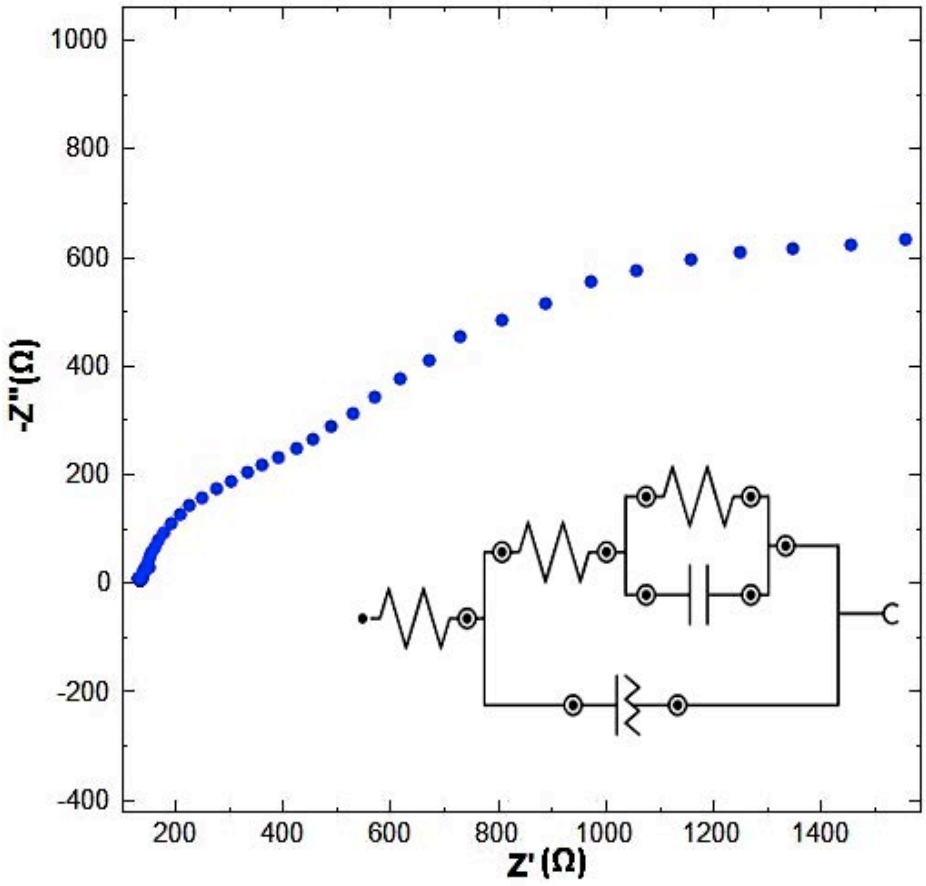

(c) Nyquist plot day 30

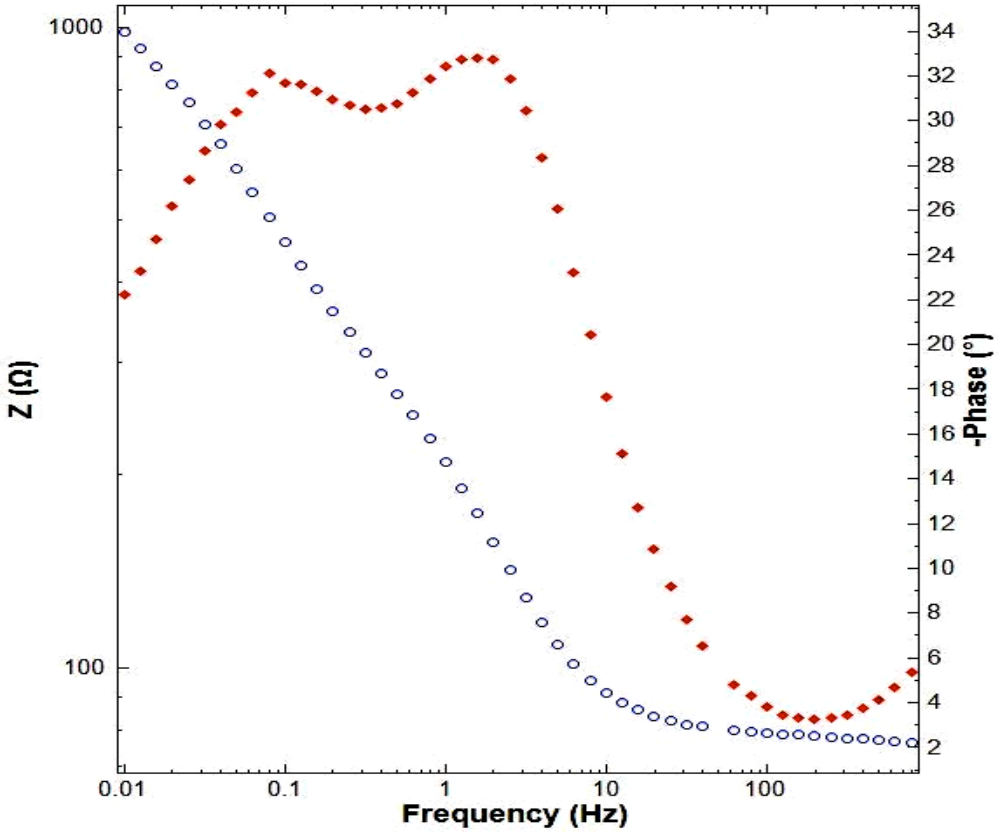

(d) Bode plot day 30

Figure 4.31 EIS of Al8Si20BN plasma-coated sample

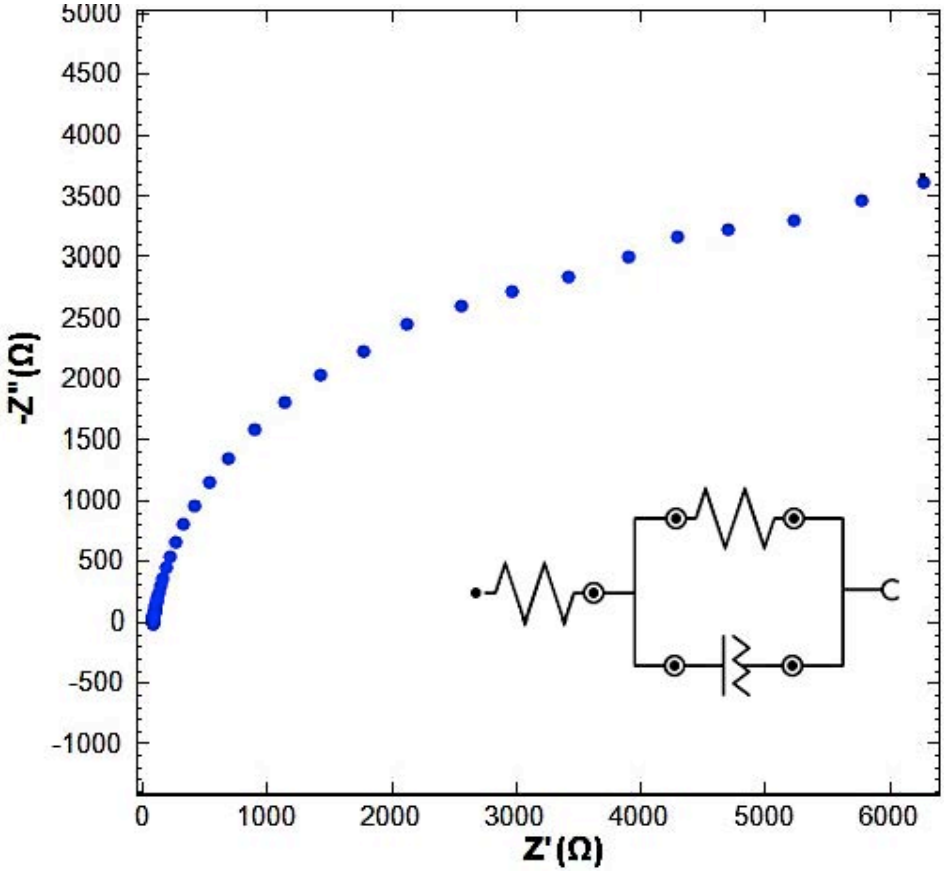

(a) Nyquist plot day 3

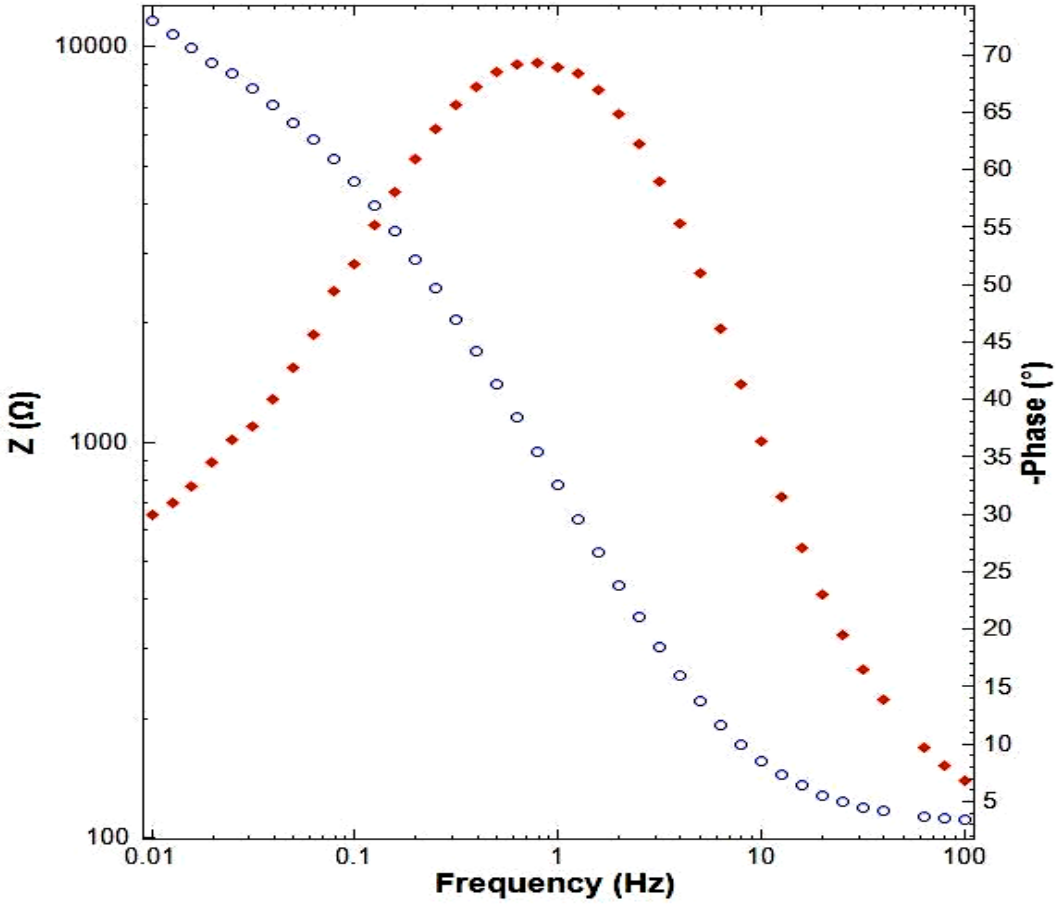

(b) Bode plot day 3

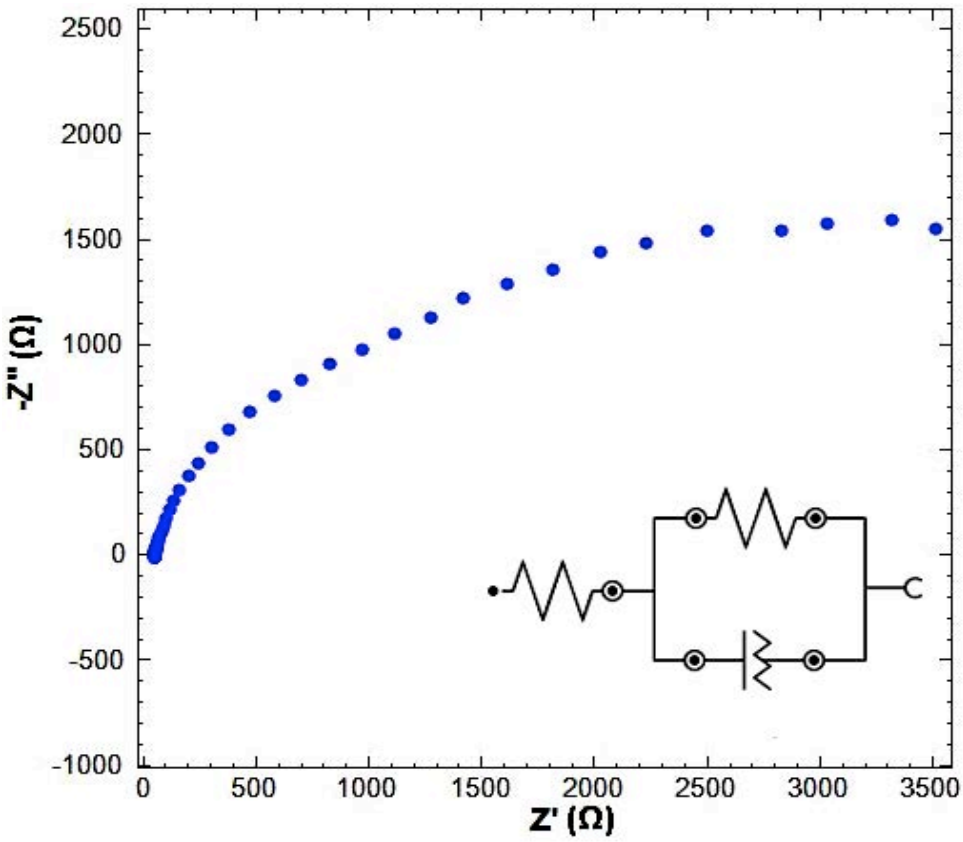

(c) Nyquist plot day 30

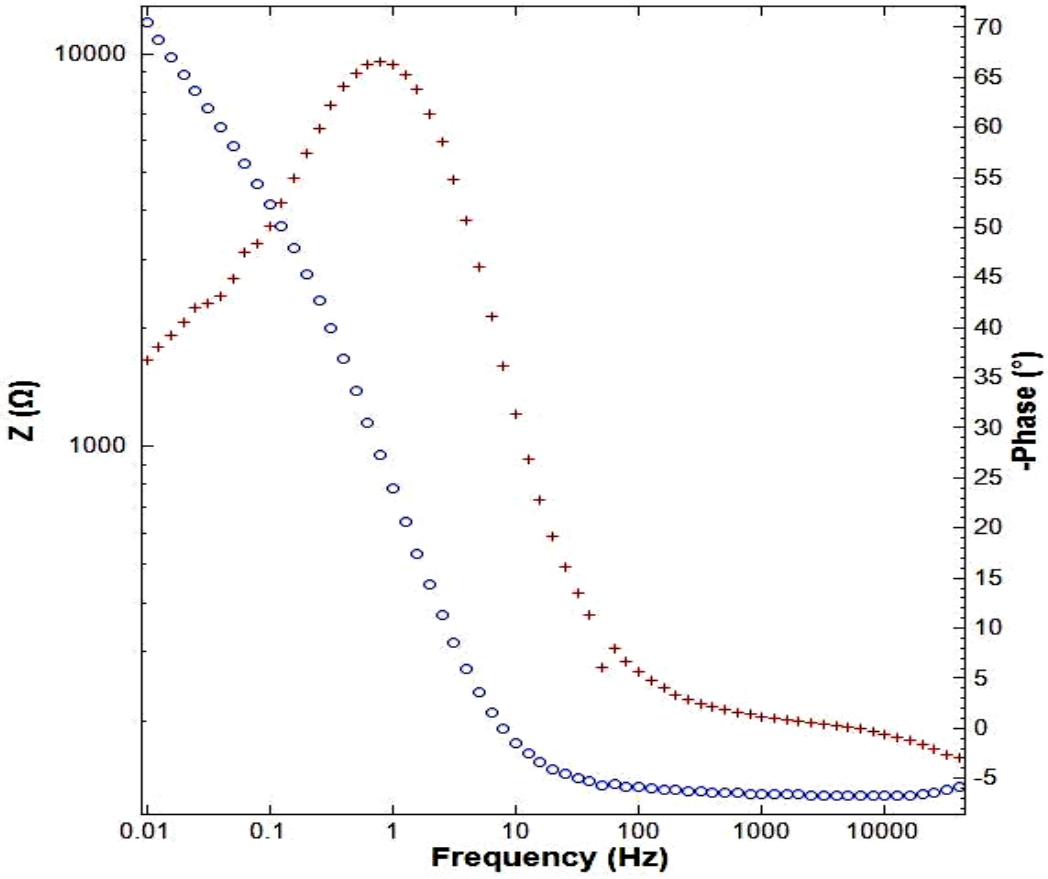

(d) Bode plot day 30

Figure 4.32 EIS of Al8Si20BN sample coated by HVOF

Table 4.8 OCP, I_{corr} and R_{CT}/kOhm of Al8Si20BN samples coated with plasma and HVOF methods in 3.5% NaCl solution for 30 days

Day	Plasma-coated Sample				HVOF-coated Sample			
	OCP		I_{Corr} / A (x 10^{-5})	R_{CT} / kOhm	OCP		I_{Corr} / A (x 10^{-5})	R_{CT} / kOhm
	Mean	SD			Mean	SD		
3	-0.678	0.00066	9.107	4.121	-1.004	0.0005	6.432	6.272
6	-0.703	0.00052	10.796	4.076	-1.087	0.0005	8.321	6.041
9	-0.726	0.00086	11.575	3.981	-1.113	0.00062	9.742	5.887
12	-0.693	0.0005	11.8937	3.913	-1.154	0.00056	7.653	5.693
15	-0.718	0.00067	12.179	3.849	-1.184	0.00083	8.889	5.460
18	-0.729	0.0098	12.648	3.707	-1.211	0.00078	9.898	5.311
21	-0.738	0.00096	13.034	3.609	-1.232	0.0010	9.589	5.185
24	-0.744	0.0014	13.244	3.204	-1.241	0.00072	10.033	5.082
27	-0.753	0.0012	13.699	2.981	-1.252	0.00058	10.957	4.973
30	-0.771	0.00095	13.977	2.491	-1.263	0.0064	11.247	4.847

4.5.4 Microstructural analysis of corrosion

FESEM micrographs of both coated samples after 30 days immersion in crude oil and seawater are shown in Figures 4.33 and 4.34. According to Figures 4.33(a), (b) and 4.34(a), (b), when samples were exposed to the oil environment, the corrosion rate on the surface of coated samples was less than in NaCl electrolyte (seawater) solution. In Figures 4.33(c), (d) the plasma-coated samples after 30 days corroded significantly and big holes formed on their surface. This coating had evident crevices and pitting corrosion in the microstructure containing inter-splat porosity. An earlier study

confirms these types of corrosion on the top surface of plasma-coated samples (Qian et al., 2010). Also, the size and amount of corrosion in NaCl solution (seawater) is obviously greater than in crude oil.

As seen in Figures 4.34 (c), (d) the amount of pitting corrosion on the HVOF sample is less than the plasma-coated sample, because fewer holes formed on the surface of the HVOF-coated sample than plasma samples, and there is no crevice corrosion. Regarding these figures, there is a big difference between the corroded and un-corroded samples with the plasma coating method in both environments, while for HVOF-coated samples the difference between corroded and un-corroded samples is considerably smaller than the plasma coating method. The HVOF coating protected the substrate from corrosion.

As conveyed by Volovitch et al. (2008), with the HVOF coating method, fine Al–Si eutectics constitute the coating matrix, which exhibit evident corrosion resistance over the α-Al dendrites. Clearly, the lower corrosion vulnerability of the matrix was due to the more electronegative eutectic Si constituent, which serves as a cathodic phase in the microgalvanic-coupled Al–Si eutectic structure. Besides, the dense network of fine Al–Si eutectic is expected to block the corrosion pervading into the matrix (Volovitch et al., 2008; Wang et al., 2014).

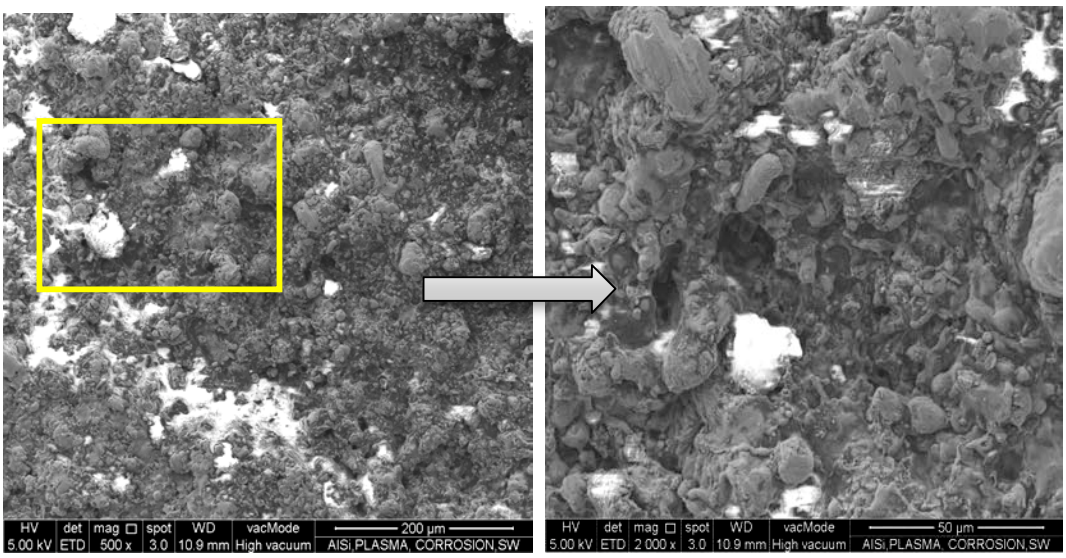

(a) FESEM-500X (b) FESEM-2000X

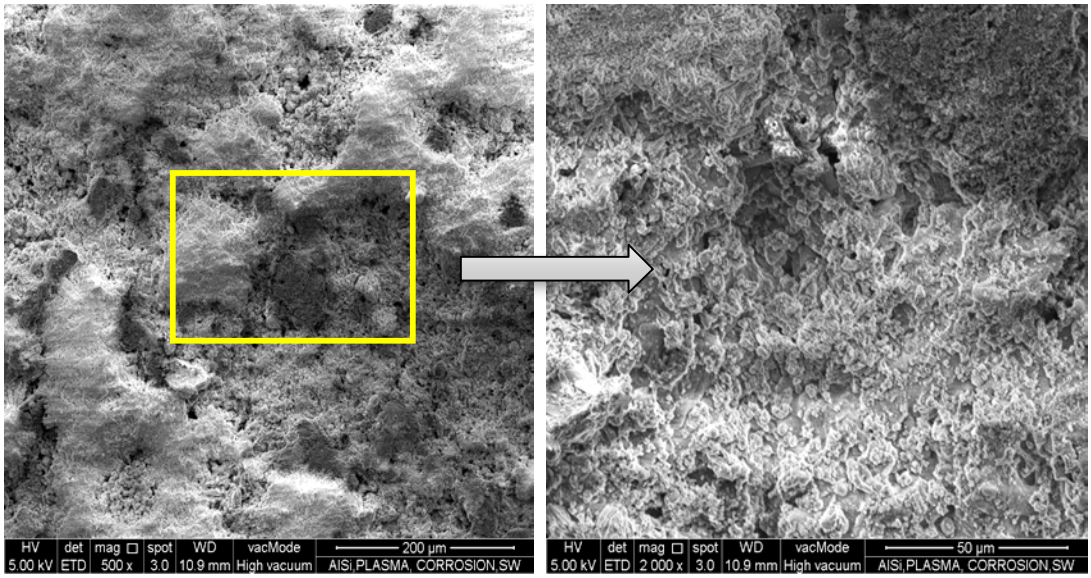

(c) FESEM-500X (d) FESEM-2000X

Figure 4.33 FESEM micrographsofAl8Si20BN plasma-coated sample surfaces after 30 days in: (a), (b) crude oil;(c), (d) seawater

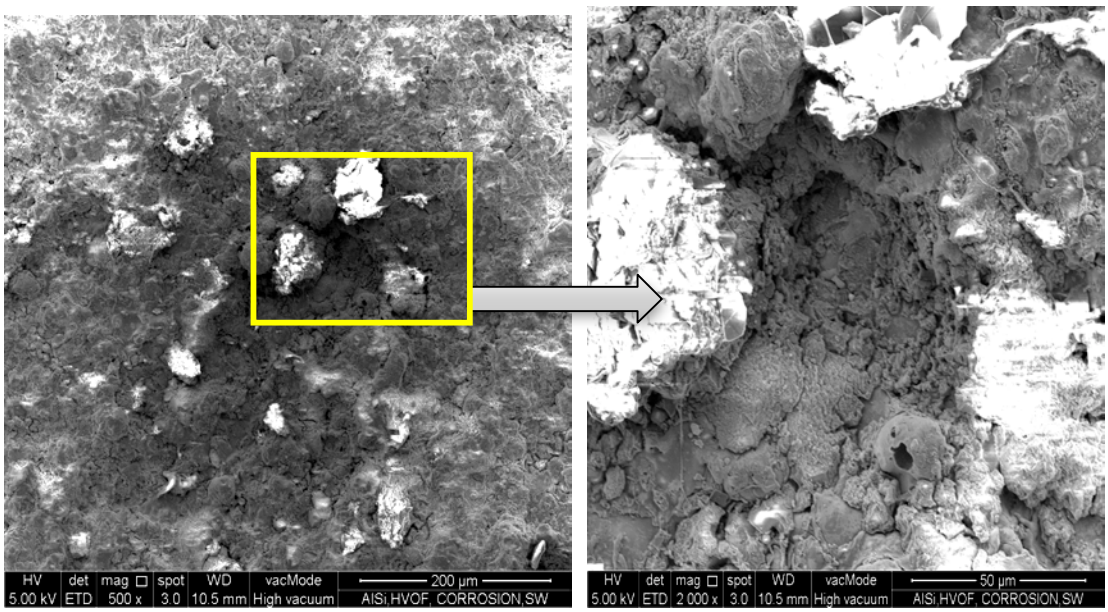

(a) FESEM-500X (b) FESEM-2000X

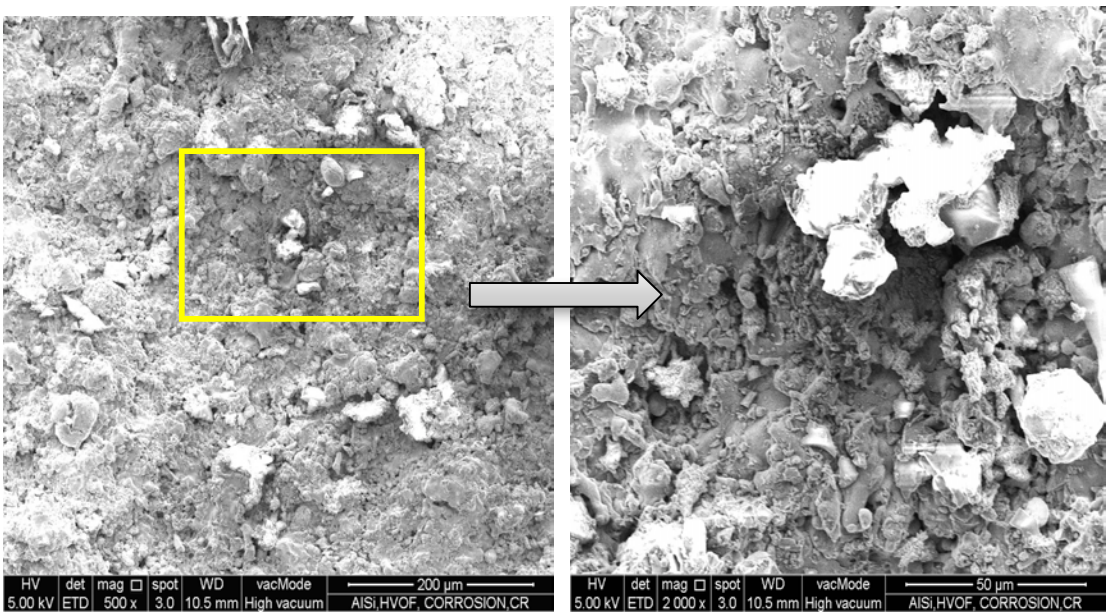

(c) FESEM-500X (d) FESEM-2000X

Figure 4.34 FESEM micrographs of Al8Si20BN sample surfaces coated by HVOF after 30 days: (a), (b) in crude oil;(c), (d) in seawater

According to the FESEMs of coated samples, the corrosion rate in 3.5% NaCl solution is significantly higher than in crude oil. The X-ray diffraction (XRD) analysis for plasma and HVOF-coated samples in 3.5% NaCl electrolyte after 30 days is presented in Figures 4.35(a), (b) respectively. It can be seen that the deposited layer

oxidized to $Al_2O_3$and SiO_2 on the coating surface, and the oxide phases in the corroded samples increased. However, there are more silica (SiO_2) peaks in the plasma method than HVOF, but the amount of alumina in HVOF-coated samples is higher.

Also, alumina has a sticky property, so it is more protective against corrosion. HVOF-coated samples are denser than plasma-coated samples. Generally with both methods, a dense deposited layer protects the substrate from the inward permeation of oxygen. The XRD results show there is no formation of any type of iron oxide on the coated samples.

Thus, it can be concluded that the coating prevents the corrosive electrolyte from penetrating the substrate, and consequently protects the substrate from the corrosive environment. The better corrosion resistance of the HVOF spray coating than plasma coating can be reasonably attributed to the α-Al (Si) (Qian et al., 2010).

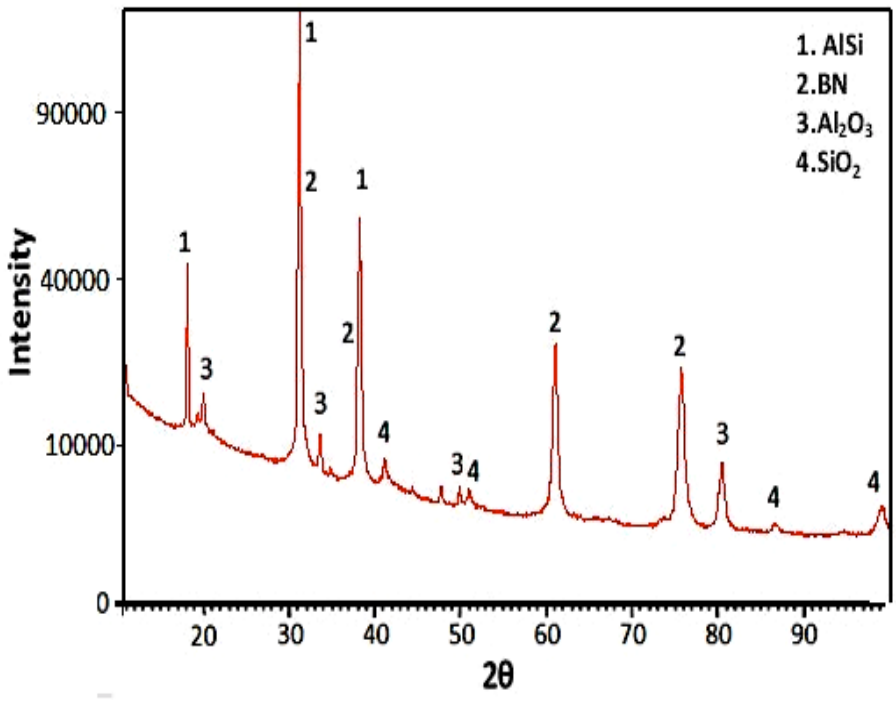

(a)

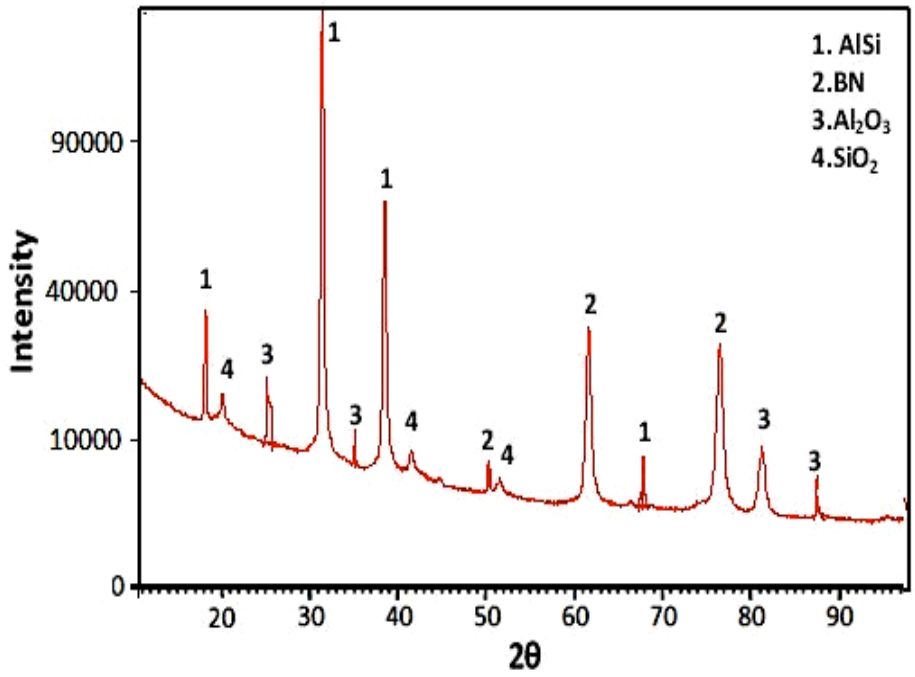

(b)

Figure 4.35 XRD results of Al8Si20BN samples in 3.5%NaCl solution after 30 days for (a) plasma, (b) HVOF coating

According to the microstructural analysis, wear and corrosion testing results, the HVOF-coated samples have higher performance than plasma-coated samples. However, both polarization and EIS results confirm the corrosion protective properties of plasma

and HVOF coatings. But the corrosion resistivity of HVOF-coated samples is higher than plasma. In addition, the tribological properties of HVOF-coated samples under different loads are more durable and the weight loss rate of these samples is limited, especially under loads of 5 N and 10 N. Therefore, from this chemical composition group, the HVOF method was selected for wear and corrosion resistivity.

4.6 Analysis of substrate coated with Carbonate Chromium-Nickel Chromium (Cr_3C_2-25%NiCr)

4.6.1 Microstructural analysis

Typical microstructures of plasma and HVOF-sprayed Cr_3C_2–25NiCr coatings are shown in Figure 4.36. This powder was deposited on the carbon steel surface. The coating surface exhibited dense microstructure with high cohesion. However, a few pores appeared as black spots in the micrograph. It has been reported that these pores are due to the un-melted and semi-melted particles in the Cr_3C_2–NiCr coatings and are identified by their spherical morphology (Dent et al., 2000; Wang and Shui, 2002).

This is considered low porosity due to the high-impact velocity of the coating particles, which causes high density and high cohesive strength of individual splats (Murthy and Venkataraman, 2006). Figure 4.36 shows the micrographs of this coating, which is uniform, homogeneous and free from surface cracks. A relatively homogenous coating without segregation is critical for improving the wear resistance of Cr_3C_2–25NiCr coating.

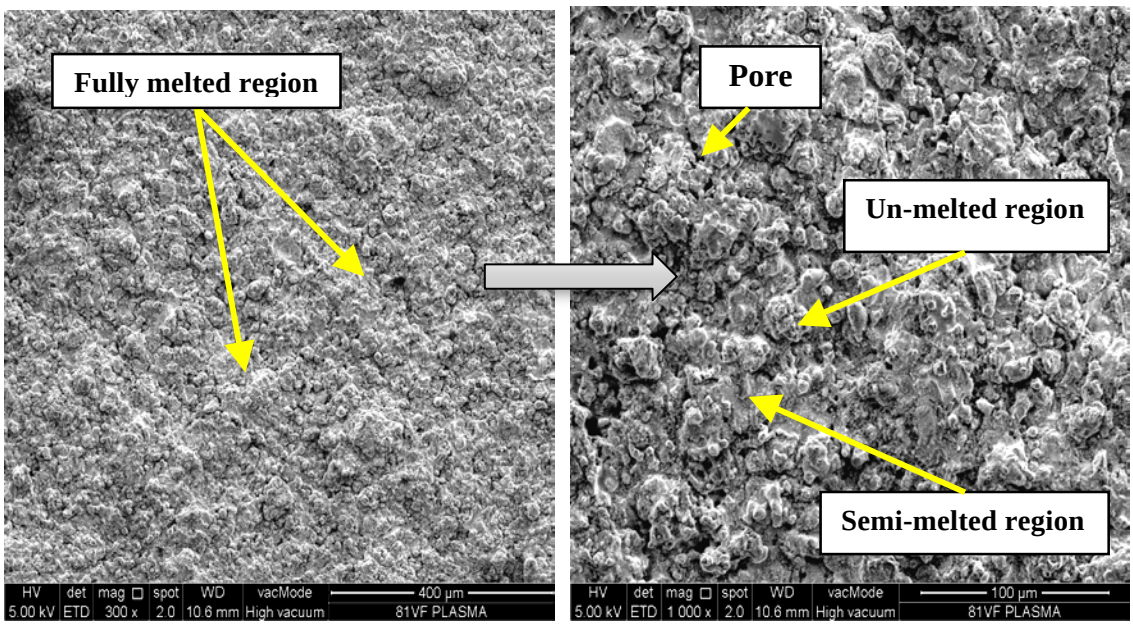

(a) Plasma (b) Plasma

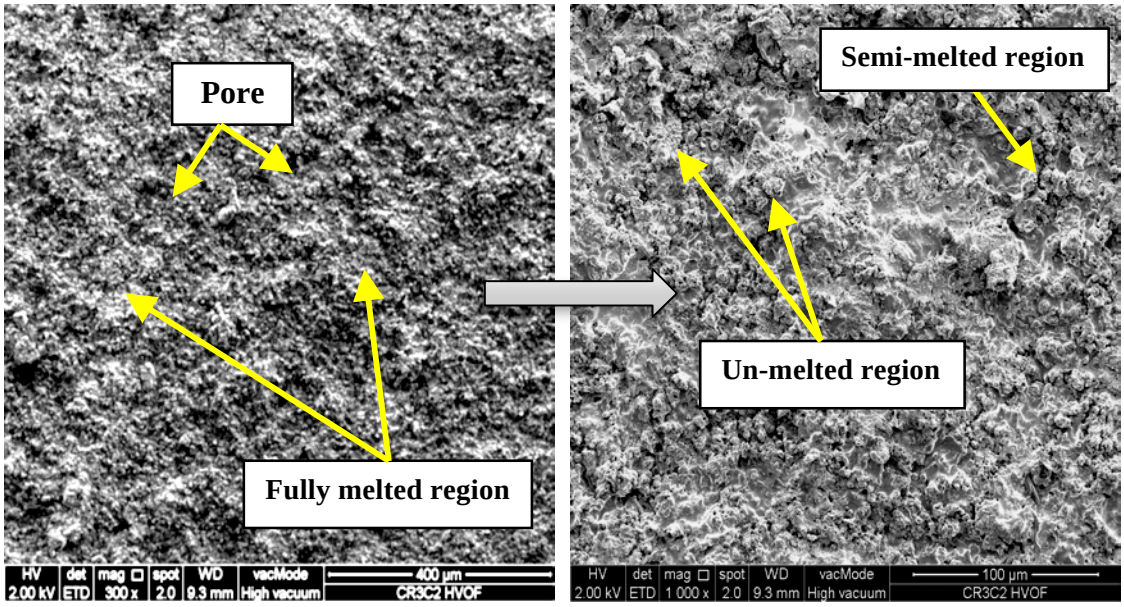

(c) HVOF (d) HVOF

Figure 4.36 FESEM of Cr_3C_2–NiCr coated samples at different magnifications: (a), (c) 300X; (b), (d) 1000X

X-ray diffraction and EDX patterns for Cr_3C_2–NiCr plasma and HVOF-coated samples are shown in Figure 4.37. According Figure 4.37(a) and (b), Cr_3C_2 and NiCr binder were the major phases identified in plasma and HVOF Cr_3C_2–NiCr coating. However, the number of peaks belonging to Cr_3C_2 in the HVOF method is higher than the plasma method. Apart from Cr_3C_2 carbide particles, Cr_7C_3 and $Cr_{23}C_6$ carbides were

also present in the X-ray diffraction analyses. Evidently, the decarburization of Cr_3C_2 resulted in the formation of Cr_7C_3 and $Cr_{23}C_6$. Nevertheless, Cr_7C_3 and $Cr_{23}C_6$ can form in diverse ways. The Cr_7C_3 carbide formed through the decarburization of Cr_3C_2 (Wang and Shui, 2002; Sahraoui et al., 2003).

Additionally, during coating deposition, the $Cr_{23}C_6$ in the plasma and HVOF Cr_3C_2–NiCr coatings appeared to precipitate. As Zimmermann and Kreye (2000) pointed out, since the main diffraction peaks of Cr_7C_3 and $Cr_{23}C_6$ coincide with the lines referring to NiCr and Cr_3C_2, their existence in the as-sprayed coating could not be confirmed solely through X-ray diffraction approach. Furthermore, the decarburization of Cr_3C_2 appeared to be linked to the heating of spray particles and oxidation of Cr_3C_2, since HVOF cermet coating is commonly deposited in ambient condition (Kato, 2000).

As confirmed by previous research findings, the main reason for carbon loss and change in carbide content is that the Cr_3C_2 particles rebound during coating formation (Sahraoui et al., 2003).

Furthermore, the EDX of the Cr_3C_2–NiCr composite for plasma and HVOF methods in Figure 4.37 (c) and Figure 4.37 (d) shows the existence of nickel, chromium, and carbon. The EDX results confirm that the highest peak belongs to the chromium, and the amount of nickel is the highest after chromium. Also there is not any oxygen detected after deposition this chemical composition by these techniques. The weight percentage of each element is provided in Figure 4.37(c) and Figure 4.37 (d) (inset).

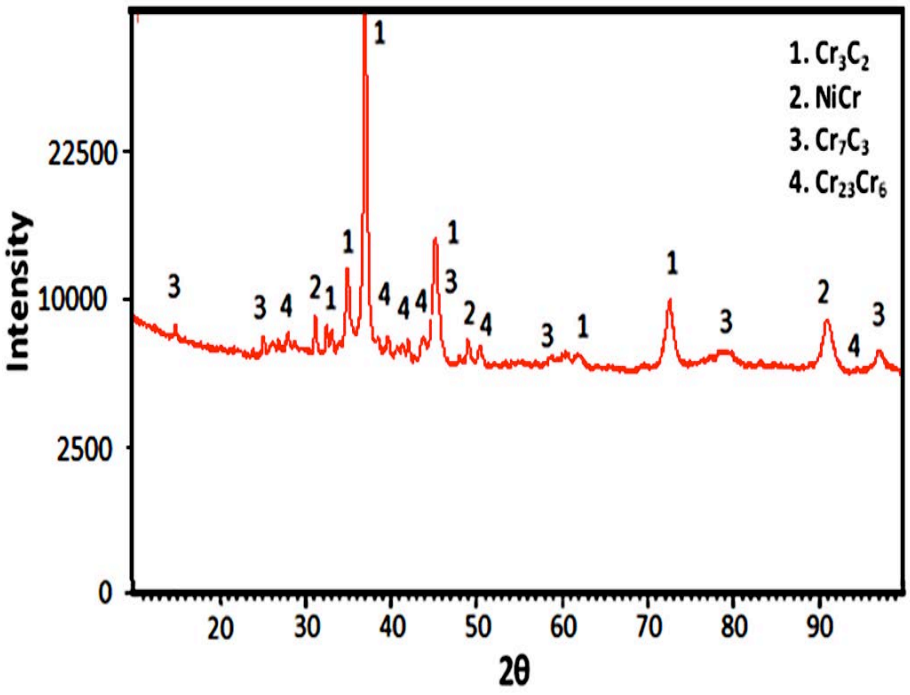
1. Cr_3C_2
2. NiCr
3. Cr_7C_3
4. $Cr_{23}Cr_6$
Intensity
22500
10000
2500
0
20
30
40
50
60
70
80
90
2θ

(a)

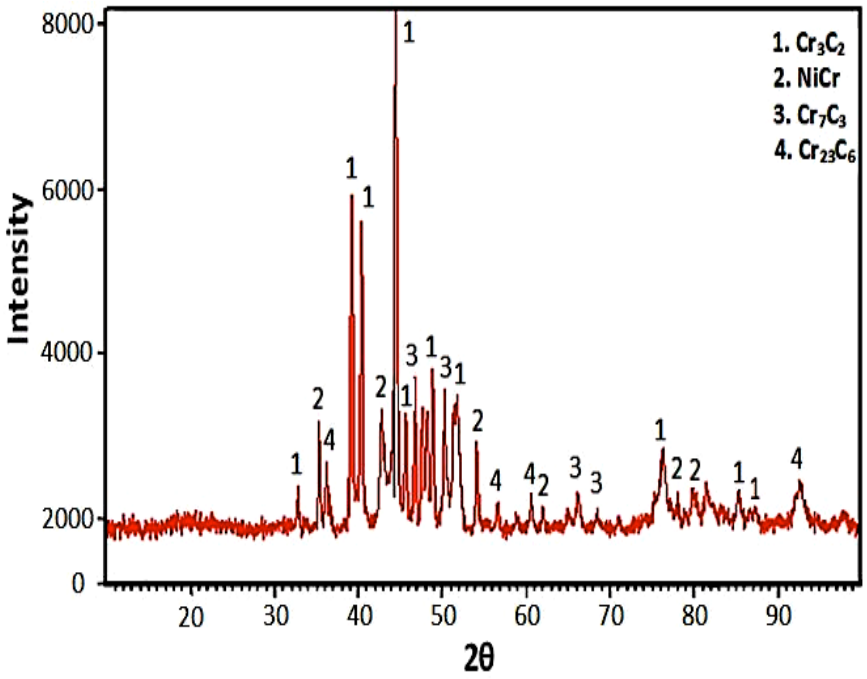
1. Cr_3C_2
2. NiCr
3. Cr_7C_3
4. $Cr_{23}C_6$
Intensity
8000
6000
4000
2000
0
20
30
40
50
60
70
80
90
2θ

(b)

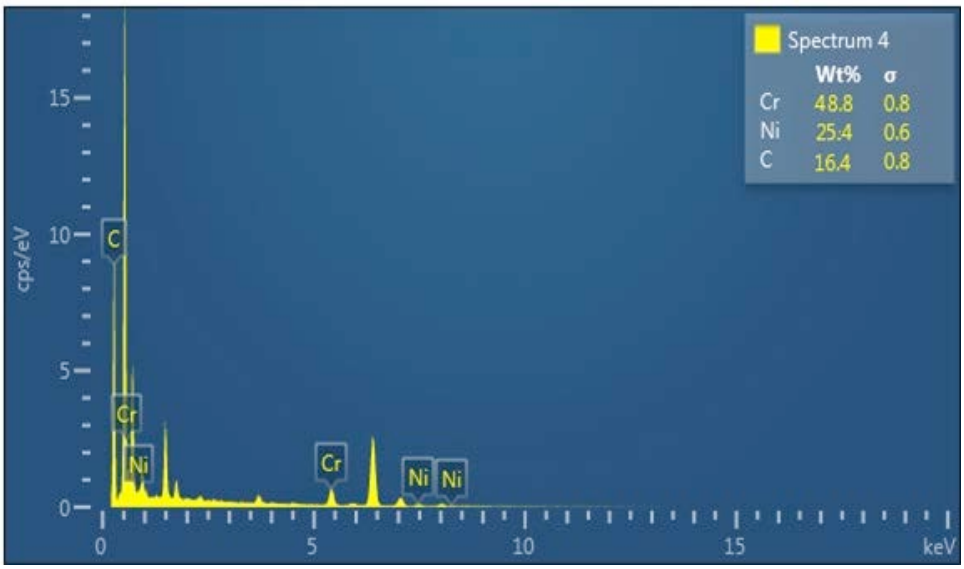

(c)

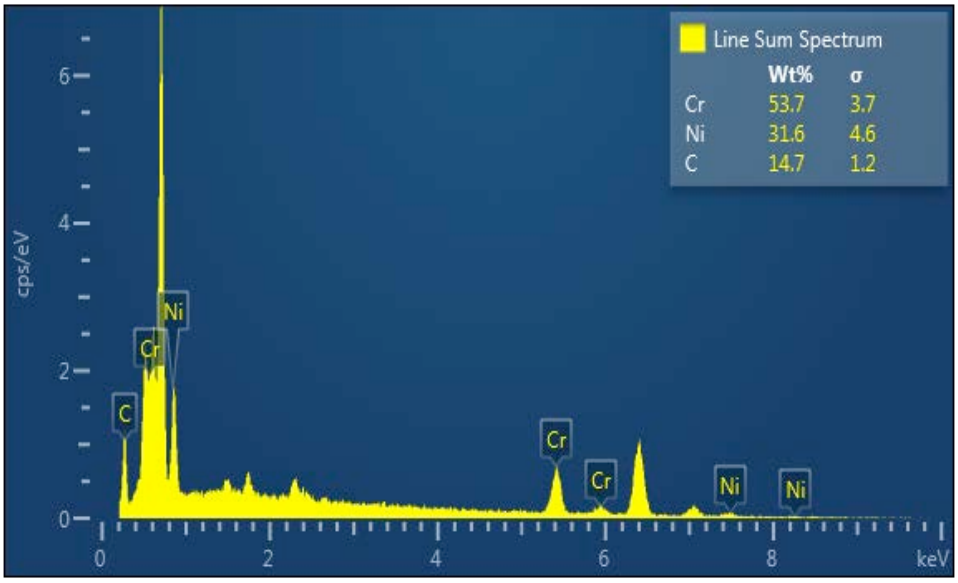

(d)

Figure 4.37 X-ray diffraction patterns for Cr_3C_2–25NiCr samples coated by (a) plasma, and (b) HVOF; and EDX of (c) plasma and (d) HVOF coated samples

4.6.2 Wear analysis

The coated sample roughness for plasma and HVOF is 6.2359 and 6.4166 μm respectively. As reported in previous studies, coating roughness plays a critical role in coating lifespan.

The average microhardness of samples coated by plasma and HVOF methods is 800-850 and 890-930 HV respectively. According to Scrivani et al. (2001), the hardness of Cr_3C_2–NiCr coated using HVOF with propane fuel consistently has 950 HV hardness. Chatha et al. (2012) reported that high volumes of carbides are well dispersed in the matrix. This factor might be responsible for higher microhardness and lower porosity values found in this type of coating.

In contrast, when maximum load was applied to the coated samples illustrated in Figure 4.38, no obvious difference was observed before the wear test. Moreover, no cracks or deformation formed at the edge of the samples after applying maximum load. Applying maximum load resulted in slight abrasion and wear in some sample surface regions, which were, however, smooth, as they were before testing (Figure 4.36). As shown in Figures 4.38(a), (b), the plasma-coated samples had bigger and rougher wear debris than the HVOF-coated samples (Figures 4.38(c), (d)). In addition, within the tracks at maximum load (20 N) a little loose wear debris was found. On the surface of the coated sample exposed to wear testing, no cracks were detected. This was associated with the elevated bonding strength between the splats and component as well as the significant role that bond strength can play in splat propagation and resistance to crack initiation.

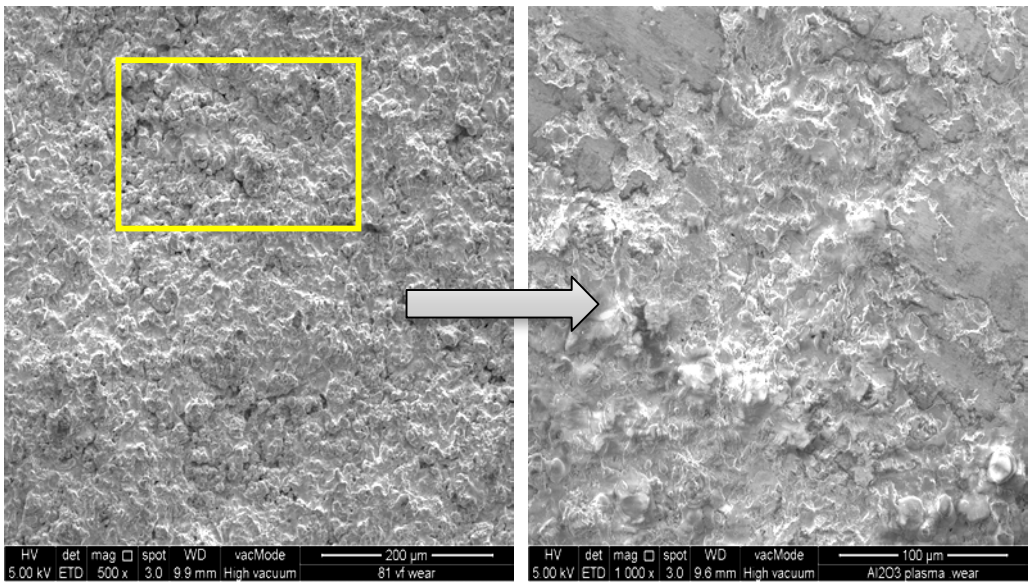

(a) Plasma (b) Plasma

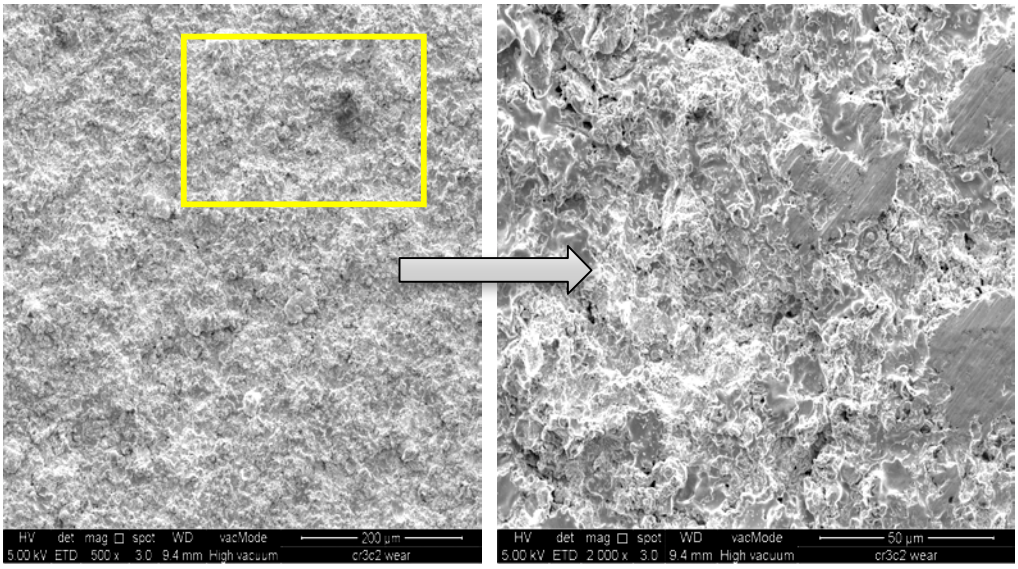

(c) HVOF (d) HVOF

Figure 4.38 FESEM of wear debris of Cr_3C_2-25NiCr coated samples under maximum load (20 N) for: (a), (b) plasma; (c), (d) HVOF coating

Table 4.9 and Figure 4.39 present the mean scores of weight loss as well as wear rate for both coating methods under varying loads. According to Figure 4.39(a), when different loads were applied on the different coated samples, the amount of wear for the HVOF-coated sample changed from 10 to 25 µm, while for the plasma-coated sample it changed from 12 to 30 µm. Thus, the average wear with the plasma method is slightly higher than the HVOF method. Figure 4.39(b) shows the maximum values of weight

loss for the plasma samples, which were 0.0039, 0.0040, 0.0087 and 0.0115 g for loads of 5, 10, 15 and 20 N respectively. This confirms the wear rate trend of plasma-coated samples.

Table 4.9 Weight loss and wear rate of Cr_3C_2–25NiCr coated samples for different loads

Loads (N)	**Rate of weight loss**		**Rate of wear (μm)**	
	Plasma-coated Sample	HVOF-Coated Sample	Plasma - coated Sample	HVOF-Coated Sample
5	0.0039	0.0033	12±2	10±1
10	0.0040	0.0034	18±3	15±2
15	0.0087	0.0073	23±2	19±3
20	0.0115	0.0098	30±3	25±2

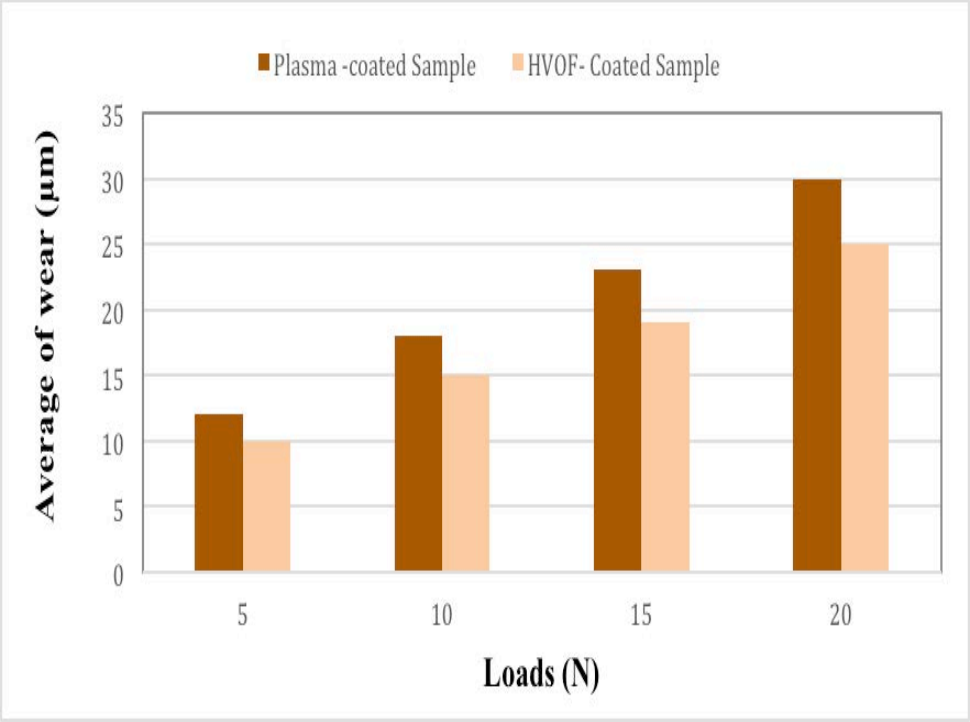

(a)

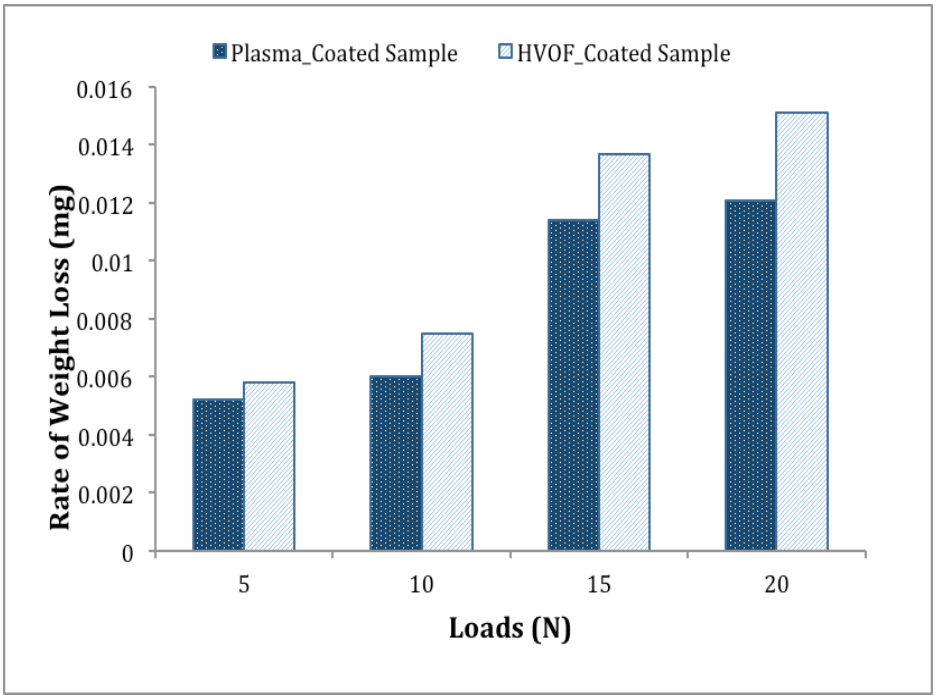

(b)

Figure 4.39 Behavior of Cr_3C_2–25NiCrplasma and HVOF-coated samples under different loads: (a) average wear; (b) weight loss rate

Generally, for Cr_3C_2–NiCr coating, NiCr alloy is a continuous matrix phase with chromium carbides as hard reinforcement phases. Because the microhardness of

chromium carbides is much higher than that of the NiCr matrix, the carbides are more resistant to cutting or gouging than the matrix alloy phase. Accordingly, the carbide phase, having higher wear resistance, would be removed at a lower rate, and the wearing off of NiCr alloy binder would occur more preferentially. Consequently, the abrasive wear of the plasma and HVOF Cr_3C_2–NiCr coating in the pin-on-disc test occurred in two steps.

The first step was the successive removal of the NiCr binder. Because the metallic Ni–Cr binder phase was deformed by the stress of compression produced by the sliding WC–6%Co plate, it exposed the carbide particles to the surface. Then the removal of carbide particles occurred by fracturing or loosening followed by subsequent pulling out by the abrasive particles. Therefore, an improvement in the matrix alloy hardness and bonding strength between carbides and the matrix may enhance the coating's abrasive wear resistance.

Different comparative studies on thermally sprayed coatings and hard chromium electroplating, suggest that the abrasive wear resistance of HVOF coatings could be 2–16 times higher than hard chromium coatings (Li et al., 2002; Vilches et al., 2011). Moreover, the wear rate is very sensitive to abrasive characteristics like chemical composition, shape, size and angularity.

Particle shape can significantly influence the wear mechanisms and determine if the particles will be able to roll or slide during three-body abrasion. Particles with angular shape can generate wear rates higher than rounded ones (Wang and Shui, 2002; Scrivani et al., 2001). Since finer, rounded particles produce less damage on both surfaces, finer carbide size coatings would exhibit a lower wear rate (Ghosh et al., 2014). Furthermore, the smaller size of chromium carbide could involve a better distribution and cohesion of reinforced particles in the binder phase, which could

decrease the pullout of the carbide particles during the sliding test and consequently produce a lower specific wear rate (Chatha et al., 2012).

4.6.3 Electrochemical corrosion analysis

Polarization curves were made for plasma and HVOF-coated samples from day 3 to day 30, and the results are tabulated in Figure 4.40 and Table 4.10. The open circuit potential (OCP) of the HVOF-coated sample (red) moved toward 0.179 at the end of day 30 from 0.089, and the OCP values for the HVOF-coated sample were more noble compared with the plasma-coated sample (blue). The OCP of the plasma-coated sample on day 3 was 0.004 while at the end of the period it was 0.071. These results suggest that the HVOF coating on carbon steel offers good protection of the carbon steel substrate against corrosion.

From the computer simulations for plasma and HVOF-coated samples on day 3, the R_s (CR) circuit diagram accurately matches the experimental data. Only one semicircle is visible in the Nyquist plot (Figures 4.41(a) and 4.42(a)). The Bode phase diagrams of plasma-coated samples (Figures 4.41(b) and 4.42(b)) shows one-phase maxima. However, the HVOF-coated samples contain more semicircles than the plasma-coated samples. The R_{ct} of plasma and HVOF samples from day 3 to day 30 are given in Table 4.10. The plasma and HVOF-coated samples with the equivalent circuit R_s (Q_1R_1) accurately fit the experimental data on day 30, because only one semicircle was observed on the Nyquist and Bode plots (Figures 4.41(c), (d) and 4.42(c), (d)).

However, the semicircle on the plasma-coated sample (Figure 4.41(c)) is smaller than on the HVOF-coated sample (Figure 4.42(c)). R_s is the solution resistance between the coated surface and reference electrode, and it is in series with one-time constants in parallel arrangement of R and Q.

Table 4.10 indicates that the R_{ct} value for HVOF-coated samples is greater than for plasma-coated samples in nearly all measurements. These results also verify the enhanced performance of HVOF coating compared with plasma coating in terms of corrosion protection of the carbon steel surface. Also, the corrosion current density of plasma-coated samples increased slightly from 7.722×10^{-8} A on day 3 to 7.637×10^{-8} A on day 30. Meanwhile, the current density of HVOF-coated samples fluctuated during this period. The corrosion current of HVOF-coated samples from day 3 to day 12 increased from 7.501×10^{-8} to 7.594×10^{-8} A, and it suddenly plunged to 7.567×10^{-8} A on day 15 and continued fluctuating until day 27 when it suddenly increased to 7.778×10^{-8}A.

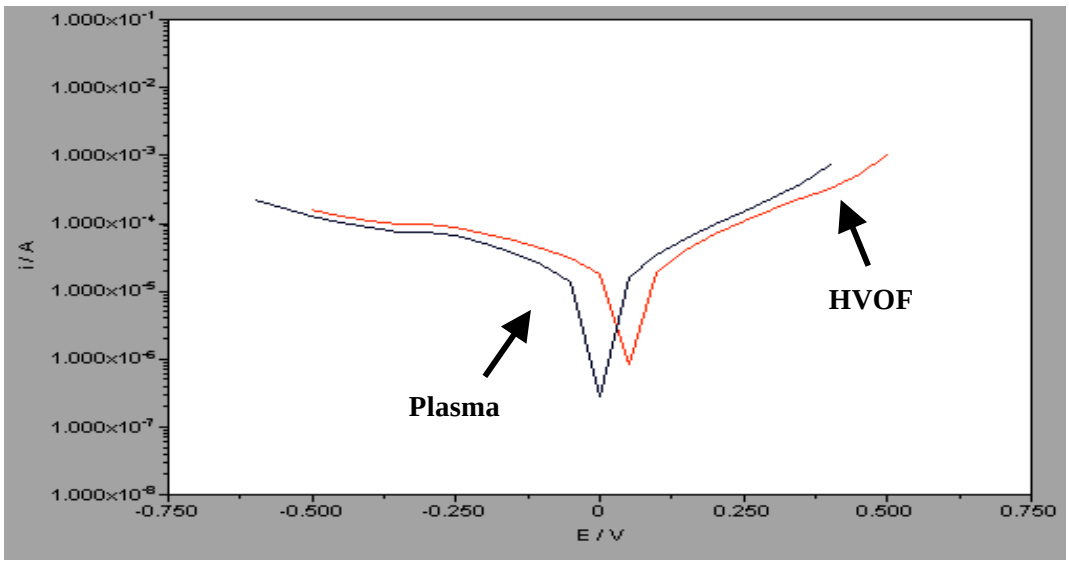

(a) 3rd day experiments

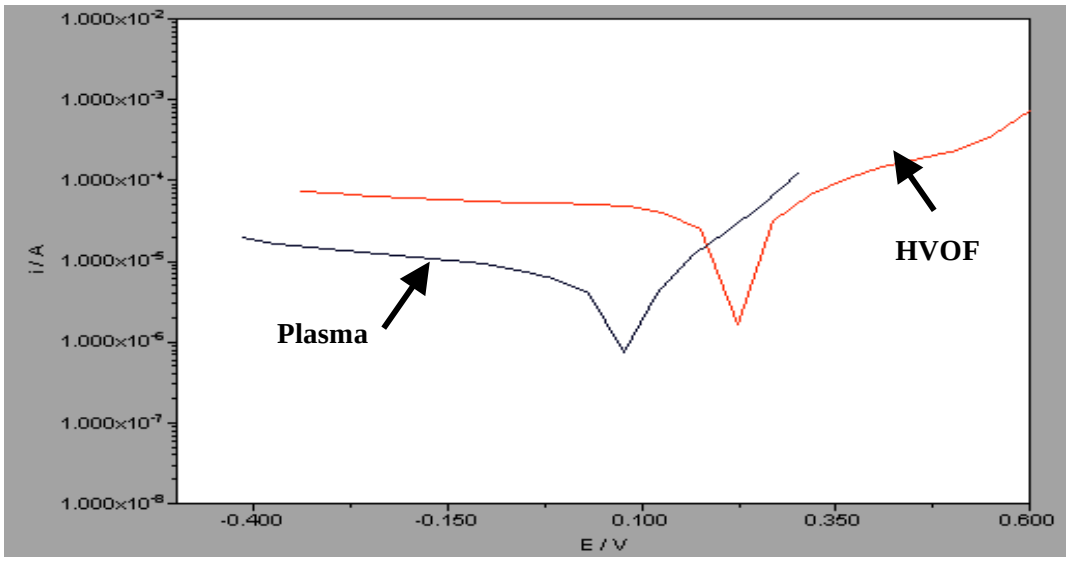

(b) 30th day experiments

Figure 4.40 Polarization curves (log I vs E) of Cr_3C_2-25NiCr coated with plasma and HVOF for: (a) 3rd day and (b) 30th day experiments

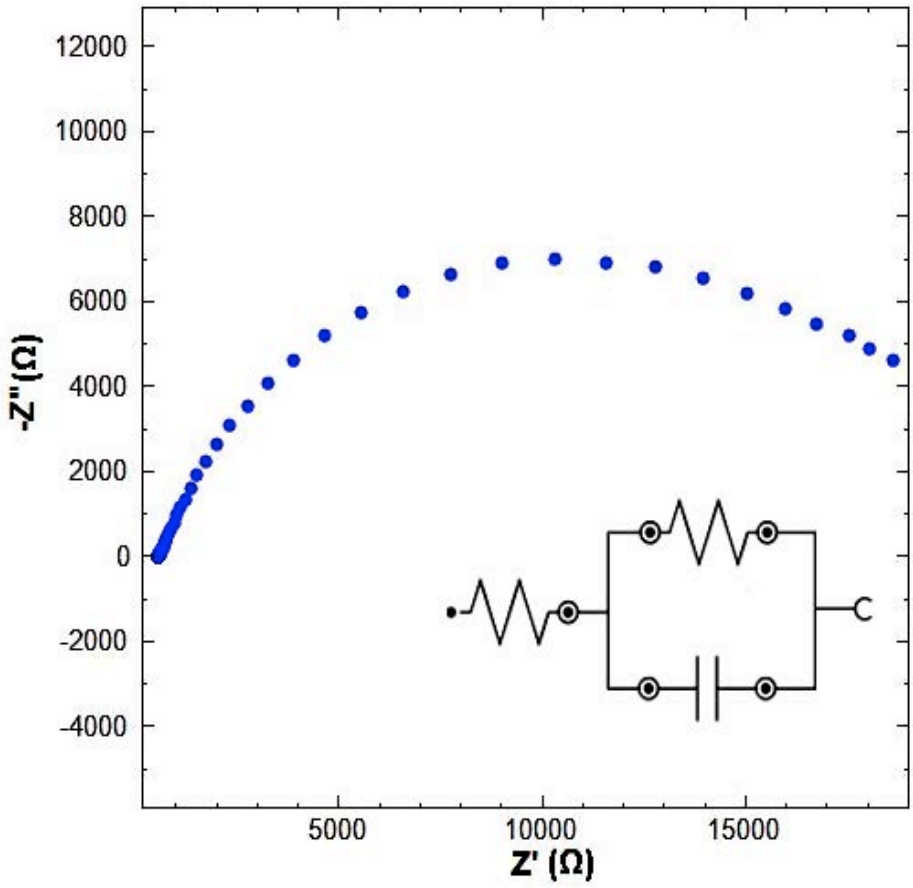

(a) Nyquist plot day 3

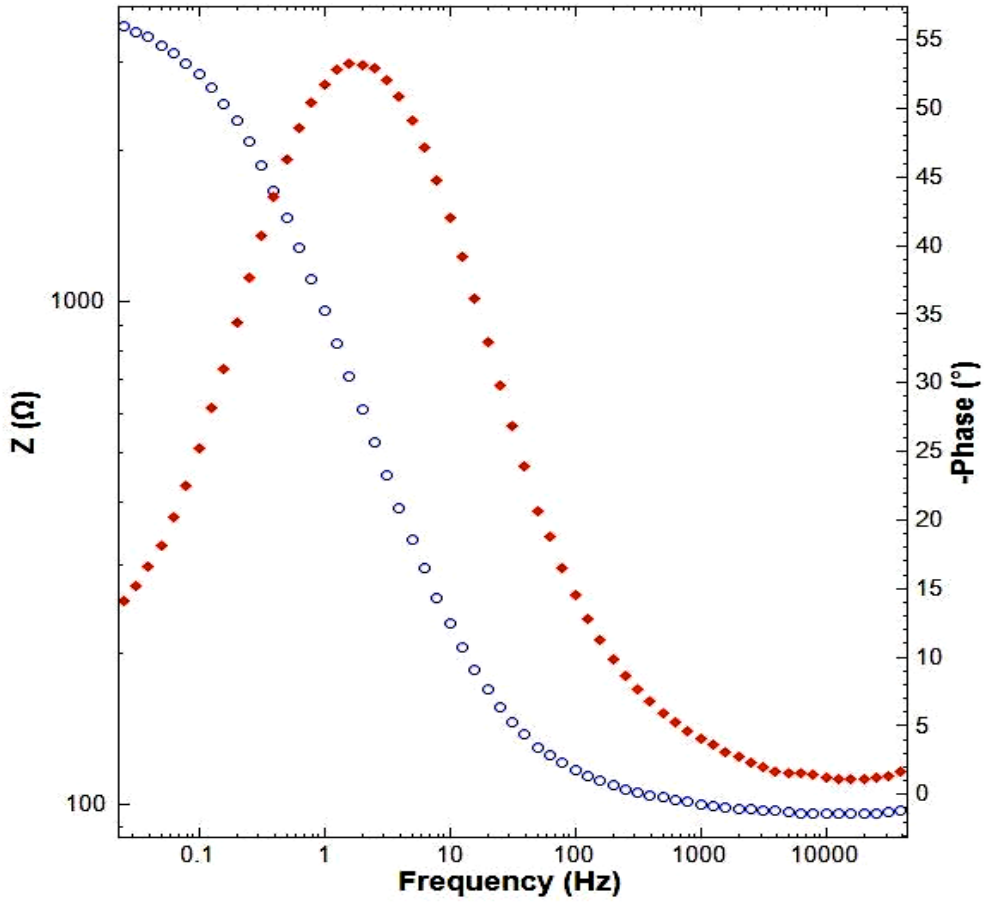

(b) Bode plot day 3

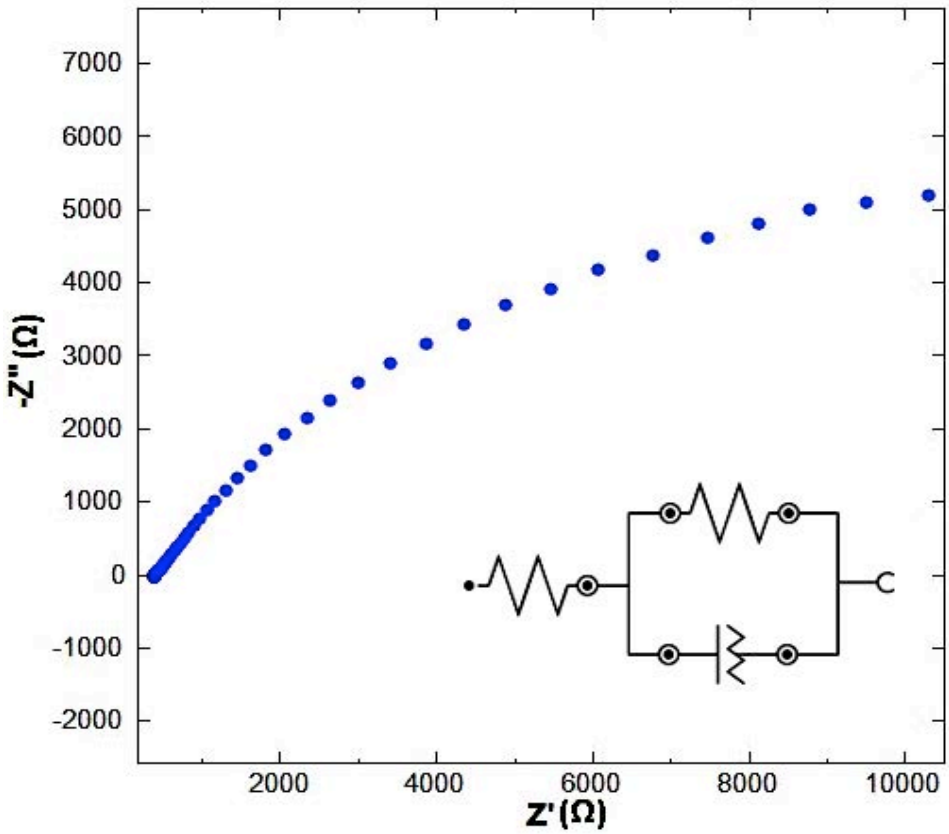

(c) Nyquist plot day 30

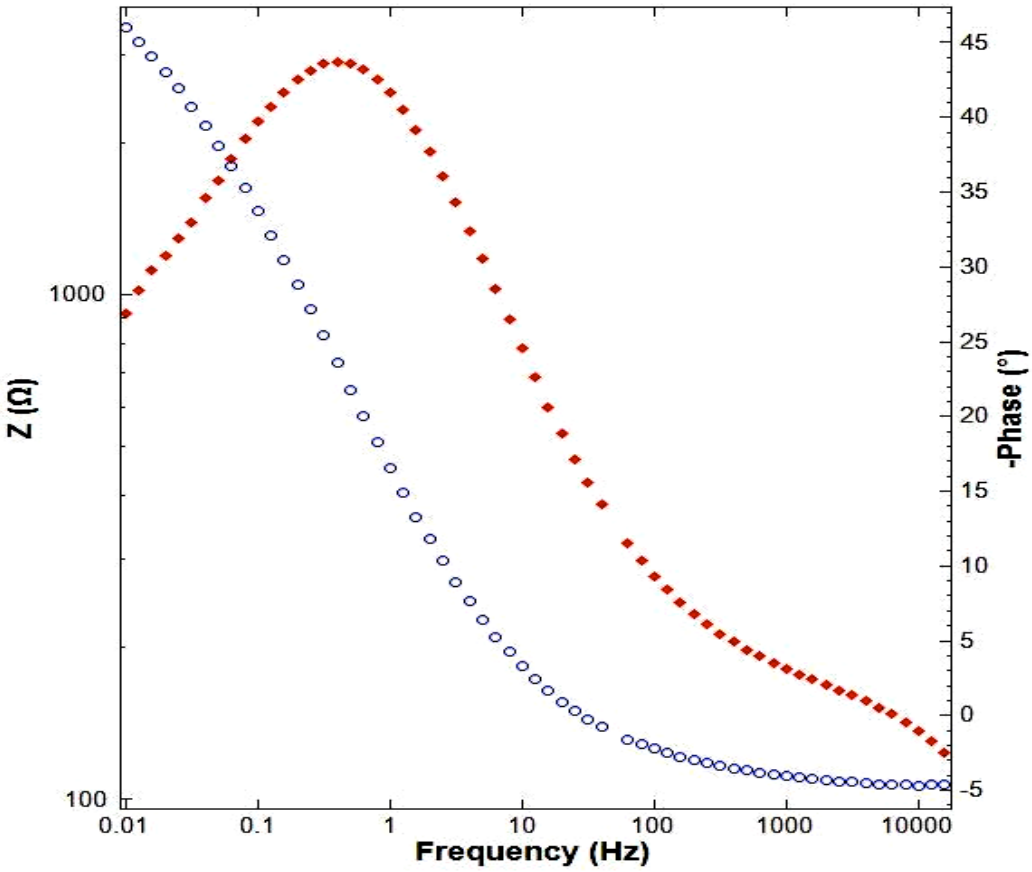

(d) Bode plot day 30

Figure 4.41 EIS of Cr_3C_2-25NiCr plasma-coated sample

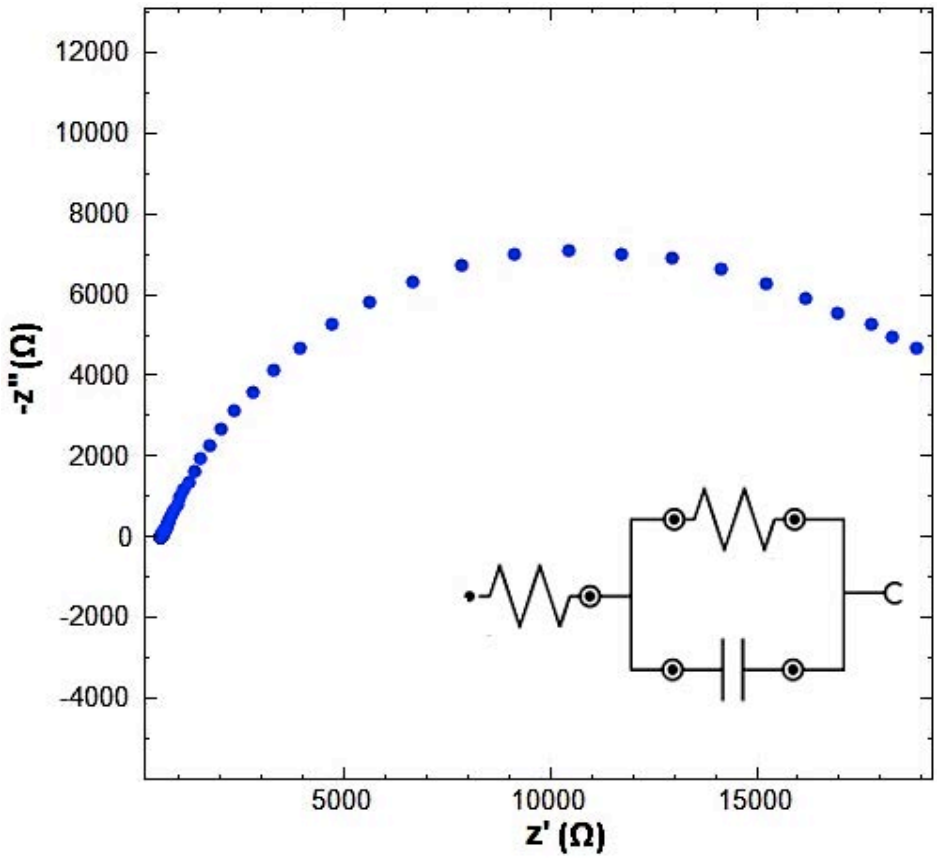

(a) Nyquist plot day 3

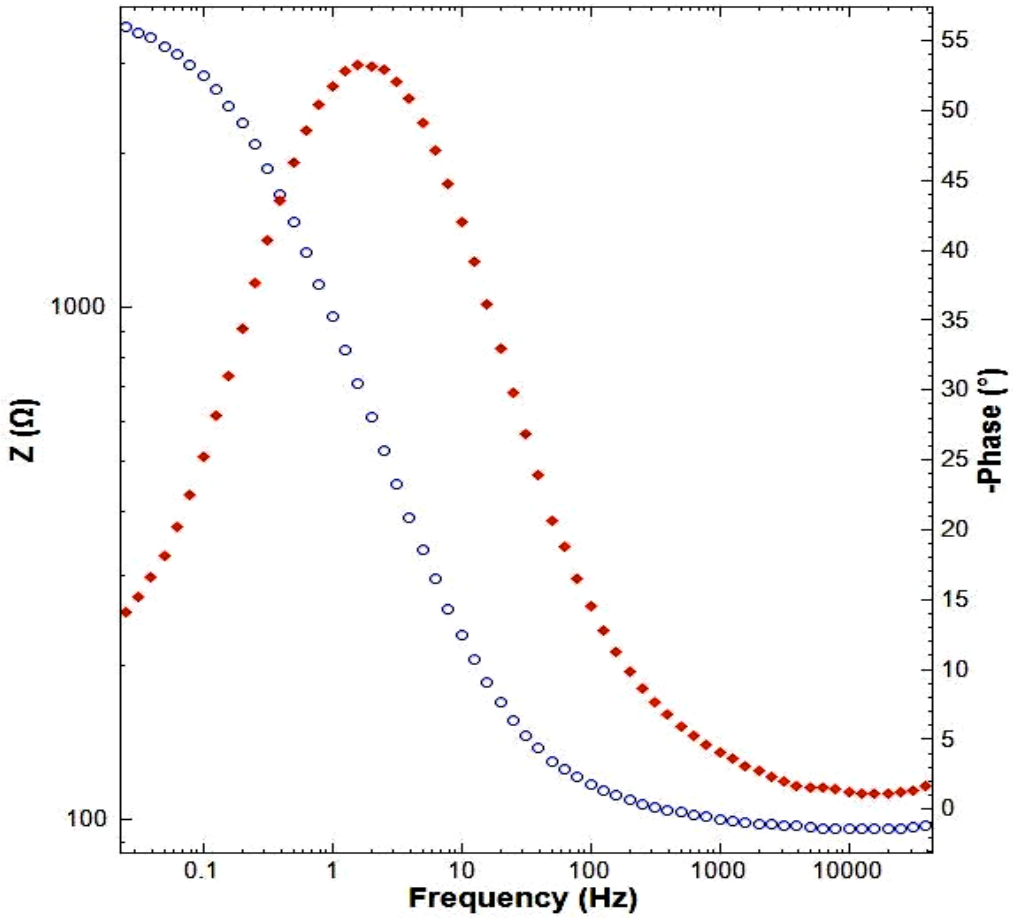

(b) Bode plot day 3

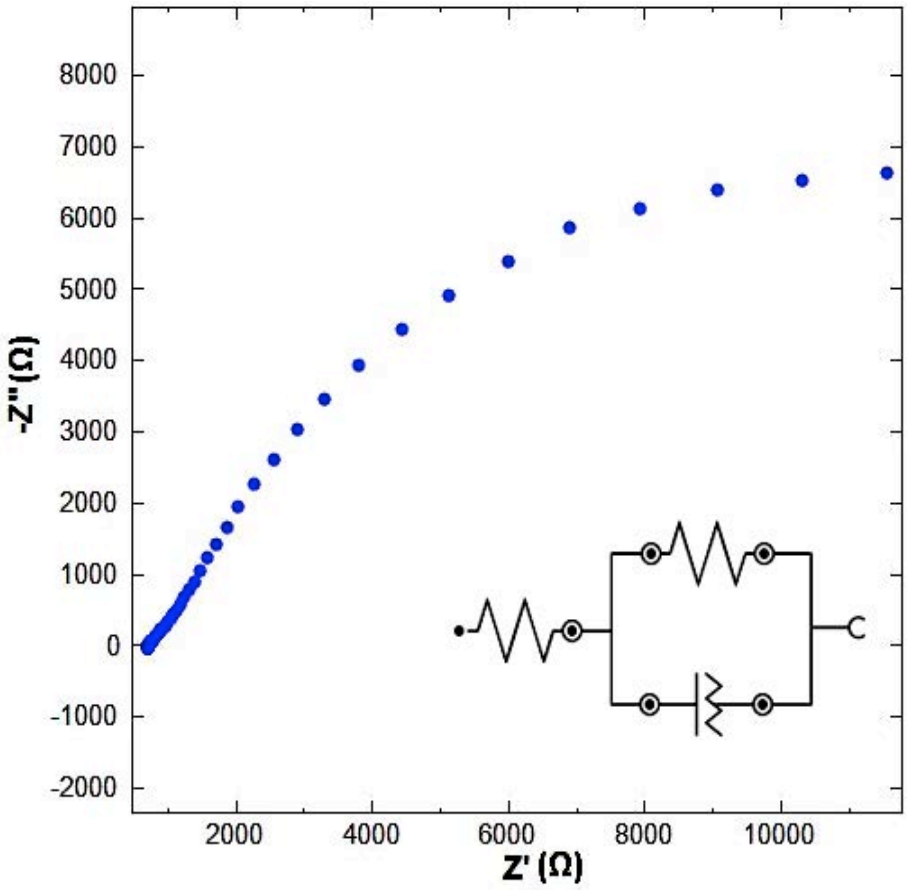

(c) Nyquist plot day 30

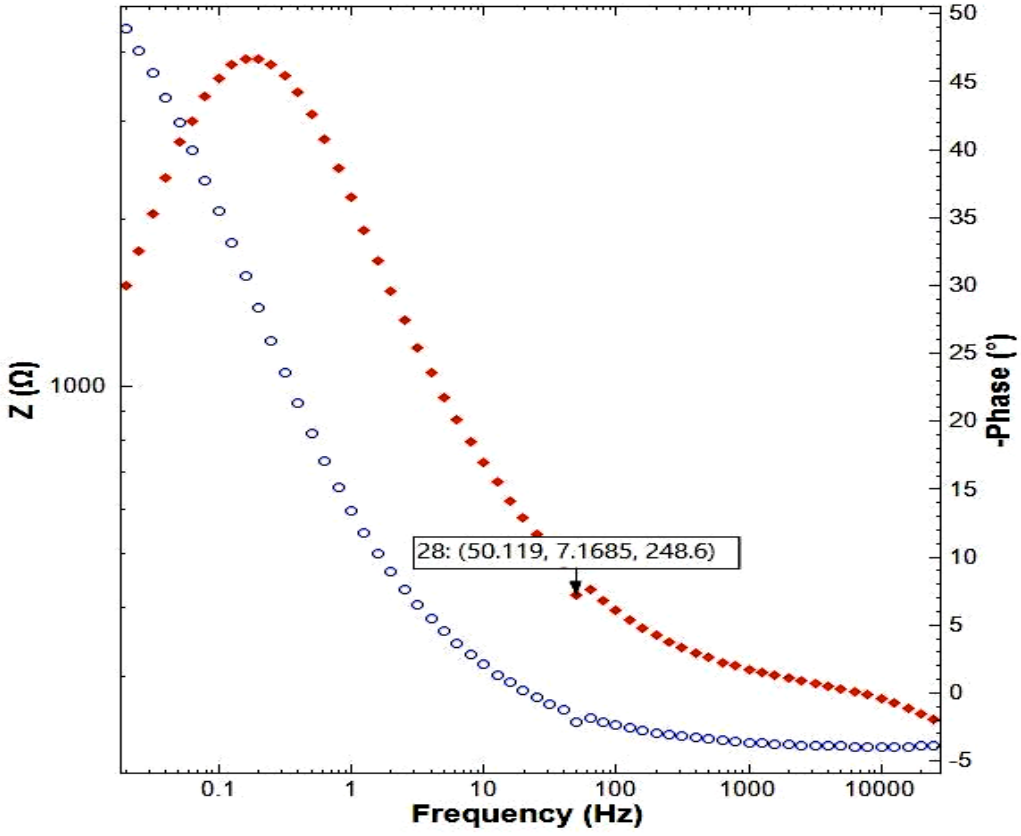

(d) Bode plot day 30

Figure 4.42 EIS of Cr_3C_2-25NiCr HVOF-coated sample

Table 4.10 OCP, I_{corr} and R_{CT}/kOhm of Cr_3C_2-25NiCr samples with plasma and HVOF coating methods in 3.5% NaCl solution for 30 days

Day	Plasma-coated Sample				HVOF-coated Sample			
	OCP		I_{Corr} / A (x 10^{-8})	R_{CT} / kOhm	OCP		I_{Corr} / A (x 10^{-8})	R_{CT} / kOhm
	Mean	SD			Mean	SD		
3	0.004	0.0005	7.722	21. 721	0.087	0.0006	7.501	22.001
6	0.011	0.00071	8.121	21.531	0.098	0.00051	7.519	21.886
9	0.016	0.0011	8.242	21.391	0.109	0.00094	7.535	21.791
12	0.022	0.00066	8.353	21.213	0.122	0.00066	7.594	21.549
15	0.029	0.0012	8.409	21.105	0.117	0.0071	7.567	21.763
18	0.038	0.0016	8.486	21.024	0.133	0.0012	7.635	21.707
21	0.049	0.00093	8.539	20.875	0.146	0.00079	7.693	21.589
24	0.057	0.00072	8.573	20.742	0.154	0.0011	7.613	21.404
27	0.064	0.00051	8.597	20.633	0.167	0.00091	7.778	21.321
30	0.071	0.00098	8.637	20.423	0.179	0.0018	7.869	21.219

4.6.4 Microstructural analysis of corrosion

FESEM micrographs of both coated samples after 30 days immersion in crude oil and seawater are shown in Figures 4.43 and 4.44. According to Figures 4.43(a), (b) and 4.44(a), (b) when samples were exposed to crude oil, the rate of corrosion on their surface was less than in NaCl electrolyte (seawater). Figures 4.44(c), (d) signify that the amount of pitting and crevice corrosion in the HVOF samples is less than plasma-coated samples (Figure 4.43 (c), (d)), because there are fewer holes created on the top surface of HVOF-coated samples than plasma samples. There is generally not a big

difference between the corroded and un-corroded samples. It is proven that the coating protects the substrate from corrosion. Therefore, the chemical composition of the coating has anti-corrosion properties in this condition.

According to the FESEMs of the coated samples, the corrosion rate in 3.5% NaCl solution is significantly higher than in crude oil. Thus, it is important to know whether these samples can be corroded by the electrolyte solution (3.5% NaCl). The X-ray diffraction (XRD) analysis for the plasma and HVOF-coated samples in NaCl electrolyte after 30 days is presented in Figures 4.45(a) and (b) respectively. It is shown that the deposited layer oxidized to chromium trioxide (CrO_3) with both coating methods.

In plasma method coating, there is also Chromium (VI) oxide peroxide (CrO_5). The oxide layer with the HVOF method is generally less than with plasma method, because the dense coating and higher amount of carbonate chromium in HVOF protects the substrate from the inward permeation of oxygen. Regarding the XRD results, no type of iron oxide was detected with either coating method. Thus, it can be concluded that the coatings prevent the corrosive electrolyte from penetrating the substrate, and consequently protect the substrate from the corrosive environment.

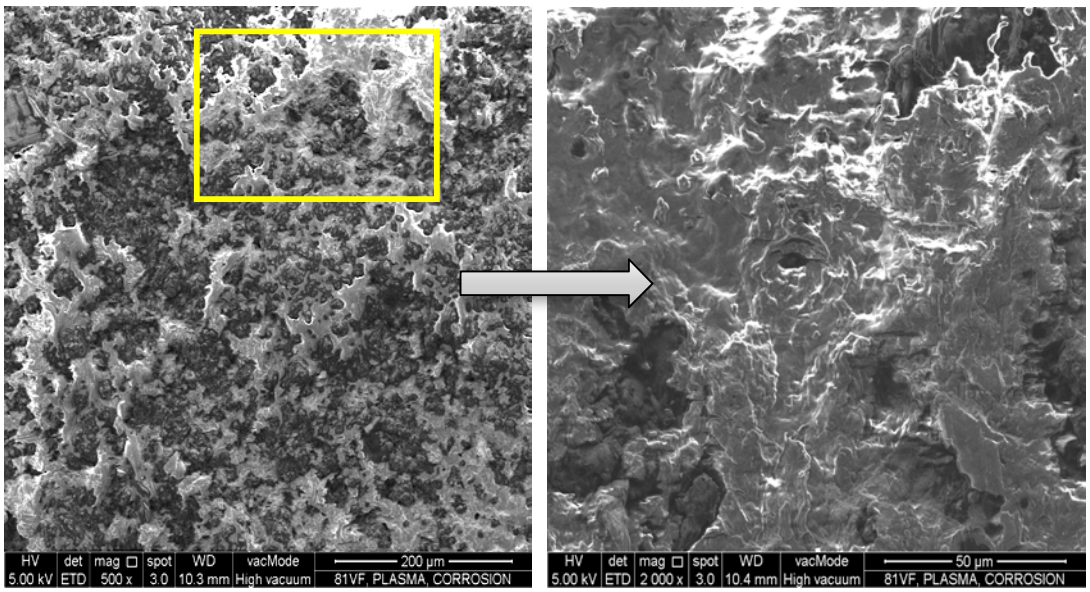

(a) FESEM-500X (b) FESEM-2000X

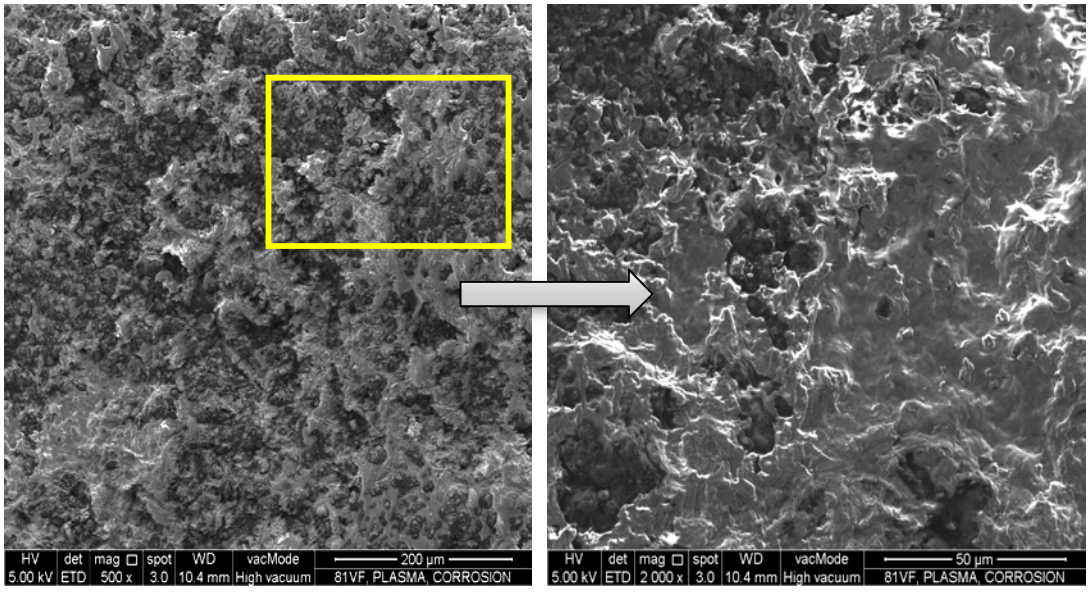

(c) FESEM-500X (d) FESEM-2000X

Figure 4.43 FESEM micrographsofCr_3C_2-25NiCr plasma-coated sample surfaces after 30 days: (a), (b) in crude oil;(c), (d) in seawater

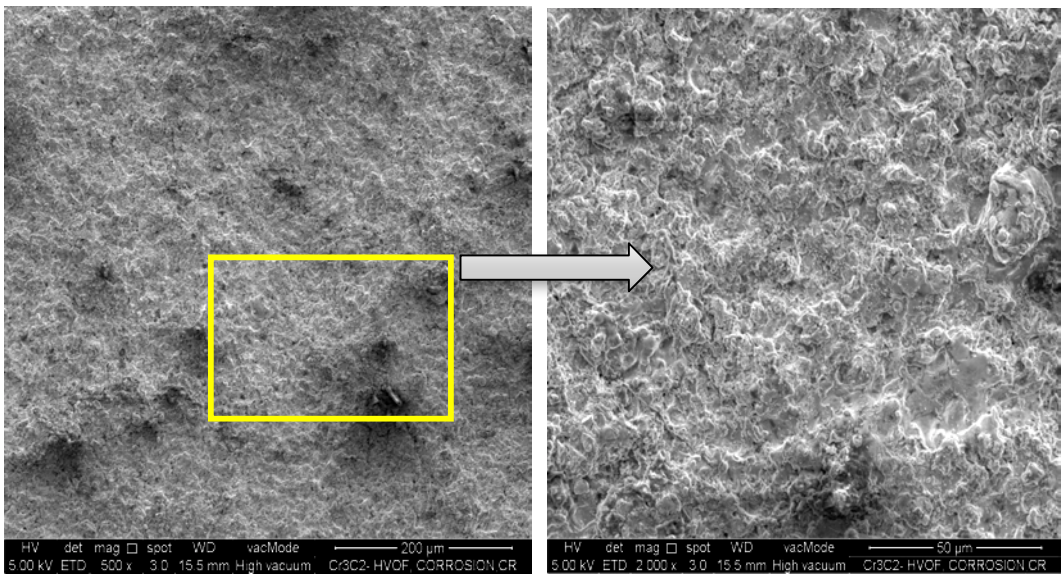

(a) FESEM-500X (b) FESEM-2000X

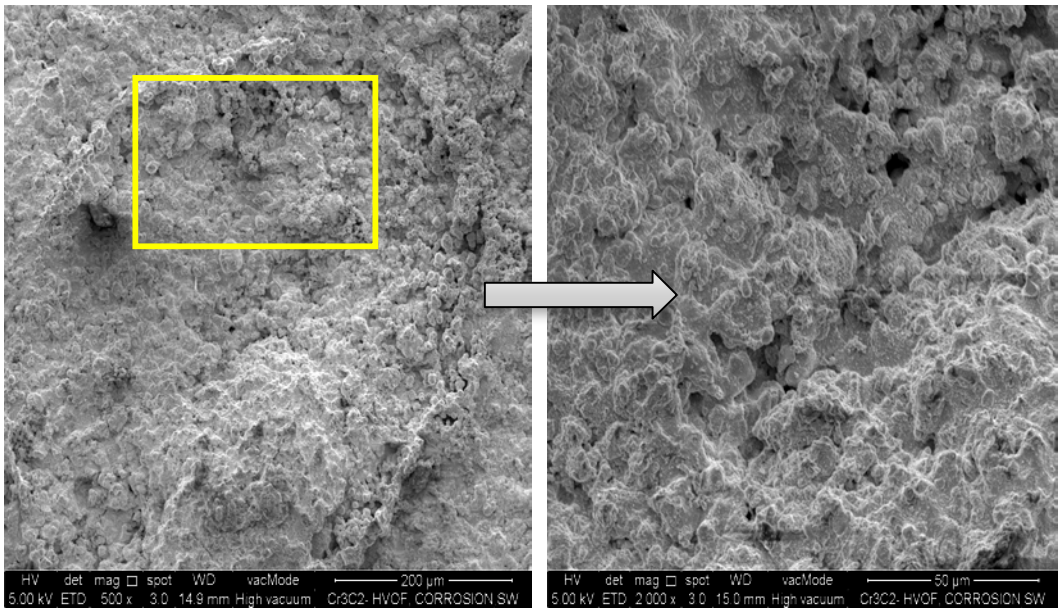

(c) FESEM-500X (d) FESEM-2000X

Figure 4.44 FESEM micrographsofCr_3C_2-25NiCr HVOF-coated sample surfaces after 30 days: (a), (b) in crude oil;(c), (d) in seawater

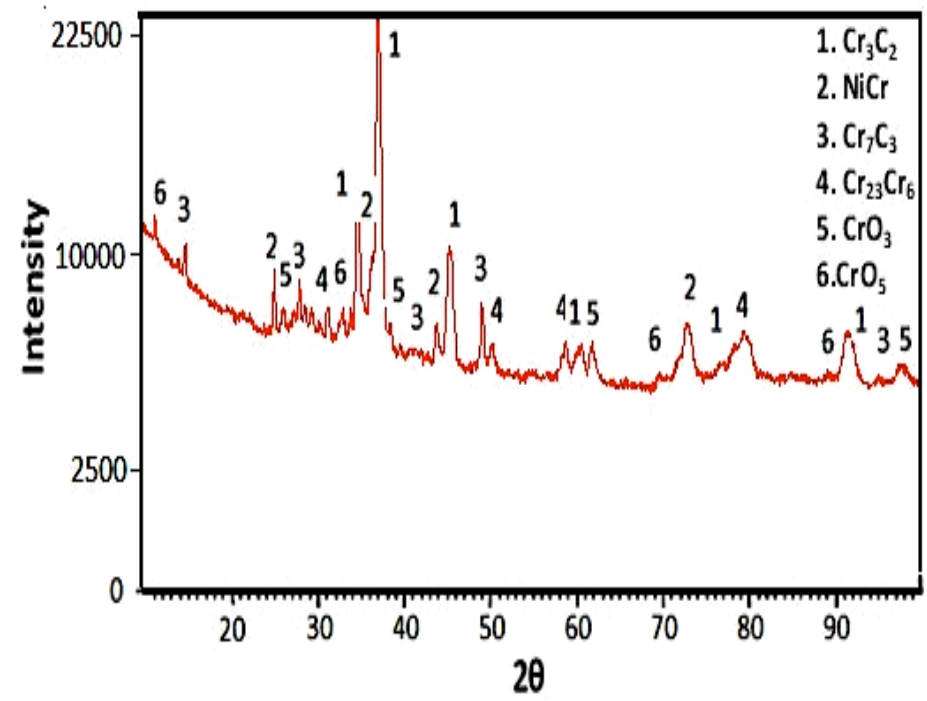

(a)

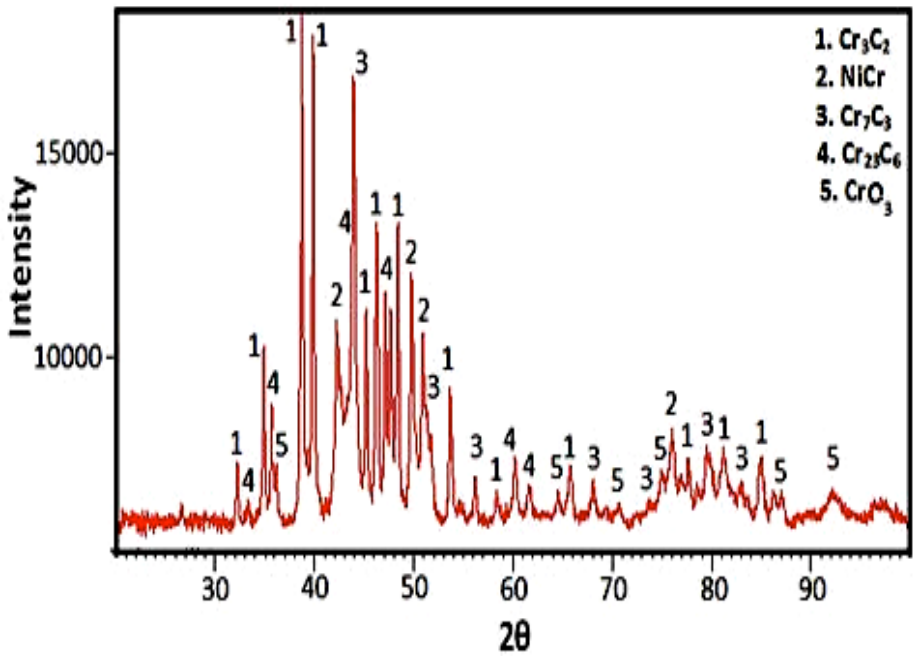

(b)

Figure 4.45 XRD results of Cr_3C_2-25NiCr coated samples in 3.5%NaCl solution after 30 days with: (a) plasma, (b) HVOF

The chemical composition of the layer deposited by HVOF and plasma methods on the surface of carbon steel can significantly change the properties of carbon steel in terms of corrosion and tribological performance. The HVOF-coated samples had higher corrosion resistance than plasma-coated samples during testing for 30 days.

Also, both polarization and EIS results confirm the superior corrosion protection properties of HVOF coating over plasma coating. In addition, the tribological properties of HVOF-coated samples under different loads applied show more durability and the weight loss rate of this sample was very limited. However, there is a small difference between the wear rate of plasma and HVOF-coated samples.

4.7 Analysis of substrate coated with Alumina-titania (Al_2O_3-13%TiO_2) powder

4.7.1 Microstructural analysis

As seen in Figure 4.46, the micrographs shows coating that is uniform, homogeneous and free from surface cracks. Applying a homogenous coating without segregation is critical for improving the wear resistance of Al_2O_3-TiO_2 coatings.

In Figures 4.46(a) and (b), with the plasma method most regions are fully melted and some are partially melted, while in Figures 4.46(c) and (d) with the HVOF method, large regions are partially melted because the powder temperature in this method was not high enough during spraying; however, some regions melted completely and the grain boundary became bigger.

The same as the plasma coating, HVOF coating displays a bimodal microstructure composed of fully melted and partially melted regions, which formed when TiO_2 had a lower melting point than Al_2O_3. There was selective melting because the temperature of the powder was not sufficiently high during spray coating (Yusoff et al., 2012). In the partially melted region, fine Al_2O_3 particles were dispersed in the TiO_2 matrix, (Mrdak, 2013; Aneziris et al., 2010; Berndt, 2001) and the fully melted region was mainly composed of Υ-Al_2O_3 (Ahn et al., 2006; McPherson, 1973).

Some pores are observed in Figure 4.46 as black spots in the micrographs, and the amount of porosity with the plasma method is less than the HVOF method. Moreover, the insufficient temperature with the HVOF method (Figures 4.46(c), (d))

caused the coated sample surface to be full of small ball shapes that stick together and are not melted inside. Nonetheless, both methods protect the substrate from the inward permeation of oxygen and the corrosive environment (Yusoff et al., 2012).

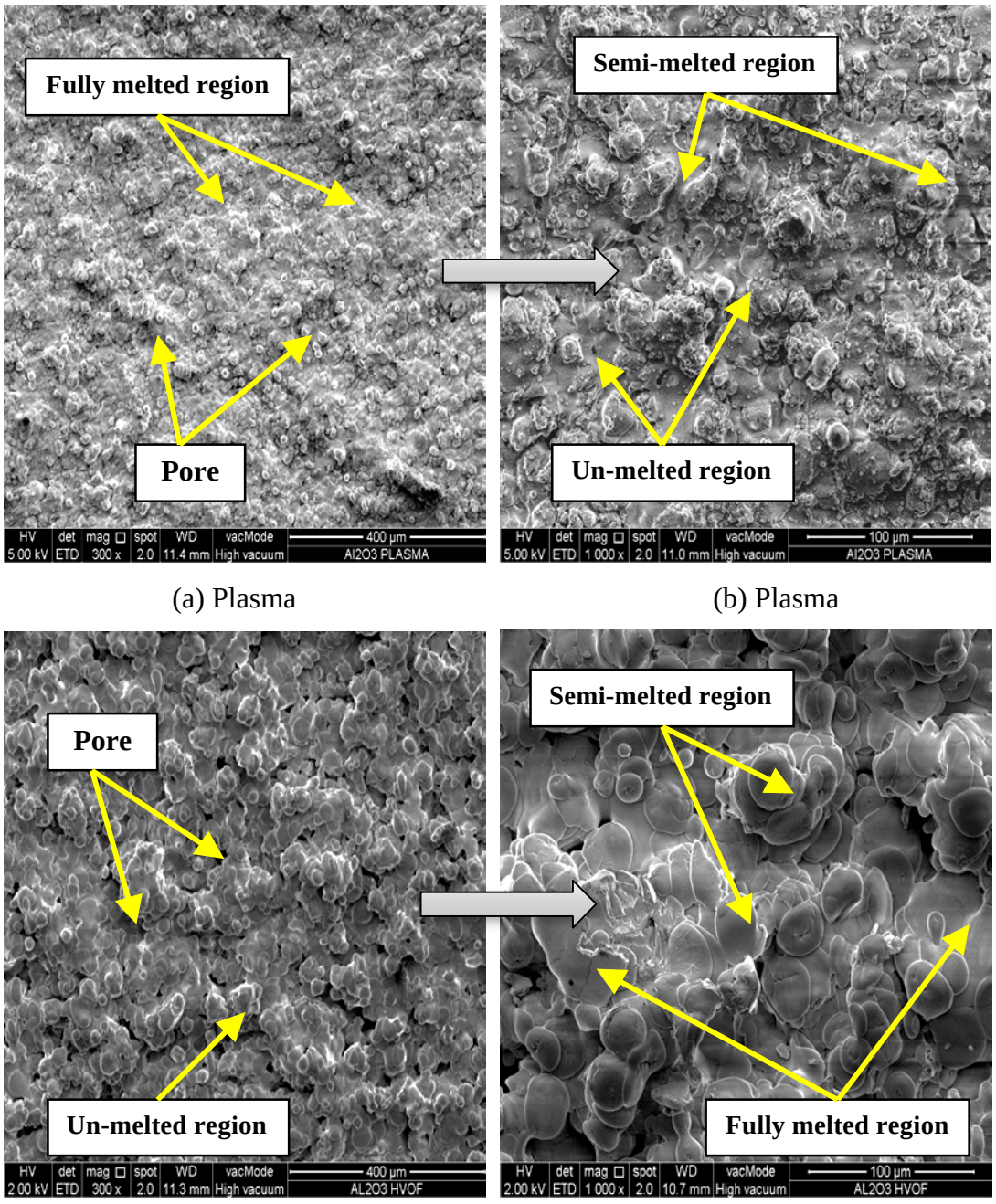

(a) Plasma (b) Plasma

(c) HVOF (d) HVOF

Figure 4.46 FESEM of Al_2O_3-13TiO_2 coated samples at different magnifications: (a), (c) 300X; (b), (d) 1000X

The X-ray diffraction and EDX of Al_2O_3-13wt% TiO_2 is presented in Figure 4.47. According Figures 4.47(a) and (b) for the plasma and HVOF methods,

respectively. The major phase formed in plasma coating (Figure 4.47(a)) was γ-Al_2O_3 with the presence of α-Al_2O_3 and rutile-TiO_2 as minor phases. As reported by McPherson (1973), γ-Al_2O_3 is homogeneously nucleated because the critical free energy for nucleation from liquid is less than that of α-Al_2O_3.

The subsequent full melting led to fewer pores; a reduced volume fraction of partially melted regions formed inside the coatings, and a reduced amount of α-Al_2O_3phases and increased γ-Al_2O_3phases were produced (Ahn, Hwang, Song, Lee, & Kim, 2006; Goberman, Sohn, Shaw, Jordan, & Gell, 2002b). The temperature during plasma coating was above 610°C so the small peak belongs to rutile-TiO_2 (Dejang et al., 2011). It is known that the performance of titanium dioxide is highly dependent on the material's phase.

With the HVOF method (Figure 4.47(b)) the intensity of α-Al_2O_3 increased, and the γ-Al_2O_3 peak intensity decreased.

Generally, when comparing the X-ray diffraction patterns of plasma coatings with HVOF coatings, the α-Al_2O_3peak intensity decreases and the γ-Al_2O_3peak intensity increases in the plasma coating, although both coatings have the same phase types. This is because the plasma method can produce a high temperature for the powder to fully melt and thus produce a denser coating than with HVOF spray. Thus, the plasma spray method can cause melting more readily during spray coating than HVOF, with lower volume fractions of pores and α-Al_2O_3 than with HVOF coating.

Furthermore, the EDX of the Al_2O_3-13TiO_2 composite for plasma and HVOF methods in Figure 4.47 (c) and Figure 4.47 (d) shows the existence of oxygen, aluminum and titanium. The EDX results confirm that the highest peak belongs to the

oxygen and the percentage of aluminum is higher than titanium. The weight percentage of each element is provided in Figure 4.47(c) and Figure 4.47 (d) (inset).

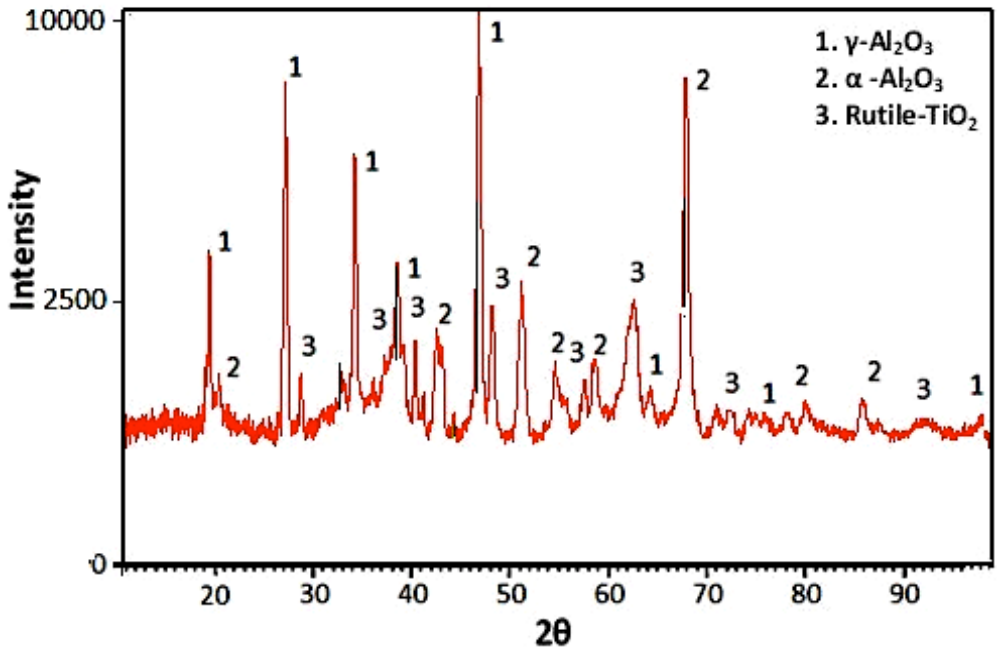

(a)

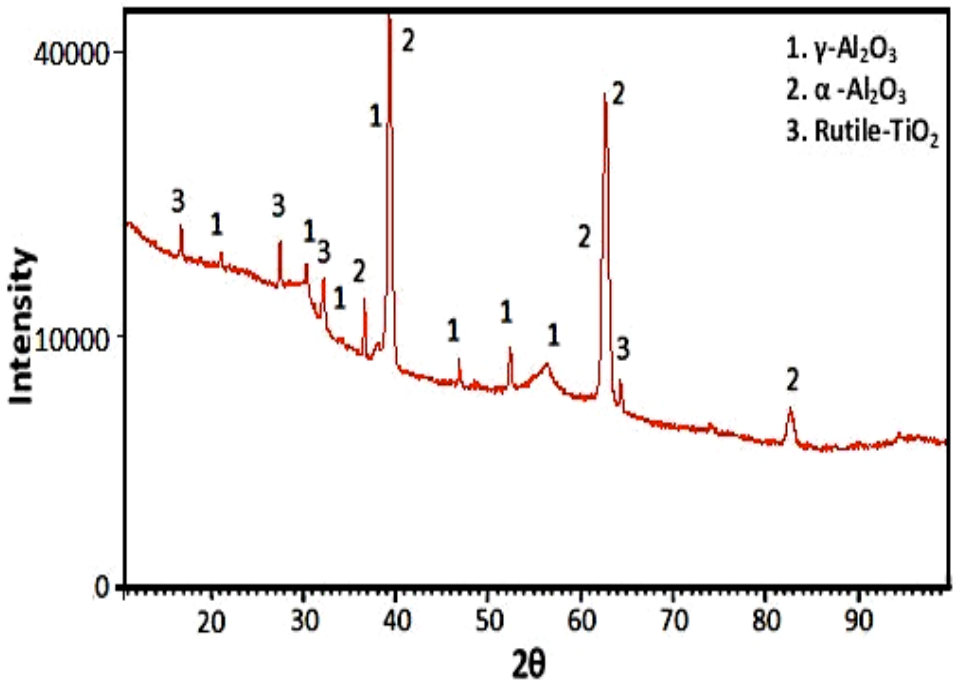

(b)

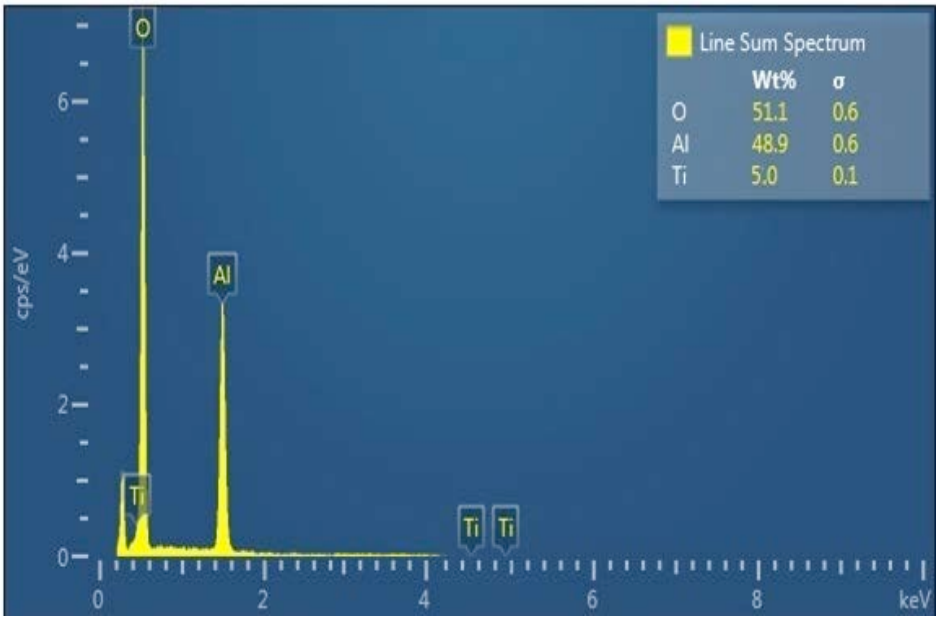

(c)

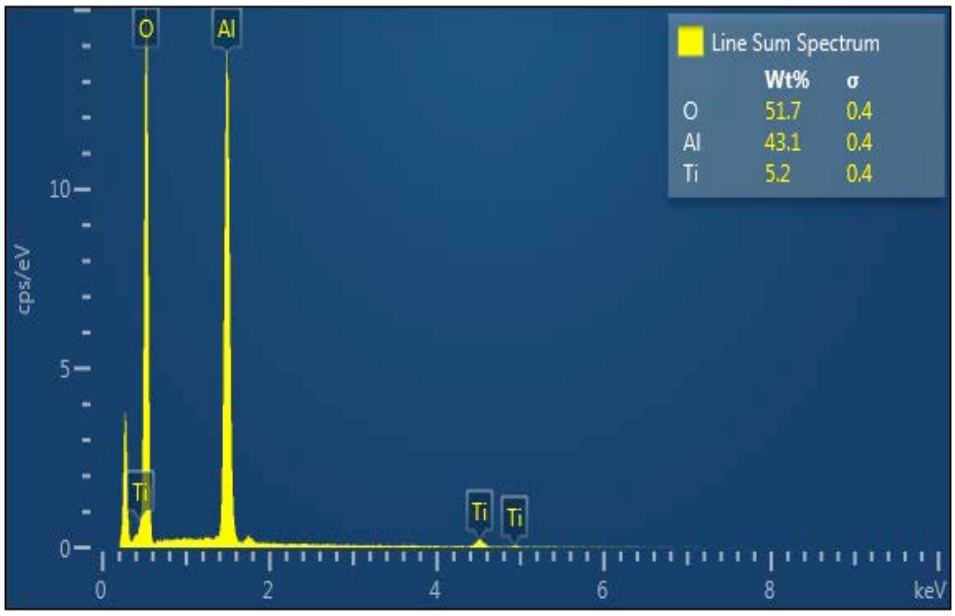

(d)

Figure 4.47 X-ray diffraction patterns of Al_2O_3-13TiO_2 samples coated by (a) plasma, and (b) HVOF; and EDX of (c) plasma and (d) HVOF coated samples

4.7.2 Wear analysis

The roughness of plasma and HVOF coatings is 3.710 and 3.732 µm respectively. As reported by Yussef et al. (2012), when applying 13wt% TiO_2 powder

on a micron scale without a bonding layer by plasma spraying, the roughness is R_a=3.70. Also, increasing the amount of TiO_2 from 3% to 13% causes the friction coefficient to diminish, because at smaller roughness, the coating life is longer (Koji Kato, 2000). In addition, having lower as-sprayed surface roughness is very important for technological applications because it reduces the number of post-deposition mechanical treatments necessary (S. H. Yao, Su, & Kao, 2011). Overall, wear increases as a result of the rapidly increasing friction rate. For this reason, soft coatings have a much reduced friction coefficient (K Kato, 2006).

The hardness of pure Al_2O_3 applied by plasma spraying technique has a microhardness of around 1000-1100 HV (Yılmaz, Kurt, Demir, & Tatlı, 2007). With HVOF, coating microhardness decreases to 880-950 HV (Singh et al., 2011). This decrease could be attributed to a combined effect of an increase in porosity, limited temperature range for the HVOF method and the presence of a lower hardness TiO_2 phase with the absence of harder α- Al_2O_3. Therefore, when using the HVOF method, the hardness decreases to 880 HV. However, this amount of TiO_2 significantly reduces the melting temperature of the oxide rather than pure Al_2O_3 (Normand et al., 2000). Also, microhardness tends to decrease by increasing the percentage of TiO_2in the chemical composition of coating, which is related to the softer nature of the TiO_2material (TiO_2: 50~55vs. Al_2O_3: 60~70, HRC) (Sánchez Vilches et al., 2011). This result is consistent with other similar studies (Singh et al., 2011; Yılmaz et al., 2007).

Finally, the wear mechanism should be investigated to evaluate the wear properties of Al_2O_3-TiO_2 coating. Studies by Wang et al., (2000) indicated that coating wear resistance is not only related to its hardness level, but also toughness, microstructure and defects(You Wang et al., 2000). They suggested that the dominant cause of wear for coatings sprayed with conventional powder is grain dislodgment, which is due to grain boundary fracture combined with lateral crack chipping. Ahn et al.

(2006) stated that serious delamination under wear condition occurs along TiO_2-rich zones in conventional coating.

In this study, the regions of wear and coarse worn debris of coated samples by plasma and HVOF under maximum load (20N) of wear testing are investigated by FESEM (Figure 4.48). In Figure 5.48, after applying maximum load for both methods of coating, horizontal micro tracks were created on the surface and the abrasion was very slight. However, according to Figures 4.48(a) and (b), the rate of wear for plasma coating is lower than HVOF coating (Figures 5.48(c) and (d)). Wang et al. (2000) reported a very thin, plastically deformed layer on the coating surface, which has a weak bond to the base coating and is liable to removal by friction. The formation and removal of the thin plastic layer behaves as a strain fatigue mechanism of wear.

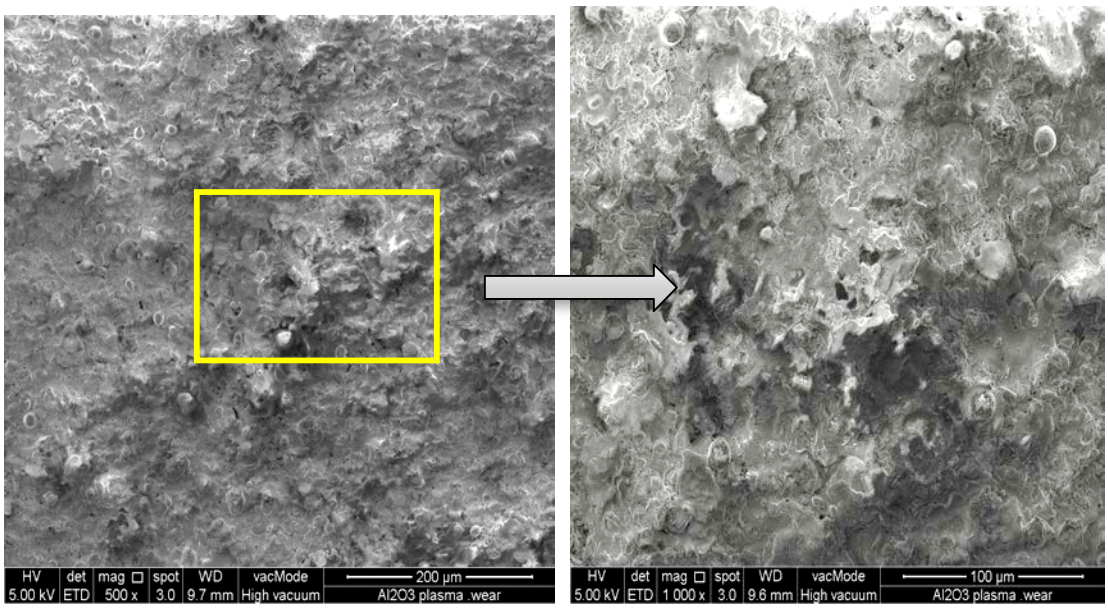

(a) Plasma (b) Plasma

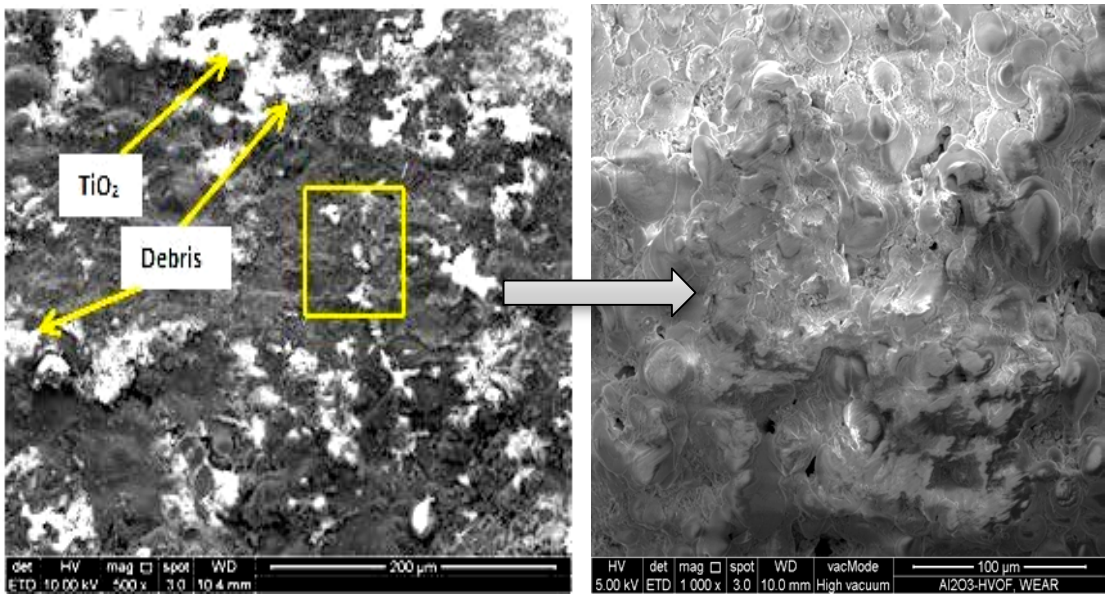

(c) HVOF (d) HVOF

Figure 4.48 FESEM of wear debris of Al_2O_3-13TiO_2 coated samples at maximum load (20 N) for: (a), (b) plasma; (c), (d) HVOF

Table 4.11 and Figure 4.49 illustrate the average wear and weight loss rate for plasma and HVOF-coated samples. As per Figure 4.49 (a), when different loads were applied on the plasma-coated and HVOF-coated samples, the amount of wears changed from 16 to 31 and 18 to 37 µm, respectively. According to Figure 4.49(b) of each sample after a 60 min cycle under loads of 5, 10, 15 and 20 N shows that the weight

loss in the case of plasma-coated samples is less than HVOF-coated samples. The wear rate result also confirms this trend. The average of wear and weight loss for plasma-coated samples is less than the HVOF method, but there is no big difference between these methods.

Table 4.11 Weight loss and wear rate of Al_2O_3-13%TiO_2 coated samples for different loads

Loads (N)	**Rate of weight loss**		**Average of wear (µm)**	
	Plasma-coated Sample	HVOF-Coated Sample	Plasma - coated Sample	HVOF-Coated Sample
5	0.0052	0.0058	16±2	18±2
10	0.006	0.0075	22±3	24±1
15	0.0114	0.0137	27±2	33±2
20	0.0121	0.0151	31±1	37±3

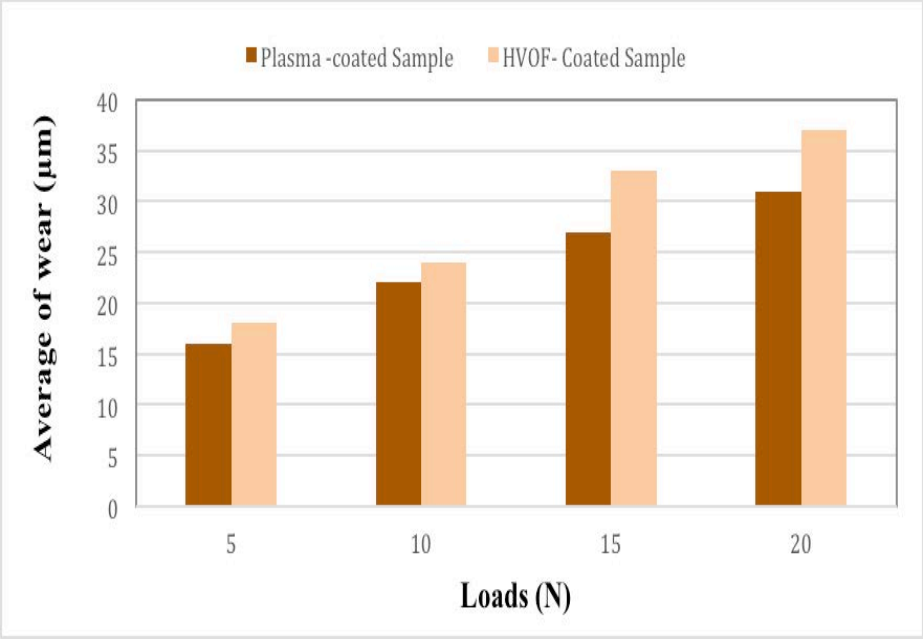

(a)

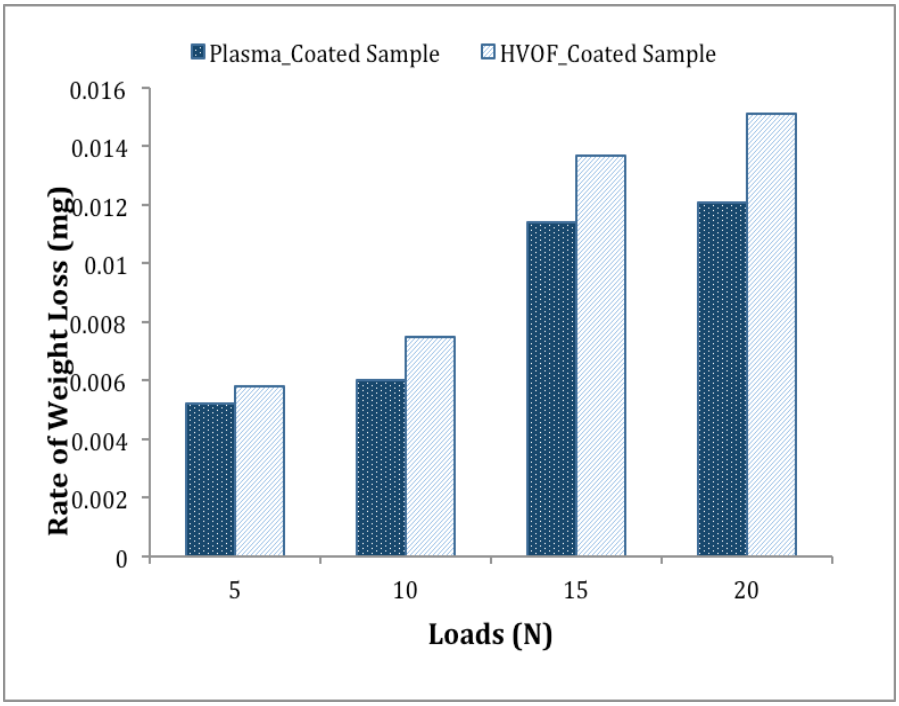

(b)

Figure 4.49 Behavior of Al_2O_3-13%TiO_2 samples coated by plasma and HVOF for different loads: (a) wear; and (b) weight loss wear

4.7.3. Electrochemical corrosion analysis

According to Figure 4.50, the open circuit potential of both plasma and HVOF shows that after an initial drop in positive potentials, the OCP of both coated samples moved towards noble regions towards the end of the 30 days, and the OCP of plasma was more positive compared to HVOF. While the I_{corr} displayed fluctuations between low and high values for both samples, the charge transfer resistances R_{ct} from Electrochemical Impedance Spectroscopy (EIS) for both samples were consistent with the OCP values from polarization measurements. The higher R_{ct} from EIS data is due to higher resistance against charge transfer across the electrode-electrolyte interface, which is consistent with more positive values in the OCP results presented in Table 4.12.

From the computer simulations for plasma- and HVOF-coated samples on day 3, the R_s (CR) circuit diagram accurately matches the experimental data. Only one semicircle is observed in the Nyquist plot (Figures 4.51(a) and 4.52(a)). The Bode phase diagrams of plasma-coated samples (Figures 4.51(b) and 4.52(b)) show one-phase maxima. However, the semicircle in the HVOF-coated sample is smaller than the plasma-coated sample. The R_{ct} of plasma and HVOF samples from day 3 to day 30 are shown in Table 4.10. The plasma-coated samples with the equivalent circuit R_s (Q_1R_1) accurately fit the experimental data on day 30, because only one semicircle is observed in the Nyquist and Bode plots (Figures 4.51(c), (d)).

The simulation results on day 30 for HVOF-coated samples show that the equivalent circuit of R_s (Q_1 [R_1 (Q_2R_2)]) accurately fits the experimental data of HVOF coating on Al_2O_3-13TiO_2 (Figures 4.52(c), (d)). The resistance between RE and WE is the solution resistance R_s, which is in series with two time constants (parallel arrangement of R and Q) that are also in series. It can be seen that the Nyquist plot

(Figure 4.52 (c)) is a "depressed semi-circle" with the center of the circle below the X-axis. The Q_1 is in parallel with R_1. R_1 is the polarization resistance of the area at the substrate/coating interface where corrosion occurs. Also, Q_2 is in parallel with a charge transfer resistor R_2, corresponding to the pores in the coated layer surface.

According to Table 4.12, the current density increased from 8.232 x 10^{-8} on day 3 to 8.653 x 10^{-8}A on day 12, but in the middle of the period it suddenly decreased to 8.589 x 10^{-8} A. This phenomenon can be related to the oxide layer created on top of the coating layer that protected the surface from electrolyte penetration, which is why the corrosion resistivity increased. After that, the corrosion current slightly rose from 8.648x 10^{-8} on day 18 to 8.787x 10^{-8}A on day 30. However, with the HVOF method the corrosion current rose from 8.607 x 10^{-8} on day 3 to 8.934 x 10^{-8} A on day 18, after which the corrosion current declined to 8.934 x 10^{-8}A on day 21 and decreased smoothly until day 27. Finally, it rocketed to 8.998 x 10^{-8}A on day 30 from 8.909x 10^{-8} A.

The higher amount of corrosion current in HVOF-coated samples rather than plasma-coated samples is attributed to the porosity and fully un-melted and semi-melted regions with the HVOF method.

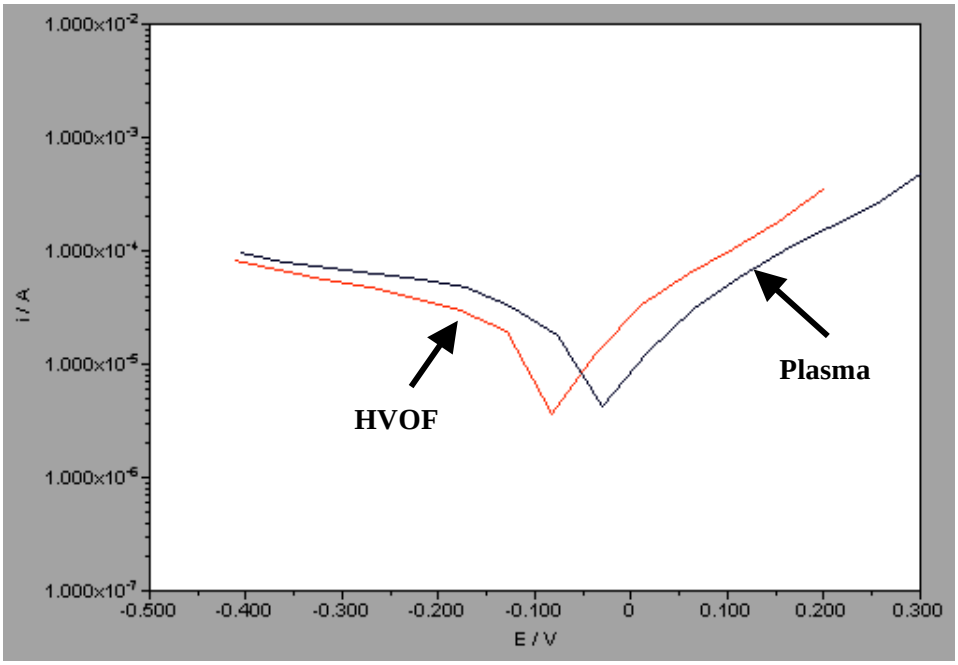

(a) 3rd day experiments

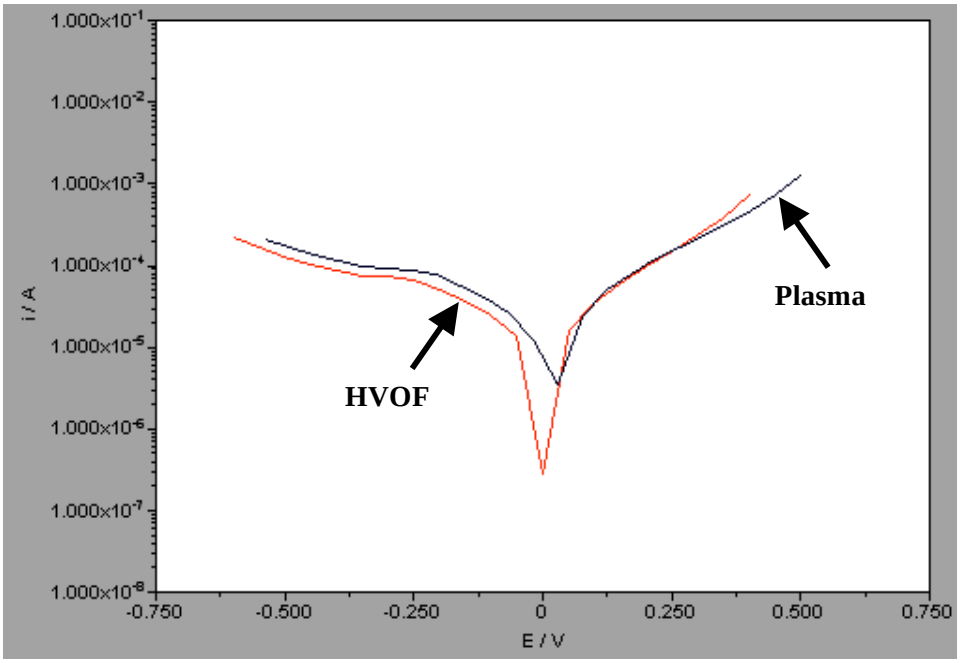

(b) 30th day experiments

Figure 4.50 Polarization curves (log I vs E) of Al_2O_3-13$TiO_2$with plasma and HVOF methods on (a) 3rd day and (b) 30th day of experiments

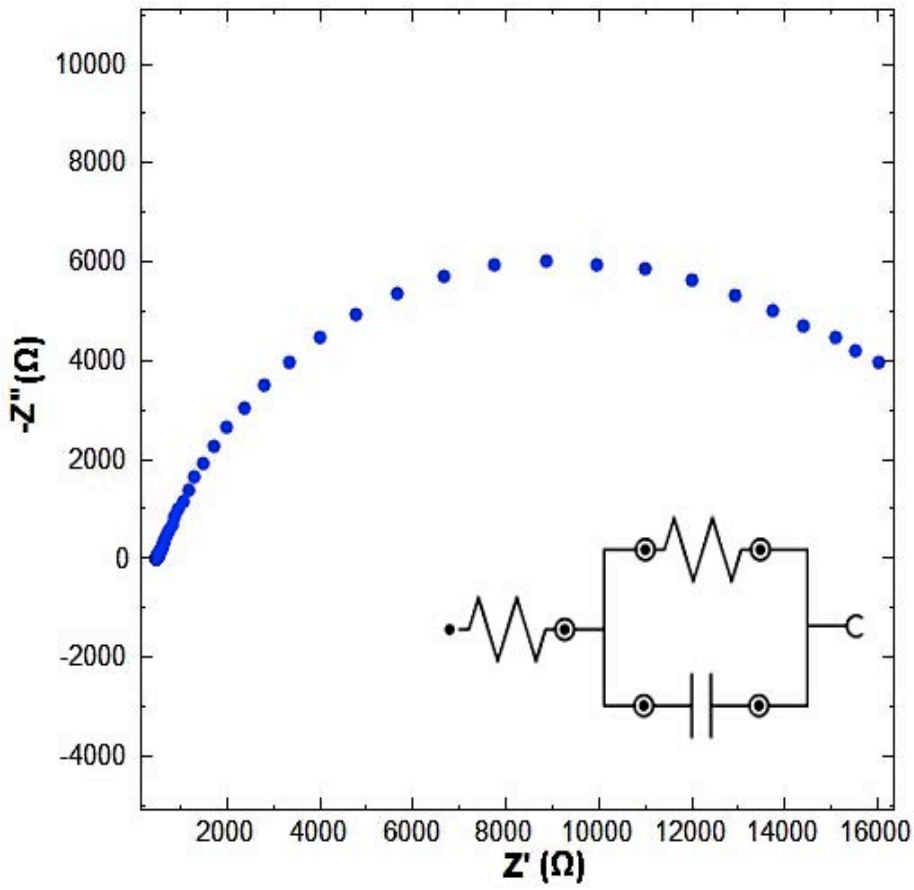

(a) Nyquist plot day 3

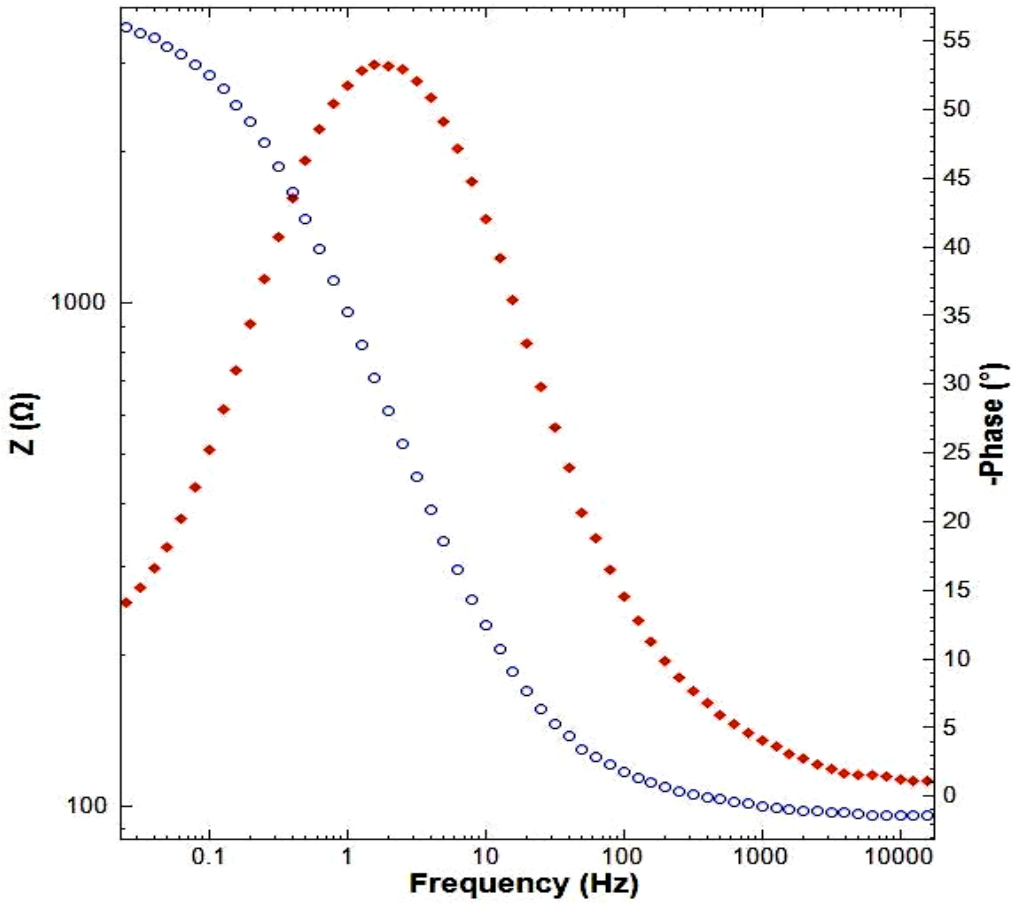

(b) Bode plot day 3

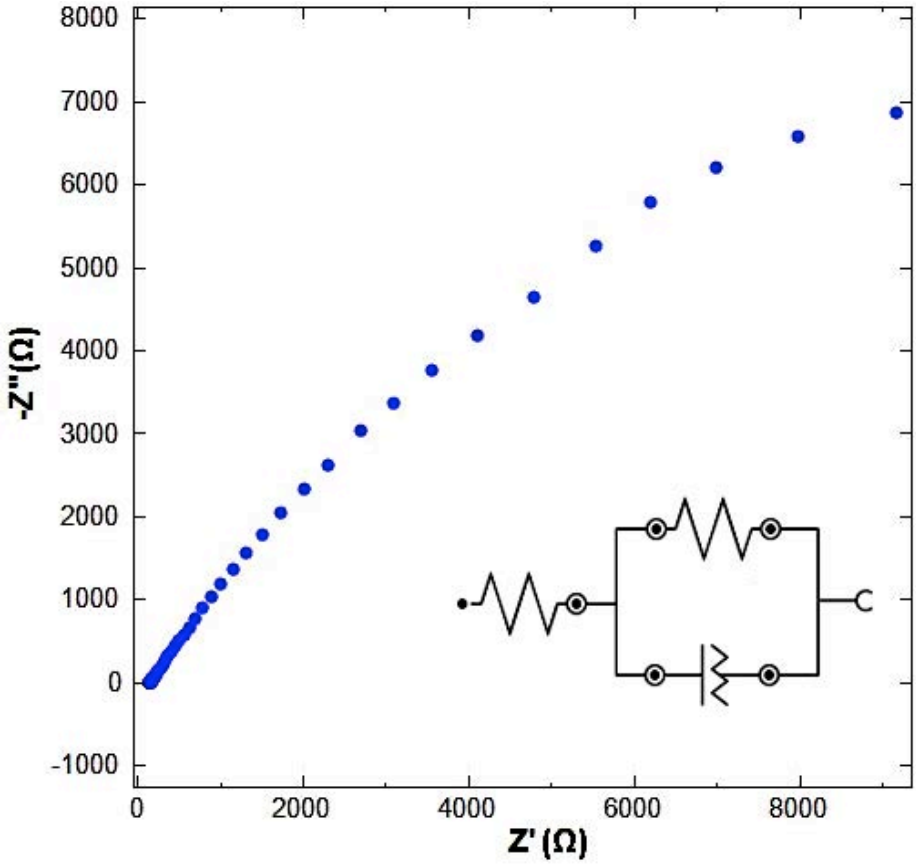

(c) Nyquist plot day 30

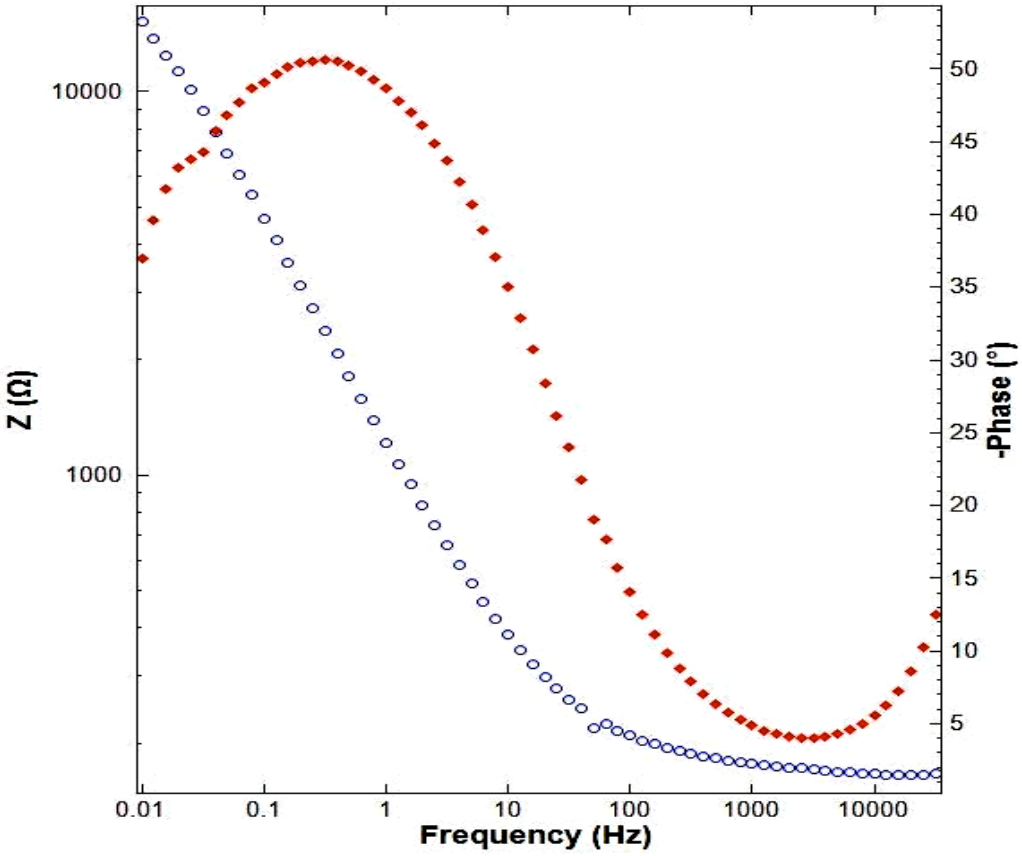

(d) Bode plot day 30

Figure 4.51 EIS of Al_2O_3-13TiO_2plasma-coated sample

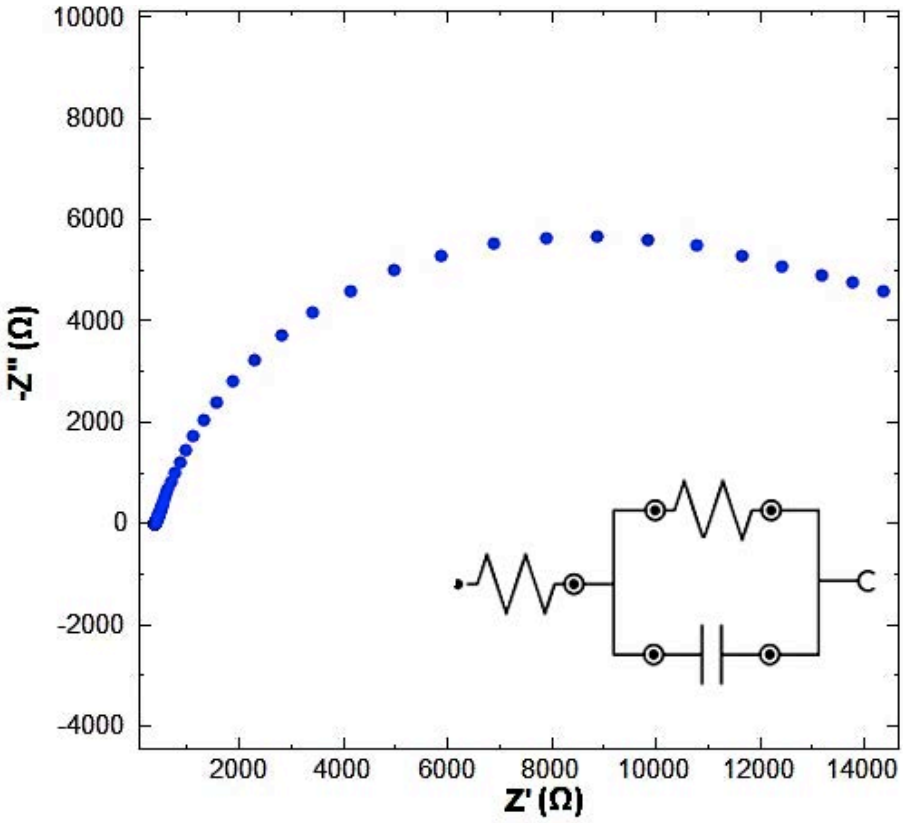

(a) Nyquist plot day 3

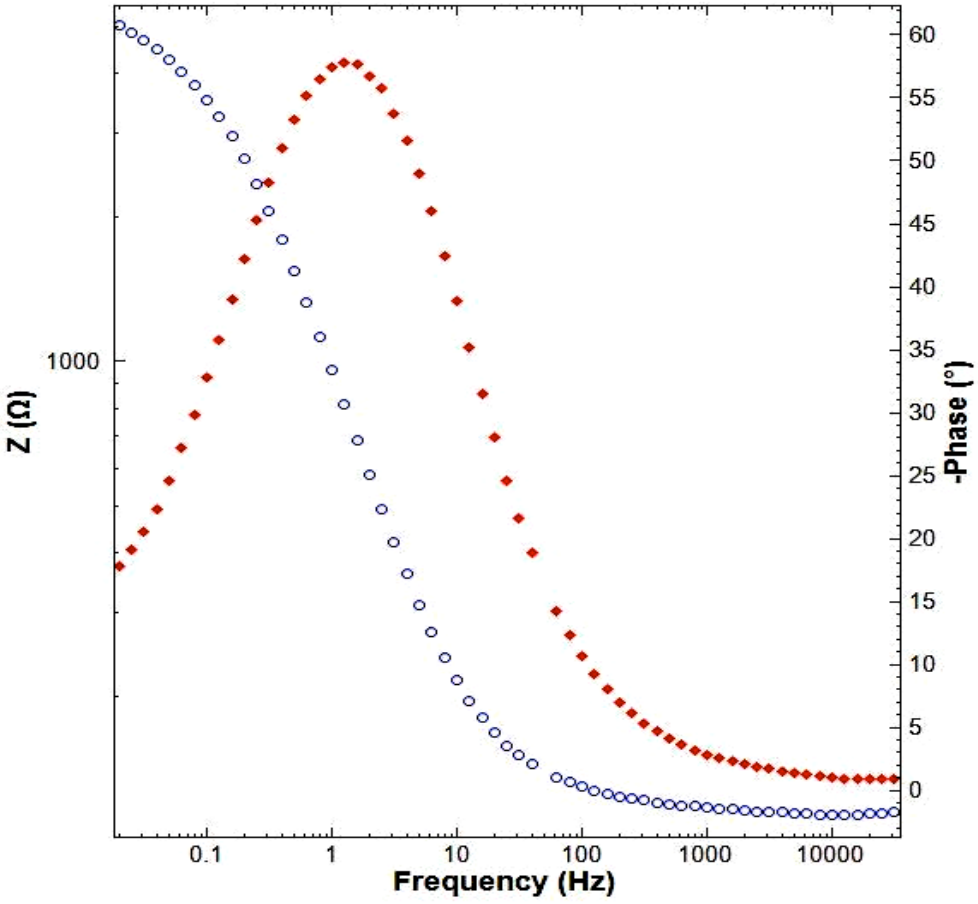

(b) Bode plot day 3

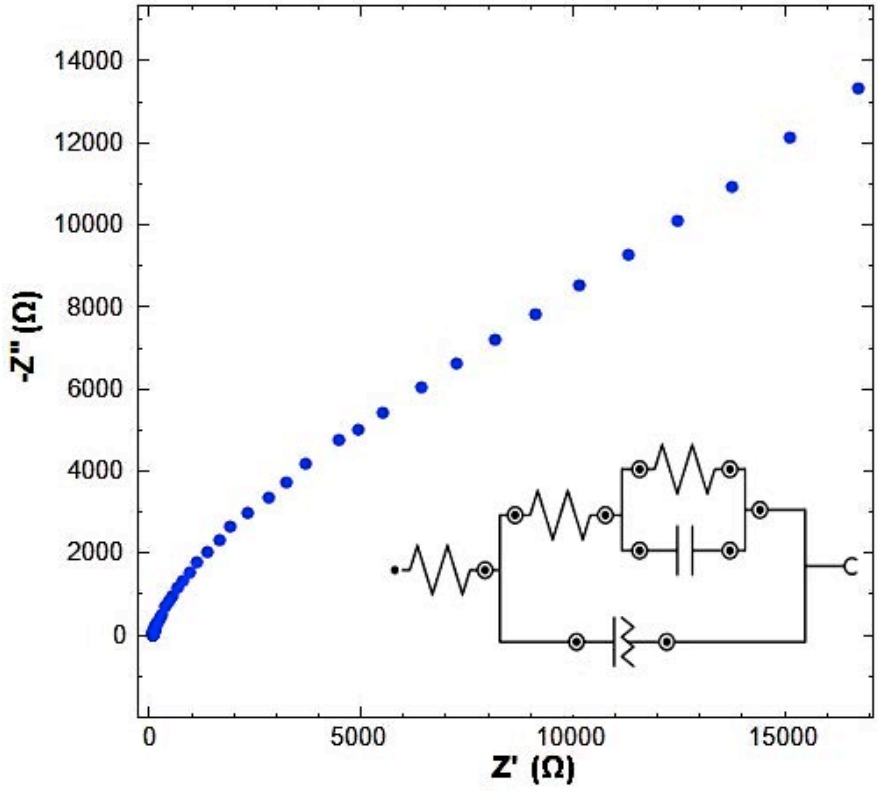

(c) Nyquist plot day 30

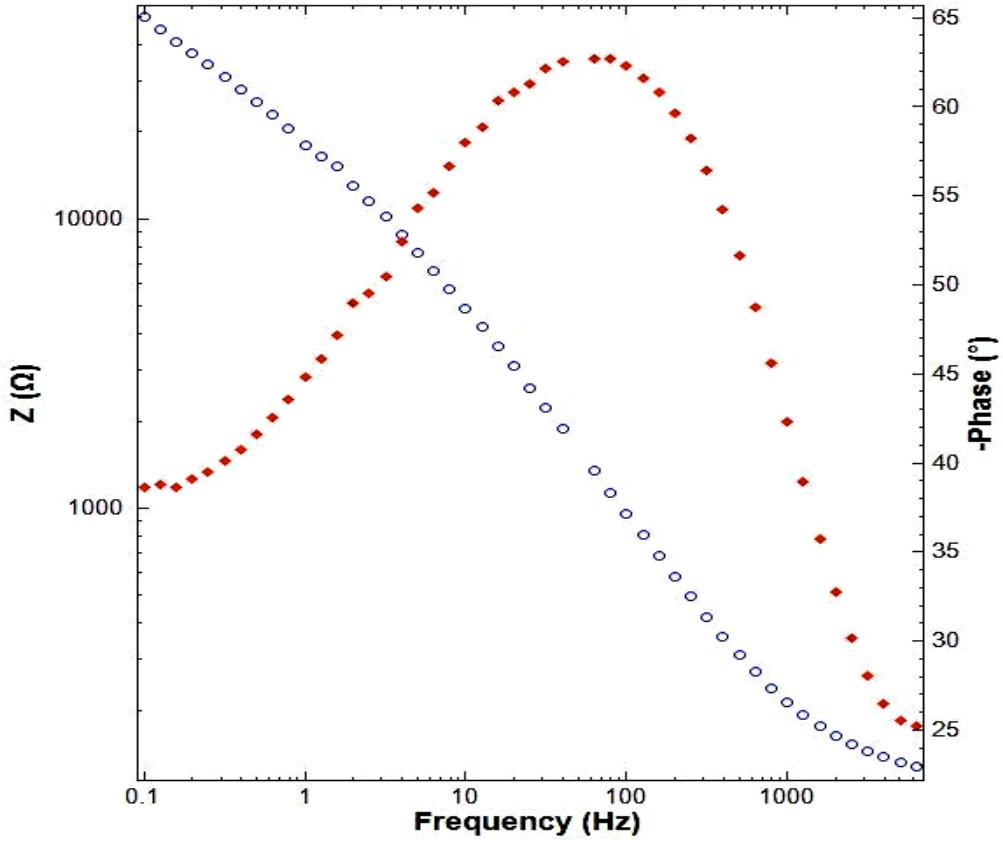

(d) Bode plot day 30

Figure 4.52 EIS of Al_2O_3-13TiO_2HVOF-coated sample

Table 4.12 OCP, I_{corr} and R_{CT}/kOhm of Al_2O_3-13TiO_2 plasma and HVOF-coated samples in 3.5%NaCl solution for 30 days

Day	Plasma-coated Sample				HVOF-coated Sample			
	OCP		I_{Corr} / A ($x 10^{-8}$)	R_{CT} / kOhm	OCP		I_{Corr} / A ($x 10^{-8}$)	R_{CT} / kOhm
	Mean	SD			Mean	SD		
3	-0.022	0.0005	8.232	18.672	-0.075	0.00073	8.607	18.003
6	-0.017	0.00062	8.322	18.421	-0.067	0.00056	8.686	17.939
9	-0.009	0.0005	8.442	18.231	-0.059	0.00076	8.695	17.841
12	-0.001	0.00086	8.653	18.273	-0.047	0.0013	8.737	17.732
15	0.007	0.00072	8.589	18.417	-0.038	0.0012	8.789	17.658
18	0.016	0.0016	8.648	18.121	-0.030	0.00067	8.948	17.523
21	0.024	0.00064	8.709	17.975	-0.022	0.00067	8.934	17.569
24	0.031	0.0011	8.733	17.712	-0.013	0.00095	8.923	17.404
27	0.038	0.00058	8.757	17.503	-0.007	0.00056	8.909	17.281
30	0.045	0.0015	8.787	17.293	0.000	0	8.998	17.183

4.7.4 Microstructural analysis of corrosion

The FESEM micrographs of the surfaces of plasma and HVOF-coated samples after 30 days immersion in crude oil and 3.5% NaCl electrolyte are shown in Figures 4.53 and 4.54 respectively.

As seen in Figures 4.53(a), (b) and 4.54(a), (b) the rate of corrosion in crude oil is less than in NaCl solution. Also, the amount of pitting corrosion with the HVOF method (Figures 4.54(c), (d)) is higher than with the plasma method (Figures 4.53(c),

(d)). Because of the temperature associated with HVOF is not high enough for adopted type of ceramics, not all powders reach melting point; thus, the amount of porosity in this coating is higher than in plasma, this causing the electrolyte to penetrate the coating. However, there is no huge difference between corroded and un-corroded samples. Previous studies demonstrated that the penetration of electrolyte through coating defects could strongly affect the electrochemical behavior of thermal spray coatings. The coating defects are mainly used by the electrolyte to reach the base carbon steel (Aneziris et al., 2010). In this case, the electrolyte does not penetrate the substrate and the XRD result confirms this, because there is no iron oxide visible in the XRD result (McPherson, 1973; Goberman et al., 2002; Aneziris et al., 2010).

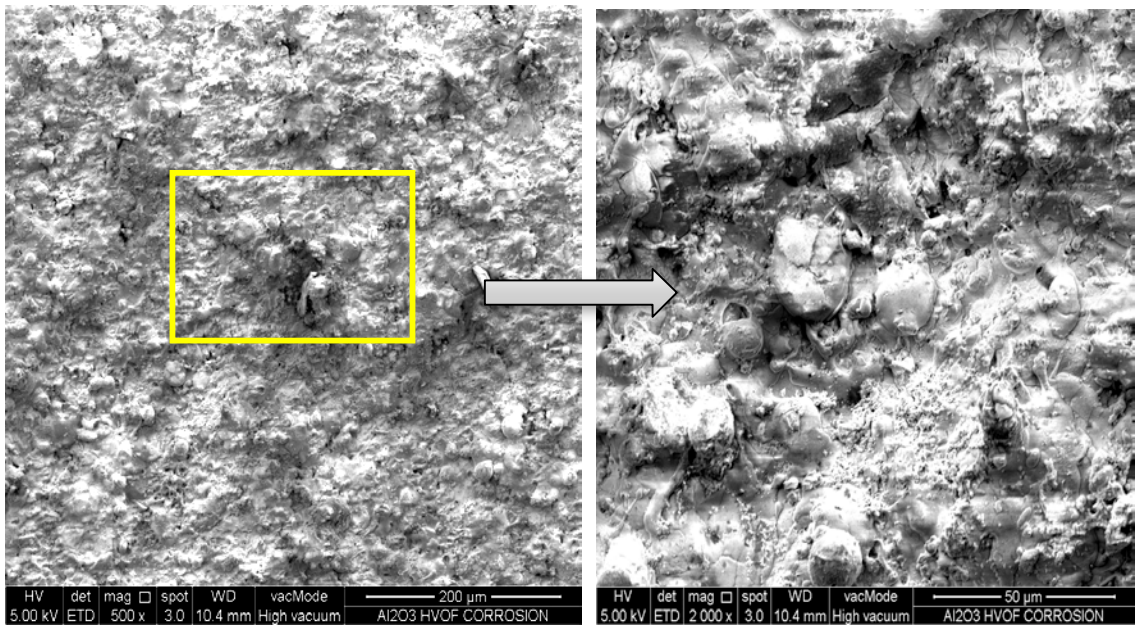

(a) (b)

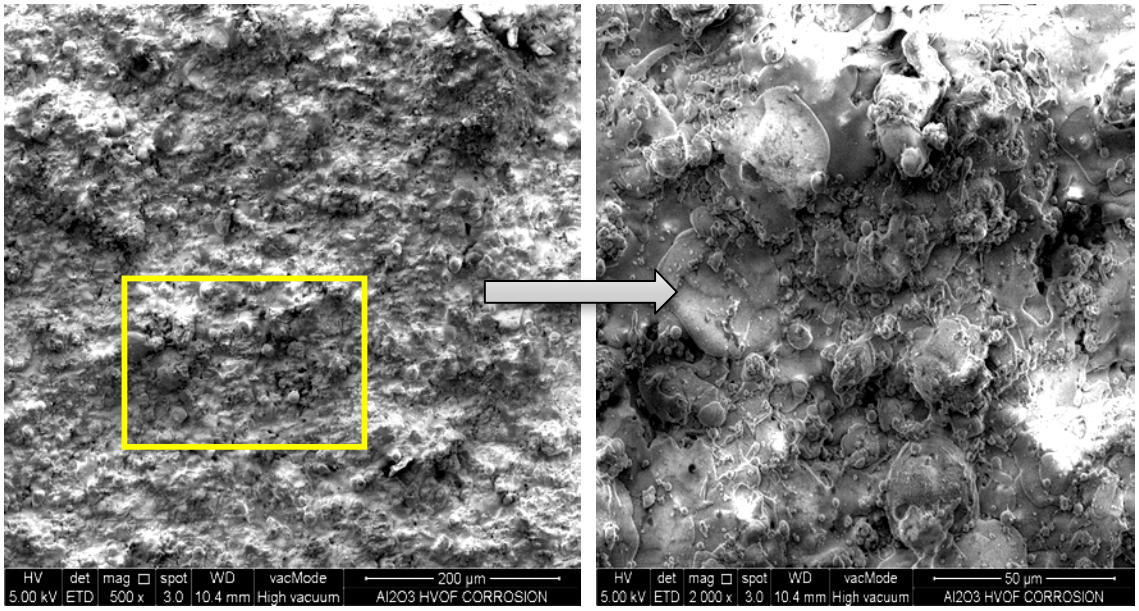

(c) (d)

Figure 4.53 FESEM micrographs of plasma-coated sample surfaces after 30 days: (a), (b) in crude oil;(c), (d) in seawater

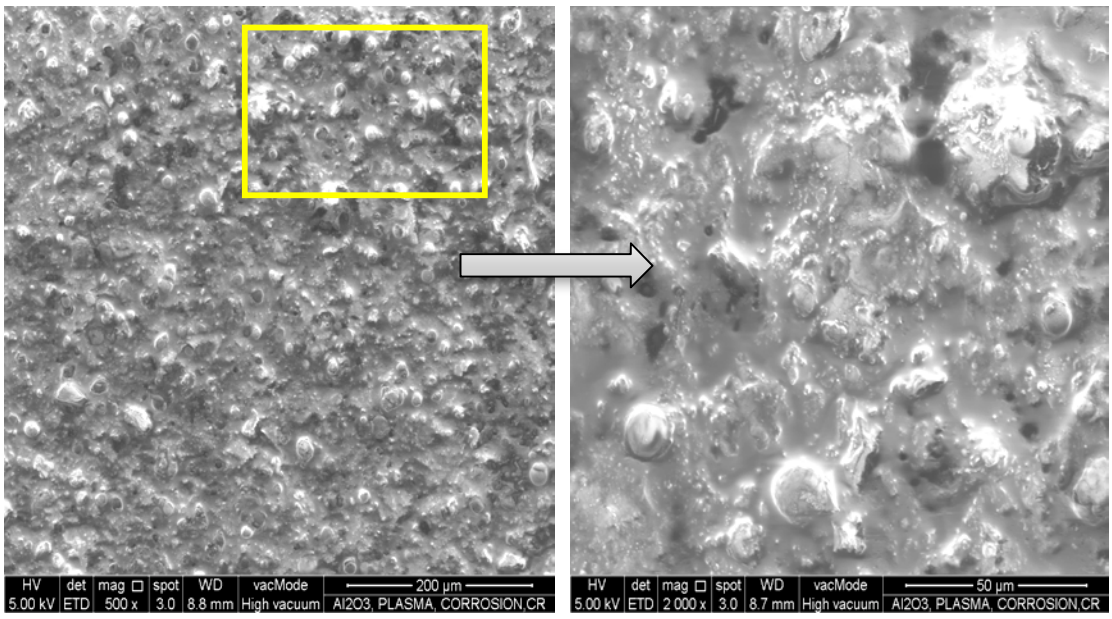

(a) (b)

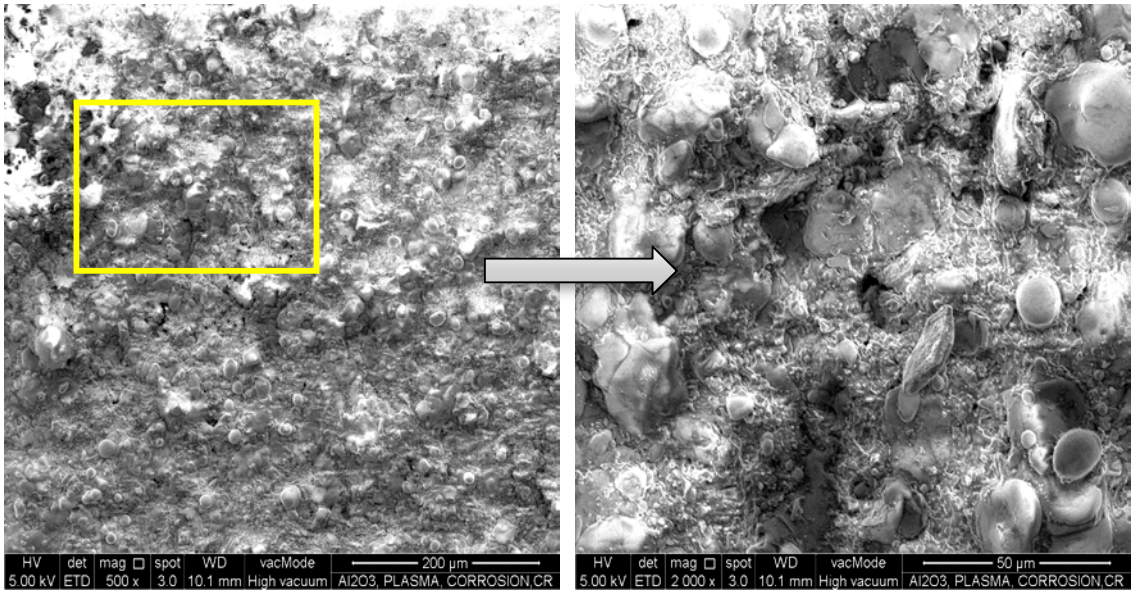

(c) (d)

Figure 4.54 FESEM micrographs of HVOF-coated sample surfaces after 30 days: (a), (b) in crude oil;(c), (d) in seawater

According to the FESEMs of the coated samples, the corrosion rate in 3.5% NaCl solution is significantly higher than in crude oil. So it is important to know if in these samples, the electrolyte solution (3.5% NaCl) can reach the substrate. The X-ray diffraction (XRD) analysis result (Figure 4.55) shows that the surface of both coating methods oxidized and produced $AlTiO_5$ on the coating surfaces. However, the oxidized

peaks for plasma coating are less than HVOF coating, because theγ-Al_2O_3phase in the plasma sample is bigger than the HVOF sample. This is a stable phase and does not need to react with more oxygen. Generally, both methods protect the substrate from the inward permeation of oxygen. According to the XRD results of both methods, there is not any type of iron oxide in the coated samples.

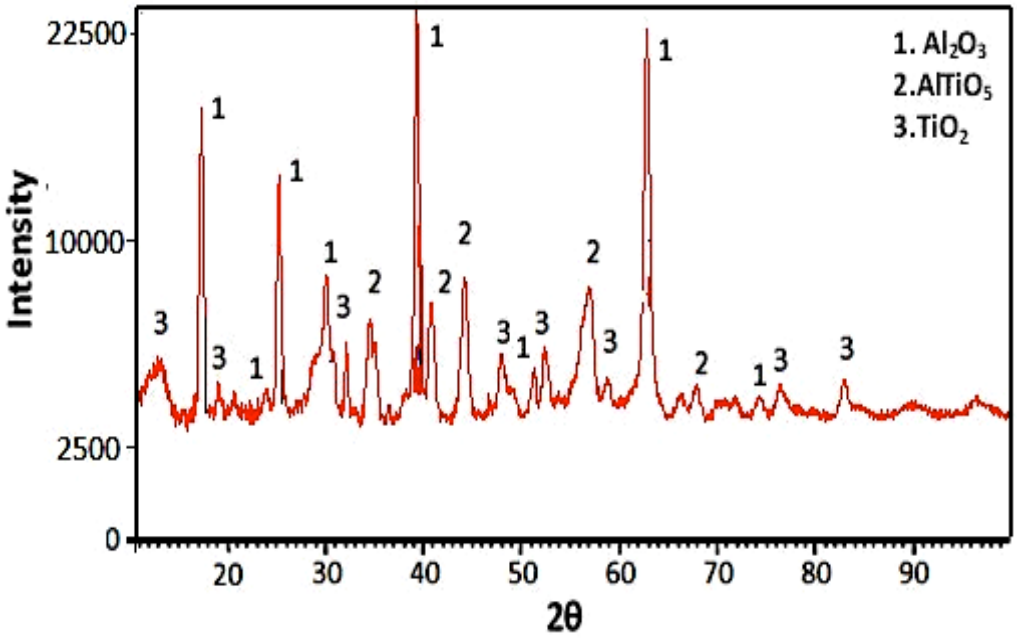

(a)

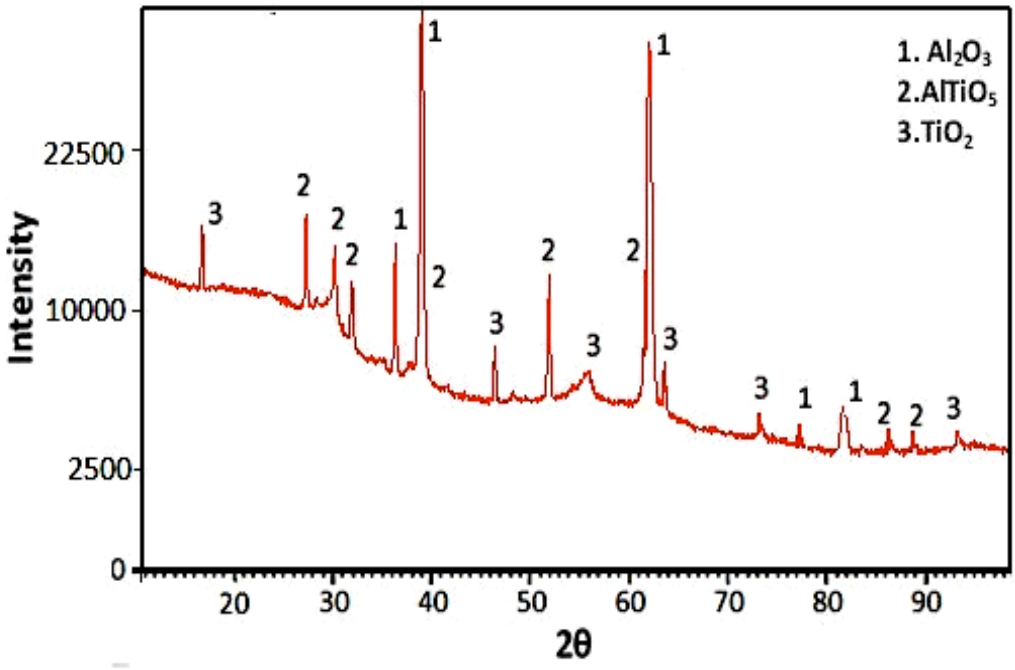

(b)

Figure 4.55 XRD results of Al_2O_3-13TiO_2 samples coated by (a) plasma, (b) HVOF, in 3.5%NaCl solution after 30 days

According to the wear and corrosion results, the Al_2O_3-13%TiO_2 chemical composite provided by the plasma coating has superior mechanical and chemical properties over the HVOF method. According to the XRD of the plasma-coated samples, 13wt% TiO_2 comprises fully and partially melted regions of γ-Al_2O_3. Also, the wear rate for plasma-coated samples under different loads is less than HVOF-coated samples. Finally, the plasma-coated samples have higher charge transfer resistance R_{ct} compared to the HVOF samples, due to the higher resistance of the Al_2O_3-13%TiO_2 with the plasma method against corrosion than with the HVOF method.

4.8 Comparisons of wear and corrosion behavior of selected samples

In this section, the behavior of mechanical and chemical properties of five different materials chosen from sections 4.3 to 4.7 are compared.

4.8.1 Comparison of wear rate

Figure 4.56 illustrates the wear rate for different types of chemical compositions under four different loads. It can be seen that the wear rates of all samples under 5 and 20N loads are minimum and maximum, respectively. The wear rate for Inconel 625 (HVOF) and NiCrCoAlY (HVOF) increased. As far as Al8Si20BN (HVOF) is concerned, the wear rate of samples under 20 N loads soars around 110 μm. For both ceramic coatings (Al_2O_3-13TiO_2 (plasma) and Cr_3C_2-25NiCr (HVOF)) the minimum wear rate was recorded. In both groups, the wear rate increased steadily, but the wear rate of Cr_3C_2-25NiCr was ultimately lower. According to this comparison, Cr_3C_2-25NiCr (HVOF) exhibits the highest wear resistivity in this research.

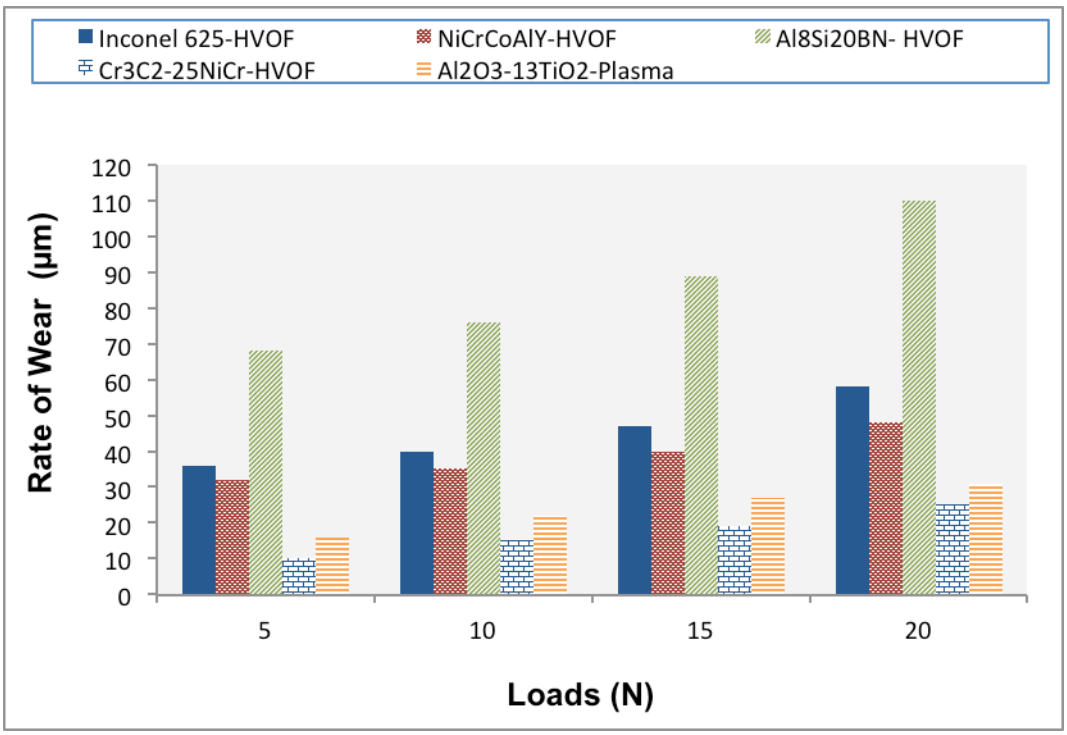

Figure 4.56 Comparison of the wear rate of selected samples from each group under different loads

4.8.2 Comparison of corrosion rate

Figure 4.57 depicts the corrosion resistivity of five different groups of material that were chosen from sections4.2 to 4.6, in 3.5%NaCl solution at 30°C, over 30 days. Regarding Figure 4.57, the corrosion resistivity of all samples at the beginning of the period was high, while at the end, the resistivity decreased and behaved differently. For example, the corrosion resistivity of Inconel 625 (HVOF) slightly decreased from day 3 to day 30. But the corrosion resistivity of NiCrCoAlY (plasma) decreased gradually from day 3 to day 12, while between day 12 and 18 it displayed fluctuating behavior.

After day 18, the corrosion resistivity decreased with a similar trend as Inconel 625 (HVOF). Al8Si20BN (HVOF) had the lowest corrosion resistivity among the samples selected from sections4.2 to 4.6. The figure shows that the R_{ct} of this sample plunged from the beginning to the end of the period. Al_2O_3-$13TiO_2$ (plasma) and Cr_3C_2-25NiCr (HVOF) have the highest corrosion resistivity among the groups. Also, the R_{ct}

trend for both types of ceramic samples is quite similar. However, Cr_3C_2-25NiCr (HVOF) has higher corrosion resistivity than Al_2O_3-13TiO_2 (plasma), as the R_{ct} of this group declined steadily from day 3 to day 30. Consequently, the Cr_3C_2-25NiCr (HVOF) sample has the highest corrosion resistivity among the samples.

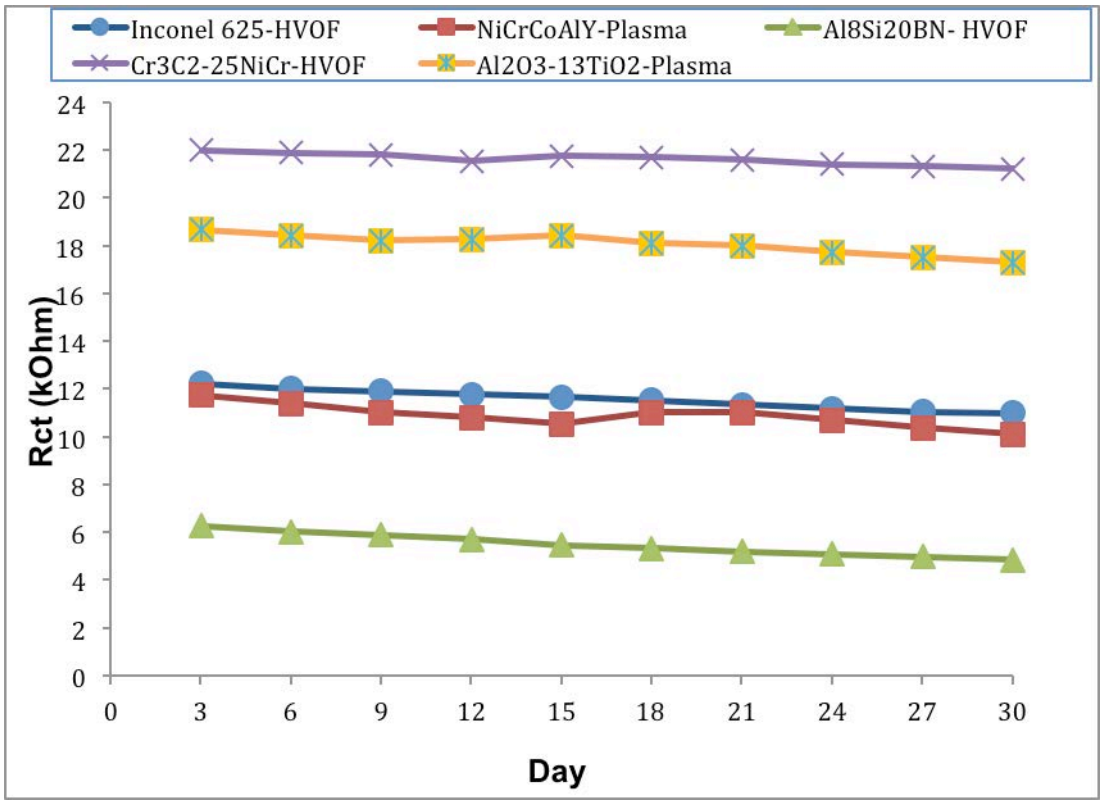

Figure 5.57 Comparison of the corrosion rate of selected samples from each group for 30 days

4.9 Summary

In this chapter the microstructure, wear and corrosion behavior of powders with different chemical compositions and various conditions was investigated. Before any type of testing, the morphology of each group of materials was investigated by XRD and FESEM. Then a pin-on-disk machine with different loads tested each group of materials. The average wear and weight loss rate were calculated and FESEMs of each sample under maximum load (20 N) were done.

To investigate the corrosion behavior of each sample, two different solutions

(seawater and crude oil) were used. The samples were suspended in crude oil for 30 days, after which the surface of the corroded samples was investigated by FESEM. An Autolab machine was used to measure potentiodynamic polarization and electrochemical impedance spectroscopy of each group of materials in 3.5% NaCl (seawater) solution; the rate of corrosion was then calculated for each group of materials. Comparison FESEMs of the corroded samples in seawater and crude oil also showed that all samples in seawater were more corroded than in crude oil.

CHAPTER 5: CONCLUSIONS AND SUGGESTION FOR FUTURE WORK

5.1 Conclusions

Carbon steel is a very common material utilized in offshore and onshore systems by oil and gas companies. This material has good properties in contrast to price. However, its behavior against aggressive environments is not so good.

Nowadays, the properties of carbon steel have been improved by overlay cladding method. This method enhances the properties of carbon steel against aggressive environments, but it causes some defects in the deposited layer and carbon steel; besides, it is time consuming and costly.

In this research, an attempt is made to increase the quality of carbon steel with two different types of thermal spray coating techniques (plasma and HVOF). Thermal spray coating can provide thick coatings of around 20 micrometers to several millimeters, depending on the process and feedstock. It also has high deposition rate as compared to other coating processes, such as electroplating, and physical and chemical vapor deposition. Coating materials available for thermal spraying include metals, alloys, ceramics, plastics and composites. However, in overlay cladding only alloy can be used. The resulting coatings with this method have very high quality, such as high density and homogeneity. This technique is also very fast and has a low cost.

In this study, five composites with different chemical compositions and specific properties were selected for deposition by plasma and HVOF methods on carbon steel substrate. For each group of materials, the corrosion, wear and microstructure were tested under different conditions. A list of conclusions for the five materials with different chemical compositions is given as follows:

1. Inconel 625 with HVOF coating has superior mechanical and chemical properties over plasma coating. Also, the wear rate of HVOF-coated samples under

different loads is lower than with the plasma method. Finally, HVOF-coated samples have higher charge transfer resistance R_{ct} compared to plasma samples, due to the higher resistance of the Inconel 625 HVOF coating against corrosion compared to plasma coating.

2. The morphological, microstructural and compositional analyses for NiCrCoAlY with both coating methods show the corrosion resistivity of this chemical composition in seawater (3.5%NaCl) and crude oil after 30 days. The rate of corrosion with HVOF coating is higher than with plasma coating. This result suggests that the potential impact of plasma thermal spraying against a corrosive environment is better than HVOF spraying systems. The wear resistance with the HVOF method is also superior to plasma-coated samples, and the wear rate with the HVOF method is lower than with plasma coating. Therefore, for this chemical composition and according to its application, plasma and HVOF methods can be selected for corrosion and wear resistivity, respectively.

3. Regarding Al8Si20BN coated by HVOF method, the microstructural analysis, wear and corrosion results show it has higher performance than plasma coating. However, both polarization and EIS results confirm the corrosion protection properties of both plasma and HVOF coating. Nonetheless, the corrosion resistivity of HVOF-coated samples is higher than of plasma. In addition, the tribological properties of HVOF-coated samples under different loads applied are more durable; also, the weight loss rate of these samples is limited, especially under loads of 5 N and 10 N. Thus, for this group of chemical composition materials, the HVOF method exhibits higher wear and corrosion resistivity.

4. Cr_3C_2-25NiCr coated samples underwent significant changes in carbon steel properties in terms of corrosion and tribological performance. HVOF-coated samples

had greater corrosion resistance than plasma-coated samples during testing for 30 days. Also, both polarization and EIS results confirm the better corrosion protection properties of HVOF coating rather than plasma coating. In addition, the tribological properties of HVOF-coated samples under different loads applied exhibit more durability. The weight loss rate of these samples is very limited, but there was a small difference between the wear rate of plasma and HVOF-coated samples.

5. According to the wear and corrosion results, the Al_2O_3-13%TiO_2 chemical composite coated by plasma displayed superior mechanical and chemical properties over the HVOF method. According to the XRD of plasma-coated samples, 13wt% TiO_2 contained fully and partially melted regions of γ-Al_2O_3. Also, the wear rate of plasma-coated samples under different loads was less than HVOF-coated samples. Finally, the plasma-coated samples displayed higher charge transfer resistances R_{ct} compared to the HVOF samples, due to the higher resistance of the Al_2O_3-13%TiO_2 plasma method against corrosion compared to the HVOF method.

A comparison of wear and corrosion behavior of powders with different chemical compositions coated by plasma and HVOF methods shows that the ceramic composite powder experienced the highest significant wear and corrosion resistivity in an aggressive environment. However, the Cr_3C2-25NiCr powder coated by HVOF method showed higher resistivity than other ceramic composite powders.

5.2 Suggestions for future work

Densely deposited Cr_3C_2-25%NiCr structure is among the structures that can be obtained with the thermal spray method when deposition is done with suitable parameters. Where corrosion is the main issue with any device or piping, increasing the percentage of NiCr can increase the efficiency of corrosion control. It is certain that depositing this cermet by any type of thermal spray coating, especially the HVOF

method, can yield magnificent corrosion resistivity structures for oil and gas piping. In addition, by depositing metal alloys, such as Nickel base alloy as a bond coat, it is possible to produce higher interface bond strength to increase piping efficiency in aggressive environments. In addition to the erosion-corrosion of each them can be investigated simultaneously. Finally this type of chemical composite materials and methods can be applied on the surface of different part of equipment and devices of refractory and investigated with different condition.

REFRENCES

Aaltonen, Timo, Adelman, J, Akimoto, T, González, B Álvarez, Amerio, S, Amidei, D, . . . Apollinari, G. (2009). Observation of electroweak single top-quark production. *Physical review letters, 103*(9), 092002.

Abdel-Salam, Mohamed RH, Fauchoux, Melanie, Ge, Gaoming, Besant, Robert W, & Simonson, Carey J. (2014). Expected energy and economic benefits, and environmental impacts for liquid-to-air membrane energy exchangers (LAMEEs) in HVAC systems: A review. *Applied Energy, 127*, 202-218.

Abioye, TE, McCartney, DG, & Clare, AT. (2015). Laser cladding of Inconel 625 wire for corrosion protection. *Journal of Materials Processing Technology, 217*, 232-240.

Abraham, Abigail Asha, Rezayi, Majid, Manan, Ninie SA, Narimani, Leila, Rosli, Ahmad Nazmi Bin, & Alias, Yatimah. (2015). A Novel Potentiometric Sensor Based on 1, 2-Bis (N'-benzoylthioureido) benzene and Reduced Graphene Oxide for Determination of Lead (II) Cation in Raw Milk. *Electrochimica Acta, 165*, 221-231.

Afrasiabi, Abbas, Saremi, Mohsen, & Kobayashi, Akira. (2008). A comparative study on hot corrosion resistance of three types of thermal barrier coatings: YSZ, YSZ+ Al 2 O 3 and YSZ/Al 2 O 3. *Materials Science and Engineering: A, 478*(1), 264-269.

Ahmed, N, Bakare, MS, McCartney, DG, & Voisey, KT. (2010). The effects of microstructural features on the performance gap in corrosion resistance between bulk and HVOF sprayed Inconel 625. *Surface and Coatings Technology, 204*(14), 2294-2301.

Ahmed, Nauman, Voisey, KT, & McCartney, DG. (2014). Supplementary Microstructural Features Induced During Laser Surface Melting of Thermally

Sprayed Inconel 625 Coatings. *Journal of thermal spray technology, 23*(3), 402-409.

Ahn, Jeehoon, Hwang, Byoungchul, Song, Eun Pil, Lee, Sunghak, & Kim, Nack J. (2006). Correlation of microstructure and wear resistance of Al_2O_3-TiO_2 coatings plasma sprayed with nanopowders. *Metallurgical and Materials Transactions A, 37*(6), 1851-1861.

Aktacir, Mehmet Azmi, Büyükalaca, Orhan, & Yılmaz, Tuncay. (2006). Life-cycle cost analysis for constant-air-volume and variable-air-volume air-conditioning systems. *Applied energy, 83*(6), 606-627.

Al-Fadhli, HY, Stokes, J, Hashmi, MSJ, & Yilbas, BS. (2006). The erosion–corrosion behaviour of high velocity oxy-fuel (HVOF) thermally sprayed inconel-625 coatings on different metallic surfaces. *Surface and Coatings Technology, 200*(20), 5782-5788.

Al-Odwani, A, Al-Tabtabaei, M, Al-Hashim, A, Carew, J, & Al-Atram, F. (2000). Erosion of construction materials in a reverse osmosis plant utilizing seawater in Kuwait. *Desalination, 129*(2), 137-145.

Aneziris, Christos G, Dudczig, Steffen, Gerlach, Nora, Berek, Harry, & Veres, Daniel. (2010). Thermal shock performance of fine grained Al2O3 ceramics with TiO_2 and ZrO_2 additions for refractory applications. *Advanced Engineering Materials, 12*(6), 478-485.

Angrisani, Giovanni, Roselli, Carlo, Sasso, Maurizio, & Tariello, Francesco. (2014). Dynamic performance assessment of a micro-trigeneration system with a desiccant-based air handling unit in Southern Italy climatic conditions. *Energy Conversion and Management, 80*, 188-201.

Antaki, George. (2008). Piping Systems. *Kirk-Othmer Encyclopedia of Chemical Technology*.

Arafin, MA, Medraj, M, Turner, DP, & Bocher, P. (2007). Transient liquid phase bonding of Inconel 718 and Inconel 625 with BNi-2: Modeling and experimental investigations. *Materials Science and Engineering: A, 447*(1), 125-133.

Astm, C. (1999). 876. *Standard test method for half-cell potentials of uncoated reinforcing steel in Concrete*.

Azarmi, F, & Salimijazi, HR. (2014). Grain growth and pore elimination in Inconel 625 deposited by APS. *Surface and Coatings Technology*.

Baboian, Robert, & Haynes, G. (2005). Corrosion of Clad Metals. *ASM Handbook, 13*, 887-890.

Bennett, A. (1986). Properties of thermal barrier coatings. *Materials Science and Technology, 2*(3), 257-261.

Berndt, Christopher C. (2001). *Thermal Spray 2001: New Surfaces for a New Millennium: Proceedings of the International Thermal Spray Conference*: ASM International.

Berndt, Marita L, & Berndt, Christopher C. (2003). Thermal spray coatings. *Corrosion: Fundamentals, Testing, and Protection, 13*, 803-813.

Biermann, Frank, & Pattberg, Philipp. (2008). Global environmental governance: Taking stock, moving forward. *Annual Review of Environment and Resources, 33*, 277-294.

Blanc, Ch, & Mankowski, G. (1997). Susceptibility to pitting corrosion of 6056 aluminium alloy. *Corrosion science, 39*(5), 949-959.

Blank, Rodney K, Gahan, Richard J, Haselhuhn Jr, Howard J, Schierbeek, Kenneth L, & Schofield, Kenneth. (1997). To compensate for effect of a deviating magnetic field in a vehicle compass: Google Patents.

Bobzin, K, Kopp, N, Warda, T, & Öte, M. (2012). Determination of the effective properties of thermal spray coatings using 2D and 3D models. *Journal of thermal spray technology*, *21*(6), 1269-1277.

Bobzin, Kirsten, Kopp, Nils, Warda, Thomas, Schulz, Christiane, Rolink, Gesa, & Weisheit, Andreas. (2013). Investigation of Wear and Corrosion Protection of AlSi20 Coatings Produced by Plasma Spraying and Laser Cladding on AZ31B. *Journal of thermal spray technology*, *22*(2-3), 207-212.

Boussu, Katleen, Van der Bruggen, Bart, Volodin, A, Snauwaert, Johan, Van Haesendonck, Christian, & Vandecasteele, Carlo. (2005). Roughness and hydrophobicity studies of nanofiltration membranes using different modes of AFM. *Journal of colloid and interface science*, *286*(2), 632-638.

Cadenas, M, Vijande, R, Montes, HJ, & Sierra, JM. (1997). Wear behaviour of laser cladded and plasma sprayed WC Co coatings. *Wear*, *212*(2), 244-253.

Cai, MeiRong, Guo, RuiSheng, Zhou, Feng, & Liu, WeiMin. (2013). Lubricating a bright future: Lubrication contribution to energy saving and low carbon emission. *Science China Technological Sciences*, *56*(12), 2888-2913.

Cailleret, Michel, Amadou, Aïssata, Andrieu-Abadie, Nathalie, Nawrocki, Artur, Adamy, Christophe, Ait-Mamar, Bouziane, . . . Pavoine, Catherine. (2004). N-Acetylcysteine prevents the deleterious effect of tumor necrosis factor-α on calcium transients and contraction in adult rat cardiomyocytes. *Circulation*, *109*(3), 406-411.

Cecchinato, Luca. (2010). Part load efficiency of packaged air-cooled water chillers with inverter driven scroll compressors. *Energy Conversion and Management*, *51*(7), 1500-1509.

Chaiwongsa, Praitoon, & Duangthongsuk, Weerapun. (2011). Hot water making potential using of a conventional air-conditioner as an air-water heat pump. *Procedia Engineering, 8*, 165-170.

Chan, MY, Deng, SM, & Xu, XG. (2009). Residential indoor humidity control in tropics and sub-tropics. *Building Services Engineering Research and Technology, 30*(2), 169-173.

Chang, Chenchen, Zhao, Jing, & Zhu, Neng. (2011). Energy saving effect prediction and post evaluation of air-conditioning system in public buildings. *Energy and Buildings, 43*(11), 3243-3249.

Chang, Cheng, Jiang, Yi, & Wei, Qingpeng. (2014). Evaluation of terminal coupling and its effect on the total delta-T of chilled water systems with fan coil units. *Energy and Buildings, 72*, 390-397.

Chatha, Sukhpal Singh, Sidhu, Hazoor S, & Sidhu, Buta S. (2012). High temperature hot corrosion behaviour of NiCr and Cr_3C_2–NiCr coatings on T91 boiler steel in an aggressive environment at 750 C. *Surface and Coatings Technology, 206*(19), 3839-3850.

Chatterjee, UK, Bose, Sanjay K, & Roy, Salil K. (2001). *Environmental Degradation of Metals: Corrosion Technology Series/14*: CRC Press.

Chen, WR, Wu, X, Marple, BR, Lima, RS, & Patnaik, PC. (2008). Pre-oxidation and TGO growth behaviour of an air-plasma-sprayed thermal barrier coating. *Surface and Coatings Technology, 202*(16), 3787-3796.

Cheng, Zhi Fang, Ding, Hong Sheng, Rong, Hui, & Zhao, Li Geng. (2013). Abrasion Resistance of Alumina-Titanium Dioxid Coating at High Temperature. *Applied Mechanics and Materials, 302*, 115-118.

Choi, WB, Chung, DS, Kang, JH, Kim, HY, Jin, YW, Han, IT, . . . Park, GS. (1999). Fully sealed, high-brightness carbon-nanotube field-emission display. *Applied physics letters, 75*(20), 3129-3131.

Contreras, A, Albiter, A, Salazar, M, & Perez, R. (2005). Slow strain rate corrosion and fracture characteristics of X-52 and X-70 pipeline steels. *Materials Science and Engineering: A, 407*(1), 45-52.

Cooper, KP, Slebodnick, P, & Thomas, ED. (1996). Seawater corrosion behavior of laser surface modified Inconel 625 alloy. *Materials Science and Engineering: A, 206*(1), 138-149.

Craig, Bruce D. (1998). Selection guidelines for corrosion resistant alloys in the oil and gas industry. *Chemical engineering world, 33*, 57-60.

Craig, Bruce D, & Smith, Liane. (2011). Corrosion Resistant Alloys (CRAs) in the oil and gas industry. *Nickel Institute Technical Series*(1), 0073.

Cramer, SD, Covino Jr, BS, Holcomb, GR, Bullard, SJ, Collins, WK, Govier, RD, . . . Laylor, HM. (1999). Thermal sprayed titanium anode for cathodic protection of reinforced concrete bridges. *Journal of thermal spray technology, 8*(1), 133-145.

Cramer, Stephen D, & Covino, Bernard S. (2003). *Corrosion: Fundamentals, Testing, and Protection* (Vol. 13A): Materials Park.

Cramer, Stephen D, & Covino, Bernard S. (2006). *Corrosion: Environments and industries* (Vol. 13): ASM International.

Daisey, Joan M, Angell, William J, & Apte, Michael G. (2003). Indoor air quality, ventilation and health symptoms in schools: an analysis of existing information. *Indoor air, 13*(1), 53-64.

Davis, Joseph R. (2001). *Surface engineering for corrosion and wear resistance*: ASM international.

Davis, Joseph R. (2004). *Handbook of thermal spray technology*: ASM international.

Dejang, N, Limpichaipanit, A, Watcharapasorn, A, Wirojanupatump, S, Niranatlumpong, P, & Jiansirisomboon, S. (2011). Fabrication and Properties of Plasma-Sprayed Al2O3/ZrO2 Composite Coatings. *Journal of thermal spray technology, 20*(6), 1259-1268.

Dent, AH, Horlock, AJ, McCartney, DG, & Harris, SJ. (2000). Microstructure formation in high velocity oxy-fuel thermally sprayed Ni–Cr–Mo–B alloys. *Materials Science and Engineering: A, 283*(1), 242-250.

Di Ferdinando, Martina, Fossati, Alessio, Lavacchi, Alessandro, Bardi, Ugo, Borgioli, Francesca, Borri, Claudia, . . . Scrivani, Andrea. (2010). Isothermal oxidation resistance comparison between air plasma sprayed, vacuum plasma sprayed and high velocity oxygen fuel sprayed CoNiCrAlY bond coats. *Surface and Coatings Technology, 204*(15), 2499-2503.

Douglas, G. (2013). Thermal Spray Coating. *ADVANCED MATERIALS & PROCESSES*, 15.

Eadie, RL, Szklarz, KE, & Sutherby, RL. (2005). Corrosion fatigue and near-neutral pH stress corrosion cracking of pipeline steel and the effect of hydrogen sulfide. *Corrosion, 61*(2), 167-173.

Eason, Paul D, Fewkes, Jason A, Kennett, Shane C, Eden, Timothy J, Tello, Karem, Kaufman, Michael J, & Tiryakioğlu, Murat. (2011). On the characterization of bulk copper produced by cold gas dynamic spray processing in as fabricated and annealed conditions. *Materials Science and Engineering: A, 528*(28), 8174-8178.

Eckert, Frank, & Klamt, Andreas. (2002). Fast solvent screening via quantum chemistry: COSMO-RS approach. *AIChE Journal, 48*(2), 369-385.

El Rayes, Magdy M, Abdo, Hany S, & Khalil, Khalil Abdelrazek. (2013). Erosion-Corrosion of Cermet Coating. *International Journal of Electrochemical Science, 8*(1).

Eliaz, N, Shemesh, G, & Latanision, RM. (2002). Hot corrosion in gas turbine components. *Engineering Failure Analysis, 9*(1), 31-43.

ElSherbini, AI, & Maheshwari, GP. (2010). Impact of shading air-cooled condensers on the efficiency of air-conditioning systems. *Energy and Buildings, 42*(10), 1948-1951.

Enos, Paul, Jiayong, Wei, & Yangji, Yan. (1997). Facies distribution and retreat of Middle Triassic platform margin, Guizhou province, south China. *Sedimentology, 44*(3), 563-584.

Espallargas, N, Berget, J, Guilemany, JM, Benedetti, AV, & Suegama, PH. (2008). Cr_3C_2–NiCr and WC–Ni thermal spray coatings as alternatives to hard chromium for erosion–corrosion resistance. *Surface and Coatings Technology, 202*(8), 1405-1417.

Fantana, F, Goldoni, D, & Grandi, G. (1992). Visualization of Ribosomal Gene Activity in Oogenesis of Reticulitermes Iucifugus (Isoptera: Rhinotermitidae) Revealed by Silver Staining. *Cytologia, 57*(2), 223-226.

Fauchais, Pierre, Montavon, Ghislain, & Bertrand, Ghislaine. (2010). From powders to thermally sprayed coatings. *Journal of thermal spray technology, 19*(1-2), 56-80.

Fernández, Ea, Cadenas, Ma, González, Ra, Navas, Carmen, Fernández, Ra, & Damborenea, J de. (2005). Wear behaviour of laser clad NiCrBSi coating. *Wear, 259*(7), 870-875.

Fervel, V, Normand, B, Liao, H, Coddet, C, Beche, E, & Berjoan, R. (1999). Friction and wear mechanisms of thermally sprayed ceramic and cermet coatings. *Surface and Coatings Technology, 111*(2), 255-262.

Fleury, Eric, Kim, Yu-Chan, Kim, Jae-Soo, Ahn, Hyo-Sok, Lee, Sang-Mok, Kim, Won-Tae, & Kim, Do-Hyang. (2002). Sliding friction and wear behavior of Al–Ni–Co–Si quasicrystalline coatings deposited by the high-velocity oxy-fuel spraying technique. *Journal of materials research, 17*(02), 492-501.

Fleury, L, Segura, J-M, Zumofen, G, Hecht, B, & Wild, UP. (2000). Nonclassical photon statistics in single-molecule fluorescence at room temperature. *Physical review letters, 84*(6), 1148.

Flitt, Harvey J, & Schweinsberg, D Paul. (2005). A guide to polarisation curve interpretation: deconstruction of experimental curves typical of the Fe/H 2 O/H+/O 2 corrosion system. *Corrosion Science, 47*(9), 2125-2156.

Frankel, GS, Stratmann, M, Rohwerder, M, Michalik, A, Maier, B, Dora, J, & Wicinski, M. (2007). Potential control under thin aqueous layers using a Kelvin Probe. *Corrosion science, 49*(4), 2021-2036.

Galvan-Martinez, R, Salazar, M, Orozco-Cruz, R, Morales-Cabrera, MA, & Contreras, A. (2013). Corrosion Study of Pipeline Steel Weld Immersed in Sour Solution. *Journal of Petroleum Science Research, 2*(4).

Ganesh, P, Kaul, R, Paul, CP, Tiwari, Pragya, Rai, SK, Prasad, RC, & Kukreja, LM. (2010). Fatigue and fracture toughness characteristics of laser rapid manufactured Inconel 625 structures. *Materials Science and Engineering: A, 527*(29), 7490-7497.

Gao, Pei-Hu, Li, Yi-Gong, Li, Chang-Jiu, Yang, Guan-Jun, & Li, Cheng-Xin. (2008). Influence of powder porous structure on the deposition behavior of cold-sprayed WC-12Co coatings. *Journal of Thermal Spray Technology, 17*(5-6), 742-749.

Gaona, M, Lima, Rogerio S, & Marple, Basil Richard. (2008). Influence of particle temperature and velocity on the microstructure and mechanical behaviour of high velocity oxy-fuel (HVOF)-sprayed nanostructured titania coatings. *Journal of materials processing technology, 198*(1), 426-435.

Geaman, Virgil, Pop, Mihai Alin, Motoc, Dana Luca, & Radomir, Irinel. (2014). TRIBOLOGICAL PROPERTIES OF THERMAL SPRAY COATINGS. *European Scientific Journal, 9*(10).

Ghosh, Subir, Choudhury, Dipankar, Das, Nabangshu Shekhar, & Pingguan-Murphy, Belinda. (2014). Tribological role of synovial fluid compositions on artificial joints—a systematic review of the last 10 years. *Lubrication Science, 26*(6), 387-410.

Ginestet, Stéphane, & Marchio, Dominique. (2010). Control tuning of a simplified VAV system: Methodology and impact on energy consumption and IAQ. *Energy and Buildings, 42*(8), 1205-1214.

Goberman, D, Sohn, YH, Shaw, L, Jordan, E, & Gell, M. (2002a). Microstructure development of Al_2O_3–13wt.% TiO_2 plasma sprayed coatings derived from nanocrystalline powders. *Acta Materialia, 50*(5), 1141-1152.

Goberman, D, Sohn, YH, Shaw, L, Jordan, E, & Gell, M. (2002b). Microstructure development of Al2O3–13wt.% TiO2 plasma sprayed coatings derived from nanocrystalline powders. *Acta Materialia, 50*(5), 1141-1152.

Goward, George W, Grey, Delton A, & Krutenat, Richard C. (1981). Thermal barrier coating for nickel and cobalt base super alloys: Google Patents.

Hartfield-Wünsch, SE, & Tung, SC. (1994). The effect of microstructure on the wear behavior of thermal spray coatings: ASM International, Materials Park, OH (United States).

Hensen, Johannes Laurentius Maria. (1991). *On the thermal interaction of building structure and heating and ventilating system*: Technische Universiteitt Eindhoven.

Herman, Herbert, & Sampath, S. (1996). Thermal spray coatings *Metallurgical and Ceramic Protective Coatings* (pp. 261-289): Springer.

Higuero, V, Belzunce, FJ, & Riba, J. (2009). High temperature oxidation of plasma and HVOF thermal sprayed CoNiCrAlY coatings in simulated gas turbine and furnace environments. *Surface Engineering, 25*(4), 319-325.

Hitchin, Roger, Pout, Christine, & Riviere, Philippe. (2013). Assessing the market for air conditioning systems in European buildings. *Energy and Buildings, 58*, 355-362.

Hoek, Eric MV, Bhattacharjee, Subir, & Elimelech, Menachem. (2003). Effect of membrane surface roughness on colloid-membrane DLVO interactions. *Langmuir, 19*(11), 4836-4847.

Huizenga, C, Abbaszadeh, S, Zagreus, Leah, & Arens, Edward A. (2006). Air quality and thermal comfort in office buildings: results of a large indoor environmental quality survey. *Center for the Built Environment*.

Islak, Serkan, Buytoz, S, Ersöz, E, Orhan, N, Stokes, J, Saleem Hashmı, M, . . . Tosun, N. (2013). Effect on microstructure of TiO_2 rate in Al_2O_3-TiO_2 composite coating produced using plasma spray method.

Javaherdashti, Reza. (1999). A review of some characteristics of MIC caused by sulfate-reducing bacteria: past, present and future. *Anti-corrosion methods and materials, 46*(3), 173-180.

Javaherdashti, Reza. (2000). How corrosion affects industry and life. *Anti-corrosion methods and materials, 47*(1), 30-34.

Jeong, Jongsoo, Saito, Kiyoshi, & Kawai, Sunao. (2011). Static characteristics and efficient control of compression-and absorption-type hybrid air conditioning system. *International journal of refrigeration, 34*(3), 674-685.

Jiang, Jie, Zhao, Huayu, Zhou, Xiaming, Tao, Shunyan, & Ding, Chuanxian. (2012). The effect of ion implantation on the oxidation resistance of vacuum plasma sprayed CoNiCrAlY coatings. *Applied Surface Science, 261*, 422-430.

Jodoin, B, Ajdelsztajn, L, Sansoucy, E, Zúñiga, A, Richer, P, & Lavernia, Enrique J. (2006). Effect of particle size, morphology, and hardness on cold gas dynamic sprayed aluminum alloy coatings. *Surface and Coatings Technology, 201*(6), 3422-3429.

Jones, D.A. (1996). *Principles and prevention of corrosion* (2nd ed.): Prentice Hall.

Jordan, Eric H, Gell, M, Sohn, YH, Goberman, D, Shaw, L, Jiang, S, . . . Strutt, P. (2001). Fabrication and evaluation of plasma sprayed nanostructured alumina–titania coatings with superior properties. *Materials Science and Engineering: A, 301*(1), 80-89.

Joudi, Khalid A, & Al-Amir, Qusay R. (2014). Experimental Assessment of residential split type air-conditioning systems using alternative refrigerants to R-22 at high ambient temperatures. *Energy Conversion and Management, 86*, 496-506.

Jubran, Bassam A, Al-Hinai, Hilal A, Zurigat, Yousef H, & Al-Salti, Sami. (2003). Feasibility of using various photovoltaic systems for window-type air-conditioning units under hot-arid climates. *Renewable energy, 28*(10), 1545-1553.

Juchniewicz, Romuald, Jankowski, Jezmar, & Darowicki, Kazimierz. (2000). Cathodic and Anodic Protection. *Materials Science and Technology*.

Kashani, H, Amadeh, A, & Ghasemi, HM. (2007). Room and high temperature wear behaviors of nickel and cobalt base weld overlay coatings on hot forging dies. *Wear, 262*(7), 800-806.

Kato, K. (2006). Classification of wear mechanisms/models. *Wear: Materials, Mechanisms and Practice*, 9-20.

Kato, Koji. (2000). Wear in relation to friction—a review. *Wear, 241*(2), 151-157.

Khan, M Adam, Sundarrajan, S, Natarajan, S, Parameswaran, P, & Mohandas, E. (2014). Oxidation and Hot Corrosion Behavior of Nickel-Based Superalloy for Gas Turbine Applications. *Materials and manufacturing processes, 29*(7), 832-839.

Knorovsky, GA, & Kwiatkowski, JJ. (1989). An initial investigation of the ultrasonic welding of Tophet C bridgewire to Hastelloy C-276: Sandia National Labs., Albuquerque, NM (USA).

Knuuttila, J, Ahmaniemi, S, Leivo, E, Sorsa, P, Vuoristo, P, & Mäntylä, T. (1998). *Wet abrasion and slurry erosion resistance of sealed oxide coatings.* Paper presented at the Thermal Spray: Meeting the Challenges of the 21st Century.

Koyuncu, Ismail, Brant, Jonathan, Lüttge, Andreas, & Wiesner, Mark R. (2006). A comparison of vertical scanning interferometry (VSI) and atomic force microscopy (AFM) for characterizing membrane surface topography. *Journal of membrane science, 278*(1), 410-417.

Krepski, Richard P. (1994). Thermal spray coating applications in the chemical process industries. *R. P. Krepski, 252*.

Kushner, B. (1992). Thermal spray coatings. *ASM International, ASM Handbook, 18*, 829-833.

Lacroix, Loıc, Blanc, Christine, Pébere, Nadine, Thompson, GE, Tribollet, Bernard, & Vivier, Vincent. (2012). Simulating the galvanic coupling between S-Al 2

CuMg phase particles and the matrix of 2024 aerospace aluminium alloy. *Corrosion Science, 64*, 213-221.

Lai, George Y. (2007). *High-temperature corrosion and materials applications*: ASM International.

Laul, Komal, Dorfman, Mitchell R, & Somoskey Jr, Ronald Eugene. (2001). Method for preparing a thermal spray powder of chromium carbide and nickel chromium: Google Patents.

Lee, DB, Ko, JH, & Kwon, SC. (2005). Oxidation of Ni–W coatings at 700 and 800° C in air. *Surface and Coatings Technology, 193*(1), 292-296.

Lee, SM, Fleury, E, Kim, JS, Kim, YC, Kim, DH, Kim, WT, & Ahn, HS. (2000). *Potential industrial applications of Al-based quasicrystals: plasma sprayed vs. HVOF sprayed coatings.* Paper presented at the MRS Proceedings.

Lei, Bing, Li, Man, Zhao, Zhongxing, Wang, Lu, Li, Ying, & Wang, Fuhui. (2014). Corrosion mechanism of an Al–BN abradable seal coating system in chloride solution. *Corrosion Science, 79*, 198-205.

Li, Bao-An, Chen, Lie-Wen, & Ko, Che Ming. (2008). Recent progress and new challenges in isospin physics with heavy-ion reactions. *Physics Reports, 464*(4), 113-281.

Li, Chang-Jiu, Ji, Gang-Chang, Wang, Yu-Yue, & Sonoya, Keiji. (2002). Dominant effect of carbide rebounding on the carbon loss during high velocity oxy-fuel spraying of Cr 3 C 2–NiCr. *Thin Solid Films, 419*(1), 137-143.

Li, Chang-Jiu, Yang, Guan-Jun, Gao, Pei-Hu, Ma, Jian, Wang, Yu-Yue, & Li, Cheng-Xin. (2007). Characterization of nanostructured WC-Co deposited by cold spraying. *Journal of thermal spray technology, 16*(5-6), 1011-1020.

Li, Zheng, & Deng, Shiming. (2007). A DDC-based capacity controller of a direct expansion (DX) air conditioning (A/C) unit for simultaneous indoor air

temperature and humidity control–Part I: Control algorithms and preliminary controllability tests. *International journal of refrigeration, 30*(1), 113-123.

Lima, RS, Moreau, C, & Marple, BR. (2007). HVOF-sprayed coatings engineered from mixtures of nanostructured and submicron Al2O3-TiO2 powders: an enhanced wear performance. *Journal of Thermal Spray Technology, 16*(5-6), 866-872.

Liu, Xue-feng, Liu, Jin-ping, Lu, Ji-dong, Liu, Lei, & Zou, Wei. (2012). Research on operating characteristics of direct-return chilled water system controlled by variable temperature difference. *Energy, 40*(1), 236-249.

Liu, Yourong, Fischer, Traugott E, & Dent, Andrew. (2003). Comparison of HVOF and plasma-sprayed alumina/titania coatings—microstructure, mechanical properties and abrasion behavior. *Surface and Coatings Technology, 167*(1), 68-76.

Liu, Z, Cabrero, J, Niang, S, & Al-Taha, ZY. (2007). Improving corrosion and wear performance of HVOF-sprayed Inconel 625 and WC-Inconel 625 coatings by high power diode laser treatments. *Surface and Coatings Technology, 201*(16), 7149-7158.

Lucci, Antonio, Demofonti, Giuseppe, & Spinelli, Carlo Maria. (2011). *CO_2 anthropogenic pipeline transportation.* Paper presented at the Proceedings of the Twenty-first International Offshore and Polar Engineering Conference, Maui, Hawaii, USA.

Lucio-Garcia, MA, Gonzalez-Rodriguez, JG, Casales, M, Martinez, L, Chacon-Nava, JG, Neri-Flores, MA, & Martinez-Villafañe, A. (2009). Effect of heat treatment on H2S corrosion of a micro-alloyed C–Mn steel. *Corrosion Science, 51*(10), 2380-2386.

Luthra, Krishan L. (1985). Kinetics of the Low Temperature Hot Corrosion of Co-Cr-Al Alloys. *Journal of the Electrochemical Society, 132*(6), 1293-1298.

Macdonald, J Ross, & Barsoukov, E. (2005). Impedance spectroscopy: theory, experiment, and applications. *History, 1*, 8.

Magnani, Francesca, Shibata, Yoko, Serrano-Vega, Maria J, & Tate, Christopher G. (2008). Co-evolving stability and conformational homogeneity of the human adenosine A2a receptor. *Proceedings of the National Academy of Sciences, 105*(31), 10744-10749.

Mann, BS, & Arya, Vivek. (2001). Abrasive and erosive wear characteristics of plasma nitriding and HVOF coatings: their application in hydro turbines. *Wear, 249*(5), 354-360.

Mansfeld, Florian. (1990). Electrochemical impedance spectroscopy (EIS) as a new tool for investigating methods of corrosion protection. *Electrochimica Acta, 35*(10), 1533-1544.

Marple, Basil Richard, Lima, Rogerio S, Moreau, Christian, Kruger, Silvio E, Xie, L, & Dorfman, MR. (2007). Yttria-stabilized zirconia thermal barriers sprayed using N2-H2 and Ar-H2 plasmas: influence of processing and heat treatment on coating properties. *Journal of thermal spray technology, 16*(5-6), 791-797.

McPherson, R. (1973). Formation of metastable phases in flame-and plasma-prepared alumina. *Journal of Materials Science, 8*(6), 851-858.

Meier, GH, & Pettit, FS. (1992). High temperature oxidation and corrosion of intermetallic compounds. *Materials science and technology, 8*(4), 331-338.

Miguel, JM, Guilemany, JM, & Vizcaino, S. (2003). Tribological study of NiCrBSi coating obtained by different processes. *Tribology International, 36*(3), 181-187.

Miyai, Yoichi. (2002). Minimization-feasible word line structure for DRAM cell: Google Patents.

Mochizuki, Hiromi, Yokota, Motohiro, & Hattori, Shuji. (2007). Effects of materials and solution temperatures on cavitation erosion of pure titanium and titanium alloy in seawater. *Wear, 262*(5), 522-528.

Mohammadi, SM Hojjat, & Ameri, Mehran. (2013). Energy and exergy analysis of a tri-generation water-cooled air conditioning system. *Energy and Buildings, 67*, 453-462.

Mrdak, Mihailo R. (2013). Karakterizacija aluminijum oksid 40% titanijum dioksid prevlake otporne na habanje. *Vojnotehnički glasnik/Military Technical Courier, 62*(1), 7-22.

Mumtaz, Kamran Aamir, Erasenthiran, Poonjolai, & Hopkinson, Neil. (2008). High density selective laser melting of Waspaloy®. *Journal of materials processing technology, 195*(1), 77-87.

Mumtaz, Kamran, & Hopkinson, Neil. (2009). Top surface and side roughness of Inconel 625 parts processed using selective laser melting. *Rapid Prototyping Journal, 15*(2), 96-103.

Murthy, JKN, & Venkataraman, B. (2006). Abrasive wear behaviour of WC–CoCr and Cr 3 C 2–20 (NiCr) deposited by HVOF and detonation spray processes. *Surface and Coatings Technology, 200*(8), 2642-2652.

Nešić, D, Tan, Ying, Moase, William H, & Manzie, Chris. (2010). *A unifying approach to extremum seeking: Adaptive schemes based on estimation of derivatives.* Paper presented at the Decision and Control (CDC), 2010 49th IEEE Conference on.

Neville, A, Perry, JM, Hodgkiess, T, & Chua, HP. (2000). Wrought and high-velocity oxy fuel sprayed Inconel 625—examination of corrosion aspects. *Proceedings of the Institution of Mechanical Engineers, Part L: Journal of Materials Design and Applications, 214*(1), 41-48.

Neville, Helen J, Bavelier, Daphne, Corina, David, Rauschecker, Josef, Karni, Avi, Lalwani, Anil, . . . Turner, Robert. (1998). Cerebral organization for language in deaf and hearing subjects: biological constraints and effects of experience. *Proceedings of the National Academy of Sciences, 95*(3), 922-929.

Ni, Hongfang, Ling, Xiang, & Peng, Weiwei. (2005). Prevention of Stress Corrosion Cracking in Weld Joint of Type 304 Stainless Steel by Glass-Bead Peening, *25*(3), 152.

Niaz, Akbar, & Bakare, Mayowa Sunday. (2015). Electrochemical corrosion testing and characterization of potential assisted passive layer on HVOF Inconel 625 coating. *Corrosion Reviews, 33*(1-2), 63-76.

Nicoletti, Erika SM, de Souza, Ricardo Dias, & Barros, Sérgio da Cunha. (2009). A practical approach to pipeline corrosion modelling: Part 2-Short-term integrity forecasting. *Journal of Pipeline Engineering, 8*(2).

Nijdam, TJ, Jeurgens, LPH, & Sloof, WG. (2005). Promoting exclusive α-Al_2O_3 growth upon high-temperature oxidation of NiCrAl alloys: experiment versus model predictions. *Acta Materialia, 53*(6), 1643-1653.

Ning, Xian-Jin, Jang, Jae-Hoon, Kim, Hyung-Jun, Li, Chang-Jiu, & Lee, Changhee. (2008). Cold spraying of Al–Sn binary alloy: Coating characteristics and particle bonding features. *Surface and Coatings Technology, 202*(9), 1681-1687.

Normand, B, Fervel, V, Coddet, C, & Nikitine, V. (2000). Tribological properties of plasma sprayed alumina–titania coatings: role and control of the microstructure. *Surface and Coatings technology, 123*(2), 278-287.

Nurminen, Janne, Näkki, Jonne, & Vuoristo, Petri. (2009). Microstructure and properties of hard and wear resistant MMC coatings deposited by laser cladding. *International Journal of Refractory Metals and Hard Materials, 27*(2), 472-478.

Parker, Marshall E, & Peattie, Edward G. (1984). *Pipe Line Corrosion and Cathodic Protection: A Practical Manual for Corrosion Engineers, Technicians, and Field Personnel*: Gulf Professional Publishing.

Pasandideh-Fard, M, Pershin, V, Chandra, S, & Mostaghimi, J. (2002). Splat shapes in a thermal spray coating process: simulations and experiments. *Journal of Thermal Spray Technology, 11*(2), 206-217.

Paul, CP, Ganesh, P, Mishra, SK, Bhargava, P, Negi, J, & Nath, AK. (2007). Investigating laser rapid manufacturing for Inconel-625 components. *Optics & Laser Technology, 39*(4), 800-805.

Pawlowski, Lech. (2008). *The science and engineering of thermal spray coatings*: John Wiley & Sons.

Perez, N. (2004). Electrochemistry and Corrosion Science (pp. 3): Kluwer Academic.

Peters, KR, Whittle, DP, & Stringer, J. (1976). Oxidation and hot corrosion of nickel-based alloys containing molybdenum. *Corrosion Science, 16*(11), 791-804.

Pindera, Marek-Jerzy, Aboudi, Jacob, & Arnold, Steven M. (2000). The effect of interface roughness and oxide film thickness on the inelastic response of thermal barrier coatings to thermal cycling. *Materials Science and Engineering: A, 284*(1), 158-175.

Potts, Philip J. (1987). *A handbook of silicate rock analysis* (Vol. 622): Blackie Glasgow; London.

Qian, M, Li, D, Liu, SB, & Gong, SL. (2010). Corrosion performance of laser-remelted Al–Si coating on magnesium alloy AZ91D. *Corrosion Science, 52*(10), 3554-3560.

R.D. Angal. (2010). Principles and Prevention of Corrosion. *Alpha Science International*, 17-28.

R.G, Kelly, J.R, Scully, D.W, Shoesmith, & R.G, Buchheit. (2002). *Electrochemical Techniques in Corrosion Science and Engineering*: Marcel Dekker.

Rai, Sanjay K, Kumar, Anish, Shankar, Vani, Jayakumar, T, Bhanu Sankara Rao, K, & Raj, Baldev. (2004). Characterization of microstructures in Inconel 625 using X-ray diffraction peak broadening and lattice parameter measurements. *Scripta materialia, 51*(1), 59-63.

Rajendran, R. (2012). Gas turbine coatings–An overview. *Engineering Failure Analysis, 26*, 355-369.

Review, R.W. (2000). *Uhlig's Corrosion Handbook* (2nd ed.): John Wiley & Sons.

Reza Javaherdashti, Chikezie Nwaoha, Henry Tan. (2013). *Corrosion and Materials in the Oil and Gas Industries*: Tailor & Francis Group.

Rezayi, Majid, Karazhian, Reza, Abdollahi, Yadollah, Narimani, Leila, Sany, Seyedeh Belin Tavakoly, Ahmadzadeh, Saeid, & Alias, Yatimah. (2014). Titanium (III) cation selective electrode based on synthesized tris (2pyridyl) methylamine ionophore and its application in water samples. *Scientific reports, 4*.

Rezeka, Sohair F, Attia, Abdel-Hamid, & Saleh, Ahmed M. (2015). Management of air-conditioning systems in residential buildings by using fuzzy logic. *Alexandria Engineering Journal, 54*(2), 91-98.

Richard Bowen, W, & Doneva, Teodora A. (2000). Atomic force microscopy studies of membranes: effect of surface roughness on double-layer interactions and particle adhesion. *Journal of colloid and interface science, 229*(2), 544-549.

Richer, P, Yandouzi, M, Beauvais, L, & Jodoin, B. (2010). Oxidation behaviour of CoNiCrAlY bond coats produced by plasma, HVOF and cold gas dynamic spraying. *Surface and Coatings Technology, 204*(24), 3962-3974.

Richer, P, Zúñiga, A, Yandouzi, M, & Jodoin, B. (2008). CoNiCrAlY microstructural changes induced during cold gas dynamic spraying. *Surface and Coatings Technology, 203*(3), 364-371.

Rigney, David V, & Schilke, Peter W. (1975). Nickle base high temperature abradable material: US Patent 3,879,831.

Roberge, WG, & Lazarian, A. (1999). Davis—Greenstein alignment of oblate spheroidal grains. *Monthly Notices of the Royal Astronomical Society, 305*(3), 615-630.

Rolink, G, Weisheit, A, Biermann, T, Bobzin, K, Öte, M, Linke, TF, . . . Kelbassa, I. (2014). Investigations of laser clad, thermal sprayed and laser remelted AlSi20-coatings on magnesium alloy AZ31B under constant and cycling thermal load. *Surface and Coatings Technology, 259*, 751-758.

Saheb, N, Laoui, T, Daud, AR, Harun, M, Radiman, S, & Yahaya, R. (2001). Influence of Ti addition on wear properties of Al–Si eutectic alloys. *Wear, 249*(8), 656-662.

Sahraoui, Tahar, Fenineche, Nour-Eddine, Montavon, Ghislain, & Coddet, Christian. (2003). Structure and wear behaviour of HVOF sprayed Cr 3 C 2–NiCr and WC–Co coatings. *Materials & design, 24*(5), 309-313.

Sampath, S, Jiang, XY, Matejicek, J, Prchlik, L, Kulkarni, A, & Vaidya, A. (2004). Role of thermal spray processing method on the microstructure, residual stress and properties of coatings: an integrated study for Ni–5 wt.% Al bond coats. *Materials Science and Engineering: A, 364*(1), 216-231.

Sánchez, Enrique, Bannier, Emilie, Vicent, Monica, Moreno, Arnaldo, Salvador, Maria Dolores, Bonache, Victoria, . . . Boccaccini, Aldo R. (2011). Characterization of nanostructured ceramic and cermet coatings deposited by plasma spraying. *International Journal of Applied Ceramic Technology, 8*(5), 1136-1146.

Sánchez Vilches, Enrique Javier, Bannier, Emilie, Vicent, Mónica, Moreno Berto, Arnaldo, Moya, Salvador, Dolores, María, . . . Boccaccini, Aldo R. (2011). Characterization of nanostructured ceramic and cermet coatings deposited by plasma spraying.

Sansoucy, E, Marcoux, P, Ajdelsztajn, L, & Jodoin, B. (2008). Properties of SiC-reinforced aluminum alloy coatings produced by the cold gas dynamic spraying process. *Surface and Coatings Technology, 202*(16), 3988-3996.

Sarbu, Ioan, & Adam, Marius. (2014). Experimental and numerical investigations of the energy efficiency of conventional air conditioning systems in cooling mode and comfort assurance in office buildings. *Energy and Buildings, 85*, 45-58.

Sarikaya, Ozkan, Anik, Selahaddin, Aslanlar, Salim, Okumus, S Cem, & Celik, Erdal. (2007). Al–Si/B 4 C composite coatings on Al–Si substrate by plasma spray technique. *Materials & design, 28*(9), 2443-2449.

Sarikaya, Ozkan, Celik, Erdal, Okumus, S Cem, Aslanlar, Salim, & Anik, Selahaddin. (2005). Effect on residual stresses in plasma sprayed Al–Si/B 4 C composite coatings subjected to thermal shock. *Surface and Coatings Technology, 200*(7), 2497-2503.

Satapathy, BK, & Bijwe, J. (2004). Performance of friction materials based on variation in nature of organic fibres: Part I. Fade and recovery behaviour. *Wear, 257*(5), 573-584.

Schütze, M, Malessa, M, Rohr, V, & Weber, T. (2006). Development of coatings for protection in specific high temperature environments. *Surface and Coatings Technology, 201*(7), 3872-3879.

Scrivani, A, Ianelli, S, Rossi, A, Groppetti, R, Casadei, F, & Rizzi, G. (2001). A contribution to the surface analysis and characterisation of HVOF coatings for petrochemical application. *Wear, 250*(1), 107-113.

Selman, Christopher. (2011). *Condensation Corrosion Modelling, Reality and Design in Deep Water Wet Gas Pipelines.* Paper presented at the The Twenty-first International Offshore and Polar Engineering Conference.

Setayesh, Hassan, Moradi, Hamed, & Alasty, Aria. (2015). A comparison between the minimum-order & full-order observers in robust control of the air handling units in the presence of uncertainty. *Energy and Buildings, 91*, 115-130.

Sexton, L, Lavin, S, Byrne, G, & Kennedy, A. (2002). Laser cladding of aerospace materials. *Journal of Materials Processing Technology*, *122*(1), 63-68.

Shahnavaz, Zohreh, Lorestani, Farnaz, Meng, Woi Pei, & Alias, Yatimah. (2015). Core-shell–CuFe2O4/PPy nanocomposite enzyme-free sensor for detection of glucose. *Journal of Solid State Electrochemistry*, *19*(4), 1223-1233.

Shankar, Vani, Bhanu Sankara Rao, K, & Mannan, SL. (2001). Microstructure and mechanical properties of Inconel 625 superalloy. *Journal of Nuclear Materials, 288*(2), 222-232.

Shen, Bo, Braun, James E, & Groll, Eckhard A. (2009). Improved methodologies for simulating unitary air conditioners at off-design conditions. *international journal of refrigeration*, *32*(7), 1837-1849.

Shukla, VN, Tewari, VK, & Jayaganthan, R. (2011). Comparison of Tribological Behavior of Cr_3C_2/NiCr Coatings Deposited by Different Thermal Spray Techniques: A Review. *Materials Science and Engineering*, *2*(1-2).

Singh, Vinay Pratap, Sil, Anjan, & Jayaganthan, R. (2011). A study on sliding and erosive wear behaviour of atmospheric plasma sprayed conventional and nanostructured alumina coatings. *Materials & Design, 32*(2), 584-591.

Somasundaram, B, Kadoli, Ravikiran, & Ramesh, MR. (2014). Evaluation of Cyclic Oxidation and Hot Corrosion Behavior of HVOF-Sprayed WC-Co/NiCrAlY Coating. *Journal of Thermal Spray Technology*, *23*(6), 1000-1008.

Sreedhar, Gosipathala, Alam, MD Masroor, & Raja, VS. (2009). Hot corrosion behaviour of plasma sprayed YSZ/Al_2O_3 dispersed NiCrAlY coatings on Inconel-718 superalloy. *Surface and Coatings Technology*, *204*(3), 291-299.

Stack, MM, & Abd El Badia, TM. (2006). On the construction of erosion–corrosion maps for WC/Co–Cr-based coatings in aqueous conditions. *Wear*, *261*(11), 1181-1190.

Stoltenhoff, T, Borchers, C, Gärtner, F, & Kreye, H. (2006). Microstructures and key properties of cold-sprayed and thermally sprayed copper coatings. *Surface and Coatings Technology*, *200*(16), 4947-4960.

Takahashi, Masahide, Fukuda, Masahiro, Fukuda, Masaaki, Fukuda, Hisato, & Yoko, Toshinobu. (2002). Preparation, structure, and properties of thermally and mechanically improved aluminum titanate ceramics doped with alkali feldspar. *Journal of the American Ceramic Society*, *85*(12), 3025-3030.

Tang, Zhi, Huang, Lu, He, Wei, & Liaw, Peter K. (2014). Alloying and Processing Effects on the Aqueous Corrosion Behavior of High-Entropy Alloys. *Entropy*, *16*(2), 895-911.

Teerijoki-Oksa, Tuija, Jääskeläinen, Satu K, Soukka, Tero, Virtanen, Arja, & Forssell, Heli. (2011). Subjective sensory symptoms associated with axonal and demyelinating nerve injuries after mandibular sagittal split osteotomy. *Journal of Oral and Maxillofacial Surgery*, *69*(6), e208-e213.

Tianyi, Zhao, Jili, Zhang, & Liangdong, Ma. (2012). On-line optimization control method based on extreme value analysis for parallel variable-frequency hydraulic pumps in central air-conditioning systems. *Building and Environment*, *47*, 330-338.

Tirmizi, Syed A, Gandhidasan, P, & Zubair, Syed M. (2012). Performance analysis of a chilled water system with various pumping schemes. *Applied Energy, 100*, 238-248.

Toma, D, Brandl, W, & Marginean, G. (2001). Wear and corrosion behaviour of thermally sprayed cermet coatings. *Surface and Coatings Technology, 138*(2), 149-158.

Toma, Diana, Brandl, Waltraut, & Köster, Uwe. (1999). Studies on the transient stage of oxidation of VPS and HVOF sprayed MCrAlY coatings. *Surface and Coatings Technology, 120*, 8-15.

Torabian, S, Haddad, E, Rajaram, S, Banta, J, & Sabate, J. (2009). Acute effect of nut consumption on plasma total polyphenols, antioxidant capacity and lipid peroxidation. *Journal of Human Nutrition and Dietetics, 22*(1), 64-71.

Trompetter, W, Hyland, M, McGrouther, Damien, Munroe, Paul, & Markwitz, Andreas. (2006). Effect of substrate hardness on splat morphology in high-velocity thermal spray coatings. *Journal of thermal spray technology, 15*(4), 663-669.

Tucker Jr, RC. (2013). Guide to General Information Sources.

Tuominen, J, Vuoristo, P, Mäntylä, T, Kylmälahti, M, Vihinen, J, & Andersson, PH. (2000). Improving corrosion properties of high-velocity oxy-fuel sprayed inconel 625 by using a high-power continuous wave neodymium-doped yttrium aluminum garnet laser. *Journal of thermal spray technology, 9*(4), 513-519.

Vardelle, M, Vardelle, A, Leger, AC, Fauchais, P, & Gobin, D. (1995). Influence of particle parameters at impact on splat formation and solidification in plasma spraying processes. *Journal of Thermal Spray Technology, 4*(1), 50-58.

Verdi, D, Garrido, MA, Múnez, CJ, & Poza, P. (2014). Mechanical properties of Inconel 625 laser cladded coatings: Depth sensing indentation analysis. *Materials Science and Engineering: A, 598*, 15-21.

Verdi, Davide, Garrido, MA, Múnez, Claudio José, & Poza, Pedro. (2015). Cr_3C_2 incorporation into an Inconel 625 laser cladded coating: Effects on matrix microstructure, mechanical properties and local scratch resistance. *Materials & Design*, *67*, 20-27.

Villalobos, Michele E, Mizuno, Akiko, Dahl, Branelle C, Kemmotsu, Nobuko, & Müller, Ralph-Axel. (2005). Reduced functional connectivity between V1 and inferior frontal cortex associated with visuomotor performance in autism. *Neuroimage*, *25*(3), 916-925.

Volovitch, P, Masse, JE, Fabre, A, Barrallier, L, & Saikaly, W. (2008). Microstructure and corrosion resistance of magnesium alloy ZE41 with laser surface cladding by Al–Si powder. *Surface and Coatings Technology*, *202*(20), 4901-4914.

Wagner, CNJ. (1978). Direct methods for the determination of atomic-scale structure of amorphous solids (X-ray, electron, and neutron scattering). *Journal of Non-Crystalline Solids*, *31*(1), 1-40.

Wang, Bu Qian, & Shui, Zheng Rong. (2002). The hot erosion behavior of HVOF chromium carbide-metal cermet coatings sprayed with different powders. *Wear*, *253*(5), 550-557.

Wang, Weimin, Katipamula, Srinivas, Huang, Yunzhi, & Brambley, Michael R. (2011). Energy Savings and Economics of Advanced Control Strategies for Packaged Air-Conditioning Units with Gas Heat: Pacific Northwest National Laboratory (PNNL), Richland, WA (US).

Wang, Xin, Kwon, Parick Y, Schrock, David, & Kim, Dave. (2013). Friction coefficient and sliding wear of AlTiN coating under various lubrication conditions. *Wear*, *304*(1), 67-76.

Wang, Y, Li, CG, Tian, W, & Yang, Y. (2009). Laser surface remelting of plasma sprayed nanostructured Al2O3–13wt% TiO2 coatings on titanium alloy. *Applied Surface Science, 255*(20), 8603-8610.

Wang, You, Jiang, Stephen, Wang, Meidong, Wang, Shihe, Xiao, T Danny, & Strutt, Peter R. (2000). Abrasive wear characteristics of plasma sprayed nanostructured alumina/titania coatings. *Wear, 237*(2), 176-185.

Wang, Yu, You, Yuwen, & Zhang, Zhigang. (2011). Experimental Investigations on a Conventional Air-conditioner Working as Air-water Heat Pump. *Procedia Engineering, 23*, 493-497.

Wei-jie, LI, Yong, LIU, Yan, WANG, Chao, HAN, & Hui-ping, TANG. (2015). Hot corrosion behavior of Ni–16Cr–xAl based alloys in mixture of Na 2. *The Chinese Journal of Nonferrous Metals, 21*(12).

Wei, P, Deng, X, Bateni, MR, & Petric, A. (2007). Oxidation and electrical conductivity behavior of spinel coatings for metallic interconnects of solid oxide fuel cells. *Corrosion, 63*(6), 529-536.

Wei, Xiupeng, Kusiak, Andrew, Li, Mingyang, Tang, Fan, & Zeng, Yaohui. (2015). Multi-objective optimization of the HVAC (heating, ventilation, and air conditioning) system performance. *Energy, 83*, 294-306.

Whitman, Bill, Johnson, Bill, Tomczyk, John, & Silberstein, Eugene. (2012). *Refrigeration and air conditioning technology*: Cengage Learning.

Woo, Yong-Bin, Lee, Seung-Jun, Jeong, Jae-Yong, & Kim, Seong-Jong. (2014). Evaluation on cavitation characteristics of CoNiCrAlY/ZrO 2–Y 2 O 3 coating layer by atmospheric pressure plasma coating process. *Materials Research Bulletin, 58*, 78-82.

Wu, YS, Zeng, DC, Liu, ZW, Qiu, WQ, Zhong, XC, Yu, HY, & Li, SZ. (2011). Microstructure and sliding wear behavior of nanostructured Ni60–TiB_2

composite coating sprayed by HVOF technique. *Surface and Coatings Technology, 206*(6), 1102-1108.

Xie, Liangde, Ma, Xinqing, Jordan, Eric H, Padture, Nitin P, Xiao, Danny T, & Gell, Maurice. (2004). Deposition mechanisms of thermal barrier coatings in the solution precursor plasma spray process. *Surface and Coatings Technology, 177*, 103-107.

Xu, Gang, He, Wan Bo, Li, Yi Qiang, Wang, Yong Gang, & Han, Gao Rong. (2011). Intragranular Porous Aluminum Titanate Ceramics with Low Thermal Expansion and High Strength Simultaneously. *Advanced Materials Research, 156*, 1713-1716.

Xu, Xiangguo, Deng, Shiming, & Chan, Mingyin. (2008). A new control algorithm for direct expansion air conditioning systems for improved indoor humidity control and energy efficiency. *Energy Conversion and Management, 49*(4), 578-586.

Xu, Xiaoning, Huang, Gongsheng, Liu, Hanwei, Chen, Liuzhi, & Liu, Qingjun. (2015). The study of the dynamic load forecasting model about air-conditioning system based on the terminal user load. *Energy and Buildings, 94*, 263-268.

Yadroitsev, I, & Smurov, I. (2010). Selective laser melting technology: from the single laser melted track stability to 3D parts of complex shape. *Physics Procedia, 5*, 551-560.

Yaghtin, AH, Javadpour, S, & Shariat, MH. (2014). Hot corrosion of nanostructured CoNiCrAlYSi coatings deposited by high velocity oxy fuel process. *Journal of Alloys and Compounds, 584*, 303-307.

Yan, Maocheng, Tallman, Dennis E, & Bierwagen, Gordon P. (2008). Role of oxygen in the galvanic interaction between polypyrrole and aluminum alloy. *Electrochimica Acta, 54*(2), 220-227.

Yang, Huojun, Xu, Zhaofeng, Xiong, Ruibin, Li, Haorong, Zhang, Tian C, Liu, Xiaoyu, & Woradechjumroen, Denchai. (2014). Simplifying manufacturers' data in unitary HVAC equipment through a DX cooling coil modeling. *Energy and Buildings, 74*, 152-162.

Yao, Sun Hui, Su, Yan Liang, & Kao, Wen Xian. (2011). Thermal Shock Performance of Al2O3/TiO2 Air Plasma Spray Coatings. *Advanced Materials Research, 328*, 853-856.

Yao, Ye, & Chen, Jing. (2010). Global optimization of a central air-conditioning system using decomposition–coordination method. *Energy and Buildings, 42*(5), 570-583.

Yau, YH, & Pean, HL. (2014). The performance study of a split type air conditioning system in the tropics, as affected by weather. *Energy and Buildings, 72*, 1-7.

Yılmaz, R, Kurt, AO, Demir, A, & Tatlı, Z. (2007). Effects of TiO< sub> 2</sub> on the mechanical properties of the Al2O3–TiO2 plasma sprayed coating. *Journal of the European Ceramic Society, 27*(2), 1319-1323.

Younis, AA, Ensinger, W, El-Sabbah, MMB, & Holze, R. (2013). Corrosion protection of pure aluminium and aluminium alloy (AA7075) in salt solution with silane-based sol–gel coatings. *Materials and Corrosion, 64*(4), 276-283.

Yu, BF, Hu, ZB, Liu, M, Yang, HL, Kong, QX, & Liu, YH. (2009). Review of research on air-conditioning systems and indoor air quality control for human health. *International journal of refrigeration, 32*(1), 3-20.

Yu, Yuebin, Woradechjumroen, Denchai, & Yu, Daihong. (2014). A review of fault detection and diagnosis methodologies on air-handling units. *Energy and Buildings, 82*, 550-562.

Yuan, FH, Chen, ZX, Huang, ZW, Wang, ZG, & Zhu, SJ. (2008). Oxidation behavior of thermal barrier coatings with HVOF and detonation-sprayed NiCrAlY bondcoats. *Corrosion science, 50*(6), 1608-1617.

Yue, Tai M, Xie, Hui, Lin, Xin, Yang, Haiou, & Meng, Guanghui. (2013). Microstructure of laser re-melted AlCoCrCuFeNi high entropy alloy coatings produced by plasma spraying. *Entropy, 15*(7), 2833-2845.

Yugeswaran, S, Selvarajan, V, Vijay, M, Ananthapadmanabhan, PV, & Sreekumar, KP. (2010). Influence of critical plasma spraying parameter (CPSP) on plasma sprayed alumina–titania composite coatings. *Ceramics International, 36*(1), 141-149.

Yusoff, NHN, Ghazali, MJ, Isa, MC, Daud, AR, Muchtar, A, & Forghani, SM. (2012). Optimization of plasma spray parameters on the mechanical properties of agglomerated Al2O3–13% TiO2 coated mild steel. *Materials & Design, 39*, 504-508.

Zavareh, M Akhtari, Sarhan, Ahmed AD, Razak, B, & Basirun, WJ. (2014). *Electrochemical Characterizations of Different Ceramic Composite Coatings on Carbon Steel Piping Using High Velocity Oxy-Fuel Spray*. Paper presented at the Proceedings of the World Congress on Engineering and Computer Science.

Zavareh, Mitra Akhtari, Sarhan, Ahmed Aly Diaa Mohammed, Razak, Bushroa Binti Abd, & Basirun, Wan Jeffrey. (2014). Plasma thermal spray of ceramic oxide coating on carbon steel with enhanced wear and corrosion resistance for oil and gas applications. *Ceramics International, 40*(9), 14267-14277.

Zavareh, Mitra Akhtari, Sarhan, Ahmed Aly Diaa Mohammed, Razak, Bushroa BintiAbd, & Basirun, Wan Jeffrey. (2015). The tribological and electrochemical behavior of HVOF-sprayed Cr 3 C 2–NiCr ceramic coating on carbon steel. *Ceramics International*.

Zhang, Dawei, & Zhang, Xinping. (2005). Laser cladding of stainless steel with Ni–Cr 3 C 2 and Ni–WC for improving erosive–corrosive wear performance. *Surface and Coatings Technology, 190*(2), 212-217.

Zhang, Haijun, Liu, Chao-Xing, Qi, Xiao-Liang, Dai, Xi, Fang, Zhong, & Zhang, Shou-Cheng. (2009). Topological insulators in Bi2Se3, Bi2Te3 and Sb2Te3 with a single Dirac cone on the surface. *Nature physics, 5*(6), 438-442.

Zhang, Lun, Liu, Xiao-Hua, & Jiang, Yi. (2012). A new concept for analyzing the energy efficiency of air-conditioning systems. *Energy and Buildings, 44*, 45-53.

Zhang, Qiang, Li, Chang-Jiu, Li, Cheng-Xin, Yang, Guan-Jun, & Lui, Siu-Ching. (2008). Study of oxidation behavior of nanostructured NiCrAlY bond coatings deposited by cold spraying. *Surface and Coatings Technology, 202*(14), 3378-3384.

Zhang, Wei-xian. (2003). Nanoscale iron particles for environmental remediation: an overview. *Journal of nanoparticle Research, 5*(3-4), 323-332.

Zhong, XC, Liu, ZW, Wu, YS, Liu, MT, & Zeng, DC. (2014). *Nano-composite coatings with improved mechanical properties and corrosion resistance by thermal spraying*. Paper presented at the IOP Conference Series: Materials Science and Engineering.

Zhu, Yonghua, Jin, Xinqiao, Du, Zhimin, & Fang, Xing. (2015). Online optimal control of variable refrigerant flow and variable air volume combined air conditioning system for energy saving. *Applied Thermal Engineering, 80*, 87-96.

Zhu, Yonghua, Jin, Xinqiao, Du, Zhimin, Fang, Xing, & Fan, Bo. (2014). Control and energy simulation of variable refrigerant flow air conditioning system combined with outdoor air processing unit. *Applied Thermal Engineering, 64*(1), 385-395.

Zhuang, Xiangling, & Wu, Changxu. (2014). Saving energy when using air conditioners in offices—Behavioral pattern and design indications. *Energy and Buildings, 76*, 661-668.

Zimmermann, Stefan, Papp, Uwe, Kreye, Heinrich, & Schmidt, Tobias. (2014). Method for coating a substrate surface and coated product: Google Patents.

(Javaherdashti, 1999, 2000)

(Aaltonen et al., 2009; Abdel-Salam, Fauchoux, Ge, Besant, & Simonson, 2014; Abioye, McCartney, & Clare, 2015; Abraham et al., 2015; Afrasiabi, Saremi, & Kobayashi, 2008; N Ahmed, Bakare, McCartney, & Voisey, 2010; Nauman Ahmed, Voisey, & McCartney, 2014; Ahn et al., 2006; Aktacir, Büyükalaca, & Yılmaz, 2006; Al-Fadhli et al., 2006; Aneziris, Dudczig, Gerlach, Berek, & Veres, 2010; Angrisani, Roselli, Sasso, & Tariello, 2014; Astm, 1999; Azarmi & Salimijazi, 2014; Baboian & Haynes, 2005; Bennett, 1986; Biermann & Pattberg, 2008; Blanc & Mankowski, 1997; Blank, Gahan, Haselhuhn Jr, Schierbeek, & Schofield, 1997; K Bobzin, Kopp, Warda, & Öte, 2012; Kirsten Bobzin et al., 2013; Cailleret et al., 2004; Cecchinato, 2010; Chaiwongsa & Duangthongsuk, 2011; Chan, Deng, & Xu, 2009; Chenchen Chang, Zhao, & Zhu, 2011; Cheng Chang, Jiang, & Wei, 2014; Chatha, Sidhu, & Sidhu, 2012; Chatterjee, Bose, & Roy, 2001; Chen, Wu, Marple, Lima, & Patnaik, 2008; Choi et al., 1999; Cooper et al., 1996; Daisey, Angell, & Apte, 2003; Dent, Horlock, McCartney, & Harris, 2000; Di Ferdinando et al., 2010; Eason et al., 2011; Eckert & Klamt, 2002; Eliaz, Shemesh, & Latanision, 2002; ElSherbini & Maheshwari, 2010; Enos, Jiayong, & Yangji, 1997; Espallargas, Berget, Guilemany, Benedetti, & Suegama, 2008; Fantana, Goldoni, & Grandi, 1992; E. Fleury et al., 2002; L. Fleury, Segura, Zumofen, Hecht, & Wild, 2000; Flitt & Schweinsberg, 2005; Frankel et al., 2007; Gao, Li, Li, Yang, & Li, 2008; Ghosh, Choudhury, Das, & Pingguan-Murphy, 2014; Ginestet & Marchio, 2010; Goberman, Sohn, Shaw, Jordan, & Gell, 2002a; Hartfield-Wünsch & Tung, 1994; Hensen, 1991; Higuero, Belzunce, & Riba, 2009; Hitchin,

Pout, & Riviere, 2013; Huizenga, Abbaszadeh, Zagreus, & Arens, 2006; Jeong, Saito, & Kawai, 2011; Jiang, Zhao, Zhou, Tao, & Ding, 2012; Jodoin et al., 2006; Joudi & Al-Amir, 2014; Jubran, Al-Hinai, Zurigat, & Al-Salti, 2003; Kashani, Amadeh, & Ghasemi, 2007; Koji Kato, 2000; Khan, Sundarrajan, Natarajan, Parameswaran, & Mohandas, 2014; Knorovsky & Kwiatkowski, 1989; Krepski, 1994; Lacroix et al., 2012; Lai, 2007; D. Lee, Ko, & Kwon, 2005; S. Lee et al., 2000; Lei et al., 2014; B.-A. Li, Chen, & Ko, 2008; C.-J. Li, Ji, Wang, & Sonoya, 2002; Z. Li & Deng, 2007; X.-f. Liu, Liu, Lu, Liu, & Zou, 2012; Z. Liu et al., 2007; Luthra, 1985; Macdonald & Barsoukov, 2005; Magnani, Shibata, Serrano-Vega, & Tate, 2008; Mansfeld, 1990; McPherson, 1973; Meier & Pettit, 1992; Miguel, Guilemany, & Vizcaino, 2003; Miyai, 2002; Mochizuki, Yokota, & Hattori, 2007; Mohammadi & Ameri, 2013; Mrdak, 2013; K. A. Mumtaz, Erasenthiran, & Hopkinson, 2008; Murthy & Venkataraman, 2006; Nešić, Tan, Moase, & Manzie, 2010; A. Neville, Perry, Hodgkiess, & Chua, 2000; H. J. Neville et al., 1998; Niaz & Bakare, 2015; Nijdam, Jeurgens, & Sloof, 2005; Ning, Jang, Kim, Li, & Lee, 2008; Nurminen, Näkki, & Vuoristo, 2009; Peters, Whittle, & Stringer, 1976; Pindera, Aboudi, & Arnold, 2000; Qian, Li, Liu, & Gong, 2010; Rajendran, 2012; Rezayi et al., 2014; Rezeka, Attia, & Saleh, 2015; Richer, Yandouzi, Beauvais, & Jodoin, 2010; Richer, Zúñiga, Yandouzi, & Jodoin, 2008; Roberge & Lazarian, 1999; Rolink et al., 2014; Saheb et al., 2001; Sahraoui, Fenineche, Montavon, & Coddet, 2003; Sampath et al., 2004; Sánchez et al., 2011; Sansoucy, Marcoux, Ajdelsztajn, & Jodoin, 2008; Sarbu & Adam, 2014; Sarikaya, Anik, Aslanlar, Okumus, & Celik, 2007; Sarikaya, Celik, Okumus, Aslanlar, & Anik, 2005; Satapathy & Bijwe, 2004; Schütze, Malessa, Rohr, & Weber, 2006; Scrivani et al., 2001; Setayesh, Moradi, & Alasty, 2015; Shahnavaz, Lorestani, Meng, & Alias, 2015; Shen, Braun, & Groll, 2009; Somasundaram, Kadoli, & Ramesh, 2014; Sreedhar,

Alam, & Raja, 2009; Stoltenhoff, Borchers, Gärtner, & Kreye, 2006; Teerijoki-Oksa, Jääskeläinen, Soukka, Virtanen, & Forssell, 2011; Tianyi, Jili, & Liangdong, 2012; Tirmizi, Gandhidasan, & Zubair, 2012; Diana Toma, Brandl, & Köster, 1999; Torabian, Haddad, Rajaram, Banta, & Sabate, 2009; D Verdi, Garrido, Múnez, & Poza, 2014; Davide Verdi, Garrido, Múnez, & Poza, 2015; Villalobos, Mizuno, Dahl, Kemmotsu, & Müller, 2005; Volovitch, Masse, Fabre, Barrallier, & Saikaly, 2008; B. Q. Wang & Shui, 2002; W. Wang, Katipamula, Huang, & Brambley, 2011; Yu Wang, You, & Zhang, 2011; Wei-jie, Yong, Yan, Chao, & Hui-ping, 2015; P. Wei, Deng, Bateni, & Petric, 2007; X. Wei, Kusiak, Li, Tang, & Zeng, 2015; Whitman, Johnson, Tomczyk, & Silberstein, 2012; Woo, Lee, Jeong, & Kim, 2014; Wu et al., 2011; Xiangguo Xu, Deng, & Chan, 2008; Xiaoning Xu, Huang, Liu, Chen, & Liu, 2015; Yadroitsev & Smurov, 2010; Yaghtin, Javadpour, & Shariat, 2014; Yan, Tallman, & Bierwagen, 2008; Yang et al., 2014; Y. Yao & Chen, 2010; Yau & Pean, 2014; B. Yu et al., 2009; Y. Yu, Woradechjumroen, & Yu, 2014; Yuan, Chen, Huang, Wang, & Zhu, 2008; Yue, Xie, Lin, Yang, & Meng, 2013; M. A. Zavareh, A. A. Sarhan, B. Razak, & W. Basirun, 2014; M. A. Zavareh, A. A. D. M. Sarhan, B. B. A. Razak, & W. J. Basirun, 2014; Zavareh, Sarhan, Razak, & Basirun, 2015; D. Zhang & Zhang, 2005; H. Zhang et al., 2009; L. Zhang, Liu, & Jiang, 2012; Q. Zhang, Li, Li, Yang, & Lui, 2008; W.-x. Zhang, 2003; Zhong, Liu, Wu, Liu, & Zeng, 2014; Zhu, Jin, Du, & Fang, 2015; Zhu, Jin, Du, Fang, & Fan, 2014; Zhuang & Wu, 2014; Zimmermann, Papp, Kreye, & Schmidt, 2014)

(Abioye et al., 2015; Afrasiabi et al., 2008; N Ahmed et al., 2010; Ahn et al., 2006; Al-Fadhli et al., 2006; Aneziris et al., 2010; Azarmi & Salimijazi, 2014; Bennett, 1986; Blanc & Mankowski, 1997; Kirsten Bobzin et al., 2013; Chatha et al., 2012; Chatterjee et al., 2001; Chen et al., 2008; Cooper et al., 1996; Dent et al., 2000; Di Ferdinando et al., 2010; Eason et al., 2011; Eliaz et al., 2002; E. Fleury et al., 2002; Gao et al., 2008; Ghosh et al., 2014; Goberman et al., 2002a; Hartfield-Wünsch & Tung, 1994; Higuero et al., 2009; Jiang et al., 2012; Jodoin et al., 2006; Koji Kato, 2000; Khan et al., 2014; Krepski, 1994; Lacroix et al., 2012; Lai, 2007; D. Lee et al., 2005; S. Lee et al., 2000; Lei et al., 2014; C.-J. Li et al., 2002; Z. Liu et al., 2007; Luthra, 1985; McPherson, 1973; Meier & Pettit, 1992; Miguel et al., 2003; Mochizuki et al., 2007; Mrdak, 2013; Murthy & Venkataraman, 2006; A. Neville et al., 2000; Niaz & Bakare, 2015; Nijdam et al., 2005; Ning et al., 2008; Nurminen et al., 2009; Peters et al., 1976; Qian et al., 2010; Rajendran, 2012; Richer et al., 2010; Richer et al., 2008; Rolink et al., 2014; Sampath et al., 2004; Sánchez et al., 2011; Sansoucy et al., 2008; Sarikaya et al., 2007; Sarikaya et al., 2005; Schütze et al., 2006; Scrivani et al., 2001; Somasundaram et al., 2014; Sreedhar et al., 2009; Stoltenhoff et al., 2006; Diana Toma et al., 1999; D Verdi et al., 2014; Davide Verdi et al., 2015; B. Q. Wang & Shui, 2002; Wei-jie et al., 2015; P. Wei et al., 2007; Woo et al., 2014; Wu et al., 2011; Yadroitsev & Smurov, 2010; Yaghtin et al., 2014; Yan et al., 2008; Yuan et al., 2008; Yue et al., 2013; Mitra Akhtari Zavareh et al., 2014; Zavareh et al., 2015; D. Zhang & Zhang, 2005; Q. Zhang et al., 2008; Zhong et al., 2014) (Aktacir et al., 2006; X. Wei et al., 2015; Zhu et al., 2015)

(Zhu et al., 2014) (Abdel-Salam et al., 2014; Jeong et al., 2011; Rezayi et al., 2014)